Electronic Structure of Transition Metal Compounds with Different Nuclearities

Von der Fakultät Chemie der Universität Stuttgart
zur Erlangung der Würde eines Doktors der Naturwissenschaften
(Dr. rer. nat.) genehmigte Abhandlung

Vorgelegt von

Heiko Bamberger

aus Böblingen

Hauptberichter:	Prof. Dr. Joris van Slageren
Mitberichter:	Prof. Dr. Rainer Niewa
Prüfungsvorsitzender:	Prof. Dr. Biprajit Sarkar
Tag der mündlichen Prüfung:	20.04.2022

Institut für Physikalische Chemie der Universität Stuttgart
2022

Erklärung über die Eigenständigkeit der Dissertation

Ich versichere, dass ich die vorliegende Arbeit mit dem Titel

Electronic Structure of Transition Metal Compounds with Different Nuclearities

selbständig verfasst und keine anderen als die angegebenen Quellen und Hilfsmittel verwendet habe. Aus fremden Quellen entnommene Passagen und Gedanken sind als solche kenntlich gemacht.

Declaration of Authorship

I hereby certify that the dissertation entitled

Electronic Structure of Transition Metal Compounds with Different Nuclearities

is entirely my own work except where otherwise indicated. Passages and ideas from other sources have been clearly indicated.

Heiko Bamberger
Januar 2022

Acknowledgment

Several people contributed either directly or indirectly to the results presented in this thesis. My special thanks go to:

My supervisor Prof. Dr. Joris van Slageren for his continuous support, the useful and informative scientific discussions and his open door policy. I am very thankful for the skills and knowledge I could acquire during this time and the leeway in my work.

Prof. Dr. Rainer Niewa who kindly accepted to referee my thesis and Prof. Dr. Biprajit Sarkar who accepted to chair the oral examination.

Prof. Dr. Biprajit Sarkar for the fruitful cooperation regarding the single-molecule magnet topic and Dr. Uta Albold for providing the interesting mono- and dinuclear compounds and especially her endurance in developing the synthesis of the dinuclear complex.

Dr. Walter Schenkeveld for the fruitful cooperation regarding the topic of iron extraction from soil and bringing this new topic to our group.

Dr. Dominik Bloos and Dr. Michal Kern for the introduction to our HFEPR spectrometer. Additional to them Dr. Samuel Lenz for support when equipment was not working as it was supposed to.

Dr. Mauro Perfetti for sharing his knowledge on molecular magnetism and for his detailed introduction to and support with SQUID magnetometry.

Dr. Philipp Hallmen for the ab-initio calculations on the mono- and dinuclear complexes.

Dr. James Byrne from the group of Prof. Andreas Kappler for the Mössbauer measurements on the soil samples.

The students who contributed to the characterization of the mononuclear complexes, namely David Hunger and Friederike Allgöwer.

The members of the low temperature department, mechanical workshop and electrical workshop.

Finally, my thank goes to the members of the entire Van Slageren group for the good discussions and for the pleasant and supportive atmosphere.

Table of Contents

Abbreviations and Symbols

χ	Susceptibility
χ_{S}	Adiabatic limit of the susceptibility
χ_{T}	Isothermal limit of the susceptibility
χ''	Out-of-phase susceptibility
χ'	In-phase susceptibility
ΔE_Q	Quadrupole splitting
δ	Isomer shift
$\hat{H}$	Hamilton operator
$\hat{S}$	Spin operator
μ_{B}	Bohr magneton
τ	Relaxation time
ε	Quadrupole shift
B	Magnetic flux density
B_{HF}	Hyperfine field
C_{Raman}	Raman coefficient
D	Axial zero-field splitting parameter
E	Energy
E	Rhombic zero-field splitting parameter
g	Landé factor, g-value
H	Magnetic field strength
I	Intensity
J	Exchange interaction
J	Total angular momentum quantum number
K_{C}	Stability constant
L	Total orbital angular momentum quantum number
M	Magnetization
M	Molecular weight
m	Magnetic moment
m_S	Magnetic spin quantum number

n_{Raman}	Raman exponent
S	Total spin quantum number
T	Temperature
t	Time
T_{B}	Blocking temperature
T_{C}	Curie temperature
T_{IRREV}	Irreversibility temperature
T_{M}	Morin temperature
T_{N}	Néel temperature
18-c-6	18-crownether-6
ac	Alternating current
arb. u.	Arbitrary units
CAHF	Configuration-averaged Hartree-Fock
CASPT2	Complete active space perturbation theory of second order
CASSCF	Complete active space self-consistent field
dc	Direct current
DFOB	Desferrioxamine B
DOM	Dissolved organic matter
EPR	Electron paramagnetic resonance
FC	Field-cooled
fFDMR	Fast frequency domain magnetic resonance
FIR	Far infrared
FTIR	Fourier-transform infrared spectroscopy
H_2L_A	1,2-bis(methanesulfonamido)benzene
H_2L_B	1,2-bis(toluenesulfonamido)benzene
H_4L_C	1,2,4,5-tetrakis(methanesulfonamido)benzene)
HFEPR	High-frequency electron paramagnetic resonance
ICP-MS	Inductively coupled plasma mass spectrometry
lcp	Left circularly polarized light
LDF	Local density fitting
MCD	Magnetic circular dichroism
NIR	Near infrared
PMT	Photomultiplier tube
PNO	Pair natural orbitals

QTM	Quantum tunneling of magnetization
rcp	Right circularly polarized light
SI-SO	State interaction with spin-orbit coupling
SIM	Single-ion magnet
SMM	Single-molecule magnet
SQUID	Superconducting quantum interference device
UV	Ultraviolet
Vis	Visible
XRD	X-ray diffraction
ZF	Zero field
ZFC	Zero-field-cooled
ZFCFC	Zero-field-cooled-field-cooled
ZFS	Zero-field splitting

Abstract

The observation of slow relaxation of magnetization in the manganese cluster $[Mn_{12}O_{12}(O_2CMe)_{16}(H_2O)_4]$ in 1993[1, 2] started the modern subject of molecular magnetism. Since then, a lot of effort has been made to develop molecular nanomagnets with the vision to make them suitable for data storage on a molecular scale[3–9].

Slow relaxation of magnetization in single-molecule magnets (SMM) is caused by an energy barrier for spin reversal which separates the spin-up and spin-down states. This means that a SMM magnetized in an external field will retain its magnetization after the field is switched off. The energy barrier U is proportional to the product of the square of the total spin S of a system and the axial zero-field splitting parameter D. Because the dependency on the spin is $U \propto S^2$, first attempts for improving the SMM properties focussed on synthesizing exchange-coupled systems with large total spins[4, 10]. However, large spins lead to low anisotropies precluding good SMM properties[11]. The currently most promising approach is to develop systems with high anisotropies which puts the focus on lanthanide and cobalt complexes.

This thesis focussed on improving the understanding of an previously reported promising cobalt-based SMM candidate[12] and analogous complexes with other first row transition metal ions. Following to that, a new radical-bridged dinuclear cobalt complex was investigated, which employs the idea of suppressing tunneling by strong spin-radical-spin interaction. Magnetometry and advanced spectroscopic methods, such as high-frequency electron paramagnetic resonance (HFEPR), far-infrared (FIR) and magnetic circular dichroism (MCD), were utilized to gain a deep insight into the compounds' properties.

Seven mononuclear transition metal complexes prepared in the group of Prof. Sarkar were investigated in this Thesis. Six of these are based on the same ligand as the previously reported[12] cobalt-based SMM $(HNEt_3)_2[1]$ ($[1] = [Co^{II}(L_A)_2]$) with varying counter ions. Two of these doubly deprotonated 1,2-bis(methanesulfonamido)benzene ligands (L_A) are known to form a strongly axially distorted tetrahedral coordination of the central ion which gives rise to excellent single-molecule magnet properties in $(\text{HNEt}_3)_2[1]$. As metal centers, Co^{2+} (**K$_2$[1]**, **(K-18-c-6)$_2$[1]**), Ni^{2+} (**K$_2$[3]**, **(HNEt$_3$)$_2$[3]**, $[3] = [\text{Ni}^{\text{II}}(\text{L}_\text{A})_2]$), Fe^{2+} (**(HNEt$_3$)$_2$[4]**, $[4] = [\text{Fe}(\text{L}_\text{A})_2]$) and Fe^{3+} (**(HNEt$_3$)[4]**) were used. The seventh complex (**(HNEt$_3$)$_2$[2]**, $[2] = [\text{Co}^{\text{II}}(\text{L}_\text{B})_2]$) features a slightly varied ligand (1,2-bis(toluenesulfonamido)benzene) where methyl groups were replaced by tolyl groups. Nickel and iron were picked as central ions to investigate if the ligand platform can induce single-molecule magnet behavior for them.

All investigated cobalt-based complexes show purely axial zero-field splitting and robust SMM properties of comparable quality to the reference compound $(\text{HNEt}_3)_2[1]$. The zero-field splitting parameters were determined as $D = -130(20)\,\text{cm}^{-1}$ for **(K-18-c-6)$_2$[1]** and $D = -110(20)\,\text{cm}^{-1}$ for **(HNEt$_3$)$_2$[2]** using magnetometry and $D = -115(1)\,\text{cm}^{-1}$ for **K$_2$[1]** using FIR spectroscopy. Slow relaxation of magnetization was observed in zero field using dynamic magnetometric measurements. Yet, quantum tunneling of the magnetization is dominant at low temperatures leading to a waist-restricted magnetization curve and no magnetic coercivity. Utilizing MCD and FIR spectroscopy, the complete structure of the free ion ^4F electronic ground state reduced to $\text{D}_{2\text{d}}$ symmetry could be analyzed for **K$_2$[1]**.

The nickel complexes show very large positive zero-field splitting parameters of $D = 58(2)\,\text{cm}^{-1}$ (**K$_2$[3]**, based on magnetometry) and $D = 76(1)\,\text{cm}^{-1}$, $E = 6.5(10)\,\text{cm}^{-1}$ (**(HNEt$_3$)$_2$[3]**, based on FIR spectroscopy). These values are among the largest positive ones observed for Ni(II) so far. The positive sign of D prevents SMM behavior.

For the iron complexes, a precise analysis of the magnetic properties was possible utilizing HFEPR spectroscopy. The g-values and zero-field splitting parameters were determined as $g_x = 2.22(4)$, $g_y = 2.01(4)$, $g_z = 2.10(6)$, $D = -3.29(6)\,\text{cm}^{-1}$, $E = 0.22(6)\,\text{cm}^{-1}$ (**(HNEt$_3$)$_2$[4]**) and $g_\perp = 1.99(4)$, $g_\parallel = 1.90(6)$, $D = -1.96(5)\,\text{cm}^{-1}$ and $E = 0.12(4)\,\text{cm}^{-1}$ (**(HNEt$_3$)[4]**). No SMM properties could be observed.

Following the idea of suppressing tunneling by strong spin-radical-spin interaction, a radical-bridged dinuclear cobalt complex was investigated in the second part of this work. The ligand used with the mononuclear cobalt complexes was adapted for this purpose by the Sarkar group because it was known to promote SMM properties by imposing a strongly axial ligand field. Introducing a second coordination site resulted in the symmetric ligand 1,2,4,5-tetrakis(methanesulfonamido)benzene ($\text{H}_4\text{L}_\text{C}$). The complex $(\text{K-18-c-6})_3[\{(\text{H}_2\text{L}_\text{C}{}^{2-})\text{Co}^{\text{II}}\}_2(\mu\text{-L}_\text{C}{}^{3\cdot-})]$ (**(K-18-c-6)$_3$[5]**),

which features a radical on the bridging ligand, was investigated using magnetometry, MCD and FIR spectroscopy. In doing so, a very strong antiferromagnetic coupling between the cobalt ions and the radical of $J_{\text{Co-Rad}} = 440(40)\,\text{cm}^{-1}$ could be observed while D is the same as for the mononuclear complexes. The coupling causes a drastic improvement of the SMM properties. Dynamic magnetic measurements evidenced slow relaxation of magnetization in zero field with relaxation times up to over 300 times longer than for $(\text{HNEt}_3)_2[1]$ at 17 K. An effective energy barrier of $U_{\text{eff}} = 267(3)\,\text{cm}^{-1}$ could be determined. In applied field, relaxation times of up to 9 h at 1500 Oe were found. The hysteresis in magnetization curves is far more pronounced compared to the mononuclear complexes and present up to 15 K. However, the shape is still waist-restricted even if the complex is diluted to a molar ratio of 5 % in a diamagnetic matrix to suppress intermolecular interactions. The most probable explanation for this is the induction of tunneling in zero field by transverse hyperfine interaction. A proof by hysteresis measurements on aligned single crystals at ultra-low temperatures could unfortunately not be shown in this work. Overall, the analysis of this radical-bridged dinuclear cobalt complex adds significant understanding on how to proceed with rational design of transition metal single-molecule magnets. It shows that findings from coupling in lanthanide polynuclear compounds can be extended to transition metal complexes with greater effect due to the significantly stronger coupling.

Besides molecular nanomagnets, this work deals in its third part with the analysis of iron extraction from soil with a biogenic ligand. This topic is of special biological interest because iron is an essential micronutrient for plants[13]. For example, it is of crucial importance in the process of chlorophyll synthesis. Iron deficiency is, thus, a serious issue for plant growth[14, 15]. The abundance of iron in soil is, due to its high abundance on earth, generally high and way above the amounts that are needed by plants[16]. Unfortunately, the physical presence alone does not guarantee an adequate supply to plants. In fact, the bio-availability of iron is often limited due to its occurrence in insoluble material like minerals or in the wrong oxidation state for direct uptake by plants[13]. Some microorganisms and plants have developed a special way to cope with this situation. They exude polydentate organic ligands, so-called (phyto)siderophores, which form complexes with iron in the soil. These complexes can be taken up by the plants and organ-

isms which improves the bio-availability of iron[13]. A better understanding of how natural occurring but inaccessible iron pools can be used for fertilization can have a major impact on food production which is an important topic for the world's growing population.

To gain better insights into the complexation process of iron by siderophores, for example the targeted iron pools, the biogenic ligand desferrioxamine B (DFOB) was applied to an aqueous extract of a podzol. Samples with different complexation times were prepared to learn about the kinetics involved. For qualitative comparison, soil extracts at different pH values were studied as well as minerals that are likely to occur in that soil. The study employed HFEPR spectroscopy and magnetometry supported by Mössbauer spectroscopy.

For the complexation kinetics and targeted pool a conclusive picture consistent between the methods could be gained. Within the first few minutes of exposure to DFOB in aqueous solution, **FeDFOB** is formed by ligand exchange from iron bound to dissolved organic matter (DOM) due to the polydenticity of DFOB and the resulting high stability constant. The next targeted iron pool was identified to be of antiferromagnetic nature but a more precise characterization could not be achieved. With regard to the acidity during soil extraction it could clearly be shown that using pH 4 or 9 leads to extracts with different composition. This difference comes directly from the extraction process because setting a redissolved sample from pH 4 to 9 does not yield the same composition as the extraction directly at pH 9. Additionally, it could be shown that the species targeted during extraction from soil are mainly of antiferromagnetic nature. No signs of the minerals **hematite**, **goethite**, **2-line ferrihydrite** or **6-line ferrihydrite**, which are typical for that podzol, could be found in the extracts. Consequently, either none of these minerals is transferred during the extraction process or they are destroyed during the process.

Overall, significant insights into the dynamics of extraction and complexation could be achieved. Still, open questions remain, like the precise identity of the antiferromagnetic phase targeted by complexation which would allow an even more detailed statement about the targeted pool.

Zusammenfassung

Mit der Beobachtung von langsamer Relaxation der Magnetisierung in dem Mangan-Cluster $[Mn_{12}O_{12}(O_2CMe)_{16}(H_2O)_4]$ im Jahr 1993[1, 2] begann das neuartige Feld des molekularen Magnetismus. Seitdem wurde großer Aufwand betrieben, molekulare Nanomagnete zu entwickeln. Die zugrundeliegende Vision ist die Speicherung von Daten auf molekularer Ebene.[3–9].

Die langsame Relaxation der Magnetisierung in Einzelmolekülmagneten wird verursacht durch eine Energiebarriere gegen Spinumkehr. Diese Barriere trennt die Spinzustände mit Ausrichtung nach oben von solchen mit Ausrichtung nach unten. Durch diese behält ein Einzelmolekülmagnet seine Magnetisierung bei, nachdem er in einem externen Magnetfeld magnetisiert und dieses Feld ausgeschaltet wurde. Die Größe der Energiebarriere U is proportional zum Produkt des Quadrats des Gesamtspins S eines Systems mal dem axialen Nullfeldaufspaltungsparameter D. Aufgrund der quadratischen Skalierung mit S konzentrierten sich die ersten Versuche zur Verbesserung der Einzelmolekülmagneteigenschaften auf die Darstellung von austauschgekoppelten Systemen mit großem Gesamtspin[4, 10]. Allerdings führt ein großer Gesamtspin zu niedriger Anisotropie was gute Einzelmolekülmagneteigenschaften ausschließt[11]. Der aktuell vielversprechendste Ansatz ist die Entwicklung von Systemen mit hoher Anisotropie, weswegen der Fokus auf Lanthanoid- und Cobaltkomplexe gerichtet wird.

Diese Arbeit konzentrierte sich darauf, das Verständnis eines zuvor veröffentlichten, vielversprechenden cobaltbasierten Einzelmolekülmagnetkandidaten[12] zu vertiefen und analoge Komplexe mit anderen leichten Übergangsmetallionen als Zentralion zu untersuchen. Daran anschließend wurde ein neuartiger radikalverbrückter zweikerniger Cobaltkomplex untersucht. Seine Auswahl als Einzelmolekülmagnetkandidat beruht auf dem Ansatz, unerwünschte Relaxationspfade durch eine starke Spin-Radikal-Spin-Wechselwirkung zu unterdrücken. Ein detaillierter Einblick in die Eigenschaften der Verbindungen wurde mittels Magnetometrie sowie spektroskopischer Methoden wie Hochfrequenzelektronenspinresonanz- (HFEPR), Ferninfrarot- (FIR) und magnetischer Zirkulardichroismus-Spektroskopie (MCD) gewonnen.

In dieser Arbeit wurden sieben einkernige Übergangsmetallkomplexe intensiv untersucht, die in der Gruppe von Prof. Sarkar hergestellt worden waren. Sechs dieser Komplexe basieren auf demselben Liganden wie der zuvor veröffentlichte[12] cobaltbasierte Einzelmolekülmagnet $(HNEt_3)_2[1]$ ($[1] = [Co^{II}(L_A)_2]$) wobei unterschiedliche Gegenionen verwendet wurden. Es ist bekannt, dass zwei der zweifach deprotonierten 1,2-bis(Methansulfonamid)benzol-Liganden (L_A) eine stark axial verzerrte tetraedrische Koordination des Zentralions verursachen, wodurch die hervorragenden Einzelmolekülmagneteigenschaften von $(HNEt_3)_2[1]$ hervorgerufen werden. Als Zentralteilchen wurden Co^{2+} ($\mathbf{K_2[1]}$, $\mathbf{(K\text{-}18\text{-}c\text{-}6)_2[1]}$), Ni^{2+} ($\mathbf{K_2[3]}$, $\mathbf{(HNEt_3)_2[3]}$, $[3] = [Ni^{II}(L_A)_2]$), Fe^{2+} ($\mathbf{(HNEt_3)_2[4]}$, $[4] = [Fe(L_A)_2]$) und Fe^{3+} ($\mathbf{(HNEt_3)[4]}$) verwendet. Der siebte Komplex ($\mathbf{(HNEt_3)_2[2]}$, $[2] = [Co^{II}(L_B)_2]$) wurde mit dem leicht veränderten Liganden 1,2-bis(Toluolsulfonamid)benzol synthetisiert, in dem die Methylgruppen gegen Tolylgruppen getauscht wurden. Nickel und Eisen wurden als Zentralteilchen ausgewählt, um zu untersuchen, ob das Ligandensystem für sie Einzelmolekülmagnetverhalten hervorrufen kann.

Alle untersuchten cobaltbasierten Komplexe zeichnen sich aus durch eine rein axiale Nullfeldaufspaltung und robuste Einzelmoleküleigenschaften in vergleichbarer Qualität zu $(HNEt_3)_2[1]$. Die Nullfeldaufspaltungsparameter wurden bestimmt zu $D = -130(20)\,\mathrm{cm^{-1}}$ für $\mathbf{(K\text{-}18\text{-}c\text{-}6)_2[1]}$ und $D = -110(20)\,\mathrm{cm^{-1}}$ für $\mathbf{(HNEt_3)_2[2]}$ mittels Magnetometrie und $D = -115(1)\,\mathrm{cm^{-1}}$ für $\mathbf{K_2[1]}$ mittels FIR-Spektroskopie. Eine langsame Relaxation der Magnetisierung im Nullfeld wurde in dynamischen magnetometrischen Messungen beobachtet. Allerdings dominiert bei tiefen Temperaturen Quantentunneln der Magnetisierung, was zu einer taillenverengten Magnetisierungskurve ohne Koerzivität führt. Weiterhin konnte für $\mathbf{K_2[1]}$ mittels MCD- und FIR-Spektroskopie die komplette elektronische Struktur des ^4F freien-Ion-Grundzustand reduziert nach D_{2d}-Symmetrie aufgeklärt werden.

Die Nickelkomplexe zeichnen sich aus durch sehr große Nullfeldaufspaltungsparameter von $D = 58(2)\,\mathrm{cm^{-1}}$ ($\mathbf{K_2[3]}$, basierend auf Magnetometrie) und $D = 76(1)\,\mathrm{cm^{-1}}$, $E = 6.5(10)\,\mathrm{cm^{-1}}$ ($\mathbf{(HNEt_3)_2[3]}$, basierend auf FIR Spektroskopie), die zu den größten bisher für Ni(II) beobachteten gehören. Einzelmolekülmagnetverhalten wird durch das positive Vorzeichen von D ausgeschlossen.

Für die Eisenkomplexe war eine präzise Analyse der magnetischen Eigenschaften mittels HFEPR-Spektroskopie möglich. Die g-Faktoren und Nullfeldaufspaltungsparameter wurden bestimmt zu $g_x = 2.22(4)$, $g_y = 2.01(4)$, $g_z = 2.10(6)$, $D = -3.29(6)\,\mathrm{cm^{-1}}$, $E = 0.22(6)\,\mathrm{cm^{-1}}$ ($\mathbf{(HNEt_3)_2[4]}$) und $g_\perp = 1.99(4)$,

$g_{\parallel} = 1.90(6)$, $D = -1.96(5)\,\mathrm{cm}^{-1}$ und $E = 0.12(4)\,\mathrm{cm}^{-1}$ (**(HNEt$_3$)[4]**). Einzelmolekülmagnetverhalten konnte nicht beobachtet werden.

Dem Ansatz folgend, dass Tunneln durch starke Spin-Radikal-Spin-Wechselwirkung unterdrückt werden kann, wurde im zweiten Teil dieser Arbeit ein radikalverbrückter zweikerniger Cobaltkomplex untersucht. Der für die einkernigen Cobaltkomplexe verwendete Ligand wurde dafür in der Sarkar-Gruppe angepasst, weil er dafür bekannt ist, durch das von ihm verursachte stark axiale Ligandenfeld Einzelmolekülmagneteigenschaften zu begünstigen. Durch die Einführung einer zweiten Koordinationsstelle resultierte so der symmetrische Ligand 1,2,4,5-tetrakis-(Methansulfonamid)benzol (H_4L_C). Der Komplex (K-18-c-6)$_3$[{($H_2L_C{}^{2-}$)Co^{II}}$_2$(μ-$L_C{}^{3\,\cdot\,-}$)] (**(K-18-c-6)$_3$[5]**), der sich durch ein Radikal auf dem verbrückenden Liganden auszeichnet, wurde mittels Magnetometrie sowie MCD- und FIR-Spektroskopie untersucht.

Die Analyse zeigte eine äußerst starke antiferromagnetische Kopplung zwischen den Cobaltionen und dem Radikal von $J_{\text{Co-Rad}} = 440(40)\,\mathrm{cm}^{-1}$ und eine unveränderte Nullfeldaufspaltung verglichen mit den einkernigen Komplexen. Durch die Kopplung wird eine deutliche Verbesserung der Einzelmolekülmagneteigenschaften verursacht. Dynamische magnetometrische Messungen zeigten eine Erhöhung der Relaxationszeiten im Nullfeld um einen Faktor von bis zu 300 verglichen mit (HNEt$_3$)$_2$[1] bei 17 K. Die effektive Energiebarriere wurde bestimmt als $U_{\text{eff}} = 267(3)\,\mathrm{cm}^{-1}$. In einem angelegten Magnetfeld wurden Relaxationszeiten von bis zu 9 h bei 1500 Oe beobachtet. Auch die Hysterese der Magnetisierungskurve ist deutlich stärker ausgeprägt und bis zu einer Temperatur von 15 K messbar. Allerdings ist die Form der Kurve auch hier taillenverengt sowohl im reinen Komplex als auch bei molarer Verdünnung auf 5 % in einer diamagnetischen Matrix, die intermolekulare Wechselwirkungen unterdrücken kann. Die wahrscheinlichste Erklärung dafür ist, dass das Tunneln im Nullfeld durch die transversale Hyperfeinwechselwirkung verursacht wird. Ein Nachweis dessen durch Hysteresemessungen an ausgerichteten Einkristallen bei ultratiefen Temperaturen konnte im Rahmen dieser Arbeit nicht erbracht werden. Alles in allem verbessert die hier vorgestellte Analyse des radikalverbrückten zweikernigen Cobaltkomplexes das Verständnis wie Einzelmolekülmagnete auf Basis von Übergangsmetallen zu designen sind. Sie zeigt ebenso, dass Erkenntnisse aus der Kopplung in mehrkernigen Lanthanoidkomplexen auf Übergangsmetallkomplexe übertragen werden können.

Der dritte Teil dieser Arbeit beschäftigt sich mit der Analyse von Eisenextraktion aus Erde mittels eines biogenen Liganden. Für die Biologie ist dieses Thema von besonderem Interesse, da es sich bei Eisen um einen essenziellen Mikronährstoff für Pflanzen handelt[13]. Beispielsweise ist es von kritischer Bedeutung in der Chlorophyllsynthese. Demzufolge ist Eisenmangel ein ernstzunehmendes Risiko für Pflanzenwachstum[14, 15]. Im Allgemeinen ist die Menge von Eisen im Boden, aufgrund seines hohen Vorkommens auf der Erde, groß und deutlich über den Mengen, die Pflanzen benötigen[16]. Unglücklicherweise stellt die Gegenwart von Eisen allein noch keine Garantie für eine ausreichende Versorgungsgrundlage für Pflanzen dar. Tatsächlich ist die biologische Verfügbarkeit oft eingeschränkt, da es unlöslich in Mineralien vorliegt oder im falschen Oxidationszustand für die direkte Aufnahme durch Pflanzen[13]. Einige Mikroorganismen und Pflanzen haben für den Umgang mit dieser Situation eine spezielle Strategie entwickelt. Sie schütten mehrzähnige organische Liganden aus, sogenannte (Phyto)Siderophore, die mit dem Eisen im Boden Komplexe ausbilden. Diese Komplexe können durch die Pflanzen und Organismen aufgenommen werden, wodurch sich die biologische Verfügbarkeit von Eisen erhöht[13]. Ein besseres Verständnis, wie nicht zugängliches, natürlich vorkommendes Eisen für Düngung verwendet werden kann, kann einen starken positiven Einfluss auf die Produktion von Nahrungsmitteln haben, die benötigt werden, um die wachsende Weltbevölkerung zu ernähren.

Um einen besseren Einblick in den Prozess der Komplexbildung durch Siderophore in Böden, wie beispielsweise die angegriffene Eisenquelle, zu gewinnen, wurde der biogene Ligand Desferrioxamin B (DFOB) einem wässrigen Extrakt von Bleicherde zugesetzt. Dabei wurden Proben mit unterschiedlicher Komplexierungszeit zubereitet, wodurch die Kinetik der Komplexierung untersucht werden konnte. Um einen qualitativen Vergleich zu ermöglichen, wurden ebenfalls Bodenextrakte, die bei verschiedenen pH-Werten entnommen wurden, sowie Mineralien, die in dieser Erde vorkommen können, untersucht. Für die Untersuchungen wurden hauptsächlich HFEPR-Spektroskopie und Magnetometrie eingesetzt, die durch Mößbauerspektroskopie ergänzt wurden.

Es konnte ein schlüssiges und zwischen den Methoden konsistentes Bild bezüglich der Kinetik der Komplexierung und der angegriffenen Eisenquelle gewonnen werden. Innerhalb der ersten Minuten nach Zusatz von DFOB zu wässriger Lösung des Bodenextrakts bildet sich **FeDFOB** durch Ligandenaustausch aus Eisen, das an gelöste organische Materie gebunden ist. Dies beruht auf der Mehrzähnigkeit von DFOB und der daraus resultierenden hohen Stabilitätskonstante von **FeDFOB**.

Das als nächste angegriffene Eisenvorkommen ist antiferromagnetischer Art. Eine genauere Identifizierung konnte jedoch nicht erreicht werden. Im Hinblick auf die Acidität des Extraktionsmediums während der Extraktion der Bodenproben konnte gezeigt werden, dass die Verwendung von pH 4 oder 9 zu Extrakten mit unterschiedlicher Zusammensetzung führt. Dieser Unterschied begründet sich direkt im Extraktionsprozess, da auch das spätere Auflösen der bei pH 4 extrahierten Probe und ihre Einstellung auf pH 9 nicht zum gleichen Produkt führt wie die direkt bei pH 9 extrahierte Probe. Weiterhin konnte gezeigt werden, dass es sich bei den aus dem Boden extrahierten Verbindungen hauptsächlich um antiferromagnetische Stoffe handelt. In den Extrakten konnten keine Spuren der Mineralien **Hämatit**, **Goethit**, **2-Linien-Ferrihydrit** und **6-Linien-Ferrihydrit**, die sich typischerweise in der untersuchten Bleicherde befinden, gefunden werden. Demzufolge wird entweder keines dieser Minerale während der Extraktion transferiert oder aber sie werden währenddessen zersetzt.

Die Ergebnisse zusammenfassend konnten wesentliche Einblicke in die Dynamik der untersuchten Extraktion und Komplexierung gewonnen werden. Gleichzeitig verbleiben offene Fragen, insbesondere bezüglich der exakten Beschreibung der antiferromagnetischen Phase, die während der Komplexierung angegriffen wird. Mit dieser Information könnte eine deutlich genauere Aussage zu den angegriffenen Eisenquellen getroffen werden.

1. Introduction

One of the largest subjects in chemistry is coordination chemistry. Its applications cover for example the large topic of biological and homogeneous catalysts. Chemically, coordination complexes always consist of at least one central atom or ion (called "coordination center") and surrounding molecules ("ligands"). The coordination center is usually metallic and may come from the whole range from light main-group elements to heavy actinides. The properties of complexes are strongly tuned by the ligands, which can range from small (e. g. carbon monoxide) to huge bioorganic molecules.

In this work, coordination complexes from two different areas of interest were investigated. The first topic (Chapters 3 and 4) deals with single molecule magnets. A subject of biochemical interest is covered in the second part with the extraction of iron from soil by a chelate complex. Introductions to each of these topics are given subsequently.

The discovery of molecular magnetism dates back to 1993 when slow relaxation of magnetization was reported in $[Mn_{12}O_{12}(O_2CMe)_{16}(H_2O)_4]$ ("Mn_{12}ac"), a cluster with twelve manganese ions, for the first time[1, 2]. This finding laid the base for a modern research area in chemistry where great advances have been achieved since then. The driving idea is to imagine a single molecular magnet as a bit with the direction of magnetization ("up" or "down") representing the bits state ("0" or "1"), which enables storing information at the molecular size level. Combining this property with magnetic hard drives led to the vision of a new technology for ultrahigh-density storage devices[1, 17] with the building block named "single-molecule magnet" (SMM).

In the last decades, a large number of SMMs have been reported[3–9]. Most of these lack a crucial property for real application, which is magnetic stability over a usable time span at reasonably high temperatures. In fact, most reported SMMs show slow relaxation of magnetization only at temperatures close to that of liquid helium. This is because the energy barrier between the ground states of different orientation of magnetization does not effectively block spin reversal in many cases. Possible reasons are that the energy barrier is too small or overcome by other effects such as tunneling. Achieving large energy barriers was first attempted by building exchange-coupled clusters of 3d metal ions with high total spin[18]. Later, strongly anisotropic metal centers, e. g. cobalt or lanthanides, were employed. Still, even though energy barriers up to several thousands of wavenumbers have been observed, difficulties remain, caused by the complexity of several pathways for magnetic relaxation. Approaches to limit or suppress these pathways are symmetry-based design of compounds or strong coupling in multi-nuclear complexes, e. g. to organic radicals.

The focus of this work lies in improving the understanding of an previously reported promising cobalt-based SMM candidate[12] and analogous complexes with other first row transition metal ions. Following to that, a new radical-bridged dinuclear cobalt complex is presented, which employs the idea of suppressing tunneling by strong spin-radical-spin interaction.

Plants and microorganisms depend on a wide variety of environmental conditions for their growth and survival. One of these is the bioavailability of trace metals that are contained in enzymes which drive crucial biochemical processes. For example, the effect of decreased solubility of iron in alkaline soils leads to visible effects on the ecosystem such as chlorosis. While iron is usually present in sufficient quantities in soils on earth, its availability for organisms is not always sufficient, especially in calcareous soils which constitutes approximately 30 % of the world's farmland.

To cope with this situation, some microorganisms have developed a very effective method for iron acquisition: They produce and exude chelating organic ligands with high affinity for iron, so called siderophores (Greek for "iron carrier") which greatly increase bioavailability of iron. This use of siderophores by bacteria[19] and fungi[20] was observed more than 50 years ago[21]. Similar ligands exuded by graminaceous plants[22] are called "phytosiderophores". A strong motivation to investigate (phyto)siderophores is their application as fertilizer to increase bioavailability of iron. Given the tremendous size of the food market, even small improvements in crop yields can have remarkable effects, helping to feed the world's growing population.

The siderophore investigated in this project is desferrioxamine B (DFOB). It features three hydroxamate groups and forms an octahedral iron chelate acting as a hexadentate chelating agent. This results in a very high estimated apparent stability constant of $\log K_{\mathrm{app}} \approx 22$ at pH 8[23]. The complexation of iron by DFOB in a podzol extract is analyzed improving the understanding of thermodynamic and kinetic effects during this extraction process.

2. Background

2.1. Molecular Magnetism

The following introduction is based on the textbooks by D. Gatteschi, R. Sessoli and J. Villain[24] and by C. Benelli and D. Gatteschi[25].

The fundamental property of molecular magnets, also called molecular nanomagnets (MNM), is bistability of magnetization of purely molecular origin. The first feature, magnetic bistability, can be observed as slow relaxation of magnetization which means that a magnetized sample maintains its magnetization on a certain time scale even after the external magnetic field used for magnetizing is switched off. The second feature, which describes the property's origin, means that the characteristics are independent of intermolecular interactions and purely based on the molecular unit which carries a spin. This is an important difference to classic magnetic materials where the magnetic properties are based on magnetic domains which easily contain billions of individual spins[26]. These spins are coupled and respond together to external stimuli forming one magnetic center. The one-dimensional size of these domains is typically in the range from 10 µm to 100 µm[27, 28].

The charm of molecular magnets in this context is the small space needed to form a magnetic center. It is formed by a single molecule, which is the reason for the name single-molecule magnet (SMM). Assuming 1.5 nm as unit cell parameters for a typical crystal, an areal density of almost $300 \cdot 10^{12}$ magnetic centers per square inch can be calculated[29]. In combination with the idea to use molecular magnets for data storage, where each magnetic center corresponds to one bit of information, this translates to an areal density of 300 Tbit/in^2. Compared to current (2017) areal densities[30] in magnet based hard drives of 1.2 Tbit/in^2 or NAND based memories with 2.5 Tbit/in^2 molecular magnets could boost the areal density by about two orders of magnitude.

A fundamental characteristic property of single-molecule magnets is the total spin quantum number S. In case the coupling between electron spins of a single center is stronger than spin-orbit coupling, S of a single magnetic center is the product of the number of unpaired electrons and $^1/_2$. For SMMs consisting of a cluster of ions, S equals the sum of the individual total spins where parallel spins are added and antiparallel spins are subtracted (giant spin model).

Additionally to S, the magnetic structure of a single-molecule magnet depends mainly on the so-called zero-field splitting which describes the energy gap between the magnetic spin states, characterized by their magnetic spin quantum number m_S, in zero field. Within the Spin-Hamiltonian formalism (see Section 2.1.2), the zero-field splitting can be represented by the axial zero-field splitting parameter D and the rhombic zero-field splitting parameter E which are then measures of the axial and rhombic anisotropy of the system.

The bistability and origin of slow magnetic relaxation of molecular magnets can be explained using a double well potential which is depicted in Figure 2.1 for the first reported single-molecule magnet $\mathrm{Mn_{12}ac}$. This manganese cluster was reported in 1993[1, 2] to show slow relaxation of magnetization. It features a total spin of $S = 10$ which arises from the presence of eight spin-up manganese(III) ($S = 2$) and four spin-down manganese(IV) ($S = {^3/_2}$) ions. This results in 21 magnetic spin states ($M_S = -S, -S + 1, ..., +S$) where the $M_S = \pm 10$ states are of lowest energy due to the negative zero-field splitting parameter, which is a property of the compound.

Applying an external magnetic field shifts all energy levels with $M_S \neq 0$ according to the Zeeman effect (Figure 2.1 b) and lifts the degeneracy of Kramers doublets, which can change relaxation pathways. A more detailed view on relaxation of magnetization is given in section 2.1.1.

In zero field, the energy barrier U between the $M_S = -10$ and $M_S = 10$ states is the barrier towards spin reversal and is equal to the energetic gap between the $M_S = \pm 10$ and $M_S = 0$ states. In the simplest case this energy barrier equals for non-Kramers systems with integer electron spin

$$U = |D| \cdot S^2 \tag{2.1}$$

and for Kramers system with half-integer spin

$$U = |D| \cdot \left(S^2 - \frac{1}{4}\right). \tag{2.2}$$

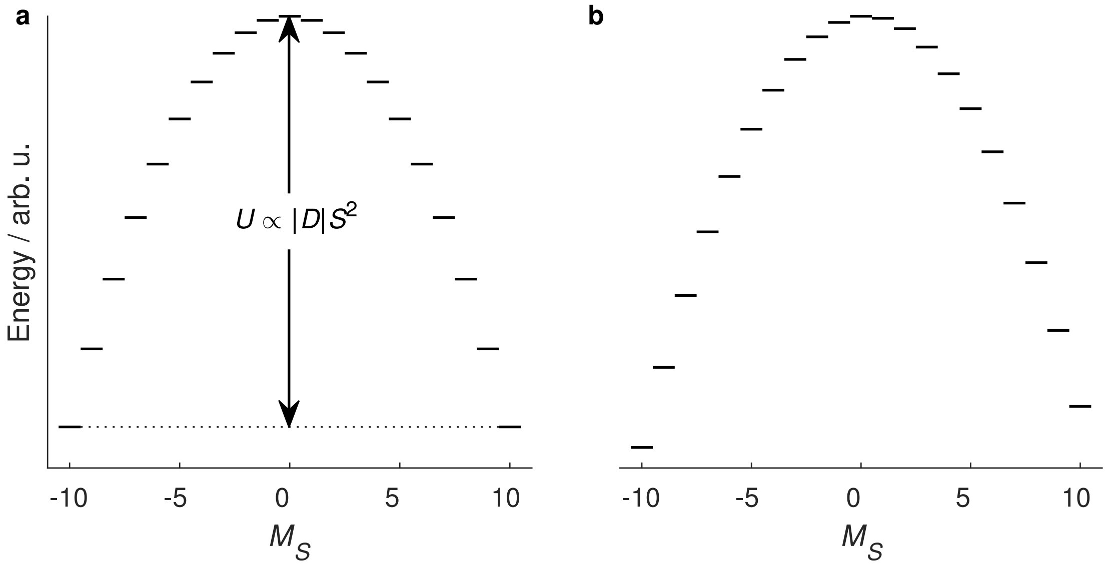

Figure 2.1: Schematic presentation of the double-well potential of Mn_{12}ac in the absence (a) of external field with indicated energy barrier U. In presence (b) of an external field the energy levels are shifted and not degenerate.

From a classical understanding, the bistability of a compound is more pronounced the higher the energy barrier towards spin reversal is. Thus, maximizing the product of D and S^2 should lead to an increasing quality of molecular magnets. While increasing S^2 is a straightforward approach which can be performed by synthesizing complexes with more and more coupled ions, the zero-field splitting of a compound is related to its molecular structure and the nature of this relationship was not understood for a long time. Additionally, the quadratic nature of the influence of the total spin seems to indicate this parameter to be the favorable way of improving the quality of molecular magnets. As a consequence, a hunt for complexes with large total spin started. In 2006, a preliminary record with $S = {}^{83}\!/_{2}$ in a Mn_{19} cluster was achieved[4] which was only surpassed in 2018 by a $Fe_{10}Gd_{10}$ cluster with $S = 60$[31]. Despite this progress to high-spin systems, the quality of molecular magnets did not increase significantly. A main observation was that with increasing spin D decreased. For example, while in Mn_{12}ac with $S = 10$ D is equal to $-0.46\,\mathrm{cm}^{-1}$[32], in the previously mentioned Mn_{19} cluster with $S = {}^{83}\!/_{2}$ no significant anisotropy is present[4].To explain this, it was shown in 1998 that indeed $S^2 \propto \frac{1}{D}$[33] and, thus, the barrier cannot be significantly improved by increasing S.

Since then, the criteria for designing decent single-molecule magnets have shifted to systems with a large energy barrier caused by large $|D|$ combined with a negative anisotropy of D and an axial system with $E = 0$. These criteria are best met in complexes with a linear or linearly distorted geometry around the central ion because the resulting ligand field then shows a favorable layout. As a consequence, a specific subclass of single-molecule magnets called single-ion magnets (SIM) formed. Here, only one metal ion is present per molecule in contrast to the previously described clusters. In the past few years great progress was made and compounds with large anisotropy, slow relaxation of magnetization in zero field and true magnetic hysteresis have been reported. For transition metal systems cobalt(II) compounds perform best and 2016 a complex with linearly distorted tetrahedral coordination was shown to exhibit slow relaxation of magnetization in zero field and a large effective energy barrier of $U_{\text{eff}} = 118\,\text{cm}^{-1}$ but is limited to waist-restricted magnetic hysteresis[12]. In 2018, a linear cobalt(II) complex was then reported to show slow relaxation of magnetization in zero field at temperatures up to 70 K with $U_{\text{eff}} = 450\,\text{cm}^{-1}$ and opening of the hysteresis curve around zero field in diluted state[34]. In lanthanide systems, much higher effective energy barriers have been reported quite earlier, e. g. $652\,\text{cm}^{-1}$ in a $[\text{Tb(Pc)}_2]$ derivative in 2013[35]. The currently most outstanding results were achieved 2018 when a dysprosium metallocene single-molecule magnet with magnetic hysteresis up to 80 K and $U_{\text{eff}} = 1541\,\text{cm}^{-1}$ was reported[9].

Another approach to improve single-molecule magnet behavior is to combine the findings from clusters and single-ion magnets. In this, compounds with two magnetic centers are designed in a way that the ions are strongly coupled because the quantum tunneling of magnetization can be suppressed by the interaction. This is best achieved by incorporating an organo-radical bridge between the two ions. For lanthanide systems (mainly dysprosium and terbium) this was shown to be a viable approach to better performance[36–40]. Still, lanthanide systems tend to not form strongly exchange coupled systems with coupling constants limited to the lower two-digit wavenumber range. In contrast, transition metal systems are known to easily feature exchange couplings in the upper three-digit wavenumber range[41]. Based on this, combining well-performing transition metal single-ion magnets with radical-bridges could be a promising approach to enhanced single-molecule magnet behavior.

2.1.1. Relaxation of Magnetization

The following introduction is based on the textbook by D. Gatteschi, R. Sessoli and J. Villain[24] and the review by S. T. Liddle et al.[29].

The central property of a molecular magnet is slow relaxation of magnetization. Thus, an understanding of the underlying relaxation mechanisms is of crucial importance to understand observations on and design criteria for molecular magnets. For example, some relaxation pathways result in not observing U as defined above as energy barrier but an effective energy barrier U_{eff}. Four types of relaxation processes may occur. Three of these involve energy exchange between the spin and the surrounding lattice, and thus are subsumed as spin-lattice relaxation. These mechanisms are the direct, Orbach and Raman processes. The fourth process is quantum tunneling of magnetization which does not involve the lattice.

Direct relaxation means that the spin system relaxes directly from one microstate to another one lower in energy. The released energy is absorbed as a lattice vibration, also called phonon. In contrast to the other processes involving phonons, it involves only a single phonon. The corresponding relaxation time given in Equation 2.3 depends on the magnetic field strength H, the temperature T and an empirical coefficient A_{direct}.

$$\tau_{\text{direct}}^{-1} = A_{\text{direct}} \cdot H^{n_{\text{direct}}} \cdot T \tag{2.3}$$

The exponent for direct relaxation n_{direct} depends on the spin system. For non-Kramers systems in zero field or Kramers systems with hyperfine interaction n_{direct} equals 2. Otherwise, for Kramers systems $n_{\text{direct}} = 4$ holds true.

The Orbach process can occur in presence of low lying energy states. The spin system is excited by absorption of one phonon. Then, under emission of a phonon of higher energy, the system relaxes to a state of lower energy. This target state might be of opposite magnetization which results in relaxation of the net magnetization. The Arrhenius law in Equation 2.4 describes the relation between relaxation time τ, attempt time τ_0, energy barrier U, Boltzmann constant k_{B} and temperature T.

$$\tau_{\text{Orbach}}^{-1} = \tau_0^{-1} \exp\left(-\frac{U}{k_{\text{B}}T}\right) \tag{2.4}$$

In contrast to the Orbach process where the involved states are real, the Raman process involves states that are of virtual nature. Namely, a superposition of two phonons absorbs the energy which is released by the relaxing spin system. The energy difference of the superimposing phonons equals exactly the released energy.

The formula in equation 2.5 gives the dependency of relaxation time τ, Raman coefficient C_{Raman}, temperature T and Raman exponent n_{Raman}.

$$\tau_{\text{Raman}}^{-1} = C_{\text{Raman}} T^{n_{\text{Raman}}} \tag{2.5}$$

As for n_{direct}, n_{Raman} depends on the investigated spin system. For non-Kramers systems $n_{\text{Raman}} = 7$ holds true and for Kramers systems $n_{\text{Raman}} = 9$. Besides that, for systems with excited states close to the ground state $n_{\text{Raman}} = 5$ and if all phonon states are occupied at temperatures way above the Debye temperature $n_{\text{Raman}} = 2$.

Quantum tunneling of magnetization (QTM) is independent of the environment of a spin system. It occurs in presence of transverse interactions between two degenerate energy levels on different sides of the energy barrier which couples the involved states. Such interactions can be rhombic zero-field splitting, transverse magnetic fields or hyperfine coupling to nuclear spins. The coupling results in two new energy states which are the symmetric and antisymmetric linear combinations of the up and down states. Thus, the spin can efficiently tunnel through the energy barrier. One criterion to suppress QTM is avoiding rhombic and higher-order off-diagonal zero-field splitting by designing highly axial systems. The tunneling rate τ_{QTM}^{-1} is described by Equation 2.6. There, H is the magnetic field strength and B_1 and B_2 are parameters of the system.

$$\tau_{\text{QTM}}^{-1} = \frac{B_1}{1 + B_2 H^2} \tag{2.6}$$

Experimentally, QTM can be observed as characteristic “steps” in M versus H measurements where magnetization drops significantly.

2.1.2. The Spin Hamiltonian Concept and Used Hamiltonians

The following introduction is based on the textbook by D. Gatteschi, R. Sessoli and J. Villain[24] and the review by M. Atanasov et al.[42].

The spin Hamiltonian is a so-called effective Hamiltonian. This means it is a simplified approach to describe a part of the eigenvalues of the complete Hamiltonian. It enables the user to analyze measurements and spectra without employing fundamental theories. An example of simplification in context of the spin Hamiltonian is that the system is not defined using orbital coordinates but spin coordinates.

Different effects contribute to the energy of states, such as the electron Zeeman effect, hyperfine interaction, zero-field splitting, nucelar Zeeman effect, nuclear quadrupole interaction, electron-electron interaction or hyperfine interaction. Their contributions can be split into independent Hamiltonians. In the following, those relevant in context of this work are introduced.

The Hamiltonian $\hat{H}_{\text{Zeeman}}$ describing the interaction between an electron spin and an external magnetic field (electron Zeeman interaction as explained in Section 2.4.2) is given by Equation 2.7. There, μ_B is the Bohr magneton, **B** is the magnetic field vector, $\hat{\mathbf{S}}$ is the spin operator and **g** is the g-tensor which connects the magnetic field and the spin vectors.

$$\hat{H}_{\text{Zeeman}} = \mu_\text{B}\mathbf{B}^\text{T}\mathbf{g}\hat{\mathbf{S}} = \mu_\text{B} \sum_{k,q=x,y,z} g_{k,q} B_k \hat{S}_q \tag{2.7}$$

Equation 2.8 gives the Hamiltonian describing the zero-field splitting $\hat{H}_{\text{ZFS}}$ as explained in Section 2.1.3. **D** is the D tensor and D and E are the axial and rhombic zero-field splitting parameters, respectively.

$$\hat{H}_{\text{ZFS}} = \hat{\mathbf{S}}^\text{T}\mathbf{D}\hat{\mathbf{S}} = D\left[\hat{S}_z^2 - \frac{1}{3}S(S+1)\right] + E\left(\hat{S}_x^2 - \hat{S}_y^2\right) \tag{2.8}$$

Several conventions for the Hamiltonian $\hat{H}_{\text{exch}}$ describing the isotropic exchange interaction J exist in literature. For the one used throughout this work ($+J\hat{\mathbf{S}}^\text{T}\hat{\mathbf{S}}$, Equation 2.9), a positive J value means an antiferromagnetic coupling while a negative J means a ferromagnetic coupling.

$$\hat{H}_{\text{exch}} = \hat{\mathbf{S}}_1^\text{T}\mathbf{J}\hat{\mathbf{S}}_2 = \sum_{i,j=x,y,z} J_{ij}\hat{S}_{1i}\hat{S}_{2j} \tag{2.9}$$

In this work, for systems without coupling (Chapters 3 and 5) simulations were performed using the sum of the Spin Hamiltonians $\hat{H}_{\text{Zeeman}}$ and $\hat{H}_{\text{ZFS}}$ as described in Equation 2.10. Systems with coupling (Chapter 4) were analyzed taking additionally $\hat{H}_{\text{exch}}$ into account resulting in the Hamiltonian given in Equation 2.11 where i and j each represent all contributing spin systems and J was assumed to be isotropic).

$$\hat{H} = \hat{H}_{\text{Zeeman}} + \hat{H}_{\text{ZFS}} \tag{2.10}$$

$$\hat{H} = \sum_i \left(\hat{H}_{\text{Zeeman},i} + \hat{H}_{\text{ZFS},i}\right) + \sum_{i<j} \hat{H}_{\text{exch},i,j} \tag{2.11}$$

2.1.3. Zero-Field Splitting

The following introduction is based on the reviews by M. Atanasov et al.[42] and by R. Boča[43].

Zero-field splitting (ZFS) means the lifting of the degeneracy of the ground state m_S-manifold in zero external field. It is caused by weak interaction of electron spins within one magnetic center due to spin-orbit coupling. Thus, it intrinsically occurs only in systems with $S \geq 1$ and quenched first-order contribution to the angular momentum. Its magnitude usually is in the order of few cm^{-1} and rarely exceeds $100\,\mathrm{cm}^{-1}$. Still, it is often significantly stronger than the effect of Zeeman interaction which gives rise to a splitting in magnetic field of $0.93\,\mathrm{cm}^{-1}\,\mathrm{T}^{-1}$ ($g = 2$, $S = {}^1\!/\!{}_2$, for more details see Section 2.4.2). For comparison, the thermal energy is about $0.695\,\mathrm{cm}^{-1}\,\mathrm{K}^{-1}$. This shows that for the observation of both effects low temperatures must be utilized to achieve a clear population difference between involved energy states.

The ZFS Hamiltonian (Equation 2.8) includes two parameters for zero-field splitting: the axial and rhombic zero-field splitting parameters D and E, respectively. In case of axial symmetry (${}^E\!/\!{}_D = 0$), the degeneracy of the spin eigenstates is lifted such that levels with nonzero m_S remain pairwise degenerate. For Kramers systems this means that all states are pairwise degenerate while for non-Kramers systems one state is degenerate from all others and the remaining are pairwise degenerate. If rhombicity is present (${}^E\!/\!{}_D \neq 0$) the described situation remains unchanged for Kramers systems but for non-Kramers systems all degeneracy is lifted. The effect of rhombicity is to mix components with $\Delta m_S = \pm 2$ in the spin interaction matrices. As an effect of this, otherwise spin-forbidden transitions are allowed between states which have in their mixed set of components a common pair which differs by $\Delta m_S = 0, \pm 1$.

Table 2.1 gives the eigenvalues of the zero-field splitting Hamiltonian for $S = 1, {}^3\!/\!{}_2, 2$. A graphical representation of the energies at zero and applied field for $S = 1, {}^3\!/\!{}_2, 2, {}^5\!/\!{}_2$ is given in Figures 2.2 and 2.3 for $g = 2$, $D = 5\,\mathrm{cm}^{-1}$ and $E = 0$ and $E = 2\,\mathrm{cm}^{-1}$, respectively. It can be seen that for $E = 0$ and at zero field the differences between the eigenvalues adjacent in energy correspond to D ($S = 1$), $2D$ ($S = {}^3\!/\!{}_2$), $D : 3D$ ($S = 2$) and $2D : 4D$ ($S = {}^5\!/\!{}_2$). For $S = 2$ and $S = {}^5\!/\!{}_2$ there is additionally the difference of $4D$ and $6D$, respectively, between the eigenvalues highest and lowest in energy. Depending on the experimental setup, these energy differences might be observed in zero field by spectroscopy which is a very clear and precise way to characterize spin systems.

Table 2.1: Eigenvalues ε of the zero-field splitting Hamiltonian for different Spins S. The values are sorted by descending energy for $D, E > 0$.

Spin S	Eigenvalues
1	$\varepsilon_1 = {}^{1}\!/_{3}D + E$
	$\varepsilon_2 = {}^{1}\!/_{3}D - E$
	$\varepsilon_3 = -{}^{2}\!/_{3}D$
${}^{3}\!/_{2}$	$\varepsilon_1 = \varepsilon_2 = +\sqrt{D^2 + 3E^2}$
	$\varepsilon_3 = \varepsilon_4 = -\sqrt{D^2 + 3E^2}$
2	$\varepsilon_1 = +2\sqrt{D^2 + 3E^2}$
	$\varepsilon_2 = 2D$
	$\varepsilon_3 = -D + 3E$
	$\varepsilon_4 = -D - 3E$
	$\varepsilon_5 = -2\sqrt{D^2 + 3E^2}$

Another finding from the eigenvalues in Table 2.1 is that the sign of D has a major influence on the spin system's energetic structure. Comparing Figures 2.2 ($D > 0$) and 2.4 ($D < 0$), the most distinct difference is that the order of the m_S states, which are marked by the slope of the corresponding energy curves, is inverted with respect to the energy. For example, in the $S = 1$ system with $D > 0$ the $m_S = 0$ state (represented by the horizontal line) is the ground state at zero field while for $D < 0$ the $m_S = 1$ states are the degenerate ground states. This can very well be observed experimentally by magnetometry because the $m_S = 0$ state does not have a connected magnetic moment, thus, the spin system's measured magnetization will drop strongly when approaching low temperatures with clear spin polarization.

2.2. Electronic Structure of Transition Metal Complexes

The following introduction is based on the textbooks by C. J. Ballhausen[44] and by A. B. P. Lever[45].

The largest impact on the electronic structure of atoms and ions is caused by electronic repulsion. Thus, the energetic state of an atom or ion depends on the distribution of their electrons between the shells. These configurations are described by term symbols of the form ^{2S+1}L. S is the total spin and L the total orbital angular momentum. $2S + 1$ is called the spin multiplicity. The

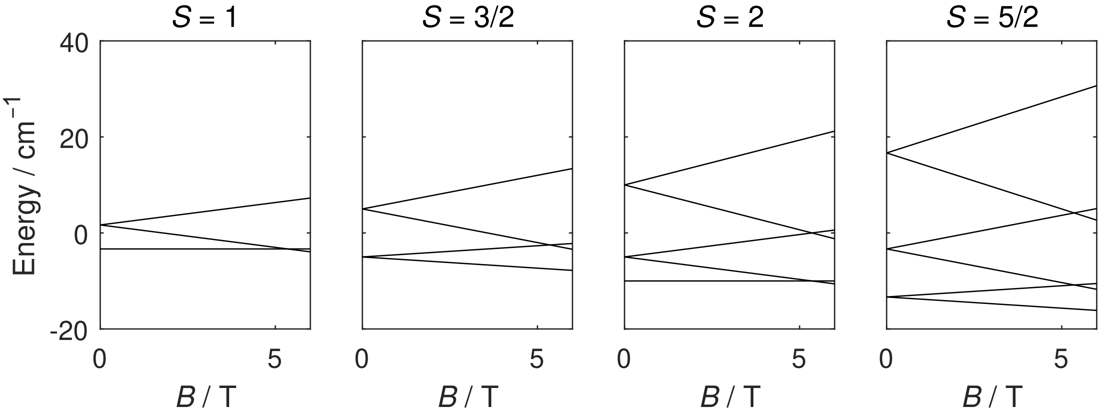

Figure 2.2: Energy levels of a spin system with $g = 2$, $D = 5\,\mathrm{cm}^{-1}$ and $E = 0$ for indicated spins in the parallel (z) direction.

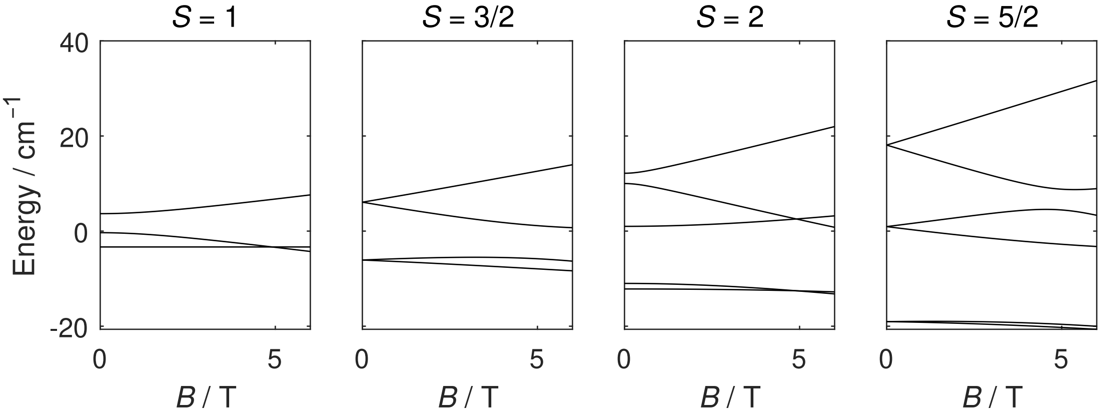

Figure 2.3: Energy levels of a spin system with $g = 2$, $D = 5\,\mathrm{cm}^{-1}$ and $E = 2\,\mathrm{cm}^{-1}$ for indicated spins in the parallel (z) direction.

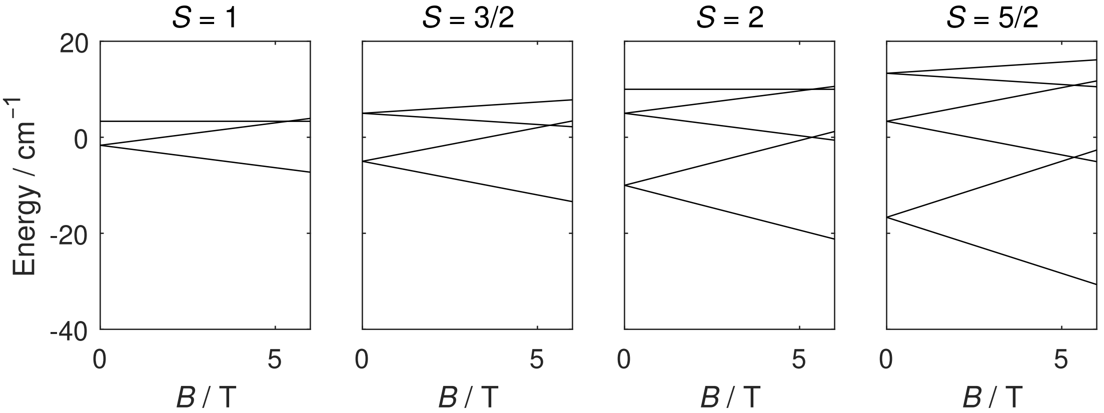

Figure 2.4: Energy levels of a spin system with $g = 2$, $D = -5\,\mathrm{cm}^{-1}$ and $E = 0$ for indicated spins in the parallel (z) direction.

electronic ground state can be derived using Hund's rules[46] and the Pauli exclusion principle[47]. In general, the ground state exhibits the maximum spin S and for that S the maximum of L. The term symbol ${}^{2S+1}L_J$ is extended by the total angular momentum J which takes values between $L+S$ and $|L-S|$ in steps of 1. According to Hund's rules the ground state has the minimum value of J when a shell is at most half-full and the maximum value of J when the shell is more than half-full.

For transition metal complexes, the next-largest interaction leading to splitting of energetic states is ligand field splitting. The effects of this interaction are caused by the electrons of the surrounding ligands and, thus, strongly depend on the local symmetry around the metal ion. Examples are given in the next sections for the ions investigated in this work.

The electronic structure of all transition metal ions as a function of ligand field strength in an octahedral environment is depicted in so called Tanabe-Sugano diagrams[48]. In these diagrams, the energy of terms divided by the Racah-Parameter B is plotted against the ligand field splitting parameter Δ divided by B. The plot is usually such that the x-axis represents the ground state energy. Labels on the y-axis denote the free-ion terms while other term symbols are in octahedral ligand field. The diagrams can be applied to ions in tetrahedral environment by using the diagram of an octahedral complex with d^{10-n} for the tetrahedral complex with d^n. At the same time, Δ_T of tetrahedral complexes is about $4/9$ of Δ_O for octahedral complexes.

2.2.1. Electronic Structure of Tetrahedral Ni(II) Complexes

The ground state electron configuration of Ni(II) is $[\mathrm{Ar}]3\mathrm{d}^8$ which results in a electronic ground state of ${}^3\mathrm{F}$ for free Ni(II). In tetrahedral $\mathrm{T_d}$ environment this state is split into the states ${}^3\mathrm{T}_1$, ${}^3\mathrm{T}_2$ and ${}^3\mathrm{A}_2$ in order of ascending energy. Excited states of the free ion are ${}^1\mathrm{D}$, ${}^3\mathrm{P}$, ${}^1\mathrm{G}$ and ${}^1\mathrm{S}$ the splitting of which in tetrahedral field is shown in the corresponding Tanabe-Sugano diagram in Figure 2.5. A more detailed investigation of Ni(II) in tetrahedral field can be found in literature[49, 50].

2.2.2. Electronic Structure of Tetrahedral Co(II) Complexes

Co(II) exhibits a ground state electron configuration of $[\mathrm{Ar}]3\mathrm{d}^7$. The corresponding term symbol of a free Co(II) is ${}^4\mathrm{F}$. Symmetry reduction in a tetrahedral ligand

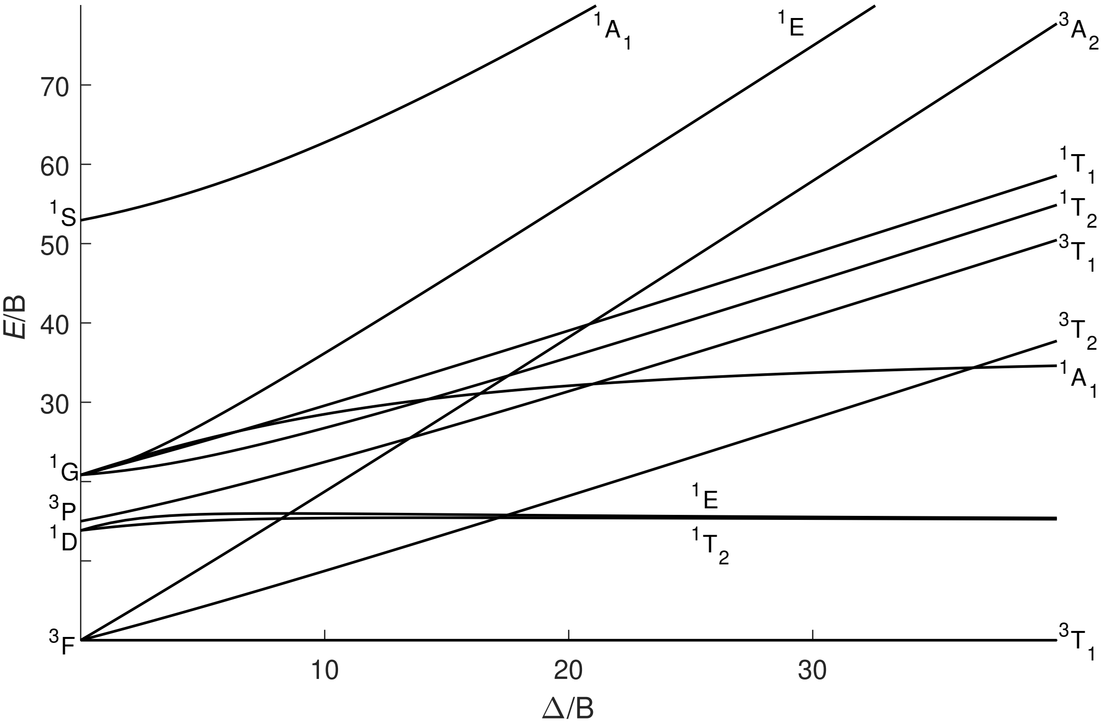

Figure 2.5: Tanabe-Sugano diagram for d^2 systems (octahedral)[51].

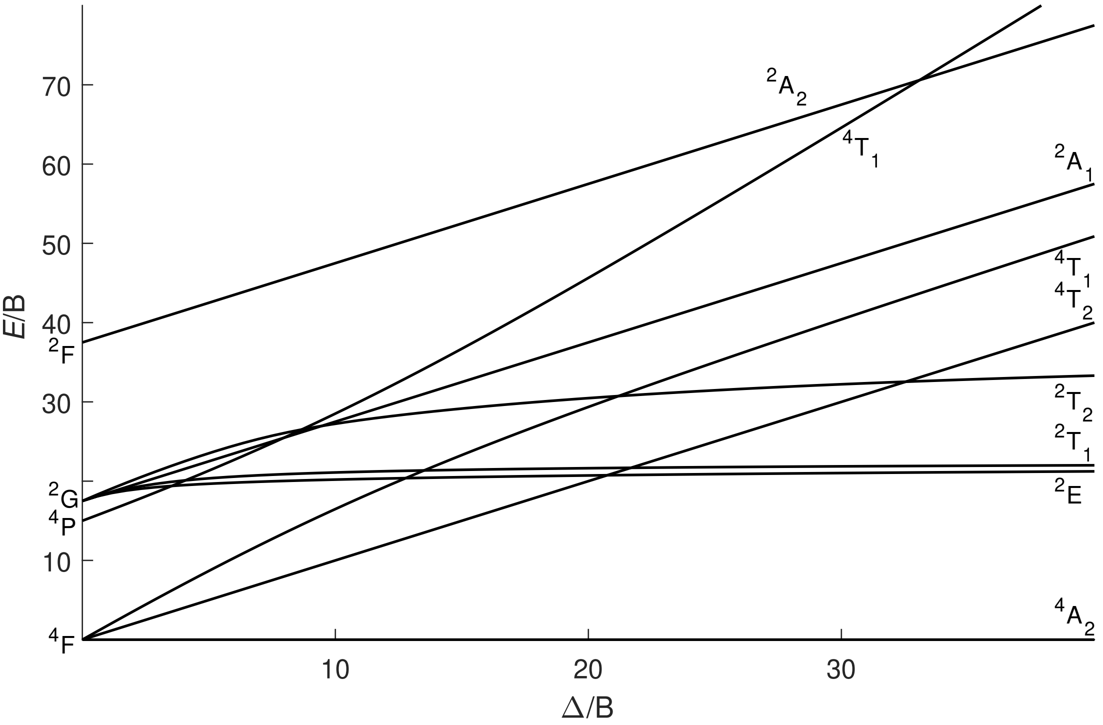

Figure 2.6: Tanabe-Sugano diagram for d^3 systems (octahedral)[51].

field leads to a splitting into the ground state term $^4\mathrm{A}_2$ and the excited terms $^4\mathrm{T}_2$ and $^4\mathrm{T}_1$. Further excited states of both the free ion and Co(II) in $\mathrm{T_d}$ symmetry can be read from the Tanabe-Sugano diagram in Figure 2.6.

Symmetry reduction from $\mathrm{T_d}$ to $\mathrm{D_{2d}}$, which corresponds to an axial distorted tetrahedron, causes further splitting of the terms. The terms originating from the $^4\mathrm{F}$ term are then split into $^4\mathrm{B}_2$ and $^4\mathrm{E}$ ($^4\mathrm{T}_2$) and $^4\mathrm{A}_2$ and $^4\mathrm{E}$ ($^4\mathrm{T}_1$). At the same time, the ground state transforms as $^4\mathrm{B}_1$.

Based on the electronic structure and with the help of perturbation theory, an estimation of the zero-field splitting caused by second-order spin-orbit coupling can be made[43]. The relation between the axial zero-field splitting parameter D and the transition energies from the ground state to the $^4\mathrm{E}$ and $^4\mathrm{B}_2$ states is given in Equation 2.12 where λ is the spin-orbit splitting parameter .

$$D = 4\lambda^2 \left[\frac{1}{E(^4\mathrm{E})} - \frac{1}{E(^4\mathrm{B}_2)} \right] \tag{2.12}$$

2.2.3. Electronic Structure of Tetrahedral Fe(II) Complexes

The ground state electron configuration of Fe(II) is [Ar]$3\mathrm{d}^6$. For a free Fe(II) ion this translates into an electronic ground state term of $^5\mathrm{D}$. In a tetrahedral ligand field this term is split into a $^5\mathrm{E}$ ground state and $^5\mathrm{T}_2$ excited state. The Tanabe-Sugano diagram showing the further splittings and excited states is depicted in Figure 2.7.

2.3. Iron in Soils

The following introduction is based on the textbook by J. W. Stucki, B. A. Goodman and U. Schwertmann[16].

Formed by nuclear fusion as one of the most stable elements, the abundance of iron in cosmic and terrestrial matter is high. By mass, it is the most abundant element in the earth. In the earth's crust, it is after oxygen, silicon and aluminum the fourth most abundant element. Regarding urban soil, iron is still the sixth most abundant element (2.2 wt.%) after the aforementioned ones (O: 49 wt.%, Si: 29 wt.%, Al: 3.8 wt.%) plus calcium (5.4 wt.%) and carbon (4.5 wt.%)[52]. Most iron is bound in a wide variety of minerals, for example olivine, pyroxenes, amphiboles, magnetite and clay minerals. Those of most relevance for this work, namely

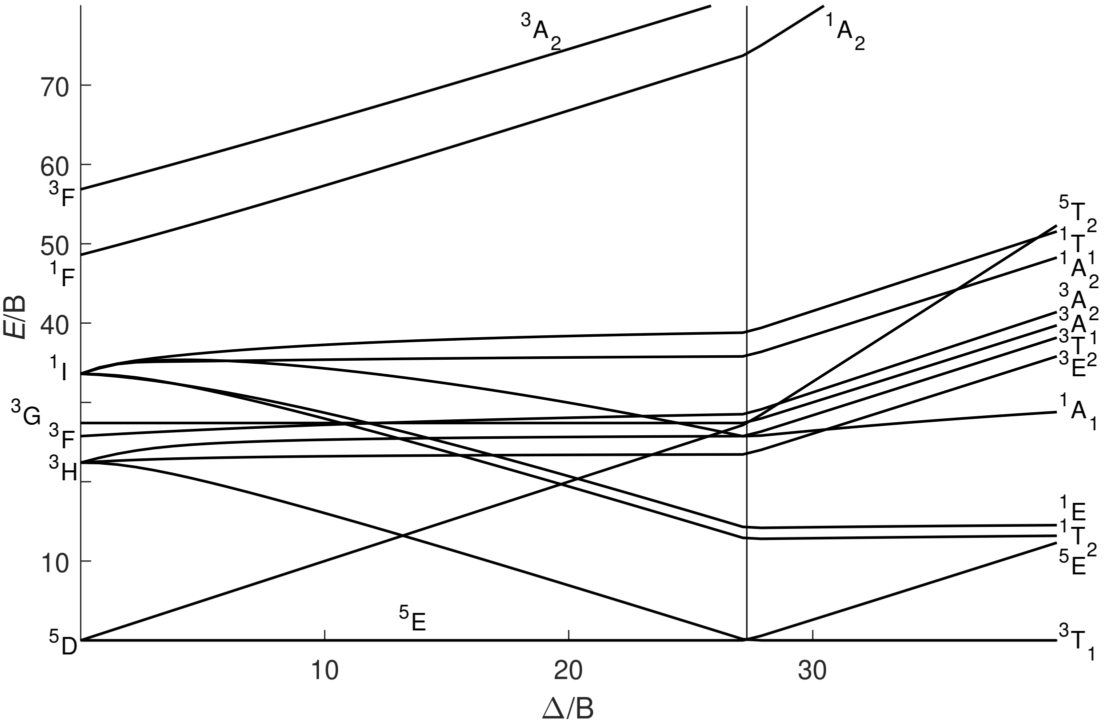

Figure 2.7: Tanabe-Sugano diagram for d^4 systems (octahedral)[51].

ferrihydrite, goethite and hematite, are discussed in more detail in the next section. Compared to its presence in solid state, the abundance of iron in solution is very small. It ranges from about 5 ppm and about 670 ppm in rivers to 3.4 ppb in oceans (all values on mass basis).

As for the oxidation state, iron exists in the environment both in the +2 and +3 state because both form stable compounds. The ratio between these two oxidation states is influenced by the environmental conditions whereupon the presence of Fe^{3+} is especially promoted by high pH values or oxidizing conditions.

2.3.1. Iron Minerals

The following introduction is based on the textbooks by R. M. Cornell and U. Schwertmann[53] and by J. W. Stucki, B. A. Goodman and U. Schwertmann[16].

A wide variety of minerals containing iron is present in the earth's crust and soils. Three of these are presented here in more detail because they are of special relevance for this work. Goethite, hematite and ferrihydrite are the minerals which are typically present in the soil on which the samples in Chapter 5 are based.

Goethite

Goethite (α-FeOOH, named after J. W. von Goethe) is an oxyhydroxide of yellow-brown color and has been used as pigment since ancient times. It is isostructural with diaspore with a orthorhombic unit cell. Its structure is based on a hexagonally close packing of O^{2-} and OH^{-} ions. Half of the octahedral interstices are occupied by Fe^{3+} ions. The occupation is such that edge-sharing double rows of filled octahedra form along the *c*-axis. These filled double rows are separated to each other by empty double rows resulting in corner-sharing of adjacent filled double rows. The distances between the oxygen ions which are shared by octahedra within the same double row are slightly shorter than the other inter-oxygen distances. As a consequence, the double chains are slightly twisted with respect to each other.

The Néel temperature T_{N} of goethite is about 393 K. Below that, it is of anti-ferromagnetic nature with the spins aligned along the *c*-axis. Within one double chain of octahedra filled with Fe^{3+} the spins are aligned parallel within each chain but antiparallel to the spins in the second chain and other closest chains.

Goethite is the most common iron oxide in soils which is explained by its high thermodynamic stability. Often it is even the only occurring iron oxide in soil all around the world. Its presence is favored at cool to moderate temperature and humid climate under both aerobic and anaerobic conditions. Goethite in soil is formed from ferrihydrite in aqueous media. Alternatively, it can directly be formed by oxidation of Fe^{2+} which is released from minerals like silicates or produced from minerals containing Fe^{3+} by microbial reduction (c. f. Section 2.3.2).

Hematite

The name of hematite comes from the Greek word haima (“blood”) which is related to its characteristic red streak. Its chemical formula is α-Fe_2O_3 and it is isostructural to corundum. This means that planes of oxygen ions are hexagonally close packed and two thirds of the resulting octahedral sites are occupied by Fe^{3+} ions. By this, pairs of $Fe(O)_6$ octahedra are formed which share one face with a corresponding octahedron in a plane adjacent along the *c*-axis. This face-sharing causes a distortion of the Fe^{3+} sublattice from ideal arrangement. Iron ions that are adjacent on both sides of a shared face are repelled by each other and shifted to non-shared faces of the octahedra. By this, also the O^{2-} sublattice is distorted such that the distances between the oxygen ions of the shared faces are smaller than those of the non-shared faces leading to a trigonal distortion of the octahedron.

The magnetic properties of hematite stand out by the presence of two transitions resulting in three different magnetic states depending on the temperature. At high temperatures above the Néel temperature T_{N} of 956 K it is paramagnetic. Between T_{N} and the Morin transition at about $T_{\mathrm{M}} = 260\,\mathrm{K}$ it is weakly ferromagnetic. Below T_{M} it is antiferromagnetic. The transition from weakly ferromagnetic to antiferromagnetic is caused by a spin flop at T_{M}. For $T < T_{\mathrm{M}}$, the spins of the Fe^{3+} ions are aligned exactly antiparallelly along the c-axis resulting in antiferromagnetism. At T_{M} a spin flop occurs such that for $T > T_{\mathrm{M}}$ the spins are aligned in the basal plan orthogonal to the c-axis. At the same time, ions which share an octahedron face along the c-axis are antiferromagnetically coupled. This results in two interpenetrating antiferromagnetic sublattices. The magnetic moments of these sublattices are not perfectly antiparallel but slightly canted resulting in weak ferromagnetism.

The presence of hematite in soil strongly depends on the regional circumstances where warmer temperatures or drier climates are favorable. It is very rarely the only iron oxide present in a soil but usually appears with goethite due to the possibility of both minerals forming from ferrihydrite. The ratio between the two varies between 0 % and 95 % of hematite. Hematite is formed from ferrihydrite in aqueous media. The transformation involves internal rearrangement and dehydration and is promoted by the structural similarity between both minerals. Additionally, most other iron oxides and hydroxides including goethite, ferrihydrite and maghemite (γ-$\mathrm{Fe_2O_3}$) can be transformed thermally to hematite.

Ferrihydrite

Ferrihydrite is in general a poorly ordered mineral. Additionally, the degree of ordering varies which can be observed in powder x-ray diffraction (XRD) patterns. The labeling of the two extremes of ordering, namely 2-line and 6-line ferrihydrite, is based on their number of lines in XRD patterns. The structure of the higher ordered 6-line ferrihydrite can be described as a defective hematite type. This means a hexagonal close packing of anions where randomly distributed $\mathrm{Fe}^{\mathrm{III}}$ sites are vacant. Structural oxygen is present both as HO^{-} and O^{2-}. An ill-defined amount of water is present and the structural water content may vary between $80\,\mathrm{g\,kg^{-1}}$ and $150\,\mathrm{g\,kg^{-1}}$ without changes in the structure.

Ferrihydrite shows superparamagnetism at room temperature due to its generally very small particle size. Blocking temperatures strongly depend on particle size and values reported in literature range from 25 K to 115 K.

Generally, ferrihydrite is a metastable oxyhydroxide and a precursor of other minerals such as goethite and hematite. It is formed in nature from aqueous Fe^{2+} by quick oxidation or by oxidation in presence of organic matter which hinders crystal nucleation. The latter makes it a common constituent of podzol B horizons, one of which was investigated in this work.

2.3.2. Relevance of Iron for Plants

The following introduction is based on the textbook by J . W. Kadereit et. al.[13] and the articles by W. Schenkeveld et. al.[14, 15].

Iron is a so-called micronutrient. This means it is an essential nutrient which is needed in small quantities ($< 2\,\mu g\, g^{-1}_{solution}$ for plants in hydroponics) for a healthy growth. It is for example incorporated in different porphyrin compounds, like in the heme groups of cytochromes, catalase and peroxidase. It also is of crucial importance as cofactor for the synthesis of chlorophyll. A visible consequence of the lack of iron is chlorosis which means that insufficient chlorophyll is produced. This results in the colors of leaves not being healthily green but pale, yellow or yellow-white.

As described in the previous section, iron is usually abundant in soil in sufficient amounts. Nonetheless, its bioavailability is often limited because only little amounts of dissolved iron are accessible. For example, iron is mainly present as insoluble iron(III) oxide in alkaline (e. g. calcareous) soils which constitute significant amounts of the world's farmland. To cope with this situation, some plants actively increase the acidity of soil with H^+ or organic acids to increase the bioavailabilty of Fe^{3+}. With the same goal, some bacteria[19] and fungi[20] exude siderophores (Greek for "iron carrier") which are organic molecules with a high affinity to form accessible complexes with Fe^{3+}. An example for such a siderophore is desferrioxamine B (DFOB) which is a hexadentate ligand (Figure 2.8). In general, iron is mostly taken up directly as Fe^{2+} by plant roots via a transport protein. For this, Fe^{3+} diffusing to the roots is actively reduced to Fe^{2+} by a reductase bound to the root cell's membrane. Graminaceous plants facilitate a second strategy in case of iron deficiency. They produce and release mugineic acid and similar compounds which form complexes with Fe^{3+} with high affinity.

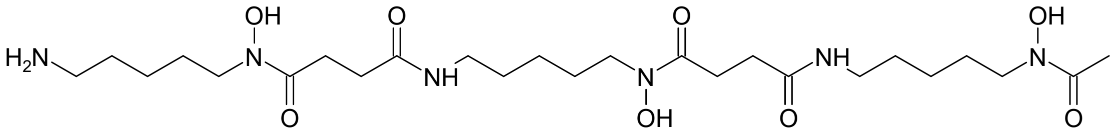

Figure 2.8: Skeletal formula of the hexadentate siderophore DFOB.

These chelating ligands are called phytosiderophores (phyto: Greek for “plant”). The formed Fe^{3+} complexes are taken up by the roots where the iron is reduced to Fe^{2+}. Because this strategy is more energy intensive than the root-external reduction of Fe^{3+} and direct uptake of Fe^{2+} as described above, it is only used when the supply with iron is not sufficient.

2.4. Experimental Methods

2.4.1. Magnetometry

The following introduction is based on the textbooks by D. Gatteschi, R. Sessoli and J. Villain[24] and by O. Kahn[54].

The standard method used for investigation of molecular magnets is magnetometry due to its widespread availability and ease of use. In most cases a SQUID magnetometer (Superconducting Quantum Interference Device) is used due to its high sensitivity. Two different types of magnetometric measurements are employed in this work, namely static and dynamic measurements.

In static or direct current (dc) measurements the static magnetic properties of a sample are analyzed. For this, a static magnetic field is applied which magnetizes the sample. Moving the sample through the magnetometer’s superconducting pick-up coils induces a current which is proportional to the magnetization of the sample. The SQUID transduces this current into a voltage which can be converted to magnetization by calibration with a reference sample (usually palladium).

Two magnetic quantities are usually of interest regarding static magnetometric measurements: magnetization M and magnetic susceptibility χ. Magnetization is defined as the negative derivative of energy E with respect to magnetic field H (Equation 2.13).

$$M = -\frac{\partial E}{\partial H} \tag{2.13}$$

Magnetic susceptibility χ is defined as the derivative of magnetization with respect to magnetic field (Equation 2.14). For weak applied fields and high temperatures, this derivative is reasonably well approximated by the ratio of magnetization and magnetic field:

$$\chi = \frac{\partial M}{\partial H} \approx \frac{M}{H}. \tag{2.14}$$

The magnetic susceptibility consists of two contributions: diamagnetic χ^{d} and paramagnetic χ^{p} susceptibility:

$$\chi = \chi^{\mathrm{d}} + \chi^{\mathrm{p}}. \tag{2.15}$$

The diamagnetic contribution is independent of temperature and applied field and always negative. It is caused by the interaction of the magnetic field with the movement of paired electrons and, thus, present in all materials. Two methods exist to correct χ, which is accessible by measurements, for the contribution of χ^{d}. Firstly, Pascal's constants[55] can be employed, which are empirically determined diamagnetic contributions of atoms, ions and bonds. Secondly, the simple approximation given in Equation 2.16 may be used. There, M corresponds to the compound's molecular weight and the factor k varies between 0.4 and 0.5.

$$\chi^{\mathrm{d}}_{\mathrm{m}} = kM \cdot 10^{-6} \mathrm{cm}^3\,\mathrm{mol}^{-1} \tag{2.16}$$

The molar paramagnetic contribution $\chi^{\mathrm{p}}_{\mathrm{m}}$ is positive and caused by unpaired electrons. It can be estimated for non-interacting spins from Curie's law as

$$\chi^{\mathrm{p}}_{\mathrm{m}} = \frac{N_{\mathrm{A}} g^2 \mu_{\mathrm{B}}^2}{3kT} S(S+1). \tag{2.17}$$

This equation can be rewritten to $\chi^{\mathrm{p}}_{\mathrm{m}} T = \frac{N_{\mathrm{A}} g^2 \mu_{\mathrm{B}}^2}{3k} S(S+1)$ which makes the plot of the product of magnetic susceptibility with temperature χT versus temperature very useful. As χT is constant for non-interacting spins, it directly shows deviations from their paramagnetic behavior. With the good approximation of $\frac{N_{\mathrm{A}} \mu_{\mathrm{B}}^2}{3k} \approx \frac{1}{8}\,\mathrm{cm}^3\,\mathrm{mol}^{-1}$ in the cgsemu unit system and $g = 2$ the expected χT-values for common values of S can be calculated and are listed in Table 2.2.

For molecular magnets, χT versus T is virtually never a constant. This temperature dependence may help identifying the ground state of a compound or exchange interactions between paramagnetic centers.

Table 2.2: Spin-only values of χT as function of the spin S for $g = 2$.

S	χT
$1/2$	0.375
1	1
$3/2$	1.875
2	3
$5/2$	4.375

Dc magnetic measurements can in some situations also be used to obtain information about spin dynamics by monitoring the decay of magnetization over time. For feasibility, the time-scale of relaxation must be longer than some seconds. An upper limit is only given by practical reasons like availability of the device. For this measurement, a magnetic field is applied to magnetize the sample. To reach an equilibrium of magnetization this is preferably done at a temperature of fast dynamics. The sample is then set to the temperature of interest and afterwards the applied field is removed. From that moment, the magnetization is measured over time. The resulting curve is then fitted to an exponential law. In many cases, a stretched exponential decay or even a combination of several stretched exponential decays is needed for a satisfying fit. The stretching factor, which ranges from 0 to 1, is a measure for the distribution of relaxation times.

Another experiment commonly performed with SMMs is the so called zero field cooled field cooled (ZFCFC) measurement where the thermo-remnant magnetization is measured. A scheme of the resulting curves of this measurement for a system with slow relaxation of magnetization is depicted in Figure 2.9. Therein, the sample is first cooled in zero applied field which leads to freezing of the non-polarized spins of the sample because the relaxation time increases. After that, a magnetic field is applied, which is weak enough to not magnetize the sample, and the sample's magnetization is measured while increasing the temperature. During the temperature increase, the relaxation time reduces which leads to a gradual magnetization of the sample (red ZFC curve in Figure 2.9). At some temperature the magnetization will again start to decrease due to the sample's paramagnetic nature resulting in a maximum of the M versus T curve. The temperature at this maximum is called the blocking temperature T_{B}. The sample reaches equilibrium when the ZFC curve superimposes with the FC curve and the corresponding temperature is called the irreversibility temperature T_{IRREV}. The FC curve (blue in Figure 2.9) is measured analogously to the ZFC curve but the field applied during

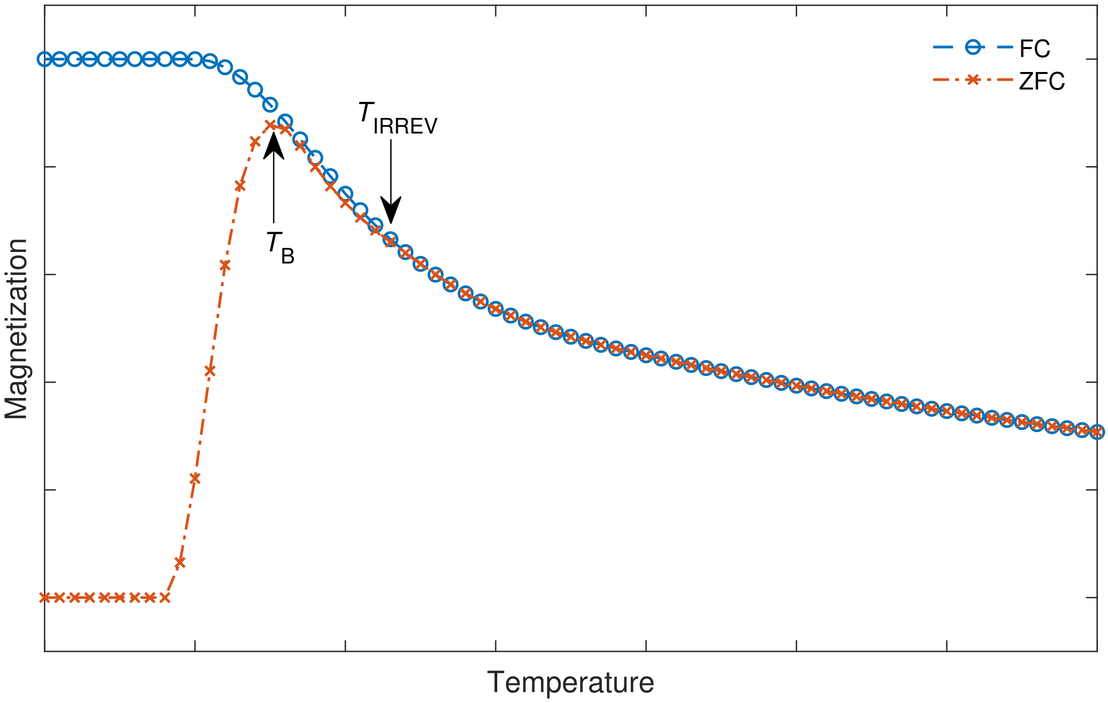

Figure 2.9: Schematic magnetization curves plotted against temperature of FC and ZFC measurements for a sample with slow relaxation of magnetization.

warm-up is already applied during cool-down. T_{B} and T_{IRREV} do not necessarily match and their difference is a measure of the distribution of relaxation times in the sample.

With alternating current (ac) magnetometric measurements the dynamic magnetic properties of a sample may be investigated for shorter time-scales than described in the paragraphs above. A small alternating magnetic field is applied to the sample, usually in the range of several hundred Hertz. Slow relaxation of magnetization is then observed if the magnetization of the sample does not oscillate in phase with the applied field and an out-of-phase component can be measured. The relation of the in-phase component χ' and out-of-phase component χ'' is described in Equation 2.18.

$$\chi_{\mathrm{ac}} = \chi' - i\chi'' \tag{2.18}$$

A measurement series involves usually variations of the applied field's frequency and the temperature. A maximum in the plot of χ'' against the frequency or temperature indicates the relaxation time τ for a specific temperature which can be calculated according to Equation 2.19 where ω is the angular frequency.

$$\omega\tau = 1 \tag{2.19}$$

For a more detailed data analysis, a measurement series of different frequencies at constant temperature can be fitted to the standard modified Debye functions[24] (Equations 2.20 and 2.21). There, χ_T and χ_S are the isothermal and adiabatic limit of the susceptibility, respectively, and α is a measure for the distribution of relaxation times being larger for wider distributions. From the Arrhenius plot based on relaxation times at different temperatures, the effective energy barrier can then be determined.

$$\chi' = \chi_\mathrm{S} + (\chi_\mathrm{T} - \chi_\mathrm{S}) \frac{1 + (\omega\tau)^{1-\alpha} \sin\left(\frac{\pi\alpha}{2}\right)}{1 + 2(\omega\tau)^{1-\alpha} \sin\left(\frac{\pi\alpha}{2}\right) + (\omega\tau)^{2-2\alpha}} \tag{2.20}$$

$$\chi'' = (\chi_\mathrm{T} - \chi_\mathrm{S}) \frac{(\omega\tau)^{1-\alpha} \cos\left(\frac{\pi\alpha}{2}\right)}{1 + 2(\omega\tau)^{1-\alpha} \sin\left(\frac{\pi\alpha}{2}\right) + (\omega\tau)^{2-2\alpha}} \tag{2.21}$$

2.4.2. EPR Spectroscopy

The following introduction is based on the textbooks by A. Abragam and B. Bleaney[56] and by J. A. Weil and J. R. Bolton[57].

Electron paramagnetic resonance (EPR) spectroscopy, also called electron spin resonance (ESR) spectroscopy, is a versatile tool to investigate the electronic and geometric structure of compounds featuring unpaired electrons. Beside its obvious suitability for the analysis of organic radicals or transition metal complexes it can, for example, be used to measure distances in molecules using spin probes. In context of this work, EPR spectroscopy was utilized to examine the electronic structure of transition metal complexes.

EPR spectroscopy bases upon the excitation of the magnetic-dipole moment of electrons. For each electron, this magnetic moment arises from its spin and is described by the magnetic spin quantum number m_S. The selection rule in EPR spectroscopy is $\Delta m_S = \pm 1$. For spin systems with rhombic zero-field splitting (see Section 2.1.3) a mixing of states occurs and m_S is no longer a good quantum number.

In the simplest case where $S = {}^1\!/_2$, only $m_S = -{}^1\!/_2 \rightarrow +{}^1\!/_2$ transitions can occur, so called intra-doublet transitions because just one doublet is involved. For systems with $S \leq 1$, inter-doublet transitions, such as $m_S = 0 \rightarrow +1$ or

$m_S = +1/2 \rightarrow +3/2$, can occur. Because these doublets are degenerate in zero magnetic field (as long as no rhombic zero-field splitting or higher order terms are present), intra-doublet transitions can only be observed when an external magnetic field is applied. This magnetic field influences the energy of the m_S spin states due to Zeeman interaction as described in Equation 2.22, lifting the degeneracy of m_S spin states with equal absolute m_S value but different sign. For the transition energy ΔE of transitions observed in EPR spectroscopy, this translates to the relation described in Equation 2.23. Here, h is the Planck constant and ν is the frequency of the irradiation used for excitation.

$$E = g_\mathrm{e}\mu_\mathrm{B} m_S B \tag{2.22}$$

$$\Delta E = h\nu = g_\mathrm{e}\mu_\mathrm{B} \left|\Delta m_S\right| B \tag{2.23}$$

The most common excitation energies used in EPR spectroscopy are around 9.5 GHz (called X-Band) but commercial spectrometers with up to 263 GHz exist. A few custom-built spectrometers even cover ranges of up to 1 THz[58]. The advantage of utilizing higher frequencies is a better resolution of transitions with similar g-values and becomes obvious when looking at Figure 2.10. Nonetheless, it is important not to rely on just a single measurement when deriving Spin Hamiltonian parameters from HFEPR spectra but to use a series of measurements with varying frequencies.

An additional advantage is the observation of inter-doublet transitions for systems with large zero-field splittings, enabling the assessment of axial and rhombic zero-field splitting parameters, which is otherwise limited to imprecise assessment from magnetometry or rarely available methods such as neutron scattering.

The drawback for high frequencies is that, according to Equation 2.23, there is a linear correlation between excitation frequency and transition field, resulting in high magnetic fields which are necessary for high-frequency EPR spectroscopy. For example, while a transition for $g = 2$ is located at 339 mT using 9.5 GHz, the same transition is located at 11.43 T when using 320 GHz. Nonetheless, this is not a crucial limitation since superconducting magnets with magnetic fields of 15 T and more are reliable and commercially available.

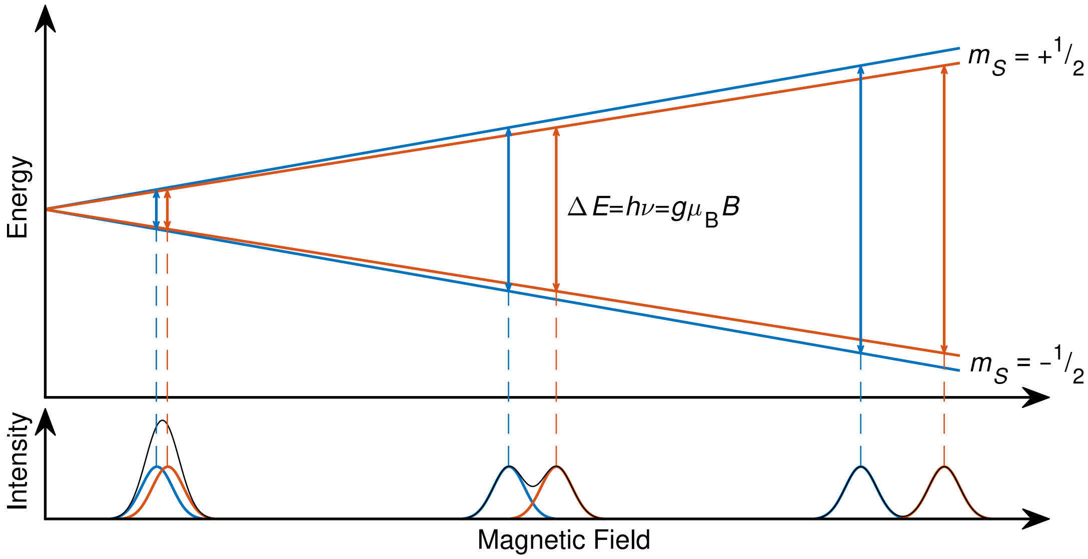

Figure 2.10: Top: Simplified energy level diagram of an $S = {}^1/_2$ system. The energy levels of two species with different but similar g-factors are shown (blue and red). The splitting of the energy levels increases with increasing magnetic field and the transition fields get more separate. Bottom: Resulting signals with finite line broadening. The black peak represents the measured signal while the blue and red peaks mark the underlying signals. For low magnetic fields the signals are very close to each other and overlapping, resulting in an unresolved feature. At higher fields and frequencies they become more separated and can be clearly distinguished.

2.4.3. Far-Infrared Spectroscopy

The electromagnetic spectrum adjacent to microwaves, which are used for EPR, at higher energies is called far infrared (FIR). It ranges from about $10\,\text{cm}^{-1}$ to $700\,\text{cm}^{-1}$. This matches very precisely the typical magnitude of zero-field splitting in transition metal based single-molecule magnets. Thus, FIR spectroscopy is a powerful tool for the direct and very precise determination of zero-field splitting parameters clearly superior to magnetometry. Because the same states are probed as in EPR spectroscopy, the same selection rule of $\Delta m_S = 1$ holds true. As with EPR, this rule might be relaxed by mixing of states (see Section 2.1.3).

The analysis of FIR spectra is complicated by not only magnetic dipole transitions occurring in this spectral range but also vibrational transitions of low energy. These transitions differ by the effect on them by an applied magnetic field which makes them distinguishable. Due to the Zeeman effect, the energy of magnetic dipole transitions will change under applied field while vibrational transitions are basically unaffected. Experimentally, the transitions can be assigned by dividing measurements at different magnetic field strengths by the measurement at zero or maximum field.

2.4.4. Optical Spectroscopy

The following introduction is based on the textbooks by W. R. Mason[59] and by A. B. P. Lever[45].

To observe transitions beyond the electronic ground state, energies larger than in the far-infrared range need to be employed. For this, optical spectroscopy comes into play. The corresponding electromagnetic spectrum ranges from the near infrared (NIR) to the visible (Vis) and ultra-violet (UV) regions which corresponds to about $5000\,\mathrm{cm}^{-1}$ to $50\,000\,\mathrm{cm}^{-1}$ (2000 nm to 200 nm). Signals observed in this range by spectroscopy correspond to transitions between electronic states of (excited) free-ion terms, e. g. d-d-transitions in transition metals. This name is due to the nature of the involved orbitals, i. e. d-orbitals. The applicable selection rule depends on the transition's nature of which magnetic dipole, electric dipole or electric quadrupole are possible. In general, the transition dipole moment needs to be non-zero for the initial and final states' wave functions ψ_i and ψ_f, respectively, for the dipole moment operator $\hat{\mu}$:

$$\langle \psi_i | \hat{\mu} | \psi_f \rangle \neq 0. \tag{2.24}$$

To fulfill this condition, the direct product of the group theoretical representations of ψ_i and ψ_f with $\hat{\mu}$ must contains $\mathrm{A_{1g}}$ which is the totally symmetric representation. For electric dipole transitions it follows, that $\Delta l = \pm 1$, where l is the angular momentum quantum number. Thus, d-d-transitions are forbidden. Additionally, the spin selection rule is $\Delta S = 0$ which means that the multiplicity of states involved in a transition must be equal. Despite the forbidden nature, d-d-transitions are regularly experimentally observed. In most cases, this can be explained by vibronic coupling. This means that the electronic transition is coupled to a simultaneous excitation of vibrational modes which lifts the transition's inversion symmetry and leads to a non-zero transition dipole moment.

Different spectroscopic methods operate in the NIR-Vis-UV range, such as luminescence and electronic absorption spectroscopy. The former one can be used to probe the structure of the electronic ground term while the latter one probes excited states. A special form of absorption spectroscopy is magnetic circular dichroism (MCD) spectroscopy. MCD spectroscopy measures the difference in absorption of left and right circularly polarized light (lcp and rcp, respectively) in presence of an external magnetic field. Because the magnetic field is applied parallel to the light beam, MCD spectroscopy can be applied to substances which are not optically active in zero field. The difference in absorption ΔA is defined as given in Equation 2.25 where A_- and A_+ correspond to lcp and rcp absorption, respectively.

$$\Delta A = A_- - A_+ \tag{2.25}$$

It is apparent that ΔA is a signed quantity which is not the case for regular absorption spectroscopy. This greatly increases the possibility to analyze and distinguish signals close in energy which is one of the major advantages of MCD spectroscopy. Observed signals are connected to so-called MCD terms (A, B and C) which describe the nature of the involved states resulting in different line shapes ($f(E)$). Equation 2.26 gives the general MCD-expression where γ is a collection of spectroscopic constants.

$$\frac{\Delta A}{E} = \gamma \mu_\mathrm{B} B \left[A_1 \left(-\frac{\partial f(E)}{\partial E} \right) + (B_0 + \frac{C_0}{k_\mathrm{B} T}) f(E) \right] \tag{2.26}$$

A visual explanation for the different terms is given in Figure 2.11. An A term occurs when a transition involves a final state which is degenerate in zero field. In the example of a $^1\mathrm{S}_0 \rightarrow {}^1\mathrm{P}_{0,\pm1}$ transition lcp is allowed to $^1\mathrm{P}_{+1}$ and rcp is allowed to $^1\mathrm{P}_{-1}$. All other transitions (also to $^1\mathrm{P}_0$) are forbidden. Because the $^1\mathrm{P}_{-1}$ and $^1\mathrm{P}_{+1}$ states are energetically split in an applied field due to the Zeeman effect, the two allowed transitions occur at slightly different energies. Additionally, since they are lcp and rcp, respectively, the sign of ΔA is different for both transitions. Both resulting signals are of equal intensity. As the energy difference is usually small, the signals overlap resulting in an effective signal which is symmetric and derivative-shaped.

B terms are caused by field-induced mixing of the wave functions at zero field. An example is given in Figure 2.11 for the two transitions $s \rightarrow p_x$ and $s \rightarrow p_y$ which are at different energies because a different environment is present along the x and y axes.

C terms are, in contrast to A and B terms, temperature-dependent as can be seen in Equation 2.26. They arise from a ground state which is degenerate at zero field. The degeneracy is lifted in an applied field. On the one hand this leads to two observed transitions with different signs as for A terms. On the other hand the Boltzmann population of the non-degenerate states is different due to very low

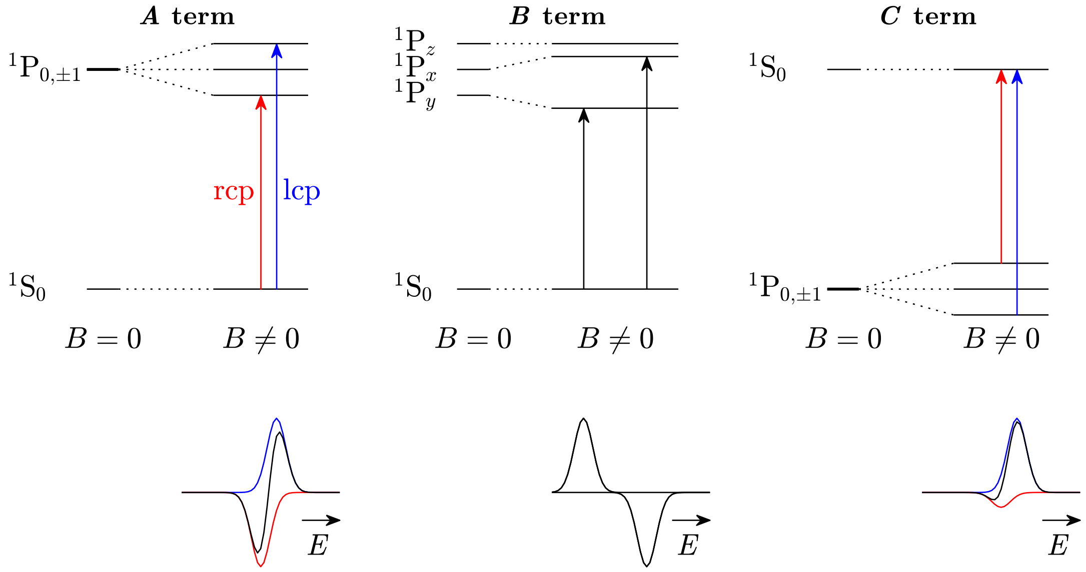

Figure 2.11: Schematic visualization of the energy levels and resulting line shapes for MCD terms A, B and C as indicated.

thermal energy which causes the signals to have different intensities. The resulting line shape is of asymmetric absorption character. leads to the temperature dependence and asymmetric shape as the population, and thus the transition intensity, of the states depends on the thermal energy which is usually very low for these measurements. In general, the intensity of C terms dominates over A and B terms at low temperatures for paramagnetic metal complexes.

3. Mononuclear Transition Metal Complexes

The project presented below was part of a collaboration with the group of Prof. Dr. Biprajit Sarkar. All compounds were synthesized and structurally characterized by Uta Albold, M.Sc. (both Institut für Chemie und Biochemie, Freie Universität Berlin at the time). Parts of the results presented in this chapter have been published in *Inorg. Chem.* **2021**, *60*, 2953–2963[60].

3.1. Aims

Using molecular nanomagnets for data storage is an idea where great progress was achieved in recent years, mainly in increasing the blocking temperature. Currently, dysprosium metallocene systems show the most outstanding properties with magnetic hysteresis at temperatures up to 80 K[8, 9, 61]. For transition metal systems, low-coordinate systems[62, 63] are performing best. In such systems, slow relaxation of magnetization in zero field was observed[12, 34, 64] but true magnetic bistability without waist-restriction in the hysteresis curve in powdered systems at or above liquid helium temperatures has not been found. Thus, in spite of all progress, using molecular magnets for data storage is still far from practical application. While reasonable design criteria for well-performing single-molecule magnets (SMM) have been identified in the last years, many aspects remain to be understood, such as correlations of the chemical structure with magnetic properties or relaxation pathways. Thus, the aim of this chapter is the detailed investigation of magnetic and electronic properties of SMM candidates to achieve a better understanding of electronic structure and to formulate magnetostructural correlations.

Static and dynamic magnetometry is the most available and in many investigations also exclusively used technique to study properties of single-molecule magnets. Because overparametrization is often an issue especially in interpretation of static magnetometry data, it is not sufficient to solely rely on this technique. In addition to SQUID magnetometry, we therefore used spectroscopic methods such as EPR, FIR and MCD spectroscopy to assess the magnetic and electronic properties of the investigated compounds. Especially with EPR and FIR spectroscopy, if they are applicable to the system, parameters can be determined with a much higher accuracy.

The previously reported Co(II) complex $(HNEt_3)_2[Co^{II}(L_A)_2]$ ($(HNEt_3)_2[1]$) with H_2L_A = 1,2-bis(methanesulfonamido)benzene) shows slow relaxation of magnetization in zero applied field in combination with a very large zero-field splitting[12]. The outstanding properties of this system arise from the chosen ligands which cause a strong axial distortion of the tetrahedral coordination sphere. It is known for some cobalt complexes that even small changes in the geometry lead to drastically changed properties of single-molecule magnets[65]. Thus, to investigate the robustness of this system, a series of analogous compounds was analyzed where in three cases the counter-ion of the complex and in one case a side group was changed to influence the geometry in solid state. We then used the aforementioned methods to gain a thorough understanding of the magnetic and electronic structure of the compounds and evaluate the influence of the geometry changes on these properties (Section 3.3).

While slow relaxation of magnetization has been found in a large number of cobalt complexes (though still often only field-induced), only a limited number of mononuclear complexes based on other transition metal atoms has been reported to show this property[62, 66–78]. In case of copper, vanadium, manganese and nickel, all reported complexes are limited to field induced slow relaxation of magnetization[66–68, 73–78]. For iron, both variants have been reported[62, 69, 71, 72]. As a consequence, we investigated if our ligand platform can induce single-molecule magnet behavior in nickel(II) (Section 3.4), iron(II) and iron(III) (Section 3.5) systems.

3.2. Investigated Compounds

Seven mononuclear complexes were investigated, which are listed in Table 3.1 with their respective label used in this work. Parts of the EPR and magnetometric measurements as well as preliminary analyses of the obtained data were carried out by David Hunger ($\mathbf{K_2[1]}$, $\mathbf{K_2[3]}$, $\mathbf{(HNEt_3)_2[4]}$) and Friederike Allgöwer ($\mathbf{(K\text{-}18\text{-}c\text{-}6)_2[1]}$, $\mathbf{(HNEt_3)_2[2]}$) under my supervision as part of their bachelor's theses.

Table 3.1: Investigated complexes and their corresponding labels.

$K_2[Co^{II}(L_A)_2]$	$\mathbf{K_2[1]}$
$(K\text{-}18\text{-}crown\text{-}6)_2[Co^{II}(L_A)_2]$	$\mathbf{(K\text{-}18\text{-}c\text{-}6)_2[1]}$
$(HNEt_3)_2[Co^{II}(L_B)_2]$	$\mathbf{(HNEt_3)_2[2]}$
$K_2[Ni^{II}(L_A)_2]$	$\mathbf{K_2[3]}$
$(HNEt_3)_2[Ni^{II}(L_A)_2]$	$\mathbf{(HNEt_3)_2[3]}$
$(HNEt_3)_2[Fe^{II}(L_A)_2]$	$\mathbf{(HNEt_3)_2[4]}$
$(HNEt_3)[Fe^{III}(L_A)_2]$	$\mathbf{(HNEt_3)[4]}$

H_2L_A: 1,2-bis(methanesulfonamido)benzene
H_2L_B: 1,2-bis(toluenesulfonamido)benzene

Six of the complexes are based on the same type of ligand, namely 1,2-bis-(methanesulfonamido)benzene (H_2L_A) which was previously identified to yield a very high zero-field splitting in a Co(II) molecular nanomagnet[12]. In one cobalt complex, the ligands were modified by that the methyl groups were replaced with tolyl groups to give 1,2-bis-(toluene-4-sulfonylamino)benzene (H_2L_B). In their doubly deprotonated state, two of these doubly negatively ligands coordinate the central metal ion via the nitrogen atoms in a strongly distorted tetrahedron. Co(II), Ni(II), Fe(II) and Fe(III) were used as central ions. Different counter ions, including K^+, $(HNEt_3)^+$ and $(K\text{-}18\text{-}crown\text{-}6)^+$ were used to balance the electronic charge of the complexes. A general structure of the complexes can be found in Figure 3.1. Detailed structural descriptions of each complex are presented in the corresponding sections.

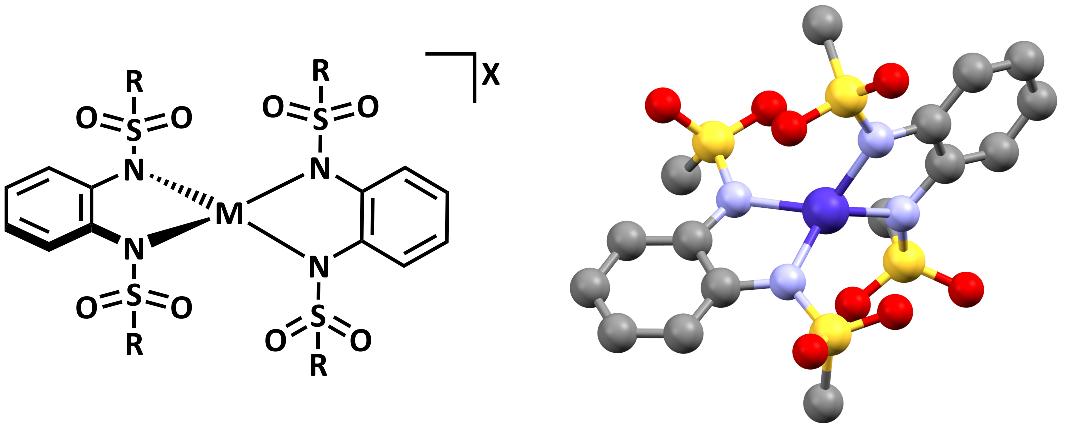

Figure 3.1: Left: General structure of the investigated mononuclear complexes. Fe(II), Fe(III), Co(II) and Ni(II) were employed as central ion (M). R was methyl except for one Co(II) complex where tolyl was used. Right: Example for a crystal structure of the Co(II) complex with R = Me. Cobalt is shown in dark blue, oxygen in red, sulfur in yellow and carbon in dark gray. In both pictures hydrogen atoms and counter ions (X) were omitted for clarity.

3.3. Cobalt Complexes

The electronic structure of the three mononuclear cobalt complexes $K_2[Co^{II}(L_A)_2]$ (**K_2[1]**), $(K\text{-}18c\text{-}6)_2[Co^{II}(L_A)_2]$ (**(K-18-c-6)$_2$[1]**) and $(HNEt_3)_2[Co^{II}(L_B)_2]$ (**(HNEt$_3$)$_2$[2]**), where H_2L_A is 1,2-bis(methanesulfonamido)benzene and H_2L_B is 1,2-bis(toluenesulfonamido)benzene, was investigated by magnetometric (Section 3.3.2) and spectroscopic (Section 3.3.3) means to investigate their performance as single-molecule magnets. The chemical structures are described in the following section.

3.3.1. Structures

All three air-stable cobalt complexes consist of a central Co(II) ion which is fourfold coordinated by nitrogen atoms from two bidentate ligands. The ligands are L_A in case of **K_2[1]** and **(K-18-c-6)$_2$[1]** and L_B in case of **(HNEt$_3$)$_2$[2]**. Complexes **K_2[1]** and **(K-18-c-6)$_2$[1]** crystallize in the monoclinic space group $P2_1/c$ with two cobalt ions per unit cell in case of **K_2[1]**. The potassium counter ions in **K_2[1]** connect the molecules to an extensive network. In **(K-18-c-6)$_2$[1]**, the potassium crown ether counter ions $(K\text{-}18\text{-}c\text{-}6)^+$ separate the individual molecules. Complex **(HNEt$_3$)$_2$[2]** crystallizes in the trigonal space group $P3_221$. The crystal structures of the complexes are shown in Figure 3.2.

The C-N and C-C bond lengths in the ligands vary from 1.397(9) Å to 1.419(9) Å and 1.37(1) Å to 1.42(1) Å (**K_2[1]**, cobalt center 1), 1.386(10) Å to 1.422(9) Å

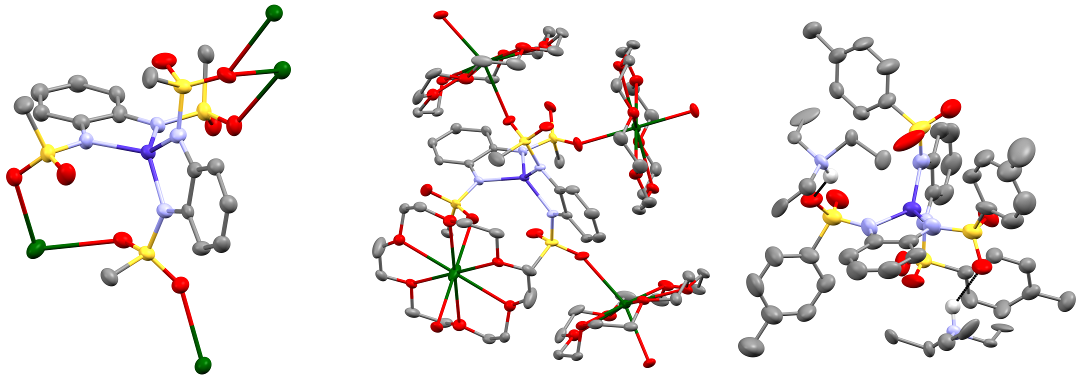

Figure 3.2: ORTEP views at 50 % probability level of the molecular structures of **K_2[1]** (left), **(K-18-c-6)$_2$[1]** (middle) and **(HNEt$_3$)$_2$[2]** (right). Cobalt is shown in dark blue, potassium in green, oxygen in red, sulfur in yellow, carbon in dark gray, hydrogen in light gray and hydrogen bonds in black. Disorder in the counterions is not represented for clarity. In all pictures solvent molecules and hydrogen atoms (except for NH groups) were omitted for clarity.

and 1.36(1) Å to 1.43(1) Å (**K$_2$[1]**, cobalt center 2), 1.410(3) Å to 1.417(3) Å and 1.378(4) Å to 1.429(3) Å (**(K-18-c-6)$_2$[1]**) and 1.39(1) Å to 1.42(1) Å and 1.39(1) Å to 1.42(1) Å (**(HNEt$_3$)$_2$[2]**), respectively, showing the presence of C-N single bonds and an aromatic ring in all cases[79]. The ligands are completely reduced resulting in a net charge of 2– for all complexes. As indicated in the abbreviations, this charge is balanced by two counterions which are K^+ in **K$_2$[1]**, $(K\text{-}18\text{-}c\text{-}6)^+$ in **(K-18-c-6)$_2$[1]** and $(HNEt_3)^+$ in **(HNEt$_3$)$_2$[2]**. The angles between the planes spanned by the N-Ar-N ligands show a nearly perpendicular orientation of the ligands, being 83.1(2)° for **K$_2$[1]** (cobalt center 1), 86.3(2)° for **K$_2$[1]** (cobalt center 2), 84.80(5)° for **(K-18-c-6)$_2$[1]** and 83.6(2)° for **(HNEt$_3$)$_2$[2]**. The N-Co-N angles of 80.4(2)° and 81.2(2)° in **K$_2$[1]** (center 1), 80.1(2)° and 80.4(2)° in **K$_2$[1]** (center 2), 80.74(7)° and 81.36(7)° in **(K-18-c-6)$_2$[1]** and 80.2(5)° and 82.4(4)° in **(HNEt$_3$)$_2$[2]**, which are much smaller than the 109.5° for an ideal tetrahedron, reveal a strong axial distortion of the tetrahedral coordination sphere. The site symmetry can be reasonably idealized to D_{2d}. All mentioned angles and bond lengths are listed in Tables 3.2 and 3.3 for better overview.

Table 3.2: Maximum and minimum C-C and aromatic bond lengths in the cobalt compounds.

	Min. C-N-bond length / Å	Max. C-N-bond length / Å	Min. aromatic bond length / Å	Max. aromatic bond length / Å
K$_2$[1] $^{(1)}$	1.397(9)	1.419(9)	1.37(1)	1.42(1)
K$_2$[1] $^{(2)}$	1.386(10)	1.422(9)	1.36(1)	1.43(1)
(K-18-c-6)$_2$[1]	1.410(3)	1.417(3)	1.378(4)	1.429(3)
(HNEt$_3$)$_2$[2]	1.39(1)	1.42(1)	1.39(1)	1.42(2)

$^{(1)}$ cobalt center 1 $^{(2)}$ cobalt center 2

Table 3.3: Angles between the planes formed by the N-Ar-N ligands and N-Co-N angles in the cobalt compounds.

	inter-ligand angle	N-Co-N angles	
K$_2$[1] $^{(1)}$	83.1(2)°	80.4(2)°	81.2(2)°
K$_2$[1] $^{(2)}$	86.3(2)°	80.1(2)°	80.4(2)°
(K-18-c-6)$_2$[1]	84.80(5)°	80.74(7)°	81.36(7)°
(HNEt$_3$)$_2$[2]	83.6(2)°	82.4(4)°	80.2(5)°

$^{(1)}$ cobalt center 1 $^{(2)}$ cobalt center 2

3.3.2. Magnetic Properties

Figure 3.3 shows the temperature dependence of the product of the magnetic susceptibility χ and the temperature T of all three complexes. At 300 K, the χT values of **K_2**[**1**] and **$(HNEt_3)_2$**[**2**] are very similar with 3.02 $cm^3\,K\,mol^{-1}$ and 3.10 $cm^3\,K\,mol^{-1}$, respectively. The value for **(K-18-c-6)$_2$**[**1**] is significantly higher at 3.60 $cm^3\,K\,mol^{-1}$. All of these values are much higher than the spin-only value of 1.875 $cm^3\,K\,mol^{-1}$ as calculated from Curie's law for $S = 3/2$ and $g = 2$. This means that the g-values are significantly larger than 2 which is caused by spin-orbit coupling. A contribution from orbital angular momentum can be excluded because there is none even in rigorously tetrahedral Co(II). Similar values have been reported for other fourfold coordinated Co(II) complexes[6, 12, 64, 80]

The χT values of **K_2**[**1**] are approximately constant down to 100 K and then decrease slowly down to 2.44 $cm^3\,K\,mol^{-1}$ at 1.8 K. For **$(HNEt_3)_2$**[**2**], the slow decrease in χT starts at 150 K and ends at 2.81 $cm^3\,K\,mol^{-1}$ at 2.5 K. Below that, there is a large drop down to 2.45 $cm^3\,K\,mol^{-1}$ at 1.8 K. In case of **(K-**

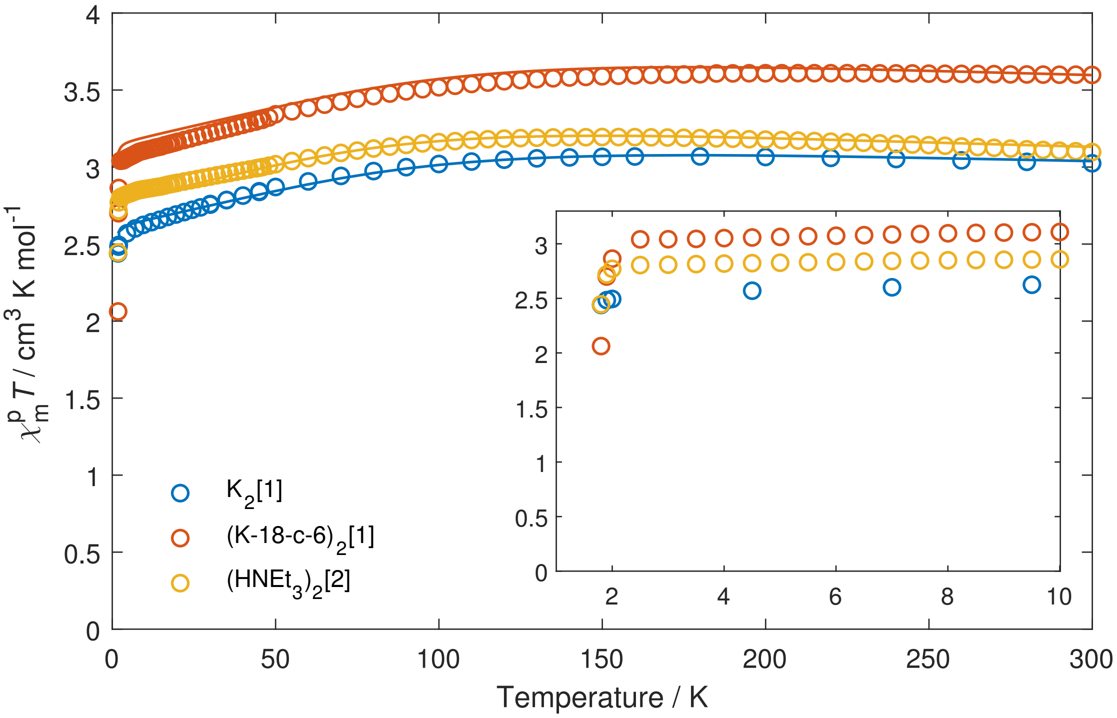

Figure 3.3: Temperature dependence of the susceptibility temperature product χT of the mononuclear cobalt complexes. Measurements (circles) were performed in applied fields of 1 kOe ($T \leq 40$ K) and 10 kOe ($T < 40$ K). Fits (lines) are obtained by simultaneous fitting with magnetization curves. The inset shows a more detailed view of the drop at low temperatures.

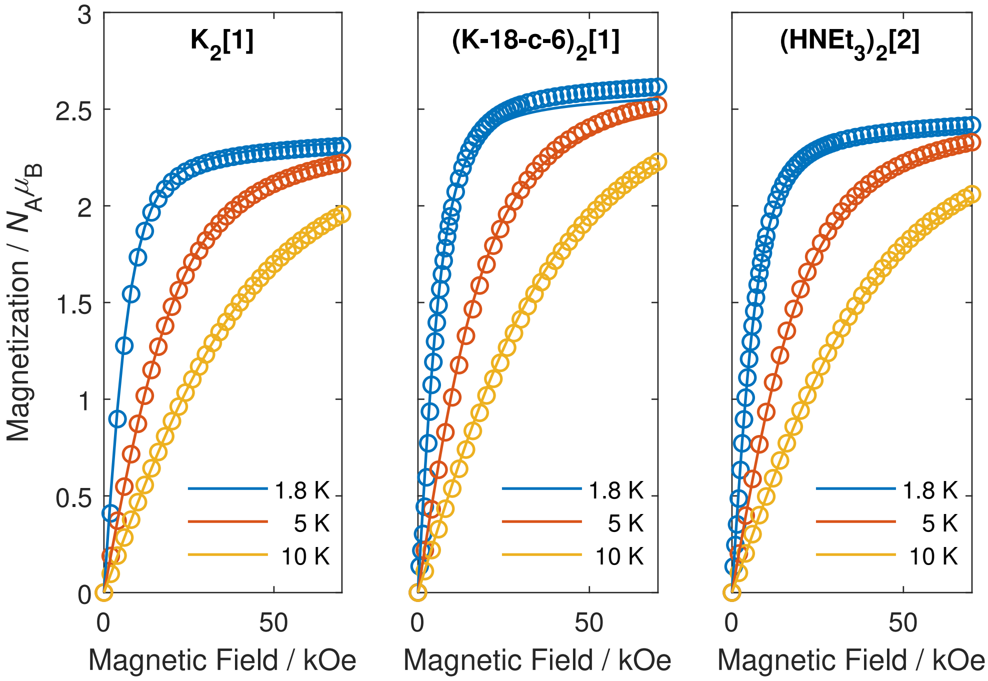

Figure 3.4: Molecular magnetization of the cobalt complexes versus applied magnetic field at temperatures as indicated. Solid lines are fits obtained by simultaneous fitting with $\chi T - T$ measurements.

18-c-6)$_2$[**1**], the χT product is constant down to 150 K, decreases then gradually to 3.04 cm^3 K mol^{-1} at 2.5 K and finally drops strongly to 2.06 cm^3 K mol^{-1} at 1.8 K. These intense drops below 2.5 K are a first indication for slow relaxation of magnetization in **(K-18-c-6)$_2$**[**1**] and **(HNEt$_3$)$_2$**[**2**]. The reason for this is that the measurements are performed by cooling the samples in zero external field to 1.8 K, then applying a small static field and gradually warming the sample while measuring the magnetic moment. Slow relaxation of magnetization causes the magnetization to take longer to reach its thermal equilibrium value. Thus, the measured values of the magnetic moment appear smaller (or larger if the field was decreased before measuring) than the equilibrium value for this temperature actually is. In general, this can be prevented by waiting for the sample to reach the thermal equilibrium before measuring (if this happens within a reasonable period of time).

Measurements of the magnetization versus the magnetic field are shown in Figure 3.4. At 1.8 K and 70 kOe, magnetization values of 2.31 $N_A\mu_B$ (**K$_2$**[**1**]), 2.62 $N_A\mu_B$ ((**K-18-c-6)$_2$**[**1**]) and 2.42 $N_A\mu_B$ ((**HNEt$_3$)$_2$**[**2**]) are obtained. Simultaneous fits of the $\chi T - T$ and $M - H$ measurements were performed for each compound using the spin Hamiltonian described in Equation 2.10. Best fits purely based on the magnetometric measurements yielded the spin Hamiltonian parameters $g_\perp = 2.12(5)$, $g_\parallel = 3.02(2)$ and $D = -100(20)\,\mathrm{cm}^{-1}$ (**K$_2$[1]**), $g_\perp = 2.20(5)$, $g_\parallel = 3.34(3)$ and $D = -130(20)\,\mathrm{cm}^{-1}$ (**(K-18-c-6)$_2$[1]**) and $g_\perp = 2.06(5)$, $g_\parallel = 3.13(3)$ and $D = -110(20)\,\mathrm{cm}^{-1}$ (**(HNEt$_3$)$_2$[2]**). Justified by the high axial geometry of the system and to avoid overparametrization, the g-tensor was assumed to be axial with $g_x = g_y = g_\perp$ and $E = 0$ was fixed. By this approach, satisfying fits were also obtained for **(K-18-c-6)$_2$[1]** and **(HNEt$_3$)$_2$[2]** (Figures 3.3 and 3.4).

For **K$_2$[1]**, spectroscopic measurements (see Section 3.3.3) revealed the zero-field splitting to be $D = -115(1)\,\mathrm{cm}^{-1}$. Its absolute value is nearly a fifth higher than the one determined by magnetometry but still within the error margin. This clearly shows the necessity to employ tools beyond magnetometry (i. e. spectroscopy) to quantify zero-field splitting parameters. Fitting the magnetic data with the D-value from FIR spectroscopy yields satisfying fits with $g_\perp = 2.08(5)$, $g_\parallel = 3.04(3)$ shown in the aforementioned Figures. All parameters are also listed in Table 3.4 for better overview.

Ab-initio calculations (LDF-CAHF/CASSCF/PNO-CASPT2/SI-SO)[81–83] were performed for **K$_2$[1]** by Philipp Hallmen (Institut für Physikalische Chemie, Universität Stuttgart). The resulting values of $g_x = 1.9859$, $g_y = 2.0019$, $g_z = 3.2518$, $D = -108.38\,\mathrm{cm}^{-1}$ and $E = 0.3028\,\mathrm{cm}^{-1}$ are in good agreement with the experimental ones and support the assumption of an axial g-tensor and $E = 0$.

Overall, the extracted parameters of the zero-field splitting belong to the largest ones found in fourfold coordinated Co(II) complexes (see Table 3.5).

Bearing in mind the indications for slow relaxation of magnetization from $\chi T - T$ measurements in mind, zero field cooled field cooled (ZFCFC) measurements were

Table 3.4: Determined g-values and zero-field splitting parameters of **K$_2$[1]**, **(K-18-c-6)$_2$[1]** and **(HNEt$_3$)$_2$[2]**.

	$g_\perp$		$g_\parallel$	D / cm^{-1}	E / cm^{-1}
(K-18-c-6)$_2$[1]	2.20(5)		3.34(4)	−130(20)	0
(HNEt$_3$)$_2$[2]	2.06(5)		3.13(3)	−110(20)	0
K$_2$[1] (1)	2.12(5)		3.02(2)	−100(20)	0
K$_2$[1] (2)	2.08(5)		3.04(3)	−115	0
	g_x	g_y	g_z		
K$_2$[1] (3)	1.99	2.00	3.25	−108	0.3

(1)free fit (2)D fixed based on FIR (3)ab-initio calculations

Table 3.5: Fourfold coordinated Co(II) complexes with $D < -50\,\mathrm{cm}^{-1}$.

Compound	D / cm^{-1}	Literature
$(Ph_4P)_2[Co(C_3S_5)_2]$	−161	Ref. [6]
$(HNEt_3)_2[Co(L^1)_2]\cdot H_2O$	−144.1	Ref. [84]
$(Bu_4N)_2[Co(L^2)_2]\cdot H_2O$	−130.8	Ref. [84]
(K-18-c-6)$_2$[1]	−130(20)	this work
K$_2$[1]	−115(1)	this work
$(HNEt_3)_2[1]$	−115	Ref. [12]
(HNEt$_3$)$_2$[2]	−110(20)	this work
$(Ph_4P)_2[Co(SePh)_4]$	−83	Ref. [80]
$[Co(AsPh_3)_2(I)_2]$	−74.7	Ref. [85]
$(Ph_4P)_2[Co(SPh)_4]$	−62	Ref. [80]
$[Co\{(NtBu)_3SMe\}_2]$	−58	Ref. [86]

H_2L^1 = *N,N′*-bis(*p*-toluenesulfonyl)oxamide
H_2L^2 = *N,N′*-diphenyloxamide

performed on all three complexes to investigate the possible occurrence of slow magnetization dynamics. The ZFCFC measurements (Figures 3.5 and A.1) show a deviation of the signals at low temperatures only in case of **(K-18-c-6)$_2$[1]**. From this deviation, a blocking temperature of 2 K can be extracted for **(K-18-c-6)$_2$[1]**.

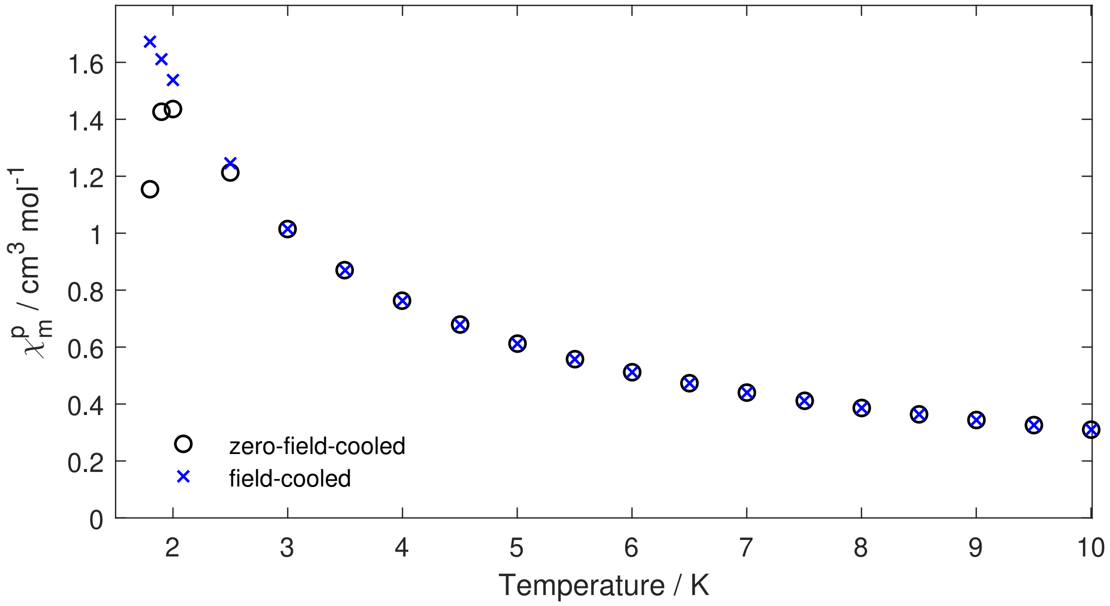

Figure 3.5: Zero field cooled field cooled measurement of **(K-18-c-6)$_2$[1]**.

Measurements of magnetic hysteresis were performed on all three samples at 1.8 K. Because the sweep rate of the magnetic field has a major influence on this kind of measurement when slow relaxation of magnetization is present, a very small sweep rate of 20 Oe s^{-1} in combination with continuous measurements was used. The resulting data are depicted in Figure 3.6. All three complexes show a waist-restricted hysteresis curve. This means that magnetic hysteresis occurs at small magnetic fields of up to 4.5 kOe (**K$_2$[1]**), 5 kOe (**(K-18-c-6)$_2$[1]**) and 4 kOe (**(HNEt$_3$)$_2$[2]**) but the diverging curves of the field-up and field-down measurements collapse at zero field. Thus, no coercivity is observed which denies a true magnetic bistability for all three Co(II) complexes. We attribute the collapse to efficient quantum tunneling close to zero field. The reason for it is most probably the hyperfine coupling of the electron spin to the cobalt nuclear spin. The presence of nuclear spin is unavoidable in cobalt because ^{59}Co with $I = {}^7\!/_2$ is the only stable isotope.

Of all three complexes **(K-18-c-6)$_2$[1]** shows the most pronounced hysteresis which is in good agreement with the fact that it was the only compound for which a blocking temperature above 1.8 K was observed in the ZFCFC measurement.

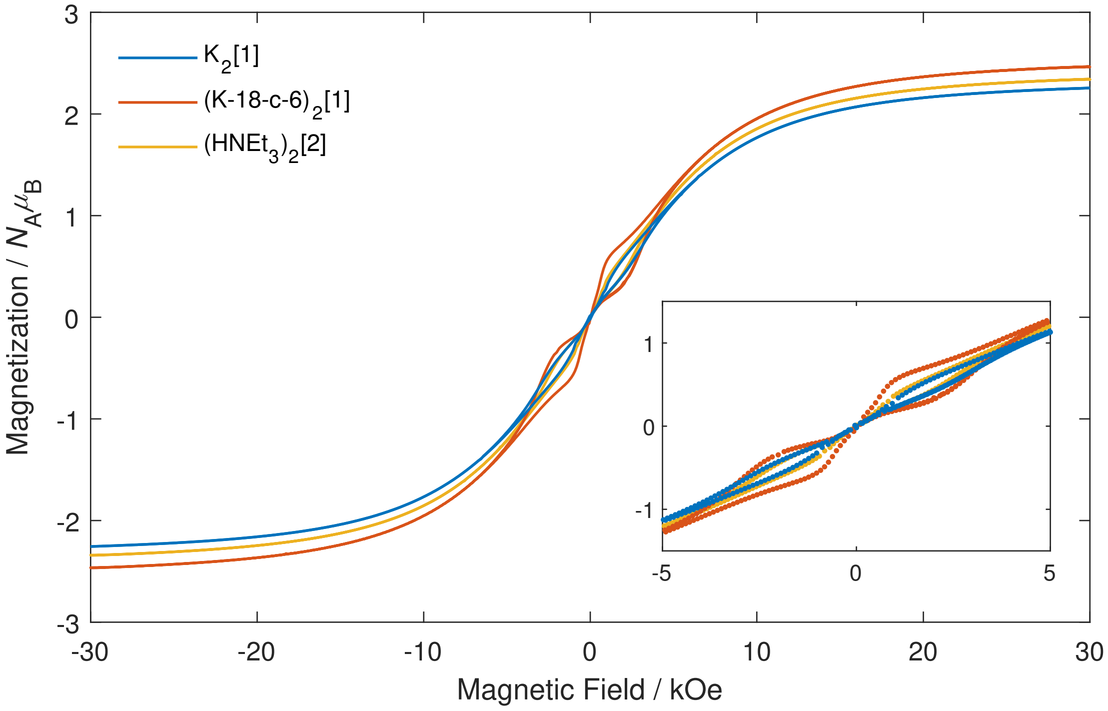

Figure 3.6: Magnetic hysteresis measurements of the mononuclear cobalt complexes recorded at 1.8 K and sweep rates of 20 Oe s^{-1}.

To investigate slow relaxation of magnetization on a faster timescale, measurements of the dynamic magnetic properties were performed at zero applied static field. The plots of χ' and χ'' versus the applied frequency are shown in Figure 3.7 for all three complexes. All out-of-phase measurements show frequency-dependent maxima in the temperature range from 2 K to 20 K indicating slow relaxation of magnetization, identifying the three complexes as single-ion magnets. The corresponding Argand plots are shown in Figure 3.8.

Simultaneous fits of the in-phase and out-of-phase susceptibility to the standard modified Debye function (Equations 2.20 and 2.21) were performed for every compound and are shown as solid lines in the plots. Reliable fits were obtained for temperatures from 6.5 K to 18 K ($\mathbf{K_2[1]}$), 3 K to 21 K ($\mathbf{(K\text{-}18\text{-}c\text{-}6)_2[1]}$) and 5 K to 18 K ($\mathbf{(HNEt_3)_2[2]}$). Parameters of the best fits are listed in the Appendix in Tables A.1, A.3 and A.4.

The longest extracted zero field relaxation time is 0.42 s for $\mathbf{(K\text{-}18\text{-}c\text{-}6)_2[1]}$ at 3 K which is in agreement with it being the only compound where a blocking temperature could be determined and having the most pronounced hysteresis curve. Additionally, $\mathbf{(K\text{-}18\text{-}c\text{-}6)_2[1]}$ shows the widest temperature range (3 K to 21 K) where relaxation times could be extracted, being between 420 ms at 3 K and 0.15 ms at 21 K. For $\mathbf{K_2[1]}$, temperatures from 6.5 K (3.67 ms) to 18 K (0.17 ms) could be used, for $\mathbf{(HNEt_3)_2[2]}$ from 5 K (26.09 ms) to 18 K (0.25 ms). A comparison of the relaxation times shows that for each of the common measured temperatures the relaxation time is longest for $\mathbf{(K\text{-}18\text{-}c\text{-}6)_2[1]}$, then $\mathbf{(HNEt_3)_2[2]}$ and shortest in case of $\mathbf{K_2[1]}$. The distribution of relaxation times, as can be seen by the non-zero parameter α, is rather large, especially at the lower temperatures. Visually, this can be seen in the χ'' vs. ν and Argand plots of $\mathbf{K_2[1]}$ and $\mathbf{(HNEt_3)_2[2]}$ where the fits are not perfect for the low temperatures, indicating a second relaxation process there, which is often attributed to quantum tunneling.

This attribution was investigated for $\mathbf{K_2[1]}$ by dynamic susceptibility measurements in a small applied field of 1000 Oe which lifts the degeneracy of the Kramers doublets and, thus, suppresses tunneling. The corresponding plots are shown in Figures A.2 and A.3 and the fitting parameters are listed in Table A.2. Visually, the fits are of higher quality compared to the ones at zero applied field, especially at low temperatures. From the numbers, the smaller α values indicate a smaller distribution of relaxation times and the relaxation times are longer by one order of magnitude below 8 K. These observations confirm the assumption of quantum tunneling as cause for additional relaxation mechanisms at zero field.

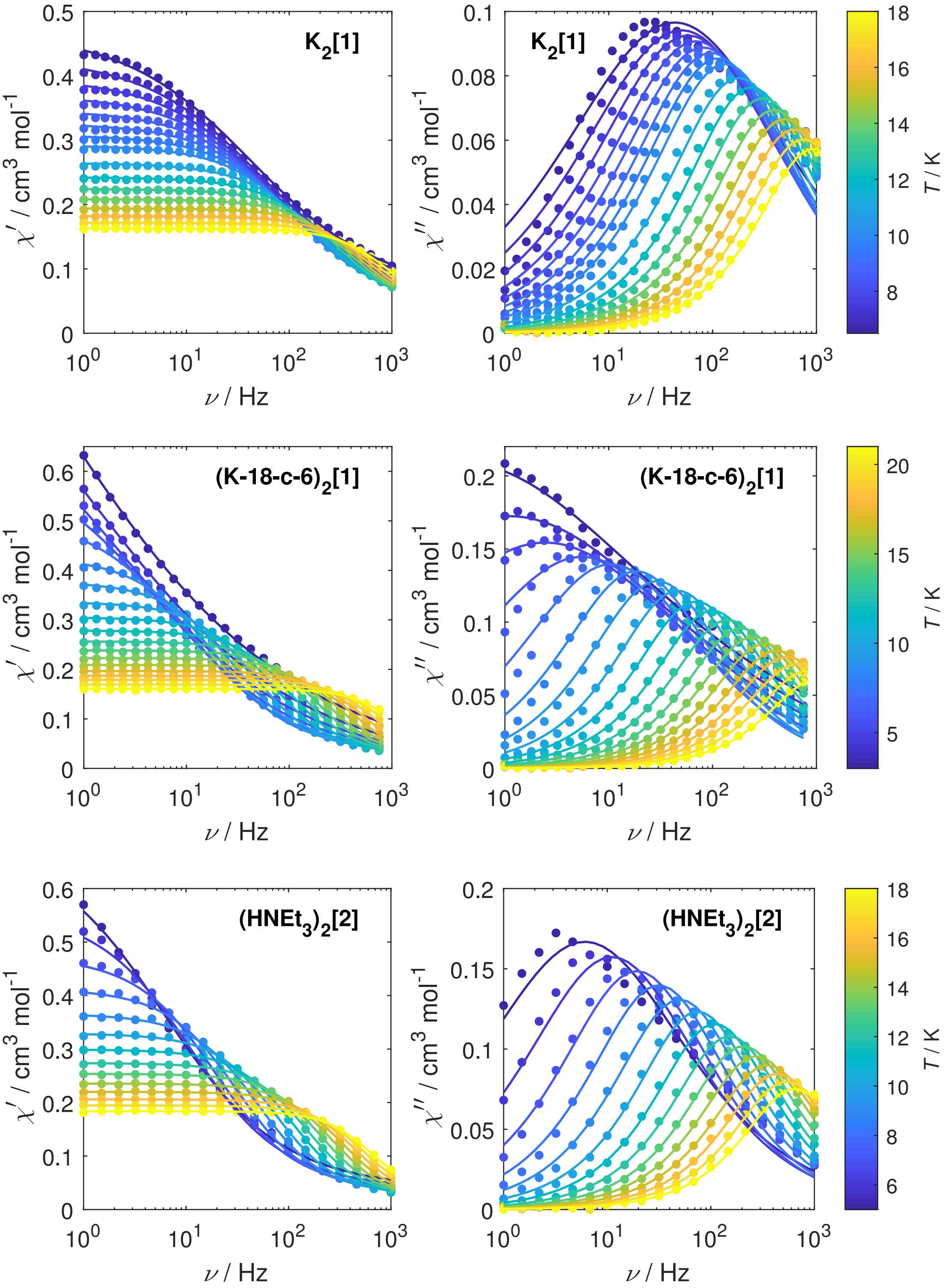

Figure 3.7: In-phase (left) and out-of-phase (right) susceptibility of $\mathbf{K_2[1]}$ (top), $\mathbf{(K\text{-}18\text{-}c\text{-}6)_2[1]}$ (middle) and $\mathbf{(HNEt_3)_2[2]}$ (bottom) at frequencies and temperatures as indicated and zero applied static field. Solid lines are simultaneous fits of in-phase and out-of-phase signals.

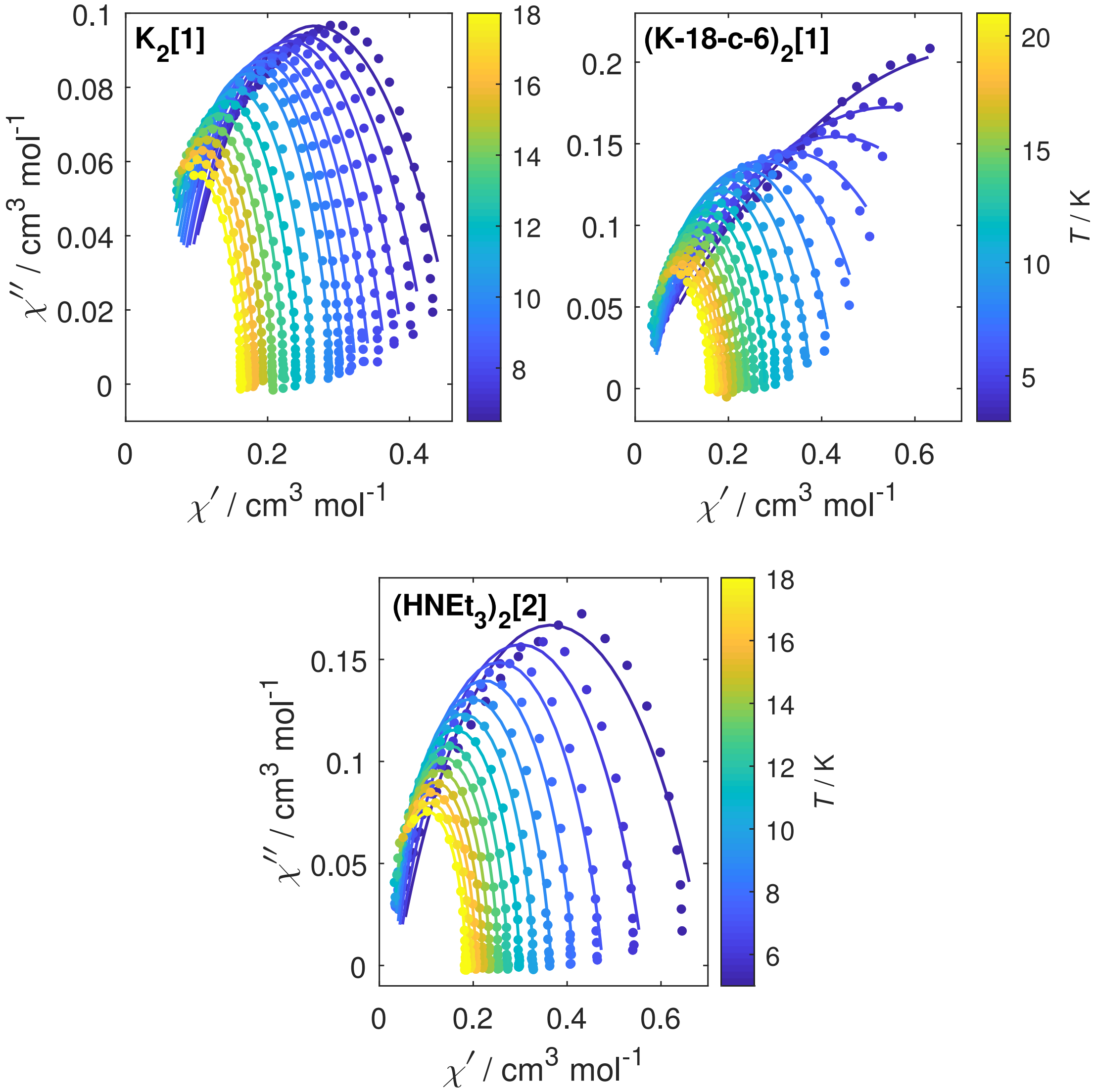

Figure 3.8: Argand plots of the mononuclear cobalt compounds at different temperatures and zero applied field. Solid lines correspond to best fits.

Overall, the relaxation in zero field is rather fast, which is in agreement with the absence of remanence in the hysteresis curves.

Arrhenius plots of ln(τ/s) against the inverse temperature are shown in Figure 3.9. The non-linear nature of the curves indicate that relaxation processes additional to Orbach-type have to be present. The horizontal stacking of the lines (where higher lying points mean a longer relaxation time) confirms the ranking of the relaxation times of the different complexes as described in the previous paragraph. A comparison with the previously investigated compound[12] (HNEt$_3$)$_2$[1] shows that the relaxation times of **(K-18-c-6)$_2$[1]** and **(HNEt$_3$)$_2$[2]** lie in the

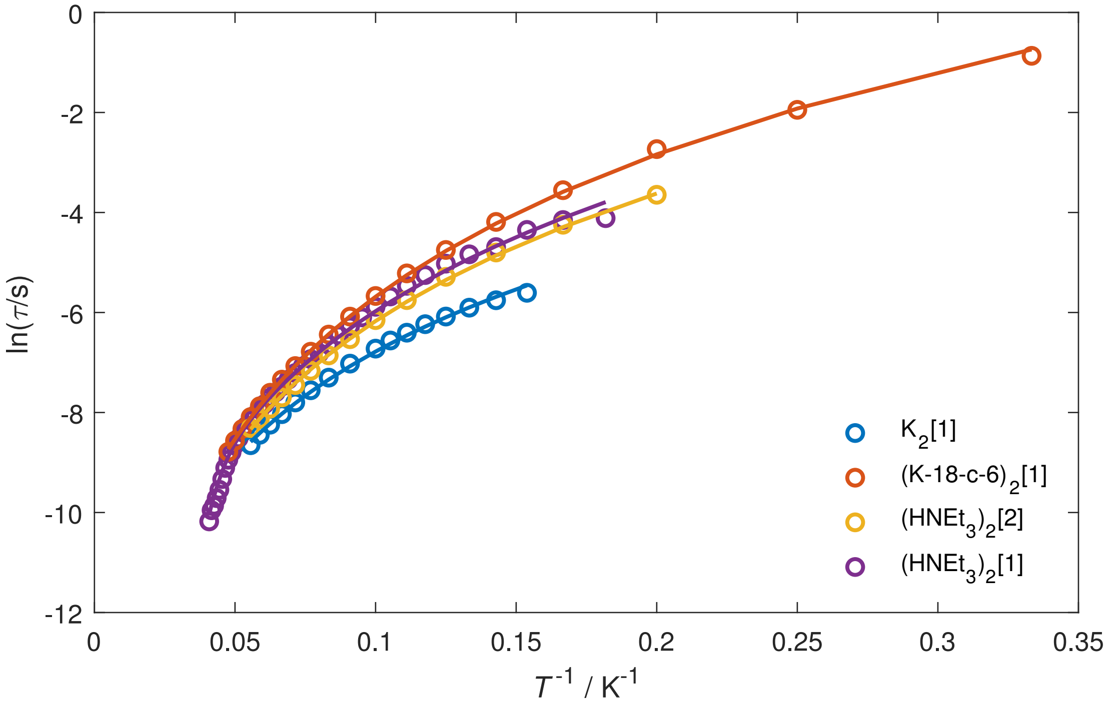

Figure 3.9: Arrhenius plot of the mononuclear cobalt compounds. $(HNEt_3)_2$[1] for comparison from [12]. Solid lines correspond to best fits based on a combination of Orbach and Raman processes.

same range, the former one even surpassing the values of $(HNEt_3)_2$[1]. Satisfactory fits of the Arrhenius plots were obtained using a combination of Orbach and Raman terms (Equations 2.4 and 2.5). In this, the effective energy barrier U_{eff} was fixed to the size of the zero-field splitting $2D$ which is acceptable because it avoids overparametrization and is a physically valid assumption as this corresponds to the barrier which must be overcome.

The fits are shown as solid lines in Figure 3.9 and the extracted parameters C_{Raman}, n_{Raman} and τ_0 are listed in Table 3.6.

Table 3.6: Best parameters obtained by fitting the Arrhenius plots of **K_2[1]**, **$(K\text{-}18\text{-}c\text{-}6)_2$[1]** and **$(HNEt_3)_2$[2]** at zero external field to a combination of Orbach and Raman relaxation process.

	C_{Raman} / $\mathrm{K}^{-n_{\mathrm{Raman}}}\mathrm{s}^{-1}$	n_{Raman}	τ_0 / 10^{-9} s	$U_{\mathrm{eff}}{}^{(1)}$ / cm^{-1}
K_2[1]	0.75(5)	3.07(6)	3(1)	236
$(K\text{-}18\text{-}c\text{-}6)_2$[1]	0.024(1)	4.09(2)	0.3(1)	260
$(HNEt_3)_2$[2]	0.10(1)	3.68(4)	5(1)	220

(1) fixed to $2D$

The Raman exponents n_{Raman} of all components lie in the same range between 3 and 4 but differ quite from the value of $n = 9$ which would be expected for Kramers ions[56] with isolated ground states. They are closer to the expected value of $n = 5$ for systems with low-lying states. Similar values have been found in other Co(II) compounds[87, 88]. The deviation is attributed to contributions of local modes. The Raman coefficients differ quite a bit with the ones of **(K-18-c-6)$_2$[1]** being the lowest one with $C_{\mathrm{Raman}} = 0.024\,\mathrm{K}^{-4.09}s^{-1}$ and **K$_2$[1]** being the largest with $C_{\mathrm{Raman}} = 0.75\,\mathrm{K}^{-3.07}s^{-1}$. The attempt times τ_0 differ by an order of magnitude being longest for **(HNEt$_3$)$_2$[2]** ($3 \cdot 10^{-9}\,s$) and shortest for **(K-18-c-6)$_2$[1]** ($3 \cdot 10^{-10}\,\mathrm{s}$).

Summarizing the results of the dynamic susceptibility measurements, magnetic relaxation in the investigated compounds is controlled by a combination of quantum tunneling at low temperatures, Raman relaxation at intermediate temperatures and Orbach processes at high temperatures. Due to the absence of magnetic field and Kramers nature of the system, the direct relaxation mechanism does not play a role.

Overall, **(K-18-c-6)$_2$[1]** performs best as a single molecule magnet with the largest D-value, largest magnetic hysteresis and longest relaxation times. Additional indications of the longest relaxation are observed in the most pronounced drop in χT over T at low temperatures, a separation of zero field cooled and field cooled susceptibility measurements and that the dynamic susceptibility data can be fitted down to the lowest temperature of the three compounds. Structurally, in this complex the Co(II) ions are most separated from each other by the large counterions while in **K$_2$[1]**, which exhibits the worst properties, they are closest. This indicates that the distance of the transition metal ions (i.e. the spin centers) may play a role here for the magnetic properties.

3.3.3. Spectroscopy

EPR and FIR spectroscopy were employed to further investigate the zero-field splitting parameters and g-factors of **K$_2$[1]** as representative for all three complexes because spectroscopic methods have a much higher accuracy in determining these parameters compared to magnetometry. Additionally, MCD spectroscopy was applied to investigate the electronic structure which is related to Spin Hamiltonian parameters by ligand-field theory.

EPR spectra of $\mathbf{K_2[1]}$ were recorded at low temperatures at frequencies between 200 GHz and 370 GHz but no transitions could be observed which confirms the magnetometry results of $D < 0$. More importantly, it demonstrates that E is negligible, which is a piece of information that cannot be easily obtained from magnetometry. EPR spectroscopy is able to yield this information because an $S = 3/2$-system (such as Co(II)) with either positive D or non-negligible E is expected to show an intra-doublet EPR signal from the magnetic ground state independently of the size of the zero-field splitting. In case of $D > 0$ (independently of the size of E), the signal results from the $m_S = -1/2$ to $m_S = 1/2$ transition because the $m_S = \pm 1/2$ states are the magnetic ground states and the selection rule of $\Delta m_S = 1$ is fulfilled. In case of $E \neq 0$, states with $\Delta m_S = 2$ are mixed. This means that the ground states $m_S = \pm 3/2$ partially have $m_S = \mp 1/2$-character. Thus, with $E \neq 0$ the transition within the ground state doublet is allowed also in a system with $D < 0$.

An inter-doublet transition between the $m_S = \pm 3/2$ and $m_S = \pm 1/2$ doublets is beyond the limits of conventional high-frequency EPR spectroscopy as the gap in zero-field corresponds to $2D$ which is expected to be in the range of $230\,\mathrm{cm}^{-1}$ which corresponds to approximately 7000 GHz. Consequently, the g-factors cannot be determined for which EPR would be the most suitable method. To reach frequencies and magnetic fields in the necessary range, specialized equipment like free-electron lasers and pulsed magnets are needed and beam time is very limited for such experiments.

An alternative to spectroscopy in the Terahertz region at very high magnetic fields is the use of light with higher frequencies in the far-infrared region and magnetic fields that can be achieved with conventional superconducting magnets. Thus, FIR spectroscopy was applied for an accurate determination of the zero-field splitting of $\mathbf{K_2[1]}$. The spectra of $\mathbf{K_2[1]}$ were measured at 5 K and fields up to 15 T on a setup designed by Jana Midlíková (Brno University of Technology) in our group[89]. Figures 3.10 and 3.11 show the obtained raw and normalized transmission spectra in the range from $30\,\mathrm{cm}^{-1}$ to $500\,\mathrm{cm}^{-1}$ and a zoom of the significant range from $170\,\mathrm{cm}^{-1}$ to $300\,\mathrm{cm}^{-1}$. Because the setup does not provide reference measurements for each field without sample, the normalized spectra were generated by dividing the transmission at each field by the transmission at zero field.

A clearly field-dependent feature is observed around $230\,\mathrm{cm}^{-1}$. The signal is attributed to the spin-allowed $m_S = \pm 3/2 \rightarrow m_S = \pm 1/2$ transition whose energy

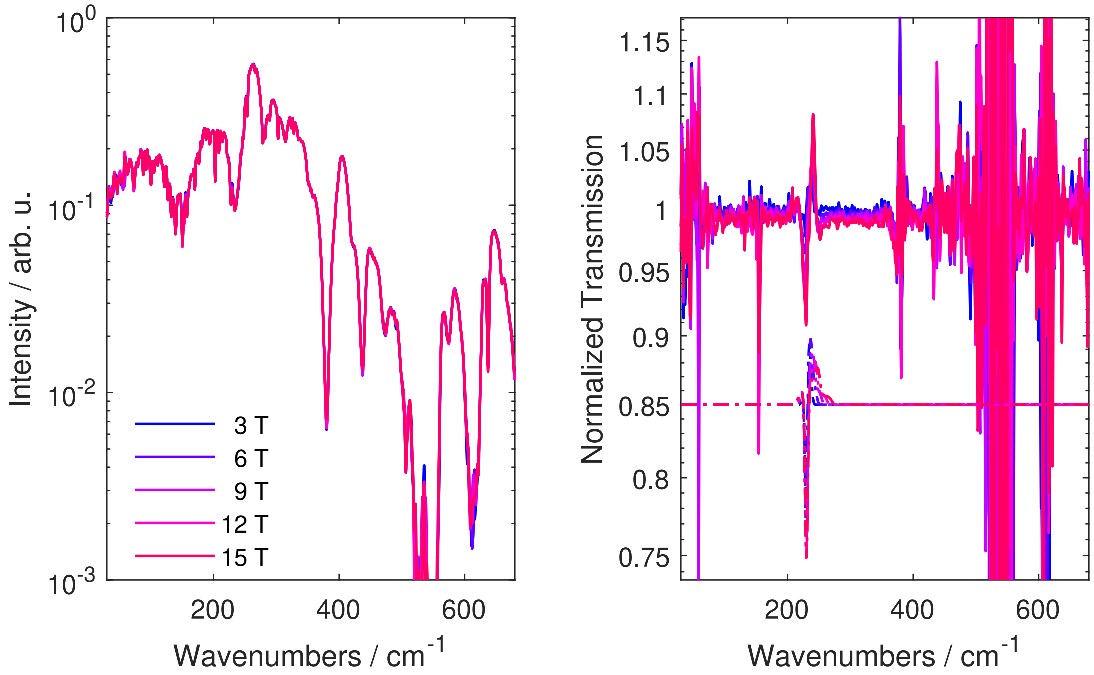

Figure 3.10: Left: Raw FIR spectra of $\mathbf{K_2[1]}$ at 5 K and magnetic fields as indicated. Right: Normalized FIR transmission spectra (solid lines) obtained by dividing each spectrum by the spectrum at zero field and simulation (dash-dotted lines).

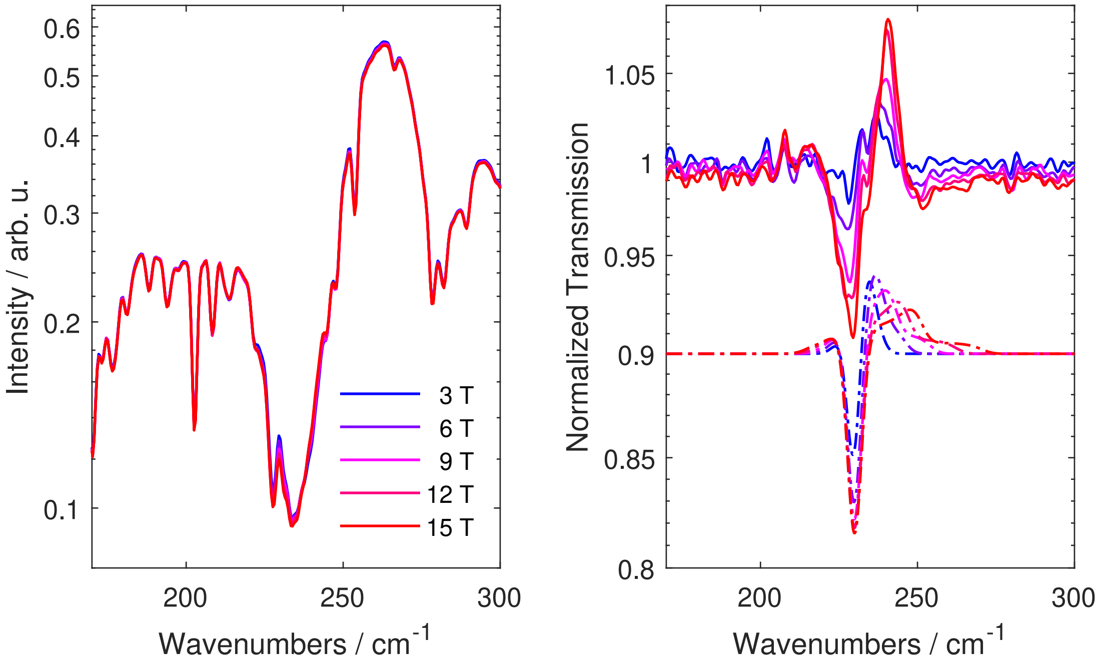

Figure 3.11: Left: Raw FIR spectra of $\mathbf{K_2[1]}$ at 5 K and magnetic fields as indicated. Right: Normalized FIR transmission spectra (solid lines) obtained by dividing each spectrum by the spectrum at zero field and simulation (dash-dotted lines). Both Figures are zoomed on the field-dependent features.

directly corresponds to the zero-field splitting of $2D$. The best fit (Figure 3.11, $D = 115(1)\,\mathrm{cm}^{-1}$, $g_{\perp} = 2.08$ and $g_{\parallel} = 3.04$) was obtained by extracting D directly from these FIR measurements. The g-factors were determined by fitting the magnetometry data with fixed $D = 115(1)\,\mathrm{cm}^{-1}$.

To gain insight into the origin of the large zero-field splitting, the electronic structure of $\mathbf{K_2[1]}$ was investigated using magnetic circular dichroism (MCD) spectroscopy. MCD spectra of $\mathbf{K_2[1]}$ and the previously investigated $(\mathrm{HNEt_3})_2[1]$ [12] as mulls in fluorolube are plotted in Figure 3.12. The comparison of both spectra shows that they are qualitatively the same, though, the signals in the spectrum of $\mathbf{K_2[1]}$ seem to be generally broader which can be an effect of the sample preparation. One broad band, which in case of $(\mathrm{HNEt_3})_2[1]$ consisted of three resolved features, is located around $7500\,\mathrm{cm}^{-1}$. Also for $\mathbf{K_2[1]}$ it is obvious that this is not a peak originating from a single transition. The main feature of the spectrum is located around $19\,000\,\mathrm{cm}^{-1}$ and consists of at least two transitions. Several additional small features are visible in the spectrum which are attributed to spin-forbidden transitions. The observed main features were fitted using Gaussians where the number of Gaussians was inspired by the observations for $(\mathrm{HNEt_3})_2[1]$. The resulting fit is shown in Figure 3.13 and the fitted peak positions are listed in Table 3.7. Additionally, the transition energies were calculated by ab-initio methods (LDF-CAHF/CASSCF/PNO-CASPT2/SI-SO, Philipp Hallmen, Institut für Physikalische Chemie, Universität Stuttgart) and are also depicted in Figure 3.13 and listed in Table 3.7. The observed transitions can be attributed to electronic states with help of the corresponding Tanabe-Sugano diagram (Figure 2.6) within $\mathrm{T_d}$ notation.

All transitions originate from the electronic ground state $^4\mathrm{A}_2(\mathrm{F})$. The transitions around $7500\,\mathrm{cm}^{-1}$ are to the $^4\mathrm{T}_1(\mathrm{F})$ state and the transitions around $19\,000\,\mathrm{cm}^{-1}$ to the $^4\mathrm{T}_1(\mathrm{P})$ state. They lie in the upper range for tetrahedral Co(II) complexes[45, 90]. One more transition to the $^4\mathrm{T}_2(\mathrm{F})$ state would be allowed. This transition is typically expected far below $5000\,\mathrm{cm}^{-1}$[45] and out of the accessible range of our MCD spectrometer. However, the zero-field FIR spectrum shows an intense band around $550\,\mathrm{cm}^{-1}$ which could be attributed to this transition and would be consistent with the calculations. The attribution as an electronic transition can be checked by comparison with an analogous compound such as $\mathbf{(HNEt_3)_2[3]}$ where this transition should not appear. Figure A.4 shows this comparison of the zero field spectra of $\mathbf{K_2[1]}$ and $\mathbf{(HNEt_3)_2[3]}$. Both spectra exhibit several strong and very close bands between $520\,\mathrm{cm}^{-1}$ and $560\,\mathrm{cm}^{-1}$ which

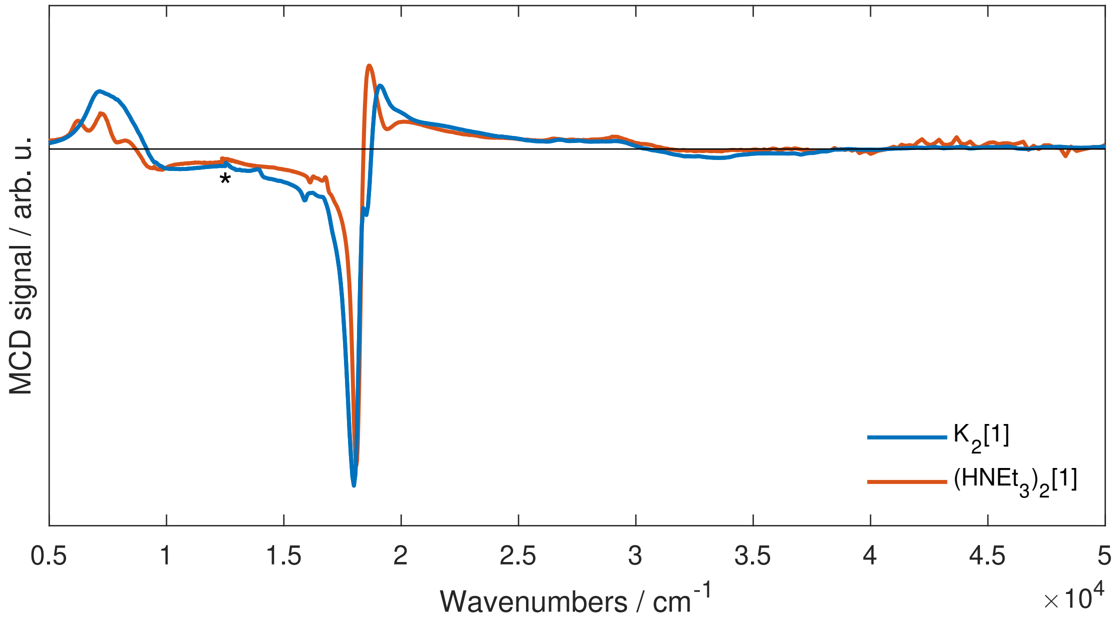

Figure 3.12: Normalized magnetic circular dichroism spectra at 1.5 K of $\mathbf{K_2}$**[1]** (blue) at 4 T and $(HNEt_3)_2$[1] (red) at 2 T. The asterisk marks the artifact due to the detector change.

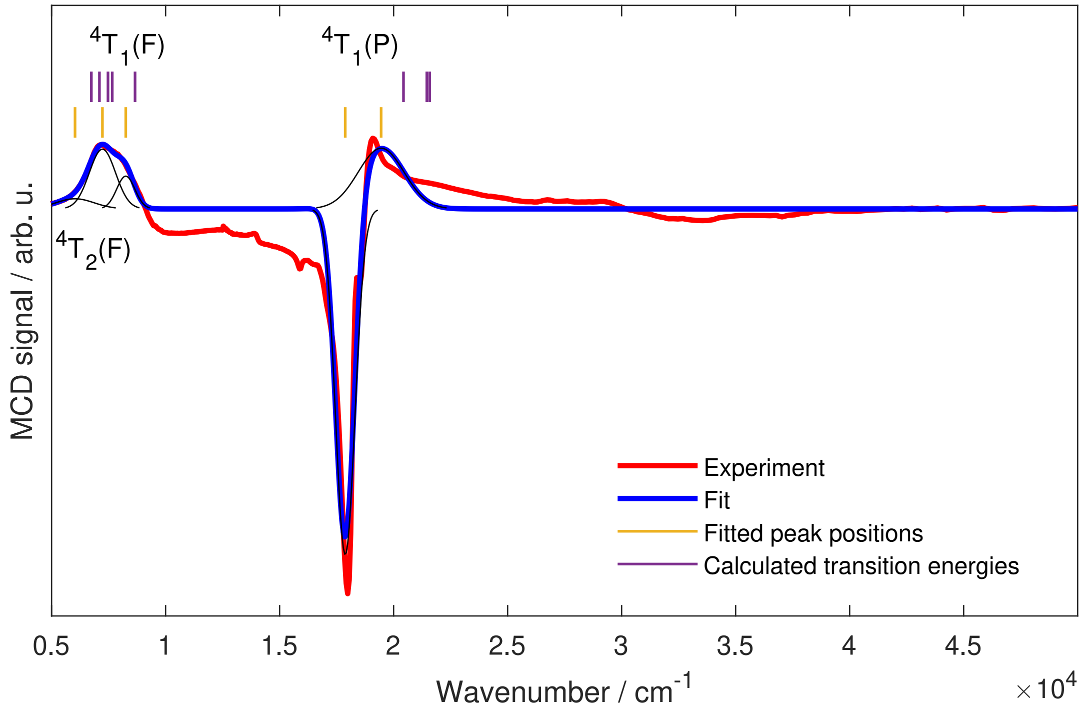

Figure 3.13: Normalized MCD spectrum of $\mathbf{K_2}$**[1]** (red) at 1.5 K and 4 T with fit of the main features (blue) based on five transitions. Black curves indicate the single Gaussians used for fitting. Extracted energies are indicated with yellow lines. Purple lines mark calculated energies.

are virtually the most intense ones observed. It cannot be excluded that an electronic transition is hidden beneath these features in **K_2[1]** but a direct attribution of peaks in this range to a $^4T_2(F)$ transition is not possible.

The fact that the observed features consist of several transitions, each, shows that T_d symmetry is not sufficient to describe the system. Instead, symmetry-lowering from T_d to D_{2d} as described in section 2.2.2 has to be considered as a result of the strong axial distortion. The fitted energies of the observed transition were attributed to the resulting states in D_{2d} symmetry (Table 3.7) and the energy level diagram is shown in Figure 3.14.

It can be seen that the $^4A_2(F)$ state is strongly split resulting in a large energy gap between the $^4B_2(T_2)$ and $^4E(T_2)$ states. As Equation 2.12 shows, this results in a large zero-field splitting D. If the $^4B_2$ transition is assumed at $550\,\mathrm{cm^{-1}}$ as described above, D can be calculated as

$$D = 4\lambda^2 \left[\frac{1}{E(^4\mathrm{E})} - \frac{1}{E(^4\mathrm{B}_2)}\right] = 4 \cdot (-172\,\mathrm{cm^{-1}})^2 \left[\frac{1}{6028\,\mathrm{cm^{-1}}} - \frac{1}{550\,\mathrm{cm^{-1}}}\right]$$
$$= -196\,\mathrm{cm^{-1}}$$

where a spin-orbit splitting parameter of $\lambda = -172\,\mathrm{cm^{-1}}$[43] is used. This result is in qualitatively good agreement with the value of $-115\,\mathrm{cm^{-1}}$ determined by FIR spectroscopy if we keep in mind that the equation is based on perturbation theory and, thus, strictly spoken only valid for small perturbations contrary to the present case.

3.3.4. Summary and Conclusion

Overall, the data obtained by magnetometry and spectroscopy shed light on the SMM properties and their origin of the investigated Cobalt compounds. The magnetic properties of **K_2[1]**, **(K-18-c-6)$_2$[1]** and **($HNEt_3$)$_2$[2]** complexes are very similar among each other and to $(HNEt_3)_2$[1] [12] and show little or no change on exchanging the counter ion or sterically demanding side groups. This demonstrates that the systems is a very robust single molecule magnet platform.

All three complexes show a large zero-field splitting caused by the axial distortion of the tetrahedral coordination. Slow relaxation of magnetization in zero field is present and controlled by a combination of tunneling, Orbach and Raman relaxation processes. In zero field, efficient quantum tunneling of the magnetization is dominant at low temperatures and prevents the magnetization curve from

Table 3.7: Energies of the electronic transitions in $\mathbf{K_2[1]}$ as observed by MCD spectroscopy and calculated for allowed transitions from the $^4A_2$ ground state.

Final state		Experiment	Ab-initio Calculations
T_d notation	D_{2d} notation	Energy / cm^{-1}	
$^4T_2(F)$	$^4B_2(T_2)$	550$^{(1)}$	516
	$^4E(T_2)$	6028	6744 7098
$^4T_1(F)$	$^4E(T_1)$	7230	7473 7660
	$^4A_2(T_1(F))$	8253	8660
$^4T_1(P)$	$^4A_2(T_1(P))$	17878	20433
	$^4E(T_1(P))$	19452	21456 21580

$^{(1)}$from FIR measurements

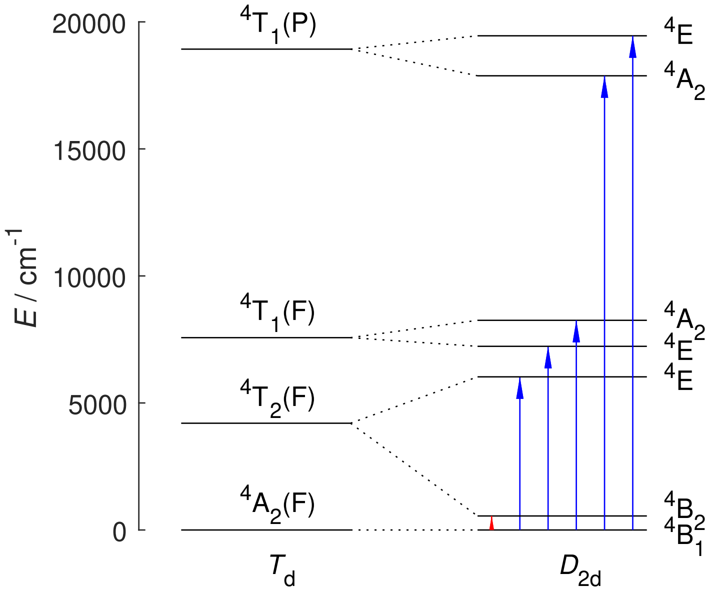

Figure 3.14: Energy level diagram derived for $\mathbf{K_2[1]}$. For D_{2d} symmetry, the energy levels are based on the experimentally observed transitions. The arrows indicate the experimental method, where red is FIR and blue is MCD spectroscopy.

exhibiting a real hysteresis with coercivity, instead showing waist restricted magnetization curves. Of all three complexes, **(K-18-c-6)$_2$[1]** performs best, exhibiting the largest *D*-value, largest hysteresis and longest relaxation times. Still, the performance of any of these complexes as single molecule magnets is far from being useful in practical applications because relaxation of magnetization happens too fast.

To improve the SMM properties of these complexes, the main source of relaxation at low temperatures, which is quantum tunneling, needs to be addressed. This can be done by suppressing quantum tunneling via exchange coupling of two metal centers. A very strong exchange coupling can be reached by employing organic bridges with unpaired electrons as it was shown for radical-bridged dilanthanide complexes[36–40]. The advantage of transition metal complexes in this context is that the exchange couplings can reach strengths up to two orders of magnitude larger than for lanthanides [41]. An approach via this route based on the complexes investigated in this section is presented in chapter 4.

3.4. Nickel Complexes

The electronic structure of the mononuclear nickel complexes $K_2[Ni^{II}(L_A)_2]$ (**K_2[3]**) and $(HNEt_3)_2[Ni^{II}(L_A)_2]$ (**$(HNEt_3)_2$[3]**) was investigated by magnetometric (Section 3.4.2) and spectroscopic (Section 3.4.3) means. The chemical structures are described in the following section.

3.4.1. Structures

The air-stable nickel(II) complexes are fashioned analogously to the cobalt complexes using L_A as ligands. Complex **K_2[3]** crystallizes in the monoclinic space group $P2_1/c$ with two nickel ions per unit cell. The potassium counter ions connect the molecules into an extensive network. **$(HNEt_3)_2$[3]** crystallizes in the orthorhombic space group $P2_12_12_1$. The crystal structures of the complexes are shown in Figure 3.15.

As for the cobalt compounds, the bond lengths in the ligand (see Table 3.8) indicate C–N single bonds and an aromatic ring. The net charge of 2− of the complex is balanced by two K^+-ions in **K_2[3]** and two ${HNEt_3}^+$-ions in **$(HNEt_3)_2$[3]** as indicated in the abbreviations. The angles between the planes spanned by the N–Ar–N system are very similar and close to 90°, being 85.91(5)° (nickel center 1) and 84.95(5)° (nickel center 2) in **K_2[3]** and 84.77(6)° in **$(HNEt_3)_2$[3]**. The

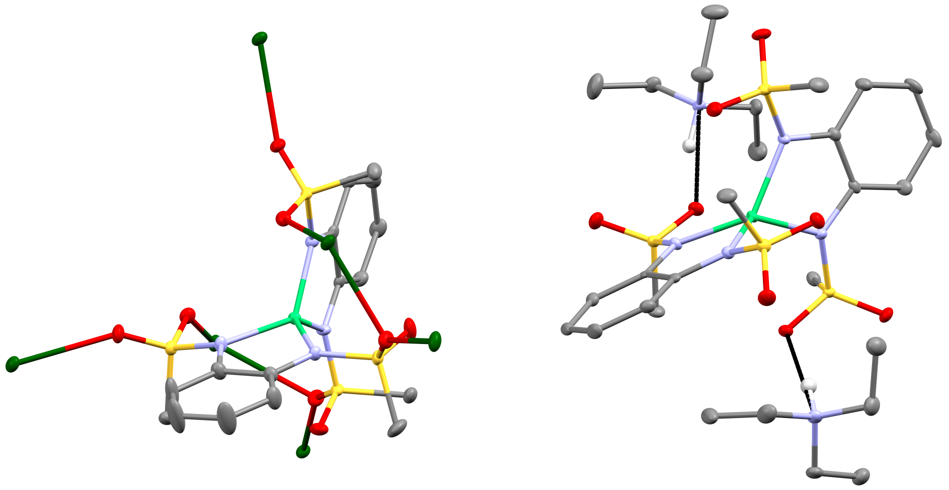

Figure 3.15: ORTEP views at 50 % probability level of the molecular structures of **K_2[3]** (left) and **$(HNEt_3)_2$[3]** (right). Nickel is shown in light green, potassium in dark green, oxygen in red, sulfur in yellow, carbon in dark gray, hydrogen in light gray and hydrogen bonds in black. In all pictures solvent molecules and hydrogen atoms were omitted for clarity.

strong axial distortion in the nickel coordination sphere is shown by the N–Ni–N angles between 80.33(8)° and 80.78(8)° which differ significantly from the ideal angle of 109.5° for a tetrahedron. All relevant angles and bond lengths are listed in Tables 3.8 and 3.9 for better overview.

Table 3.8: Maximum and minimum C–N and aromatic bond lengths in the nickel compounds.

	Min. C–N-bond length / Å	Max. C–N-bond length / Å	Min. aromatic bond length / Å	Max. aromatic bond length / Å
$\mathbf{K_2[3]}$ (1)	1.410(3)	1.414(3)	1.376(4)	1.420(4)
$\mathbf{K_2[3]}$ (2)	1.407(3)	1.414(3)	1.377(4)	1.420(3)
$\mathbf{(HNEt_3)_2[3]}$	1.406(4)	1.418(3)	1.375(4)	1.414(4)

(1) nickel center 1 (2) nickel center 2

Table 3.9: Angles between the planes formed by the N–Ar–N ligands and N–Ni–N angles in the cobalt compounds.

	inter-ligand angle	N–Ni–N angles	
$\mathbf{K_2[3]}$ (1)	85.91(5)°	80.78(8)°	80.42(8)°
$\mathbf{K_2[3]}$ (2)	84.95(5)°	80.71(8)°	80.33(8)°
$\mathbf{(HNEt_3)_2[3]}$	84.77(6)°	80.6(1)°	80.7(1)°

(1) nickel center 1 (2) nickel center 2

3.4.2. Magnetic Properties

The temperature dependence of the susceptibility temperature product χT was measured for both complexes and is shown in Figure 3.16. At 300 K, the χT values are 1.22 cm^3 K mol^{-1} ($\mathbf{K_2[3]}$) and 1.41 cm^3 K mol^{-1} ($\mathbf{(HNEt_3)_2[3]}$) which are the expected values for a spin of $S = 1$ and g-values of $g = 2.21$ and $g = 2.37$, respectively. The χT values of $\mathbf{K_2[3]}$ are approximately constant down to 100 K. Below that, they start to decrease continuously, dropping to 0.05 cm^3 K mol^{-1} at 1.8 K. For $\mathbf{(HNEt_3)_2[3]}$, the χT values are approximately constant down to 150 K, then start to decrease and finally drop to 0.06 cm^3 K mol^{-1} at 1.8 K. The drop to values close to zero at 1.8 K indicates a large zero-field splitting with an $m_S = 0$ ground state and, thus, $D > 0$ for both complexes.

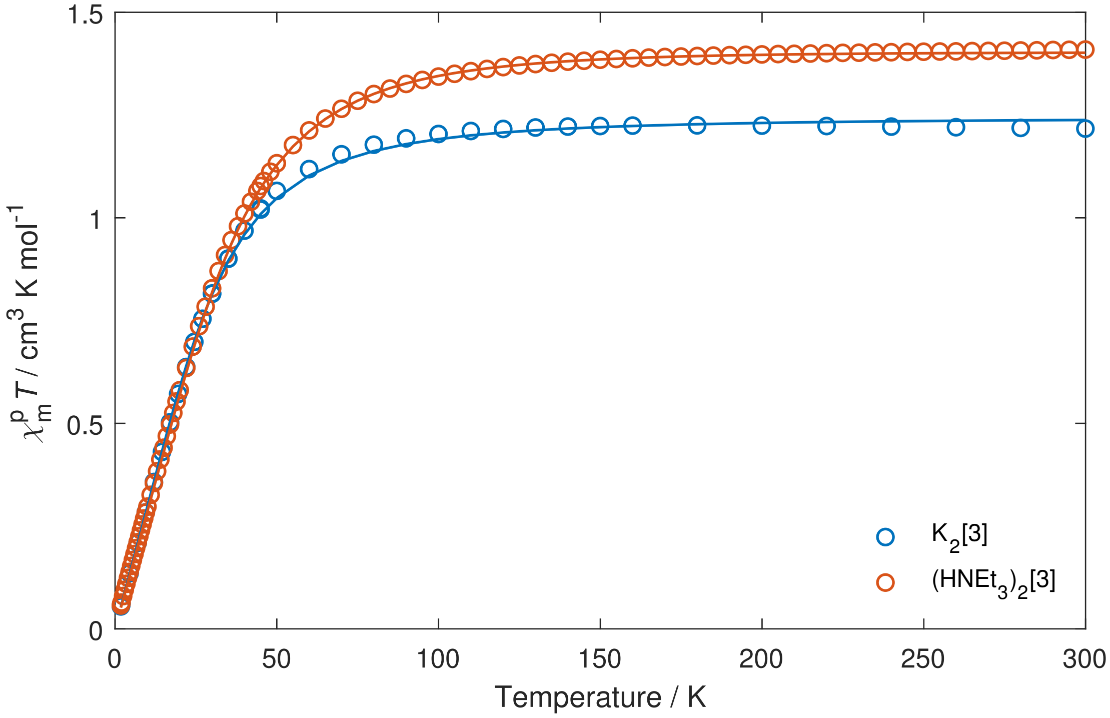

Figure 3.16: Temperature dependence of the susceptibility temperature product χT of the mononuclear nickel complexes. Measurements (circles) were performed in applied fields of 1 kOe ($T \leq 40$ K) and 10 kOe ($T < 40$ K). Fits (lines) are achieved by simultaneous fitting with magnetization curves ($\mathbf{K_2[3]}$) and FIR spectra ($\mathbf{(HNEt_3)_2[3]}$).

Figure 3.17 shows measurements of the magnetization M plotted versus the dimensionless quantity $\mu_B B / k_B T$ for both complexes. This type of plot was chosen because it directly shows the presence of zero-field splitting if curves at different temperatures fall not onto one curve. The regular plot of magnetization versus magnetic field is shown in Figure A.5. At the maximum field of 70 kOe and 1.8 K, magnetization values of $0.36\,N_A\mu_B$ ($\mathbf{K_2[3]}$) and $0.35\,N_A\mu_B$ ($\mathbf{(HNEt_3)_2[3]}$) are obtained. These values are significantly lower than the expected saturation values of $2\,N_A\mu_B$ (for $g = 2$), which again indicates a large positive zero-field splitting in agreement with the χT measurements.

Simultaneous fits of the $\chi T - T$ and $M - H$ measurements were performed for each compound using the spin Hamiltonian described in Equation 2.10. Best fits purely based on the magnetometric measurements yielded the spin Hamiltonian parameters $g_{\text{iso}} = 2.23(2)$ and $D = 58(2)\,\text{cm}^{-1}$ ($\mathbf{K_2[3]}$) and $g_{\text{iso}} = 2.38(2)$ and $D = 68(3)\,\text{cm}^{-1}$ ($\mathbf{(HNEt_3)_2[3]}$). Including an anisotropic g-value or rhombic zero-field splitting did not yield better fits and, consequently, was not used to avoid overparametrization. In addition, a strong correlation between $g_\perp$ and E

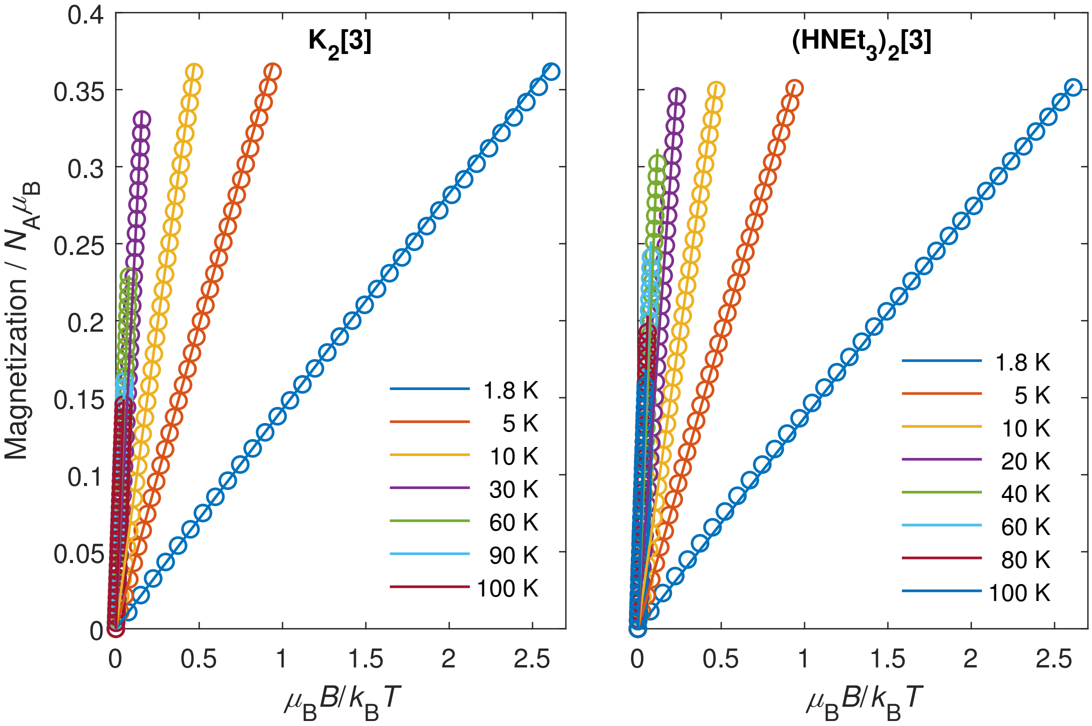

Figure 3.17: Molecular magnetization of the nickel complexes versus the reduced magnetic field at temperatures as indicated. Solid lines are fits achieved by simultaneous fitting with $\chi T - T$ measurements (**$\mathbf{K_2}$[3]**) and FIR spectra (**$\mathbf{(HNEt_3)_2}$[3]**).

was found. Satisfying fits were obtained by this approach and are shown for **$\mathbf{K_2}$[3]** as solid lines in Figures 3.16, 3.17 and A.5.

For **$\mathbf{(HNEt_3)_2}$[3]**, FIR spectroscopy (see Section 3.4.3) was used to refine the parameters. A fit based on the zero-field splitting parameters D and E extracted from FIR measurements yielded the parameters $g_\perp = 2.49(4)$, $g_\parallel = 2.08(4)$, $D = 76(1)\,\mathrm{cm^{-1}}$ and $E = 6.5(10)\,\mathrm{cm^{-1}}$. These values are in reasonable agreement with the ones determined solely from magnetometry. The axial g-tensor corresponds to an isotropic g-value of $g_{\mathrm{iso,FIR}} = \frac{g_x+g_y+g_z}{3} = \frac{2.49+2.49+2.08}{3} = 2.35$ which means that the error margins of $g_{\mathrm{iso,FIR}}$ and the g_{iso} from magnetometry overlap. The D parameter from FIR spectroscopy is about 10 % larger, which is not within the common error margin. Additionally, an E term had to be included which also contributes to the zero-field splitting. However, because g-is partially correlated with D and E the deviation is compensated by a slightly smaller value of $g_{\mathrm{iso,FIR}}$ compared to g_{iso} leading to an equally good fit of χT in both cases with and without the insights from FIR spectroscopy.

Ab-initio calculations (LDF-CAHF/CASSCF/PNO-CASPT2/SI-SO)[81–83] were performed for **$\mathbf{(HNEt_3)_2}$[3]** by Philipp Hallmen (Institut für Physikalische

Table 3.10: Determined g-values and zero-field splitting parameters of **K$_2$[3]** and **(HNEt$_3$)$_2$[3]**.

	g_{iso}			D / cm^{-1}	E / cm^{-1}
K$_2$[3]	2.23(2)			58(2)	0
(HNEt$_3$)$_2$[3] (1)	2.38(2)			68(3)	0
	$g_\perp$	$g_\parallel$			
(HNEt$_3$)$_2$[3] (2)	2.49(4)	2.08(6)		76(1)	6.5(10)
	g_x	g_y	g_z		
(HNEt$_3$)$_2$[3] (3)	2.70	2.56	1.98	105	-12.6

(1)free fit (2)fit based on D and E from FIR (3)ab-initio calculations
(a)nickel center 1 (b)nickel center 2

Chemie, Universität Stuttgart) yielding values of $g_x = 2.7028$, $g_y = 2.5565$, $g_z = 1.9788$, $D = 104.93\,\text{cm}^{-1}$ and $E = -12.56\,\text{cm}^{-1}$. The g-values are of rhombic nature and exhibit a stronger anisotropy of g_x and g_y to g_z than the ones from FIR. Their $g_{\text{iso,ab-initio}}$ of 2.41 in in good agreement with the other g_{iso} values. The D and E parameters are significantly larger but confirm the sign of D as positive. All parameters are also listed in Table 3.10 for better overview.

Overall, the zero-field splitting parameters found in the investigated complexes are to my knowledge the highest positive zero-field splittings reported for nickel(II) complexes (see Table 3.11).

To investigate for slow relaxation of magnetization, dynamic susceptibility measurements were performed on **K$_2$[3]**. Overview measurements (Figure A.6) with a limited set of temperatures and frequencies in a reasonable range revealed constant values of χ' and χ'' over the whole temperature and frequency range. The noisy and negative data at 1 Hz can be explained by the small values of χ' and χ'' while at the same time there is only little averaging over measurement cycles during the measurements at low frequencies. No signs of slow relaxation of magnetization are observed. This behavior is to be expected, given the positive sign of D. As described in Section 2.1.3 the positive D results in the magnetic state with the lowest m_S quantum number to be the ground state. For Non-Kramers ions like Ni(II), this implies the $m_S = 0$ state to be the ground state and, consequently, the ground state itself being the state over which relaxation of magnetization would take place. In a figurative view this means that the m_S states do not form a double-well potential where magnetization could be trapped on one side.

Table 3.11: Ni(II) complexes with $|D| > 25\,\mathrm{cm}^{-1}$ or slow relaxation of magnetization.

Compound	D / cm^{-1}	E / cm^{-1}	Literature
$\mathbf{(HNEt_3)_2[3]}$ $^{(1,2)}$	76(1)	6.5(10)	this work
$\mathbf{K_2[3]}$ $^{(2)}$	58(2)	0	this work
Ni(II)-substituted rubredoxins $^{(1)}$	55		Ref. [91]
$[\mathrm{Ni}\{^i\mathrm{Pr_2P(Se)NP(Se)}^i\mathrm{Pr_2}\}_2]$ $^{(1,2)}$	45.4(2)	1.91(2)	Ref. [92]
$\mathrm{Ni(SPh)_4}^{2\text{-}}$ $^{(1)}$	44		Ref. [91]
$\mathrm{Ni(PPh_3)_2I_2}$ $^{(1,2)}$	27.92(5)	4.71(5)	Ref. [93]
$[\mathrm{Ni(NCS)_2(nqu)_2(H_2O)_2}]\cdot 2\mathrm{nqu}$ $^{(5,7)}$	−5.86(69)	0	Ref. [77]
$[\mathrm{Ni(pydc)(pydm)}]\cdot\mathrm{H_2O}$ $^{(5,7)}$	−13.7	0.07	Ref. [74]
$[\mathrm{Ni(pydm)_2}](\mathrm{dnbz})_2$ $^{(5,7)}$	−15.4		Ref. [78]
$[\mathrm{Ni(Me_6tren)Cl}](\mathrm{ClO_4})$ $^{(1,3)}$	−120 to −180	1.63	Ref. [94]
$\mathrm{K}\{\mathrm{Ni(N[CH_2C(O)NC(CH_3)_3]_3)}\}$ $^{(3)}$	−200	1.7	Ref. [95]
$[\mathrm{Ni(MDABCO)_2Cl_3}]\mathrm{ClO_4}$ $^{(1,4,7)}$	−400 to −535	0.18	Ref. [75]

$^{(1)}$parameters based on spectroscopy $^{(2)}$tetrahedral $^{(3)}$trigonal-pyramidal
$^{(4)}$trigonal-bipyramidal $^{(5)}$octahedral $^{(6)}$pentagonal-bipyramidal
$^{(7)}$exhibits (field-induced) slow relaxation of magnetization

3.4.3. Spectroscopy

FIR spectroscopy in an applied field was employed to precisely determine the electronic structure of $\mathbf{(HNEt_3)_2[3]}$. The resulting spectra are plotted in Figures 3.18 and 3.19. The normalized spectra show several strong peaks over the whole range from $30\,\mathrm{cm}^{-1}$ to $500\,\mathrm{cm}^{-1}$, especially around $50\,\mathrm{cm}^{-1}$, $85\,\mathrm{cm}^{-1}$, $120\,\mathrm{cm}^{-1}$, $133\,\mathrm{cm}^{-1}$, $166\,\mathrm{cm}^{-1}$, $225\,\mathrm{cm}^{-1}$, $280\,\mathrm{cm}^{-1}$, $380\,\mathrm{cm}^{-1}$, $440\,\mathrm{cm}^{-1}$ and $475\,\mathrm{cm}^{-1}$. All of the signals above $100\,\mathrm{cm}^{-1}$ and the one at $50\,\mathrm{cm}^{-1}$ do not show a conclusive field-dependent behavior. Additionally, at their positions the transmission spectrum shows strong peaks which leads to increased noise in the normalized presentation and likely implies a predominant vibrational character of the signals. Consequently, those signals were excluded from further analyses. Two features, around $69\,\mathrm{cm}^{-1}$ and $85\,\mathrm{cm}^{-1}$, remain for analysis as expected for an $S = 1$ system, corresponding to $D \pm E$ in zero-field. From this, $D = 76(1)\,\mathrm{cm}^{-1}$ and $E = 6.5(10)\,\mathrm{cm}^{-1}$ can be extracted. Fitting magnetometry data with this constraint yielded the previously mentioned parameters of $g_\perp = 2.49(4)$, $g_\parallel = 2.08(4)$, $D = 76(1)\,\mathrm{cm}^{-1}$ and $E = 6.5(10)\,\mathrm{cm}^{-1}$ on which the simulations in Figures 3.18 and 3.19 are based. The small ratio of E/D shows that the zero-field splitting is highly axial for the nickel(II) complexes just like in the case of the cobalt complexes of Chapter 3.3.

From literature[45, 50] it is known that tetrahedral nickel(II) complexes exhibit their strongest band, which is usually split, in the region of $16\,000\,\mathrm{cm}^{-1}$. This

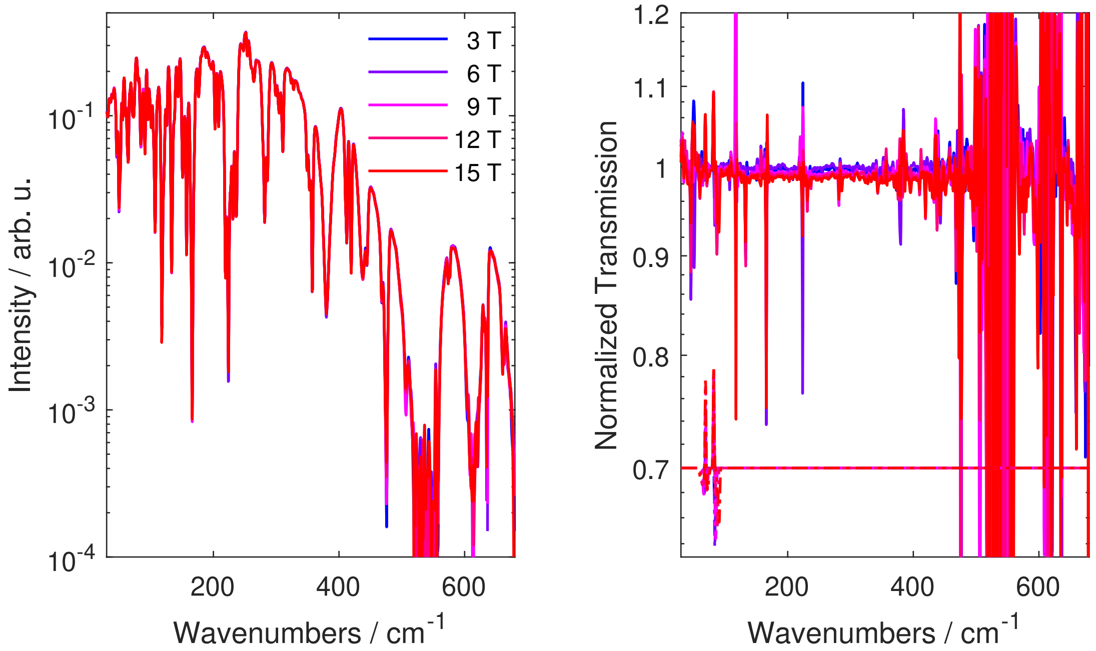

Figure 3.18: Left: FIR transmission spectra of **(HNEt$_3$)$_2$[3]** at 5 K. Right: Normalized FIR transmission spectra (solid lines) obtained by dividing each spectrum by the spectrum at zero field and simulation (dash-dotted lines). The indicated magnetic fields are valid for both Figures.

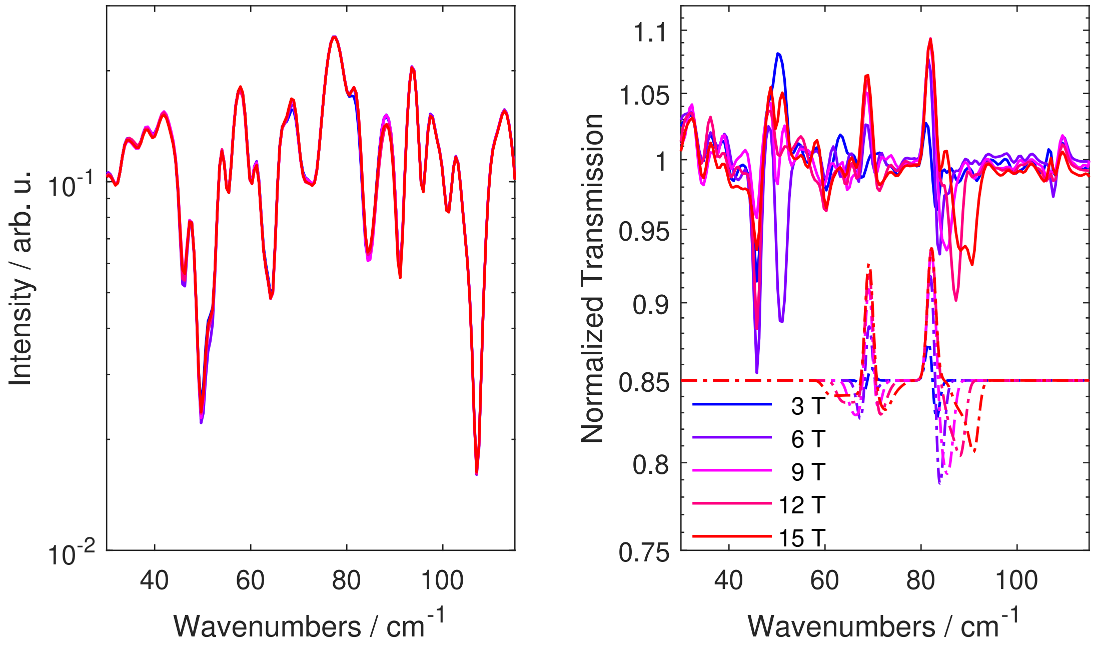

Figure 3.19: Left: FIR transmission spectra of **(HNEt$_3$)$_2$[3]** at 5 K. Right: Normalized FIR transmission spectra (solid lines) obtained by dividing each spectrum by the spectrum at zero field and simulation (dash-dotted lines). The indicated magnetic fields are valid for both Figures. Both Figures are zoomed on the field-dependent features.

band is assigned to the $^3T_1(F)\rightarrow{}^3T_1(P)$ transition. On both sides of that, bands of spin-forbidden transitions are located. A second band of spin-allowed transitions with significantly weaker intensity is located in the near infrared near between 6500 cm^{-1} and 10 000 cm^{-1} and corresponds to the $^3T_1\rightarrow{}^3A_2$ transition. At even lower energies, the $^3T_1\rightarrow{}^3T_2$ transition can sometimes be observed.

Field-dependent MCD spectra of **K₂[3]** are depicted in Figure A.7 and show bands in the aforementioned regions. All observed features below 33 500 cm^{-1} exhibit field-dependency and are, thus, caused by *C* term transitions. Signals above 33 500 cm^{-1} are attributed to noise. The spectrum at 10 T was fitted using Gaussians (Figure 3.20).

The observed transitions were identified according to literature[49, 50] and the energies of spin-allowed transitions are listed in Table 3.12. Some signals were attributed to spin-forbidden transitions which are listed in Table 3.13

Ab-initio calculations (LDF-CAHF/CASSCF/PNO-CASPT2/SI-SO, Philipp Hallmen, Table 3.12) show on the one hand significant energy differences between the energies of Ni centers 1 and 2. On the other hand, further splitting of the transition as it is expected from symmetry reduction from T_d to D_{2d} is observed. Especially, the $^3T_2(F)$ state is strongly split into a ^3E state around 5000 cm^{-1} to 6000 cm^{-1} and a $^3B_2$ state around 11 500 cm^{-1}, the latter one being very close to the $^3B_1(^3A_2)$ (D_{2d} notation) state at about 11 800 cm^{-1} (12 000 cm^{-1} for Ni center 2).

3.4.4. Summary and Conclusion

The performed investigations, especially FIR spectroscopy, reveal a large and highly axial zero-field splitting in **$(HNEt_3)_2$[3]** with zero-field splitting parameters of $D = 76(1)\,\mathrm{cm}^{-1}$ and $E = 6.5(10)\,\mathrm{cm}^{-1}$ which results in a E/D ratio of 0.09 This zero-field splitting is among the highest positive values reported in literature for nickel(II) compounds.

For **K_2[3]**, *D* was determined as 58(2) cm^{-1} solely based on magnetometry. However, the precision of this value should not be overestimated because for **$(HNEt_3)_2$[3]** the zero-field splitting parameters were unambiguously determined by FIR spectroscopy and differed by about 10 cm^{-1} from the values determined by magnetometry. This shows, again, nicely that magnetometry alone is not a sufficient method to investigate systems where *g*, *D* and *E* are correlated.

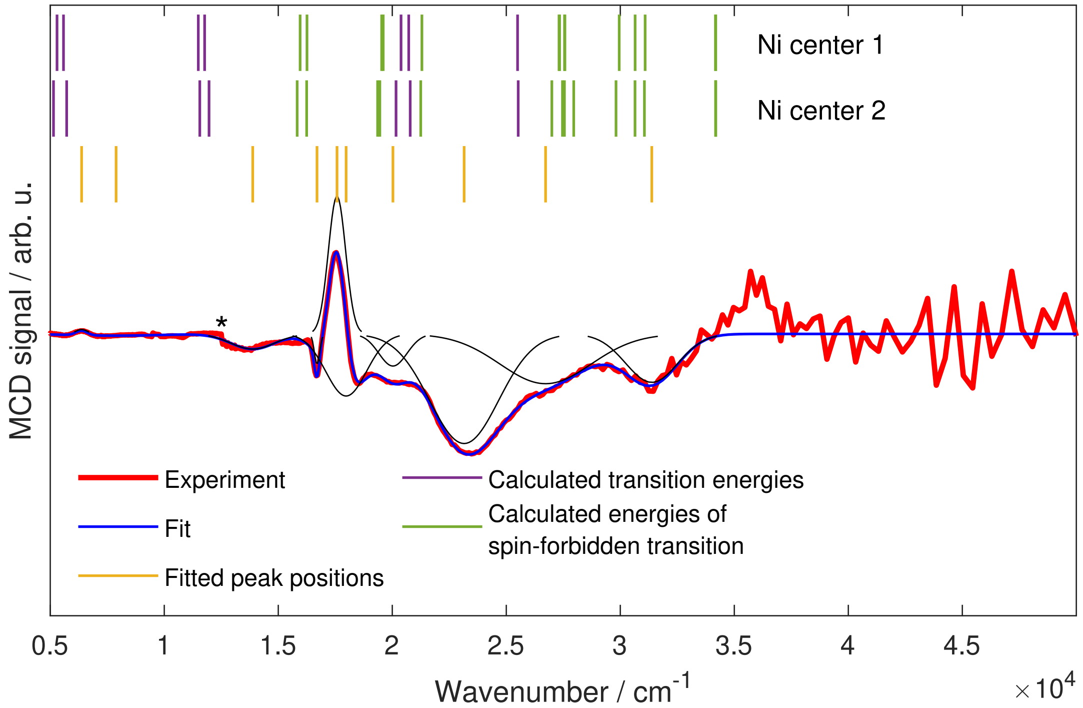

Figure 3.20: Normalized MCD spectrum of **K$_2$[3]** (red) at 1.5 K and 10 T with fit of the main features (blue). Black curves indicate the single Gaussians used for fitting. Extracted energies are indicated with yellow lines. Purple lines mark calculated energies of allowed transition while green lines mark forbidden transitions. The asterisk marks artifacts due to change of the detector.

Table 3.12: Energies of the spin-allowed electronic transitions in **K$_2$[3]** as observed by MCD spectroscopy and calculated for allowed transitions from the ^{3}T$_1$ ground state.

Final state	Experiment	Ab-initio Calculations	
		Ni center 1	Ni center 2
T$_d$ notation	Energy / cm^{-1}		
^{3}T$_1$(F)		4764 4958	4538 4732
^{3}T$_2$(F)	6375 7887	5297 5581 11492	5142 5720 11558
^{3}A$_2$(F)		11770	11963
^{3}T$_1$(P)	16699 17576 17975	20384 20721 25494	20164 20786 25522

Table 3.13: Energies of the spin-forbidden electronic transitions in **K_2[3]** as observed by MCD spectroscopy from the $^3T_1$ ground state.

Final state T_d notation	Experiment Energy / cm^{-1}
$^1A_1(G)$	13880
$^1T_2(G)$	20029 23151 26723
$^1T_1(G)$	31381

As for the cobalt(II) complexes in the previous section, it was shown for the nickel(II) complexes that the highly axial coordination geometry results in a highly axial electronic structure. In contrast to the cobalt systems ($S = 3/2$), where D was negative, for the nickel complexes ($S = 1$) D is positive, thus, making slow relaxation of magnetization impossible in this non-Kramers ion.

3.5. Iron Complexes

The electronic structure of the mononuclear iron complexes $(HNEt_3)_2[Fe^{II}(L_A)_2]$ (**$(HNEt_3)_2$**[4]) and $(HNEt_3)[Fe^{III}(L_A)_2]$ (**$(HNEt_3)$**[4]) was investigated by magnetometric (Sections 3.5.2 and 3.5.4) and spectroscopic (Sections 3.5.3 and 3.5.5) means. The chemical structures are described in the following section.

3.5.1. Structures

Both iron complexes are fashioned analogously to the cobalt and nickel complexes using L_A as ligands. They differ in the oxidation state of the central iron ion, which is +2 in **$(HNEt_3)_2$**[4] and +3 in **$(HNEt_3)$**[4], and, consequently, in the number of counter ions as which $(HNEt_3)^+$ is used. **$(HNEt_3)_2$**[4] is sensitive to oxidation in air while **$(HNEt_3)$**[4] is sensitive to hydrolysis. **$(HNEt_3)_2$**[4] crystallizes in the orthorhombic space group $P2_12_12_1$ with one iron ion per unit cell. Complex **$(HNEt_3)$**[4] crystallizes in the monoclinic space group $P2_1/c$ with one iron ion per unit cell. The crystal structures of the complexes are shown in Figure 3.21.

Similar to the previous mononuclear complexes of Chapters 3.3 and 3.4, the bond lengths in the ligand (see Table 3.14) indicate C-N single bonds and an aromatic ring. Of all investigated mononuclear complexes, the angles between the planes

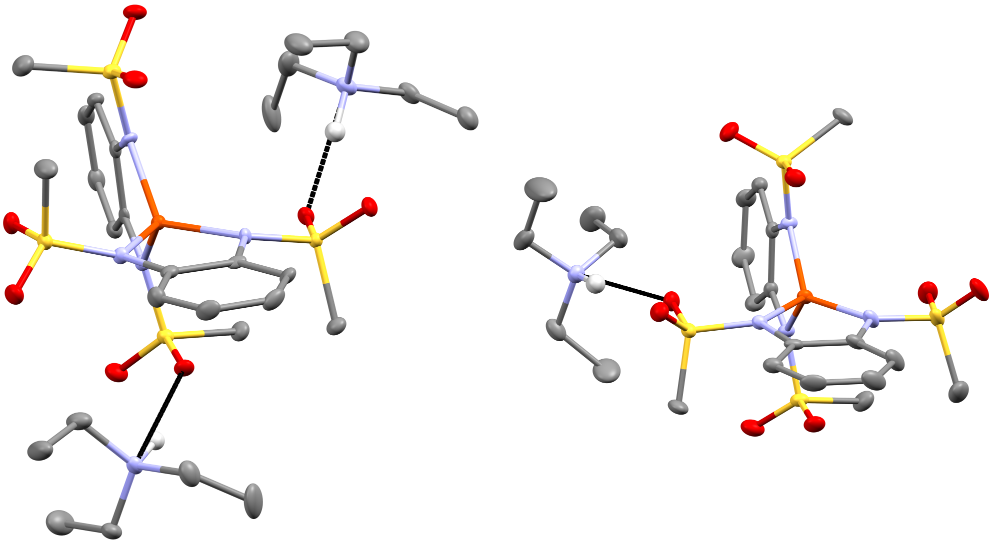

Figure 3.21: ORTEP views at 50 % probability level of the molecular structures of **$(HNEt_3)_2$**[4] (left) and **$(HNEt_3)$**[4] (right). Iron is shown in orange, oxygen in red, sulfur in yellow, carbon in dark gray, hydrogen in light gray and hydrogen bonds in black. In all pictures solvent molecules and hydrogen atoms (except for NH groups) were omitted for clarity.

Table 3.14: Maximum and minimum C–N and aromatic bond lengths in the iron compounds.

	Min. C–N-bond length / Å	Max. C–N-bond length / Å	Min. aromatic bond length / Å	Max. aromatic bond length / Å
$(HNEt_3)_2$[4]	1.423(4)	1.408(5)	1.379(5)	1.408(5)
$(HNEt_3)$[4]	1.426(3)	1.412(3)	1.384(4)	1.415(3)

Table 3.15: Angles between the planes formed by the N–Ar–N ligands and N–Fe–N angles in the cobalt compounds.

	inter-ligand angle	N–Fe–N angles	
$(HNEt_3)_2$[4]	86.13(8)°	79.93(12)°	79.97(12)°
$(HNEt_3)$[4]	88.72(4)°	81.14(8)°	81.64(8)°

spanned by the N–Ar–N system are the closest ones to 90° in these iron complexes with 86.13(8)° in **$(HNEt_3)_2$[4]** and 88.72(4)° in **$(HNEt_3)$[4]**. The strong axial distortion of the tetrahedral coordination sphere is also present here with N–Co–N angles of 79.93(12)° and 79.97(12)° in **$(HNEt_3)_2$[4]** and 81.14(8)° and 81.64(8)° in **$(HNEt_3)$[4]**. All relevant angles and bond lengths are listed in Tables 3.14 and 3.15 for better overview.

3.5.2. Magnetic Properties of $(HNEt_3)_2$[4]

Figure 3.22 shows the susceptibility temperature product of **$(HNEt_3)_2$[4]** plotted versus the temperature. The high-temperature value of $3.39\,\mathrm{cm^3\,K\,mol^{-1}}$ corresponds to an $S = 2$ spin system with $g_{\mathrm{iso}} = 2.13$. The χT value is virtually constant down to 30 K from where it gradually decreases to $1.80\,\mathrm{cm^3\,K\,mol^{-1}}$ at 1.8 K.

Magnetization measurements (Figure 3.23) show a distinctive temperature dependence of the magnetization curves hinting for a small zero-field splitting. At 1.8 K and 70 kOe the value of the magnetization is $3.64\,N_{\mathrm{A}}\mu_{\mathrm{B}}$ which is quite a lot below the expected saturation of $4.26\,N_{\mathrm{A}}\mu_{\mathrm{B}}$ for an $S = 2$ system with $g_{\mathrm{iso}} = 2.13$.

Simulations of the χT versus T and M versus H measurements were performed based on parameters determined by high-frequency EPR spectroscopy ($g_x = 2.22$, $g_y = 2.01$, $g_z = 2.10$, $D = -3.29\,\mathrm{cm^{-1}}$, $E = 0.22\,\mathrm{cm^{-1}}$) and are shown in Figures 3.22 and 3.23.

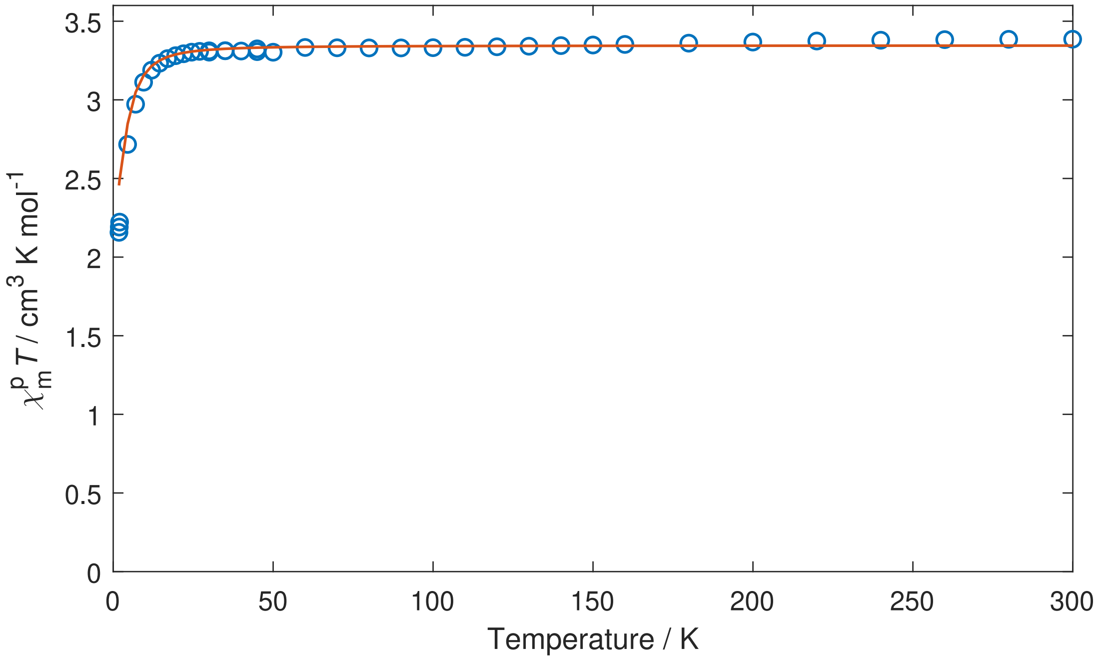

Figure 3.22: Temperature dependence of the susceptibility temperature product χT of **(HNEt$_3$)$_2$[4]**. Measurements (circles) were performed in applied fields of 1 kOe ($T \leq 40$ K) and 10 kOe ($T < 40$ K). Fits (lines) are based on HFEPR fits.

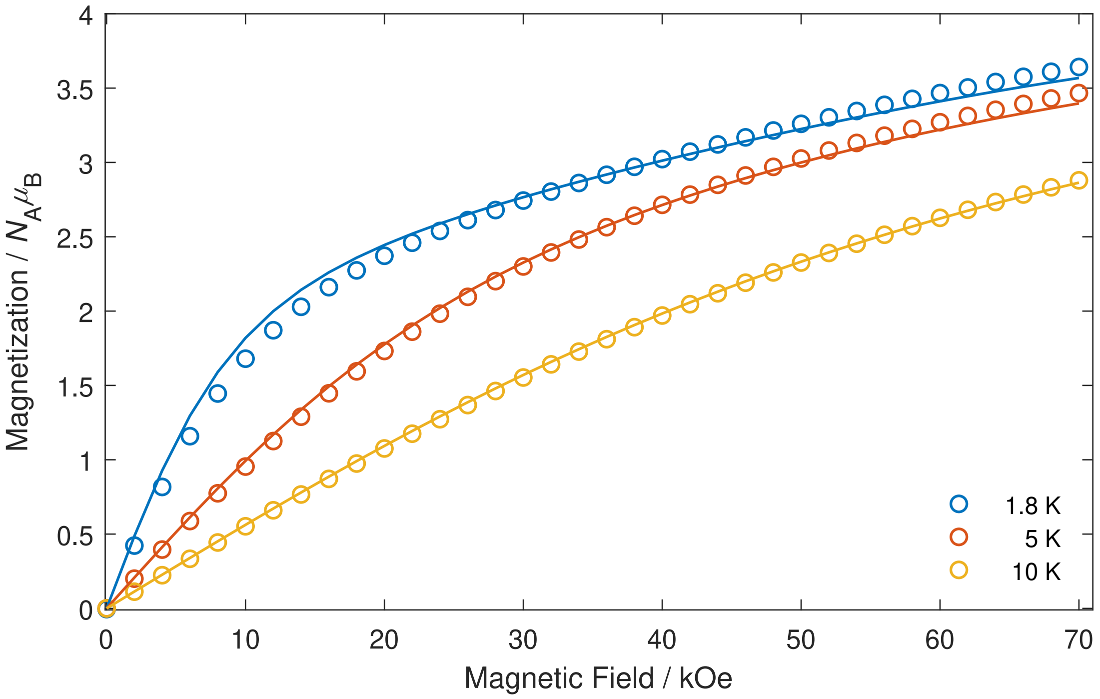

Figure 3.23: Molecular magnetization of **(HNEt$_3$)$_2$[4]** versus applied magnetic field at temperatures as indicated. Solid lines are fits based on HFEPR fits.

Dynamic susceptibility measurements of **$(HNEt_3)_2$[4]** were performed in zero field and at 1 000 Oe applied field but no signs of slow relaxation of magnetization was found (Figure A.8).

3.5.3. Spectroscopy of $(HNEt_3)_2$[4]

High-frequency EPR spectroscopy (HFEPR) is the perfect method to determine g-values and small zero-field splitting parameters. Thus, **$(HNEt_3)_2$[4]** was subjected to extensive HFEPR investigations. Fast frequency domain magnetic resonance (fFDMR) measurements[58] (frequency-field-map in Figure 3.24) revealed zero-field transitions around 300 GHz and 400 GHz. A third zero-field transition was found by conventional HFEPR measurements at about 100 GHz (Figure A.9). The three transitions' energy ratio of $400 : 300 : 100 = 4 : 3 : 1$ corresponds to the ratio of $4D : 3D : 1D$ of the energy differences between the zero-field energy levels for an $S = 2$-system with $E = 0$ (Section 2.1.3). In that, $4D$ corresponds to the $m_S = 0 \rightarrow \pm 2$, $3D$ to the $m_S = \pm 1 \rightarrow \pm 2$ and $1D$ to the $m_S = 0 \rightarrow \pm 1$ transition. Because the $4D$-transition (where $\Delta m_S = \pm 2$) can be observed, it

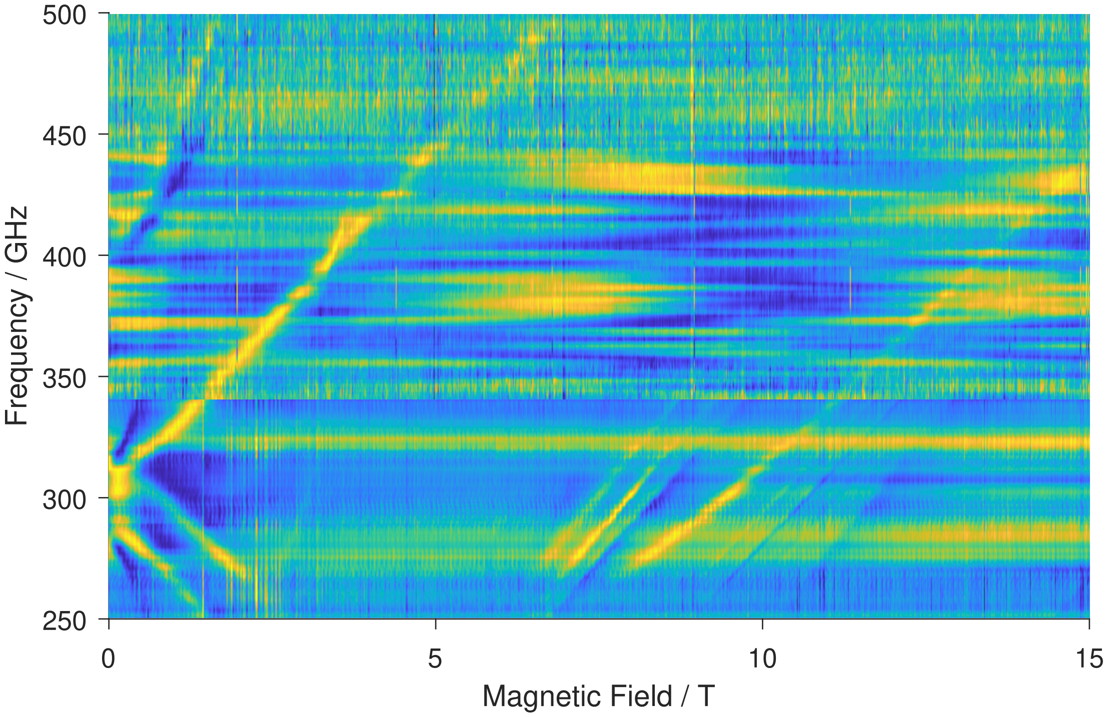

Figure 3.24: Fast Frequency Domain Magnetic Resonance spectra of **$(HNEt_3)_2$[4]** at 12 K.

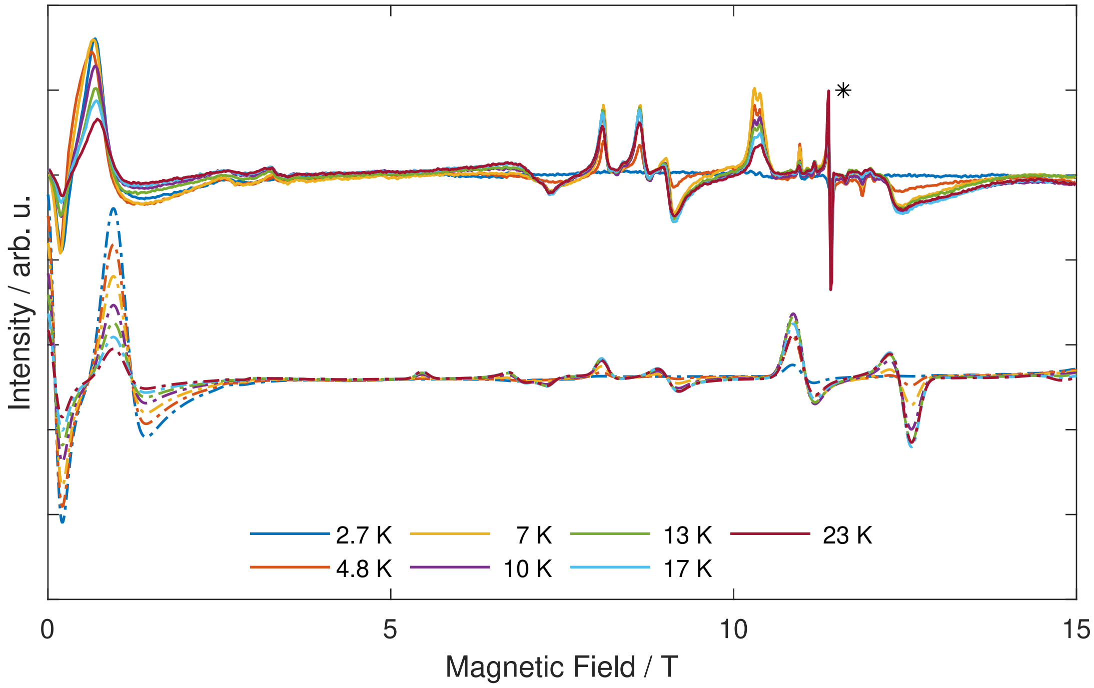

Figure 3.25: Measured (solid lines) and simulated (dash-dotted lines) high-frequency EPR spectra of **$(HNEt_3)_2$[4]** at 320 GHz and temperatures as indicated. $g = 2$-signals are marked with an asterisk.

can be directly concluded that $E \neq 0$ This results in shifts of the energy levels in zero-field leading to a splitting of the doublets which are degenerate for $E = 0$ and is (beside a rhombic g-tensor) the reason for the large number of observed signals.

Temperature dependent measurements at 320 GHz (Figure 3.25) revealed that the intensity of the zero-field transition around 300 GHz is highest at low temperatures and drops with increasing temperature. At the same time, the spectrum at 2.7 K shows only this feature plus a small signal of a $g = 2$-impurity. Consequently, it is unequivocal that this transition originates from the ground state. Together with the previously observed energy ratios of the three zero-field transitions, which results in the transition around 300 GHz to be a $3D$-transition between the $m_S = \pm 2$ and $m_S = \pm 1$ states, it becomes clear that $m_S = \pm 2$ is the ground state and thus D is negative.

Starting from these three conclusions, namely $D < 0$, $E \neq 0$ and ZFS $\approx$ 100 GHz a set of HFEPR spectra at different frequencies was fitted (Figure 3.26) using the Hamiltonian described in Equation 2.10. A satisfying fit where all features are present was achieved for a rhombic g-tensor and a small E where $|{}^{E}/_{D}| = 0.07$

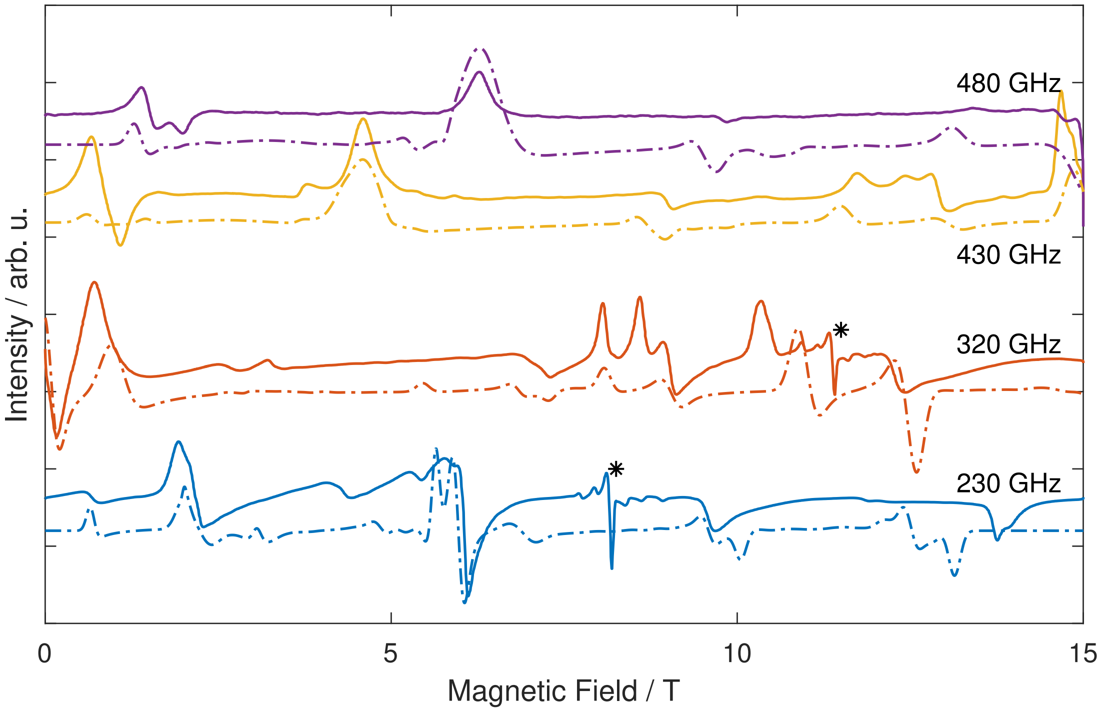

Figure 3.26: Measured (solid lines) and simulated (dash-dotted lines) high-frequency EPR spectra of **$(HNEt_3)_2$[4]** at 12 K and frequencies as indicated. $g = 2$-signals are marked with an asterisk.

with the parameters $g_x = 2.22(4)$, $g_y = 2.01(4)$, $g_z = 2.10(6)$, $D = -3.29(6)\,\mathrm{cm}^{-1}$, $E = 0.22(6)\,\mathrm{cm}^{-1}$ (Figure 3.26).

High modulation currents were used to obtain the spectra, which leads to a warming of the sample and an uncertainty in the sample temperature. Because of this uncertainty and the strong temperature dependence of the features' intensities resulting from the small zero-field splitting, the relative intensities of the simulated spectra match only partially. For this reason, Figure A.10 shows a zoom of the measurements and simulations.

The position of a small number of features could not be reproduced perfectly. One example for this is in the measurement at 320 GHz the peak at 10.36 T which is at 10.87 T in the simulation. Using the levelsplot function of the simulation software EasySpin allows to investigate the field/frequency dependence of this peak. Comparing this dependence with the frequency-field-map shows that at the higher frequencies of 430 GHz and 480 GHz the simulated position of this peak matches the experimental position. It can be concluded that the parameter set of a rhombic g-tensor and D and E is too small to perfectly reproduce all spectra simultaneously because a perfect fit of the 10.36 T-feature requires a larger E

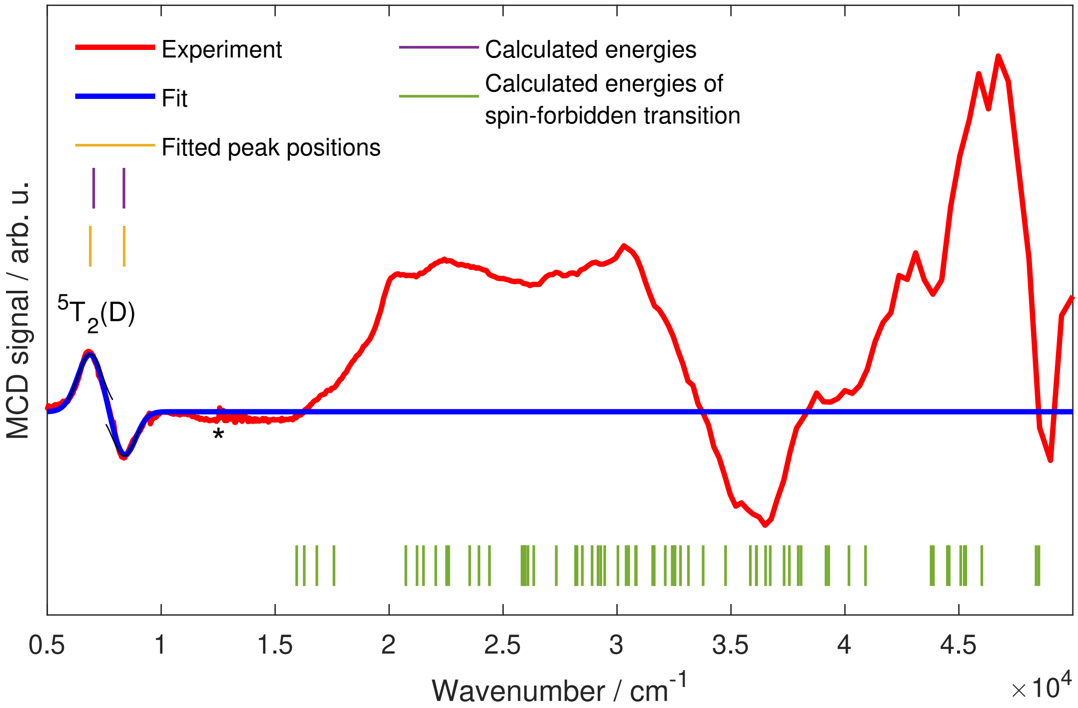

Figure 3.27: Normalized MCD spectrum of **$(HNEt_3)_2$[4]** (red) at 1.5 K and 8 T with fit of the main features (blue) based on two allowed transitions. Black curves indicate the single Gaussians used for fitting. Extracted energies are indicated with yellow lines. Purple lines mark calculated energies of allowed transition while green lines mark forbidden transitions. The asterisk marks artifacts due to change of the detector.

of about 0.6 cm^{-1} while fitting the feature at 0.7 T (both at 320 GHz) requires $E = 0.22$ which is both largely independent of any g-value. Possibly, the inclusion of high-order operators could help to resolve this as it was recently shown for other iron compounds[96] but was beyond the scope of this work.

Ab-initio calculations (LDF-CAHF/CASSCF/PNO-CASPT2/SI-SO)[81–83] performed by Philipp Hallmen (Institut für Physikalische Chemie, Universität Stuttgart) on this complex yield a parameter set of $g_x = 2.009$, $g_y = 2.069$, $g_z = 2.225$, $D = 7.40\,\mathrm{cm}^{-1}$ and $E = 2.29\,\mathrm{cm}^{-1}$. The numbers of the g-values are very close to the experimental ones but the assignment to the principal directions is different. The zero-field splitting parameters are far off from the experimental ones and also the sign of D, which was unequivocally determined by HFEPR spectroscopy is opposite. An explanation for the different sign might be that the ratio of $|{}^{E}\!/\!{}_{D}|$ is close to $^1\!/\!_3$ for which case the sign has no meaning.

Literature of tetrahedral Fe(II) compounds shows broad bands in the near infrared (NIR) region near 4000 cm^{-1} to 6000 cm^{-1} which are sometimes split[45].

Table 3.16: Energies of the electronic transitions in **$(HNEt_3)_2$[4]** as observed by MCD spectroscopy and calculated for allowed transitions from the ^{5}E ground state.

Final state	Experiment	Ab-initio Calculations
T_d notation	Energy / cm^{-1}	
^{5}E(D)		900
$^5T_2$(D)		1085
	6890	7039
	8377	8365

The bands correspond to the allowed transitions from the electronic ground state ^{5}E to the $^5T_2$ excited state (see Figure 2.7 for the corresponding Tanabe-Sugano diagram). In the MCD spectrum of **$(HNEt_3)_2$[4]** (Figure 3.27), two bands are observed between 5000 cm^{-1} to 10 000 cm^{-1}. Numerous additional features of equal and higher intensity are observed in the UV/Vis region which can be either ligand-based, charge-transfer or spin-forbidden transitions. The energies of the bands in the NIR region match very well with energies calculated by ab-initio methods (LDF-CAHF/CASSCF/PNO-CASPT2/SI-SO, Philipp Hallmen) and are given in Table 3.16. Additionally, the calculations show plenty of spin-forbidden transitions in the UV/Vis region, the quintet ground state to triplet and singlet excited states transitions of which are shown in Figure 3.27.

3.5.4. Magnetic Properties of $(HNEt_3)$[4]

Magnetic susceptibility and magnetization data of the iron(III) complex **$(HNEt_3)$[4]** were measured. Fits of HFEPR measurements revealed that the measured mass of the sample prepared for magnetometry had to be corrected by −25 % which is accounted for in the following plots and analyses. This is a valid procedure because the parameters determined by EPR spectroscopy, which is a very precise tool in this case, lead to a close to perfect fit of χT vs. T and M vs. H curves. Additionally, an incorrectness in the measured mass cannot be excluded since the pellet was prepared under difficult conditions in a glove box. Because of the limited available sample amount, the measurement could not be repeated with a newly prepared sample and the mass could not be remeasured because of the way the sample was prepared.

The χT product plotted versus the temperature is shown in figure 3.28. The high-temperature value of 4.18 $cm^3\,K\,mol^{-1}$ corresponds to $g_{iso} = 1.95$ for an $S =$

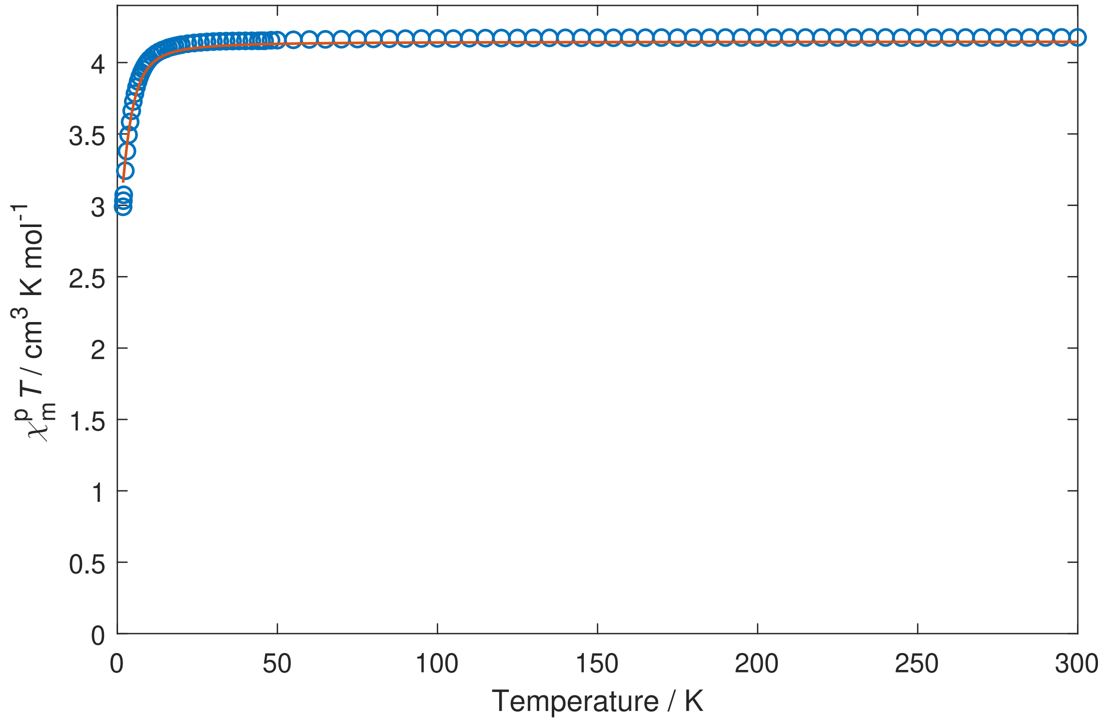

Figure 3.28: Temperature dependence of the susceptibility temperature product χT of **(HNEt$_3$)[4]** with a corrected sample mass of $-25\,\%$. Measurements (circles) were performed in applied fields of 1 kOe ($T \leq 40\,\mathrm{K}$) and 10 kOe ($T < 40\,\mathrm{K}$). Fits (lines) are based on HFEPR fits.

$^5/_2$ spin system. This value is virtually constant down to 20 K from where it starts do decrease to reach $2.99\,\mathrm{cm^3\,K\,mol^{-1}}$ at 1.8 K. The shape of the curve indicates a small zero-field splitting of much smaller than $20\,\mathrm{K} \approx 14\,\mathrm{cm^{-1}}$ to be present.

Measurements of the magnetization versus magnetic field (Figure 3.29) show a strong temperature dependence of the magnetization values, indicating a small zero-field splitting. At 1.8 K and 70 kOe, a magnetization value of $4.26\,N_\mathrm{A}\mu_\mathrm{B}$ is obtained. This value is only slightly smaller than the expected $4.88\,N_\mathrm{A}\mu_\mathrm{B}$ for $g = 1.95$ and $S = {}^5/_2$, indicating that saturation is almost reached.

Simulations of $\chi T - T$ and $M - H$ measurements were performed based on parameters determined by EPR spectroscopy ($g_\perp = 1.99$, $g_\parallel = 1.90$, $D = -1.955$ and $E = 0.12$, see next section) and are shown in Figures 3.28 and 3.29.

Probing the SMM properties, dynamic susceptibility measurements were performed but showed no out-of-phase signals (Figure A.11).

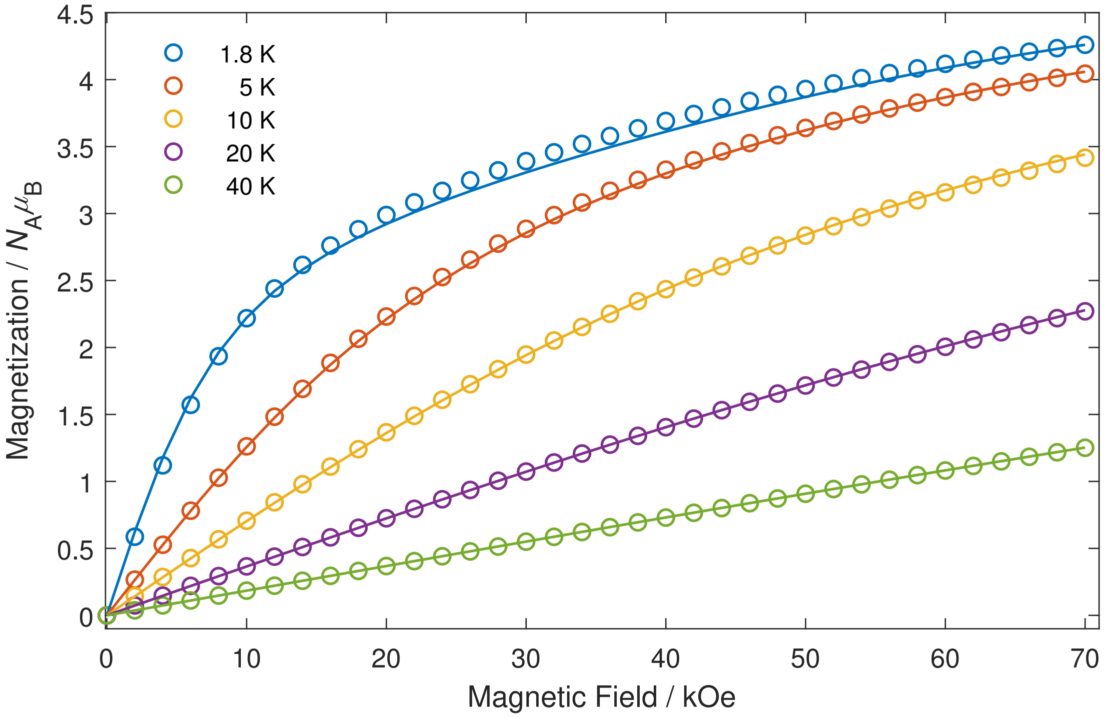

Figure 3.29: Molecular magnetization of **(HNEt$_3$)[4]** versus applied magnetic field at temperatures as indicated with a corrected sample mass of −25 %. Solid lines are fits based on HFEPR fits.

3.5.5. Spectroscopy of (HNEt$_3$)[4]

As for **(HNEt$_3$)$_2$[4]**, high-frequency EPR spectroscopy is the perfect method for an accurate determination of ZFS parameters and g-values for **(HNEt$_3$)[4]** because of the small expected zero-field splitting based on the magnetometry measurements. Thus, different HFEPR measurements were performed. Fast frequency domain magnetic resonance measurements (Figure 3.30) revealed zero-field transitions around 230 GHz and 350 GHz. A third zero-field transition was found by conventional HFEPR measurements at about 120 GHz (Figure A.12). The three transitions' energy ratio of $350 : 230 : 120 \approx 6 : 3.9 : 2.1$ corresponds very closely to the ratio of $6D : 4D : 2D$ of the energy differences between the zero-field energy levels for an $S = {}^5\!/_2$-system with $E = 0$ (Section 2.1.3). In that context, $6D$ corresponds to the energy difference between the $m_S = \pm{}^1\!/_2$ and $m_S = \pm{}^5\!/_2$ states, $4D$ to the difference of $m_S = \pm{}^3\!/_2$ and $m_S = \pm{}^5\!/_2$ and $2D$ to $m_S = \pm{}^1\!/_2$ and $m_S = \pm{}^3\!/_2$. Because the $6D$-transition (where $\Delta m_S = \pm 2$) can be observed, it can be directly concluded that $E \neq 0$ which shifts the energy of the Kramers doublets in zero-field with respect to each other.

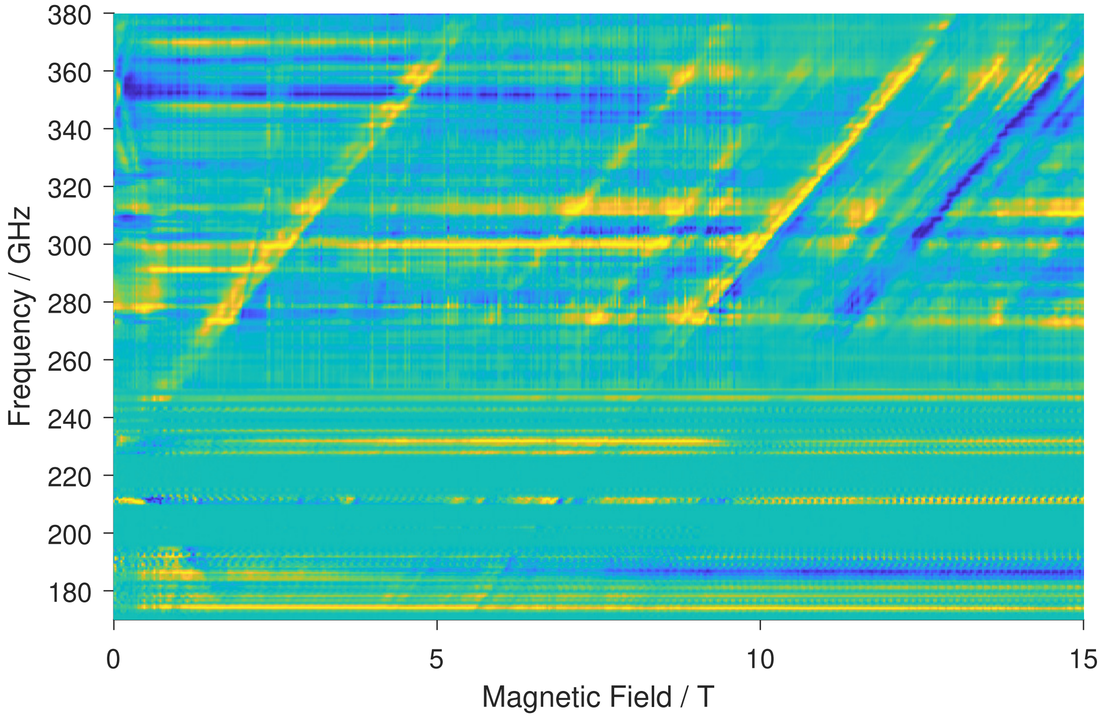

Figure 3.30: Fast Frequency Domain Magnetic Resonance spectra of **$(\mathbf{HNEt_3})$[4]** at 7 K.

The signal at $g = 2$ consisting of five peaks is attributed to a small impurity of iron(III) for which a small D causes the observed peak pattern.

Additionally, a set of temperature dependent HFEPR measurements was performed at 320 GHz and 375 GHz (Figures 3.31 and 3.32). It is apparent that all observed peaks appear doubled very closely together. In a perfectly powdered sample, this can be caused by two very similar but non-equal paramagnetic centers being present in the sample. However, the crystal structure did not contain any evidence for this. Alternatively, effects like this can occur during sample preparation, namely during pellet pressing.

Based on the initial guess for the zero-field splitting from fFDMR measurements, the temperature dependent HFEPR spectra were fitted based on the Hamiltonian described in Equation 2.10. A satisfying fit (Figures 3.31 and 3.32) was achieved with the parameters $g_\perp = 1.99(4)$, $g_\parallel = 1.90(6)$, $D = -1.955(50)\,\mathrm{cm}^{-1}$ and $E = 0.12(4)\,\mathrm{cm}^{-1}$.

This set of parameters is very surprising. Since Fe(III) has five unpaired electrons and is high-spin in this case, only a very small zero-field splitting (way below $1\,\mathrm{cm}^{-1}$) and g-values much closer to 2 would be expected as it is usu-

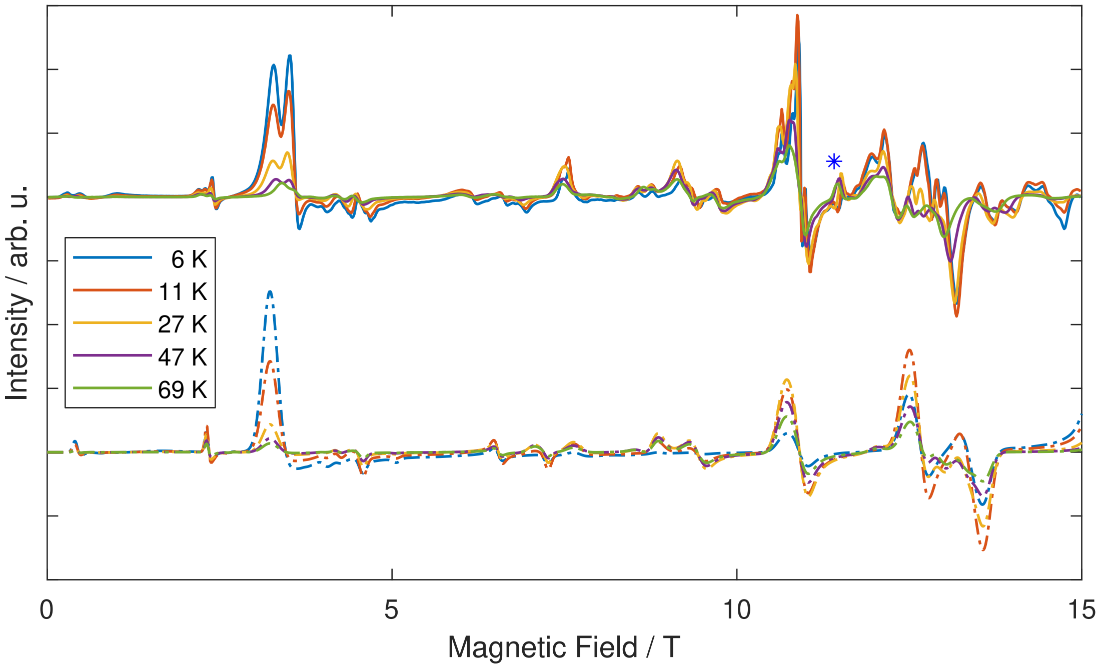

Figure 3.31: Measured (solid lines) and simulated (dash-dotted lines) high-frequency EPR spectra of **(HNEt$_3$)[4]** at 320 GHz and temperatures as indicated. $g = 2$-signals are marked with an asterisk.

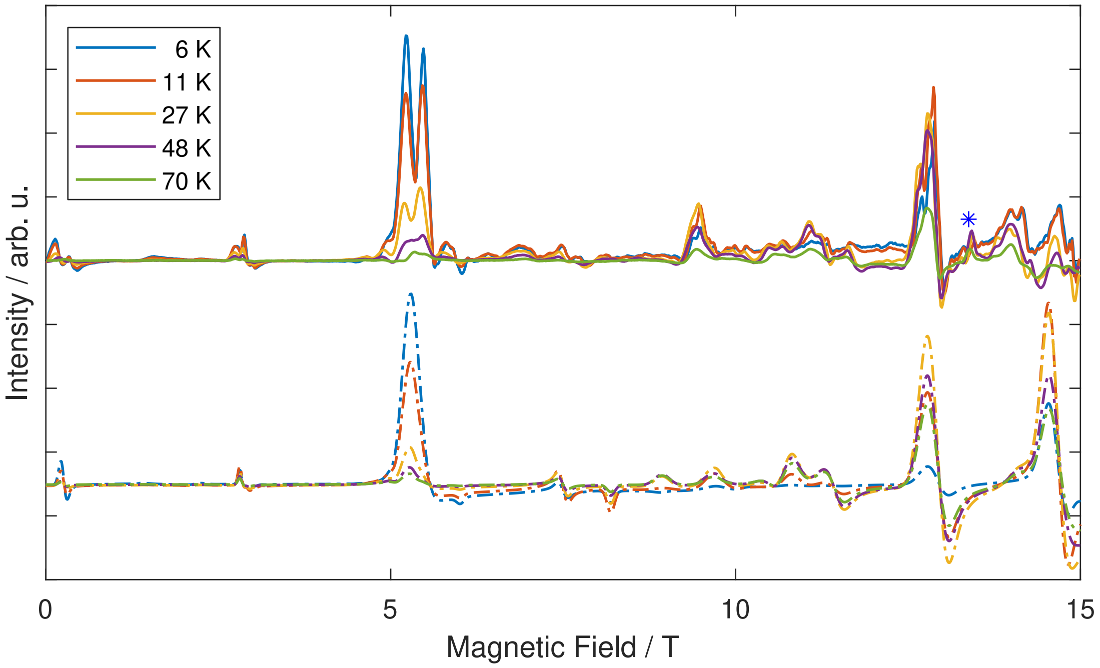

Figure 3.32: Measured (solid lines) and simulated (dash-dotted lines) high-frequency EPR spectra of **(HNEt$_3$)[4]** at 375 GHz and temperatures as indicated. $g = 2$-signals are marked with an asterisk.

ally the case for isoelectronic Mn(II) compounds. Ab-initio calculations (LDF-CAHF/CASSCF/PNO-CASPT2/SI-SO)[81–83] (Philipp Hallmen (Institut für Physikalische Chemie, Universität Stuttgart)) confirm this expectation with values of $g_{\mathrm{iso}} = 2.002$, $D = -0.25\,\mathrm{cm}^{-1}$ and $E = 0.006\,\mathrm{cm}^{-1}$ but agree at least in the sign of D.

3.5.6. Summary and Conclusion

The magnetic properties of complexes **(HNEt$_3$)$_2$[4]** and **(HNEt$_3$)[4]** were precisely determined. The g-tensor is slightly axial in case of **(HNEt$_3$)$_2$[4]** and rhombic in **(HNEt$_3$)[4]**. Both compounds have small zero-field splittings with small $|E/D|$-ratios of 0.07 (**(HNEt$_3$)$_2$[4]**) and 0.06 (**(HNEt$_3$)[4]**) None of them show SMM properties. While these findings are not surprising for **(HNEt$_3$)$_2$[4]**, for **(HNEt$_3$)[4]** discrepancies between expectations based on literature were found in form of unusually high zero-field splitting parameters. The inconsistency of observation and expectation could not be resolved in the scope of this work. Additional measurements like MCD should be performed to investigate the ligand field of the complex and find possible reasons for this unusually large zero-field splitting.

4. Radical-Bridged Dinuclear Cobalt Complex

The project presented below was part of a collaboration with the group of Prof. Dr. Biprajit Sarkar. All compounds were synthesized and structurally characterized by Uta Albold, M.Sc. (both Institut für Chemie und Biochemie, Freie Universität Berlin at the time). Parts of the results presented in this chapter have been published in *Angew. Chem. Int. Ed.* **2019**, *58*, 9802–9806[97].

4.1. Aims

The findings from the mononuclear cobalt-based complexes in the previous chapter in combination with knowledge about suppression of tunneling in radical-bridged dilanthanide complexes[36–40] led to the synthesis of the dinuclear, radical-bridged cobalt complex $(\text{K-18-c-6})_3[\{(\text{H}_2\text{L}_\text{C}{}^{2-})\text{Co}^{\text{II}}\}_2(\mu\text{-L}_\text{C}{}^{3\cdot-})]$ (**(K-18-c-6)$_3$[5]**) where $\text{H}_4\text{L}_\text{C}$ is 1,2,4,5-tetrakis(methanesulfonamido)benzene. The structure of this compound is based on the described mononuclear complexes in this work and Reference [12] and features a bridging ligand containing an unpaired electron. We investigated the electronic and magnetic properties of this compound to gain insight into the effect of strong exchange coupling on its properties as a single-molecule magnet.

4.2. Structure

(K-18-c-6)$_3$[5] features two cobalt(II) ions which are bridged by a radical-containing aromatic ligand. The complex is fully air and moisture stable. It crystallizes in the space group $P2_1/c$ and exhibits an inversion center in the middle of the bridging ligand. The crystal structure is shown in Figure 4.1.

The cobalt ions are coordinated by four nitrogen atoms forming an axially elongated tetrahedron. Four 18-crown-6 encased potassium counterions crystallize per

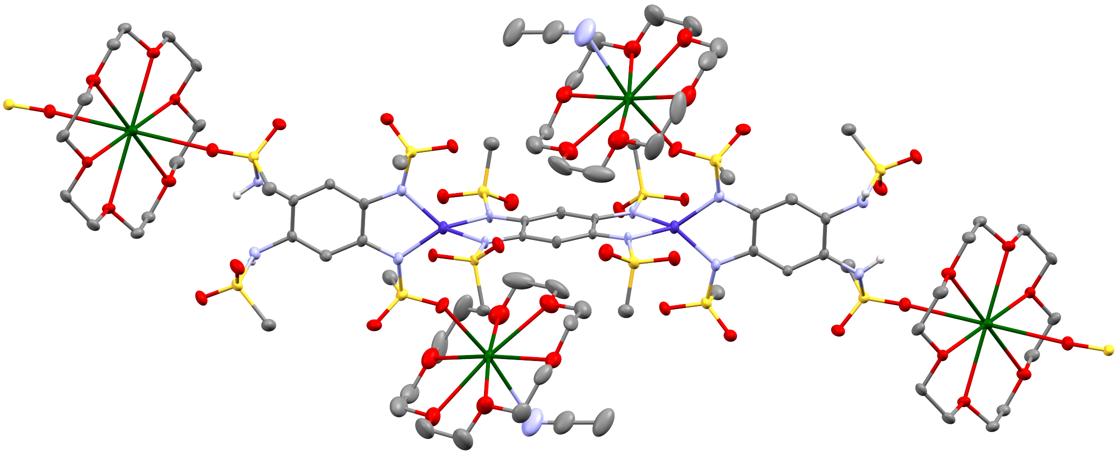

Figure 4.1: ORTEP views at 50 % probability level of the molecular structure of **(K-18-c-6)$_3$[5]**. Cobalt is shown in dark blue, potassium in green, oxygen in red, sulfur in yellow, carbon in dark gray and hydrogen in light gray. Hydrogen atoms (except for NH groups) were omitted for clarity.

unit cell, two of which are shared between neighboring molecules to form a polymeric chain. Thus, a ratio of three positively charged counterions per molecule results, confirming the triply negatively charged nature of the bridging ligand. The bridging and ancillary ligands are nearly perpendicularly oriented with an angle of 83.52(6)°. The C–N bonds in the bridging ligand (1.383(5) Å and 1.387(5) Å) are shorter than in the ancillary ligands (1.402(5) Å and 1.413(5) Å). At the same time, the N–Co–N angle to the bridging ligand (80.8(1)°) is smaller than to the ancillary ligand (82.4(1)°). The C–C bond lengths show no remarkable difference between the ligands and are in the range of 1.386(6) Å to 1.441(5) Å.

Compared to the mononuclear complexes, the cobalt-ligand bond lengths, bond angles and distortions are virtually identical. Using the SHAPE geometry analysis program[98] with the coordination polyhedron of the mononuclear cobalt complexes from Chapter 3 as a reference, the distortion values are very small and vary from 0.014 to 0.02 for (HNEt$_3$)$_2$[1], **(HNEt$_3$)$_2$[2]** and **(K-18-c-6)$_2$[1]**. For **K$_2$[1]** it is slightly higher at 0.054.

4.3. Magnetic Properties

Magnetic susceptibility measurements were performed to investigate the zero-field splitting and nature and strength of the magnetic couplings in **(K-18-c-6)$_3$[5]**. Temperature dependent measurements of the susceptibility (Figure 4.2) show a

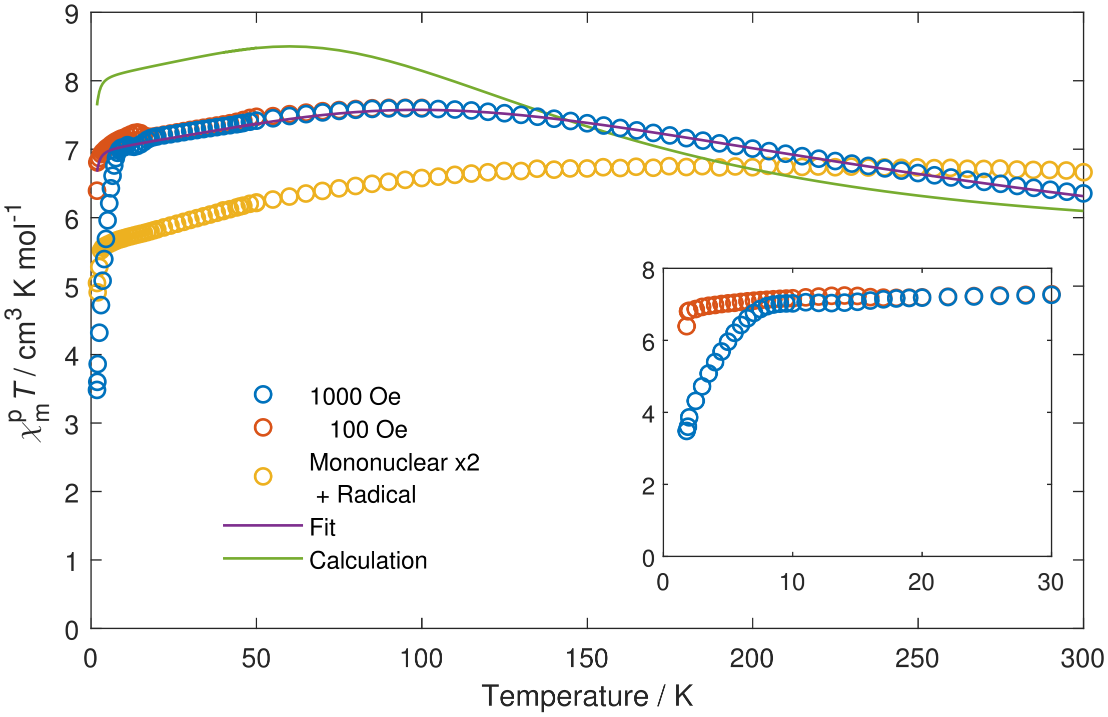

Figure 4.2: Temperature dependence of the susceptibility temperature product χT of **(K-18-c-6)$_3$[5]** (blue, red). Yellow circles show the expected curve for an uncoupled system based on $(HNEt_3)_2[1]$ and a radical (see main text). The lines correspond to the best fit (purple) and simulations based on values derived from ab-initio calculations (green). Measurements (blue circles) were performed in applied fields of 1 kOe ($T \leq$ 40 K) and 10 kOe ($T > 40$ K). The inset shows a more detailed view of the drop at low temperatures.

curved line with a χT-value of 6.36 cm^3 K mol^{-1} at 300 K. This value increases to a maximum of 7.60 cm^3 K mol^{-1} at 95 K. From there it decreases to 7.02 cm^3 K mol^{-1} at about 7 K. For measurements at 1000 Oe, a distinct drop to 3.48 cm^3 K mol^{-1} at 1.8 K is observed at low temperatures. As in the case of the mononuclear complexes in the previous chapter, this drop is an indication of slow relaxation of magnetization because the magnetic moment is not in thermal equilibrium with the surroundings. Measurements at a weaker applied field of 100 Oe, where relaxation is faster (vide infra), show a much smaller drop at low temperatures. From the latter measurements, a χT value of 6.81 cm^3 K mol^{-1} at 2 K can be extracted.

The room temperature value of 6.36 cm^3 K mol^{-1} is close to 6.14 cm^3 K mol^{-1} which is the expected value for the sum of non-interacting cobalt ions and an $S = {}^1\!/_2$ radical spin and can be calculated with Equation 2.17 assuming g_{Co} as the average g-value of $(HNEt_3)_2[1]$ [12] and $g_{\mathrm{Rad}} = 2$: $\chi_m T/(\mathrm{cm^3\,K\,mol^{-1}}) = 2 \cdot (2.48^2/8) \cdot (3/2) \cdot (5/2) + (2^2/8) \cdot (1/2) \cdot (3/2) = 6.14$.

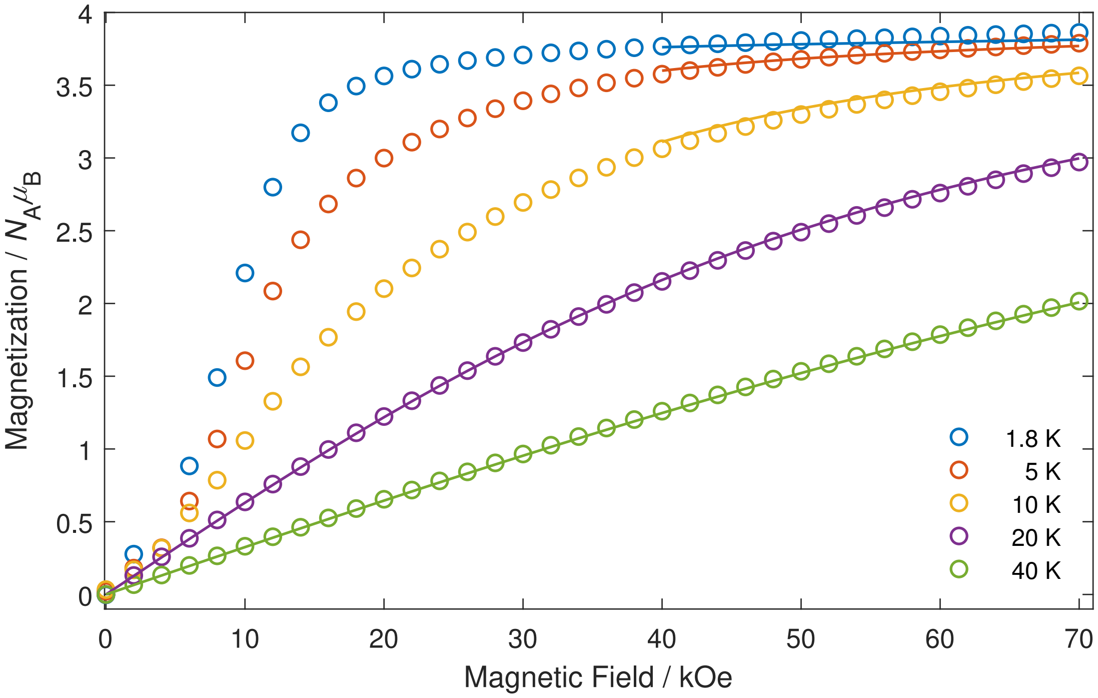

Figure 4.3: Molecular magnetization of **(K-18-c-6)$_3$[5]** versus applied magnetic field at temperatures as indicated (circles). Only ranges unaffected by magnetic hysteresis were simulated (lines).

Comparing the χT-curve of the dinuclear complex with a curve obtained by taking twice the χT-values of the mononuclear complex $(HNEt_3)_2$[1] plus those for a $g = 2$ radical (yellow circles in Figure 4.2) shows differences especially at low temperatures. In numbers, the χT-values around room temperature of **(K-18-c-6)$_3$[5]** (6.36 cm^3 K mol^{-1}) are slightly smaller than the summed values (6.66 cm^3 K mol^{-1}), which is in agreement with antiferromagnetic exchange interaction in **(K-18-c-6)$_3$[5]**. The significantly higher values of χT at low temperatures can be explained by a ferrimagnetic high-spin ground state which would correspond to $S = {}^5\!/_2$ in the giant spin model (c. f. Section 2.1).

Measurements of magnetization versus magnetic field (Figure 4.3) exhibit a magnetization value of 3.86 $N_A\mu_B$ at 1.8 K and 7 T.

The $\chi T - T$ and $M - H$-curves of **(K-18-c-6)$_3$[5]** were fitted simultaneously on the basis of the Hamiltonian of Equation 4.1 which is based on the generalized Hamiltonian described in Equation 2.11 where $E = 0$ was assumed based on the results of Chapter 3. For the $M - H$-curves, only ranges unaffected by magnetic hysteresis, as described later in this chapter, were taken into account. The best fit, shown in Figures 4.2 and 4.3, was achieved with the values $J_{\text{Co-Rad}} = 440(40)\,\text{cm}^{-1}$,

$D_{\mathrm{Co}} = -115(15)\,\mathrm{cm}^{-1}$, $g_{\mathrm{Co},\parallel} = 2.85(3)$ and $g_{\mathrm{Co},\perp} = 2.09(7)$ while $g_{\mathrm{Rad}} = 2$ was fixed. The values are in agreement with the previous interpretations, confirming the exchange coupling as antiferromagnetic and the ferrimagnetic, high-spin ground state.

$$\hat{H}_J = \sum_{i=1}^{2}\Big(J_{\text{Co-Rad}}\hat{\mathbf{S}}^{\mathrm{T}}_{\mathrm{Co},i}\hat{\mathbf{S}}_{\mathrm{Rad}} + D_{\mathrm{Co},i}\left[\hat{S}^2_{\mathrm{z,i}} - \frac{1}{3}S_{\mathrm{Co}}(S_{\mathrm{Co}}+1)\right] + \mu_{\mathrm{B}}\mathbf{B}^{\mathrm{T}}\cdot\mathbf{g}_{\mathrm{Co},i}\cdot\hat{\mathbf{S}}_{\mathrm{Co},i}\Big) + \mu_{\mathrm{B}}\mathbf{B}^{\mathrm{T}}\cdot\mathbf{g}_{\mathrm{Rad}}\cdot\hat{\mathbf{S}}_{\mathrm{Rad}} \quad (4.1)$$

Multireference ab-initio calculations (LDF-CAHF/CASSCF/PNO-CASPT2/SI-SO)[81–83, 97] were performed by Philipp Hallmen (Institut für Physikalische Chemie, Universität Stuttgart) to gain more information on the values of D and J. The resulting value $D = -110\,\mathrm{cm}^{-1}$ is in excellent agreement with the experimentally determined value. J was calculated to be $174\,\mathrm{cm}^{-1}$ and the nature of the exchange coupling is in agreement with the experiment while the absolute value is off by a factor of 2.5. Because g-values could not be calculated by this method, g-values of $(\mathrm{HNEt}_3)_2$[1] were used to simulate the $\chi T - T$-curve based on the theoretical values of D and J. The result is shown in Figure 4.2. There, the maximum of χT is calculated at a lower temperature than it is found in the experiment. This shows that the calculation underestimates the interaction. Consequently it can be concluded that the description of spin-orbit coupling, which leads to the zero-field splitting, is better than that of dynamical correlations, which lead to the coupling constant J. This is an effect of the calculation procedure but a more accurate one is not feasible due to the size of the system.

The indication of slow relaxation of magnetization, which is seen by the distinctive drop of χT at low temperatures, was investigated in a first step by performing ZFCFC measurements. The corresponding plot (Figure 4.4) shows a deviation of the ZFC and FC measurements below 15 K and, thus, an irreversibility temperature of 15 K.

Magnetic hysteresis measurements (Figure 4.5) confirm this result as they show an opening of the hysteresis loop up to temperatures of 15 K which is quite unusual for cobalt single-molecule magnets[3, 5, 34, 63, 99]. The hysteresis stretches to more than 35 kOe at 1.8 K and is much more pronounced than in the mononuclear complexes where the magnitude of the hysteresis was only up to 5 kOe in **(K-18-c-6)$_2$[1]**. Unfortunately, the waist-restriction at zero field is present as in the mononuclear complexes meaning that the coercive field is very small. In a recently published linear Co(II)-complex[34] the waist-restriction diminished under dilution

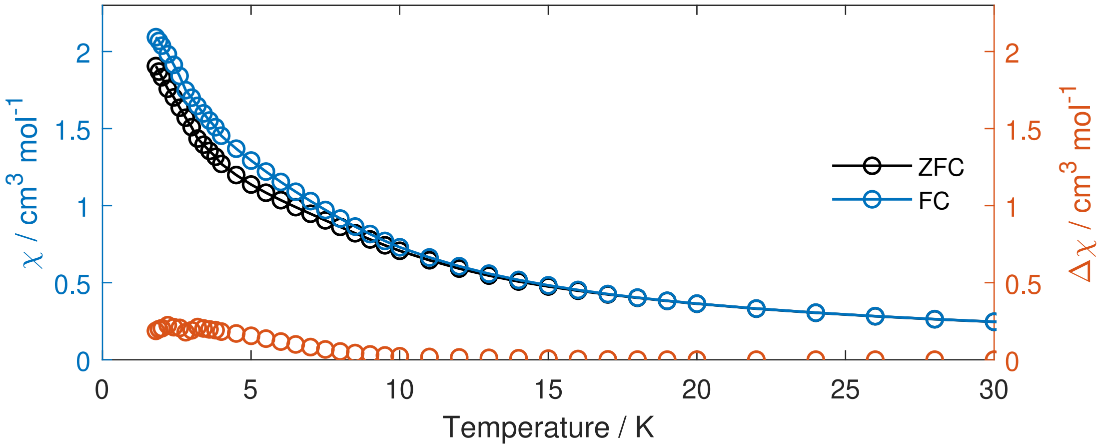

Figure 4.4: ZFCFC measurement of **(K-18-c-6)$_3$[5]** at an applied static field of 1000 Oe.

in a diamagnetic zinc analog. A version of **(K-18-c-6)$_3$[5]** where the cobalt ions are replaced by zinc was not available. Instead, the diamagnetic mononuclear complex (K-18c-6)$_2$[Zn^{II}(L$_A$)$_2$], which crystallizes in the same space group as **(K-18-c-6)$_3$[5]**, was used for magnetic dilution. The diluted sample of **(K-18-c-6)$_3$[5]** was prepared by mixing **(K-18-c-6)$_3$[5]** and (K-18c-6)$_2$[Zn^{II}(L$_A$)$_2$] dissolved in acetonitrile in a molar ratio of 1:19. The solution was then dried in vacuum for several hours. The resulting sample is diluted to 5 % of **(K-18-c-6)$_3$[5]** and its hysteresis curve compared to the pure sample's is shown in Figure 4.6. No significant change in the hysteresis can be observed. This indicates that either a dilution of 5 % is not sufficient to cancel effects of intermolecular interaction on the relaxation, or that the main cause for relaxation is an intramolecular mechanism.

The dynamic susceptibility of **(K-18-c-6)$_3$[5]** was measured in zero field and plots of χ' and χ'' versus the applied frequency are shown in Figure 4.7. The out-of-phase signal shows frequency-dependent maxima in the temperature range from 2 K to 30 K indicating slow relaxation of magnetization. This range is significantly larger than in the mononuclear complexes where slow relaxation could be observed up to only 20 K. The corresponding Argand plot is shown in Figure 4.8.

Reliable simultaneous fits of χ' and χ'' to modified Debye functions (Equations 2.20 and 2.21) could be obtained between 2 K and 29 K. The resulting fit parameters are listed in Table A.5. In contrast to the mononuclear compounds, the fit reproduces the zero field data in the whole frequency and temperature range very well indicating that there is only one relaxation pathway. A comparison of the $\chi_T - \chi_S$ values with the χ^P values from dc measurements (Figure A.13) shows

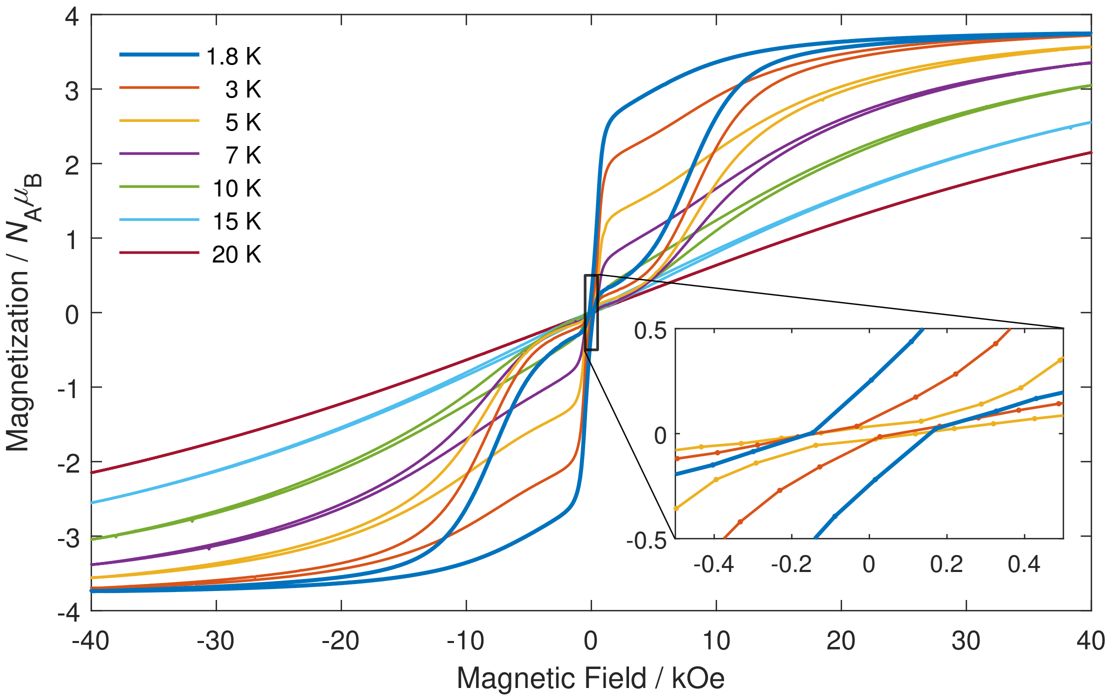

Figure 4.5: Magnetic hysteresis measurements of **(K-18-c-6)$_3$[5]** recorded at sweep rates of 20 Oe s^{-1} and temperatures as indicated.

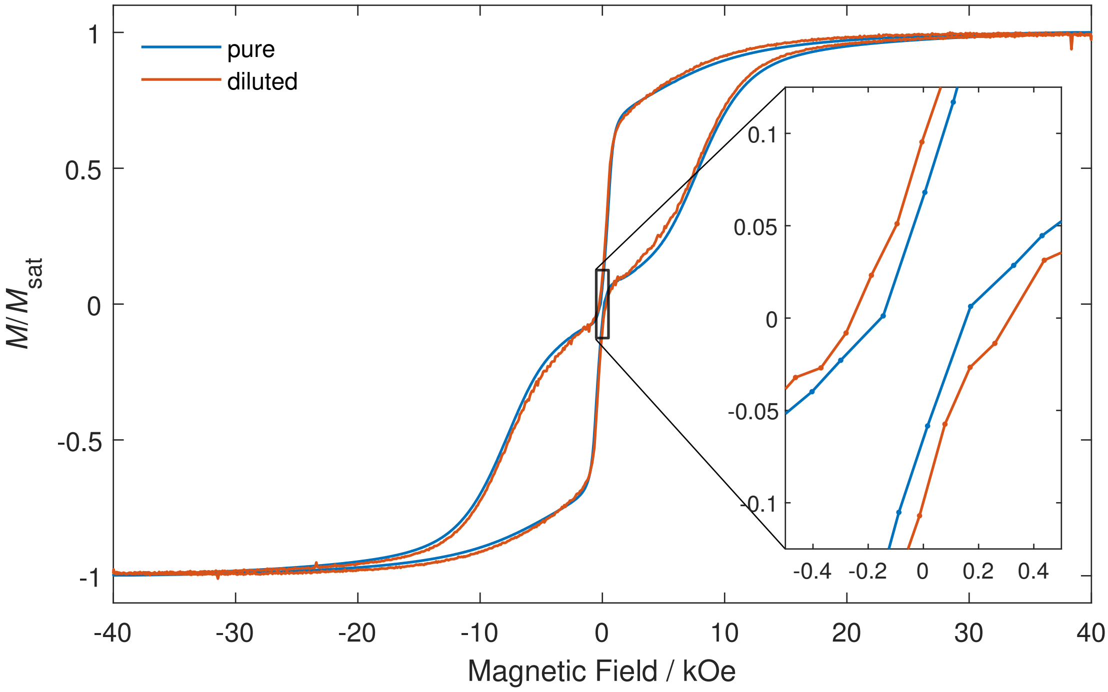

Figure 4.6: Magnetic hysteresis measurements of **(K-18-c-6)$_3$[5]** in pure state and diluted to 5 % in (K-18c-6)$_2$[Zn^{II}(L$_A$)$_2$] recorded at 1.8 K and sweep rates of 20 Oe s^{-1}.

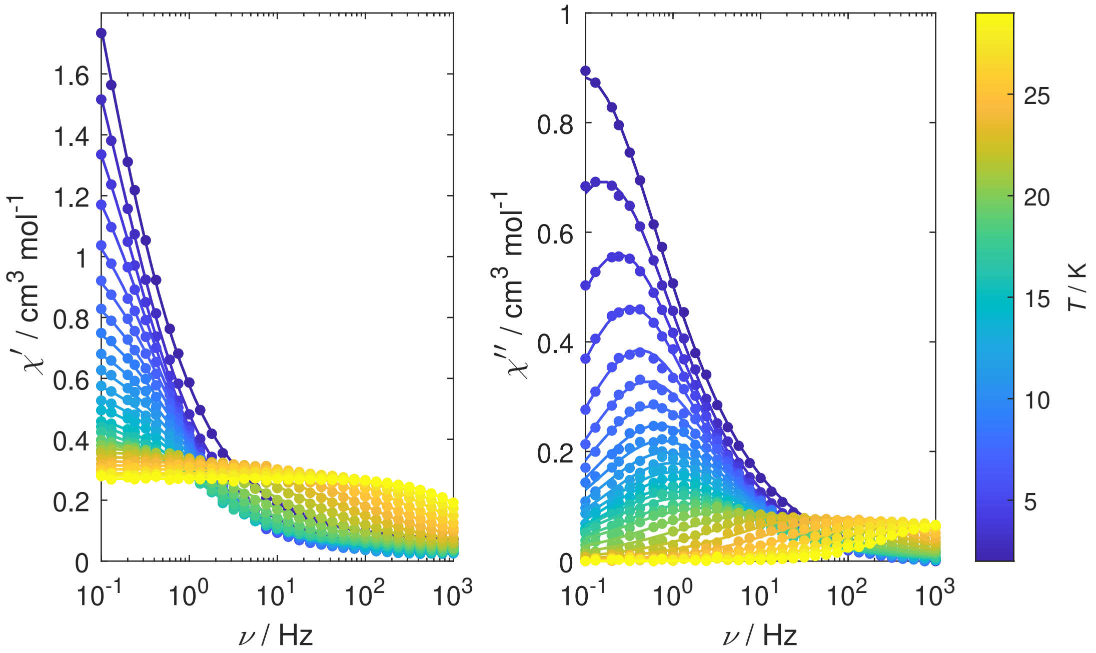

Figure 4.7: In-phase (left) and out-of-phase (right) susceptibility of **(K-18-c-6)$_\mathbf{3}$[5]** at frequencies and temperatures as indicated and zero applied static field. Solid lines are simultaneous fits of in-phase and out-of-phase signals.

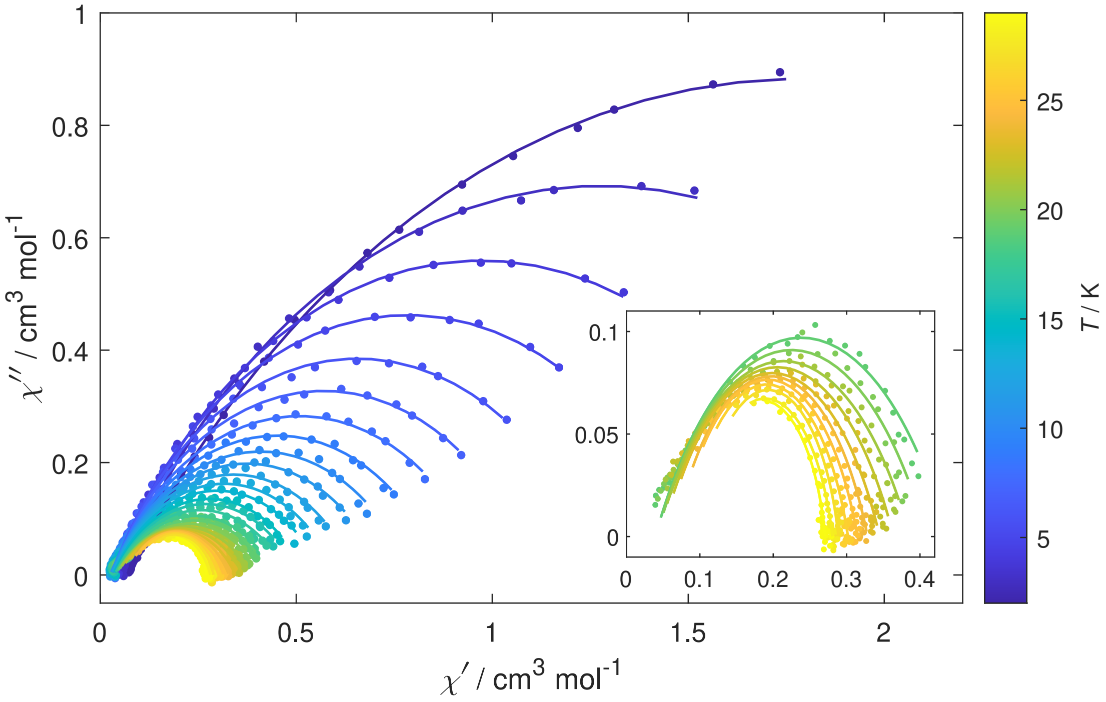

Figure 4.8: Argand plot of **(K-18-c-6)$_\mathbf{3}$[5]** at different temperatures and zero applied field. Solid lines correspond to best fits.

very good agreement which demonstrates that the whole sample participates in the slow relaxation process. Values for α of up to 0.4 indicate that there is a significant distribution in the relaxation times.

The longest extracted relaxation time is 1.7 s at 2 K. An Arrhenius plot of $\ln(\tau/\mathrm{s})$ versus T^{-1} (Figure 4.9) shows that the relaxation time τ decreases only slowly above 17 K. Between 2 K to 12 K it drops by a factor of ten and reaches a hundredth of the starting value at 21 K. Above 17 K, τ drops very fast and linearly in the plot. This linear decrease in the Arrhenius plot indicates an exponential temperature dependence above 17 K. The whole curve can be fitted very well to the sum of the terms described in Equations 2.4 and 2.5 consisting of an exponential term corresponding to the Orbach relaxation process and a power law term usually assumed to represent the Raman process:

$$\tau^{-1} = C_{\mathrm{Raman}} T^{n_{\mathrm{Raman}}} + \tau_0^{-1} \exp\left(\frac{-U_{\mathrm{eff}}}{k_{\mathrm{B}} T}\right).$$

The fits are shown as solid lines in Figure 4.9 and the extracted parameters for **(K-18-c-6)$_3$[5]** are $C_{\mathrm{Raman}} = 0.29(2)\,\mathrm{s}^{-1}\,\mathrm{K}^{-n}$, $n_{\mathrm{Raman}} = 1.20(3)$, $\tau_0 = 2.4(5) \cdot 10^{-10}\,\mathrm{s}$ and $U_{\mathrm{eff}} = 267(3)\,\mathrm{cm}^{-1}$.

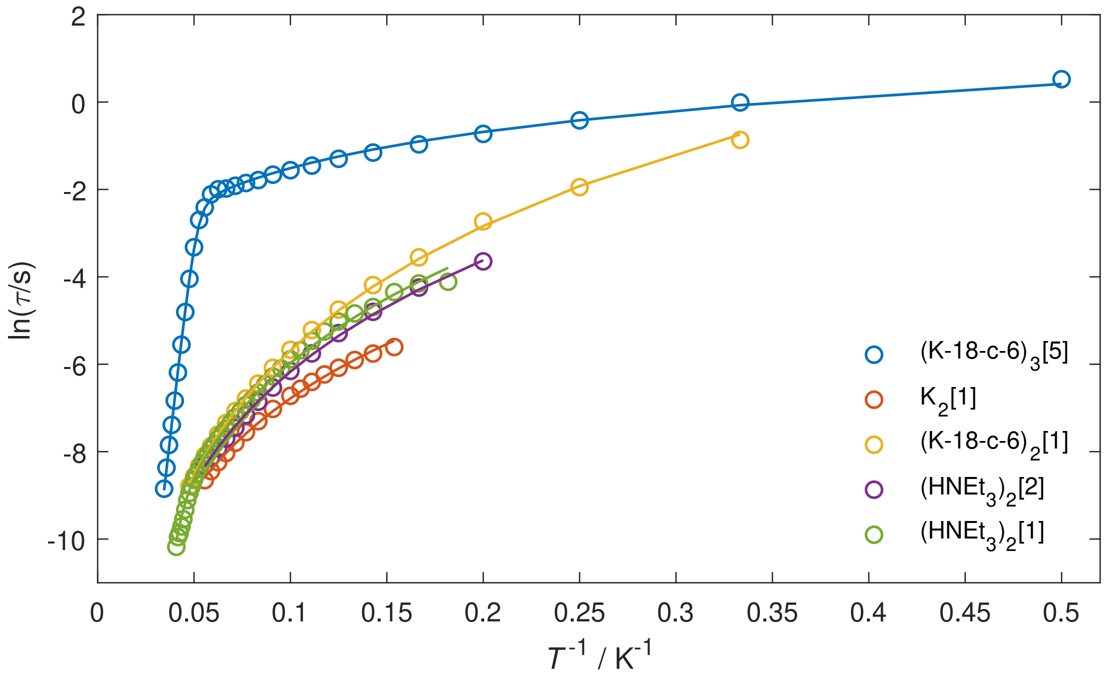

Figure 4.9: Arrhenius plot of **(K-18-c-6)$_3$[5]** and the mononuclear cobalt complexes discussed in the previous chapter. Solid lines correspond to best fits based on a combination of Orbach and Raman processes.

The effective energy barrier is very close to the value of $|2D| = 230(30)\,\mathrm{cm}^{-1}$ as determined by fitting the dc susceptibility. This is a pleasant finding as often the effective energy barrier in single-molecule magnets is found to be significantly smaller than $2D$[6, 12, 80, 84–86]. As already described in Section 3.3, n_{Raman} is expected to be between 4 and 9. The value close to 1 determined here demonstrates that the power law term does not describe a Raman process. Instead, $n = 1$ is expected for the direct process. However, this process is not expected to be active because the ground Kramers doublet is degenerate in zero field. At the same time, quantum tunneling of the magnetization, which could be another source of relaxation, is not expected to be temperature dependent as the relaxation is observed to be.

In comparison with the relaxation times of the mononuclear complexes discussed in the previous chapter, the relaxation times are generally much longer by factors of up to 560 and 320 at 17 K for **K$_2$[1]** and **(K-18-c-6)$_2$[1]**, respectively. A detailed comparison of the ratios is plotted in Figure 4.10. This difference must be caused by suppression of the Raman process which was a main cause for relaxation in the mononuclear complexes and is not present in **(K-18-c-6)$_3$[5]**.

In combination with the findings from the hysteresis measurements, whose shape suggests the presence of efficient quantum tunneling, two possible explanations for relaxation behavior are thinkable. Firstly, the relaxation can be influenced by the hyperfine interaction of the $I = {}^{7}\!/_{2}$ cobalt nuclear spin with the electron spin. Secondly, a temperature dependence of the phonon collision rate which is a factor in quantum tunneling[100] could cause the observed behavior. Regarding the first case, while tunneling cannot be induced by rhombic ZFS because **(K-18-c-6)$_3$[5]** is a Kramers system, it can be induced by transverse hyperfine interaction which may cause a sizable tunnel splitting. Additionally, the axial component may lead to level splittings without mixing, possibly activating the direct process. This direct process then leads to a temperature dependence as observed in the experiment for the relaxation time. Hyperfine values of several hundred MHz and signs of hyperfine-induced quantum-tunneling have been reported for cobalt[64]. In contrast, although manganese(III) exhibits similar hyperfine values[101], single-molecule magnets based on Mn(III) typically do not show hyperfine-induced relaxation. To clarify these observations, hysteresis measurements on aligned single-crystals of **(K-18-c-6)$_3$[5]** at ultralow temperatures might be able to demonstrate if hyperfine interaction is the cause for the observed relaxation behavior as it was shown in Ref. [64] for a different tetrahedral Co(II) complex.

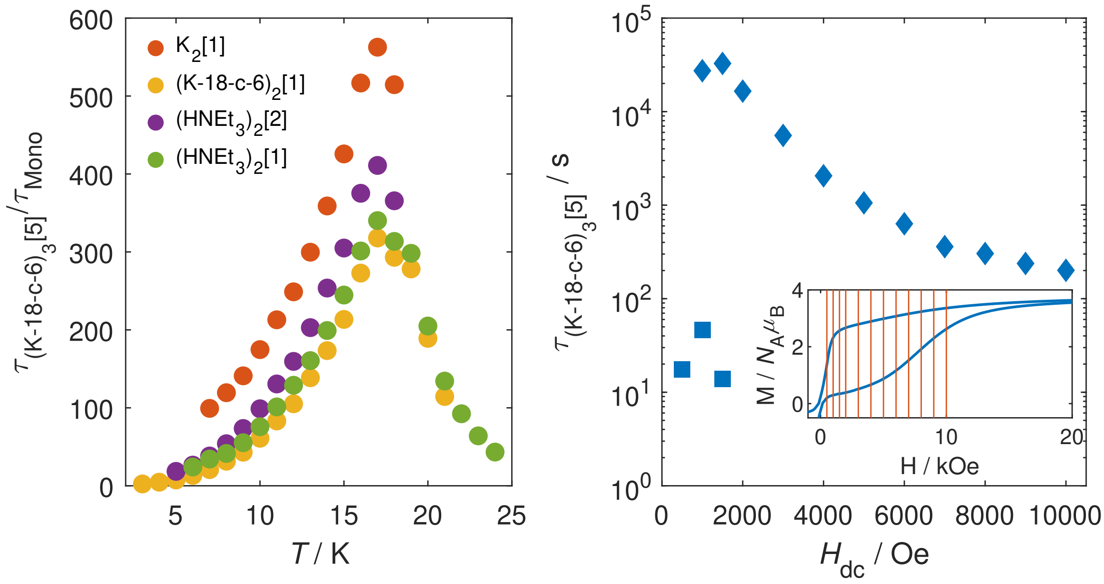

Figure 4.10: Left: Ratios $\tau_{\mathbf{(K\text{-}18\text{-}c\text{-}6)_3[5]}}/\tau_{\mathrm{Mono}}$ of the relaxation times of the dinuclear complex **(K-18-c-6)$_3$[5]** and the mononuclear cobalt complexes discussed in the previous chapter. Right: DC magnetization relaxation times at 1.8 K obtained from stretched exponential fits of the magnetization decay for **(K-18-c-6)$_3$[5]**. At low fields, two distinct fast (squares) and slow (diamond) relaxation processes are observed. The inset shows the measurement positions in the hysteresis loop.[97]

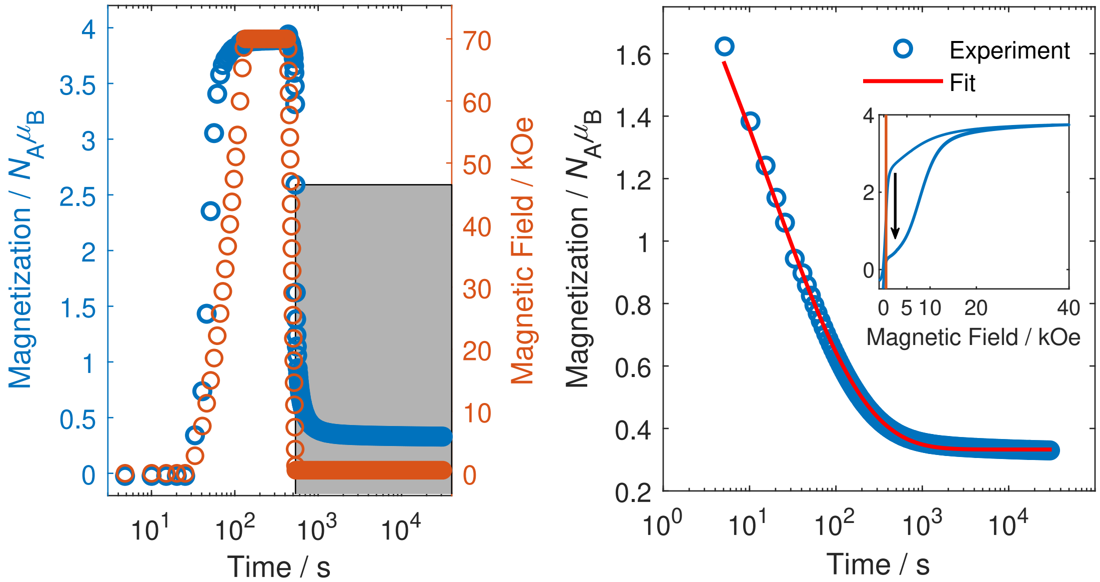

Figure 4.11: Left: Measurement sequence for the dc magnetization decay measurement at 500 Oe and 1.8 K. Data in the gray area were used for fitting and are separately shown in the right plot. Right: dc relaxation measurement of **(K-18-c-6)$_3$[5]** at 500 Oe with exponential fit. The value and fit at $t = 0$ are not visible due to the logarithmic plot type. The inset shows the position in the hysteresis loop.

The relaxation in applied fields is expected to be much slower because of the strong hysteresis. To measure this relaxation, at 1.8 K the magnetic field was first ramped to the sample's saturation limit and, after short equilibration, to the desired field at which the decaying magnetic moment was measured over the time t. A sketch of this sequence and the measurement at 500 Oe are depicted in Figure 4.11.

$$M(t) = M_1(0)\exp\left(-\left(t/\tau_1\right)^{b_1}\right) + M_\infty \tag{4.2}$$

$$M(t) = M_1(0)\exp\left(-\left(t/\tau_1\right)^{b_1}\right) + M_2(0)\exp\left(-\left(t/\tau_2\right)^{b_2}\right) + M_\infty \tag{4.3}$$

The resulting M versus t curves were fitted to stretched exponential decay functions as described in Equation 4.2. For the measurements at 1000 Oe and 1500 Oe, the sum of two stretched exponential decay functions had to be used to describe the $M-t$ curve properly (Equation 4.3). Additionally, for the measurements from 1000 Oe to 2000 Oe it was necessary to fix the M_∞ value to the expected one based on the Spin Hamiltonian to reach proper fit convergence. The measurements and fits at fields above 500 Oe are shown in Figures A.14 to A.19 with the fit results being listed in Table A.6. A plot of the relaxation times can be seen in Figure 4.10.

The resulting stretch factors b of roughly 0.4 to 0.5 indicate that there is a significant distribution in the relaxation times. The necessity to use a biexponential model at 1000 Oe and 1500 Oe demonstrates that at these fields there are two dominant relaxation processes. The biexponential model is further justified by the observation that the two processes differ significantly in their relaxation times and that the relaxation times from the combined model are in the same order of magnitude as the corresponding relaxation times at higher and lower fields where a single decay was used for fitting.

The relaxation times in applied field of the fast process are in the range from 14 s to 46 s. The slow process, however, has relaxation times of above 15 000 s (ca. 4 h) between 1000 Oe and 2000 Oe with a maximum of 32 736(6) s (ca. 9 h) at 1500 Oe which decrease to 201(1) s at 10 000 Oe. Compared to relaxation times of current state of the art transition metal SMMs the relaxation time in applied fields is much longer. For example, in $Co(C(SiMe_2ONaphthyl)_3)_2$ 660 s were reported under the same conditions[34]. Table 4.1 lists a comparison of radical ligand-containing single molecule magnets demonstrating that **(K-18-c-6)$_3$[5]** excels by exhibiting the best combination of air and moisture sensitivity and relaxation times.

Table 4.1: Overview of radical ligand-containing single-molecule magnets. A review can be found in Ref.[7] Values are quoted for best SMM in class.[97]

Compound	ZF slow relaxation	J / K	U_{eff} / K	τ / s at ca. 2 K	air sensitivity	Lit.
$(\textbf{K-18-c-6})_3[\textbf{5}]$	Yes	633	331	1.7 (0 Oe) $3.2 \cdot 10^4$ (1.5 kOe)	air and moisture stable	this work
$[(\text{TPyA})_2\text{Fe}_2{}^{\text{II}}(\text{L-NPh}^{2\text{-}})]^{2+}$	Yes	>2500	72	0.01 (0 Oe)	air sensitive(a)	[41]
$(\text{NMe}_4)_2[\text{LFeCl}_2]$(b)	Yes	233	79	0.2 (0 Oe)	air sensitive(a)	[102]
$[\text{Co}(\text{R-hfpip})_2(\text{D2py}_2(\text{TBA}))]_2$(c)	Yes	n/a	139	$5.4 \cdot 10^5$ (0 kOe)	very air sensitive(a)	[103, 104]
$[(\text{CoTPMA})_2\text{-}\mu\text{-bmtz}^{\cdot-}](\text{O}_3\text{SCF}_3)_3{\cdot}\text{CH}_3\text{CN}$	No	180	39	0.009 (800 Oe)	likely air sensitive(a)	[105]
$[(\text{dmp}_2\text{Nin})\text{Co}_2(\text{N}(\text{SiMe}_3)_2)_2(\text{Et}_2\text{O})_2]^+$	No	199	37	0.05 (1.2 kOe)	air sensitive(a)	[106]
$[\text{Co}_2(\text{tphz})(\text{tpy})_2](\text{PF}_6)_3$	No	>1400	–	0.00013 (600 Oe)	air sensitive(a)	[107]
$[\text{K}(18\text{-c-}6)][((\text{Me}_3\text{Si})_2\text{N})_2(\text{THF})\text{Ln}]_2(\text{N}_2)$	Yes	78(d)	327(e)	$5.2 \cdot 10^4$ (0 Oe)(f)	very air sensitive(a)	[36, 37]
$[(\text{Cp*}_2\text{Dy})_2(\mu\text{-bpym})][\text{BPh}_4]$	Yes	29	126	2 (0 Oe)(f)	very air sensitive(a)	[39]
$[\text{Dy}(\text{hfac})_3(\text{boaDTDA})]_2$	Yes	n/a	102	0.00014 (0 Oe)	air sensitive(a)	[108]
$[\text{Dy}_3(\text{hfac})_6(\text{bptz}^{\cdot-})_3]$	Yes	9.5(g)	60	0.02 (0 Oe)	air sensitive(a)	[109]
$\text{Cp}_2\text{Co}[\text{Dy}(\text{tmhd})_3]_2(\text{bptz})$	Yes	n/a	12	0.008 (0 Oe)	air stable	[110]
$[\text{Dy}_4(\mu_3\text{-OH})_4(\text{BPyTz}^{\cdot-})_2(\text{TFA})_2(\text{DBM})_4)]_4$	Yes	n/a	31	0.01 (0 Oe)	air stable	[111]

(a) No direct discussion of the sensitivity can be found in the paper. The description of synthesis and physical measurement precautions in the supplementary information, as well as the strong reduction agent used, suggest the compound is air sensitive.

(b) This is a single-chain magnet, for which the energy barrier derives from a combination of zero-field splitting and exchange interaction. Thus, a comparison to single-molecule magnet (energy barrier derives solely from zero-field splitting) is not really valid.

(c) These are poorly defined, non-isolable metal-carbene species generated by in situ photoirradiation at low temperatures.

(d) For Ln=Gd (e) For Ln=Er (f) At ca. 7 K (g) From ab initio calculations

4.4. Spectroscopy

As discussed in the previous chapter, far-infrared spectroscopy in magnetic field could yield a value for the zero-field splitting of the mononuclear complexes which is significantly more precise than the estimate based on magnetometry. Consequently, far-infrared spectroscopy was also applied to the radical-bridged dinuclear compound. The spectra were recorded by Dr. Milan Orlita (Laboratoire National des Champs Magnétiques Intenses, Grenoble) at a temperature of 4 K and magnetic fields up to 11 T. The transmission spectra, where every measurement was divided by the reference measurement at the same field, and the normalized transmission spectra, where every transmission spectrum was divided by the measurement at 0 T, are shown in Figures 4.12 and 4.13. The reference measurements were obtained under the same conditions as the sample measurements but instead of the sample an aperture was placed in the beam path. The aperture reduced the diameter of the beam path which was necessary to reduce the intensity of the incident light on the detector element to prevent it from being damaged by overload.

A clearly field-dependent feature is located at about 419 cm^{-1}. Additionally, a weak feature is observed around 236 cm^{-1} but a clear field dependence cannot be identified. Also, the feature's intensity does not exceed the noise significantly. Overall, the signal-to-noise ratio of both features is poor. The field dependence of the signals is depicted in Figure A.20 in more detail. The possible signal at 236 cm^{-1} would fit very well to the observations in the mononuclear complexes where zero-field splittings in the range around 230 cm^{-1} were observed. The signal at 419 cm^{-1} demonstrates that the coupling of the cobalt-radical-cobalt system leads to new states with significantly higher energy compared to the mononuclear system. Using the Spin Hamiltonian and determined parameters for **(K-18-c-6)$_3$[5]** as described in the previous section to calculate the energy levels yields Kramers doublets where the lowest in energy are located at 235 cm^{-1}, 308 cm^{-1}, 389 cm^{-1}, 421 cm^{-1} and 662 cm^{-1} with respect to the ground state. The first and fourth of these energies fit very well to the ones observed by FIR spectroscopy. Additionally, the reference measurements (Figure A.21) show baseline features at 315 cm^{-1} and 382 cm^{-1} which could hide signals with low intensities as they are observed here. A repetition of the FIR measurements aiming for a better signal-to-noise ratio could yield a better insight. However, a simulation of the FIR spectra based on the Spin Hamiltonian parameters did not yield a satisfying match with the experimental spectra as only the transition at 235 cm^{-1} seems to be allowed.

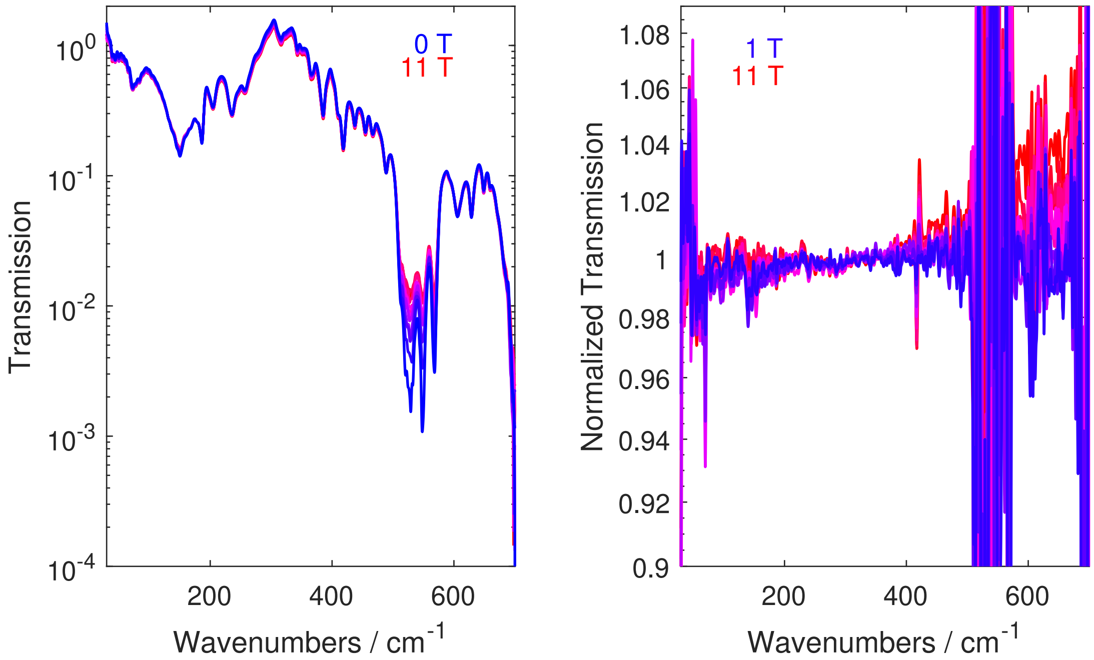

Figure 4.12: Left: FIR transmission spectra of $\mathbf{K_2[1]}$ at 4.2 K and magnetic fields between 0 T and 11 T. Right: Normalized FIR transmission spectra obtained by dividing each transmission spectrum by the transmission spectrum at zero field.

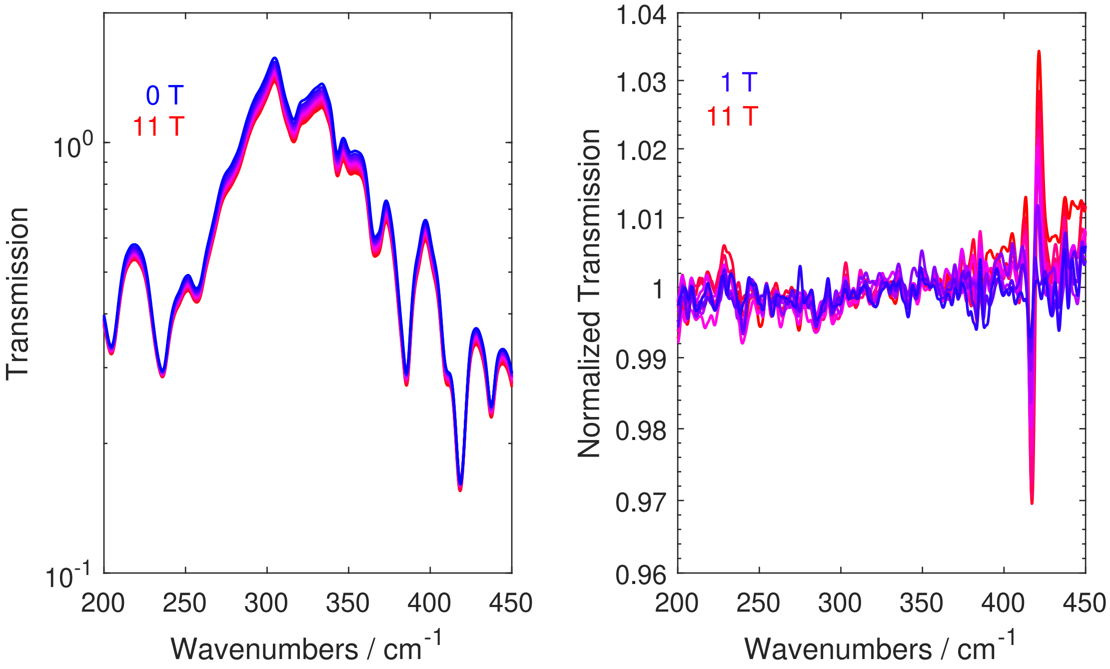

Figure 4.13: Left: FIR transmission spectra of $\mathbf{K_2[1]}$ at 4.2 K and magnetic fields between 0 T and 11 T. Right: Normalized FIR transmission spectra obtained by dividing each transmission spectrum by the transmission spectrum at zero field. Both Figures are zoomed on the field-dependent features.

An alternative way to explain the main feature at 419 cm^{-1} based on $D \approx 115\,\mathrm{cm}^{-1}$ of the mononuclear compound might be an anisotropic coupling constant. The use of such can shift the simulated main feature to higher energies. A proof of this would be an exceptional finding because up to now FIR spectroscopy was not used to determine the anisotropy of a coupling constant. However, the proof could not be achieved in the scope of this work.

As an additional step in characterization, MCD was measured. The aim behind this was to gain insight into the electronic structures and to compare it with the mononuclear compounds'. Based on the negligible structural changes around the cobalt ions and the energies which correlate to the electronic structure compared to the coupling strength, a significant change in the electronic structure is not expected. A comparison of these measurements is shown in Figure 4.14.

Overall, the peak positions remain nearly unchanged. The most obvious difference in the spectra are the relative signal intensities. In the mononuclear compounds $(HNEt_3)_2$[1] and **K$_2$[1]** the peak close to 18 000 cm^{-1} has the highest absolute intensity by a factor of six compared to the features in the near-infrared region at about 7000 cm^{-1}. However, in **(K-18-c-6)$_3$[5]** this feature's intensity is smaller

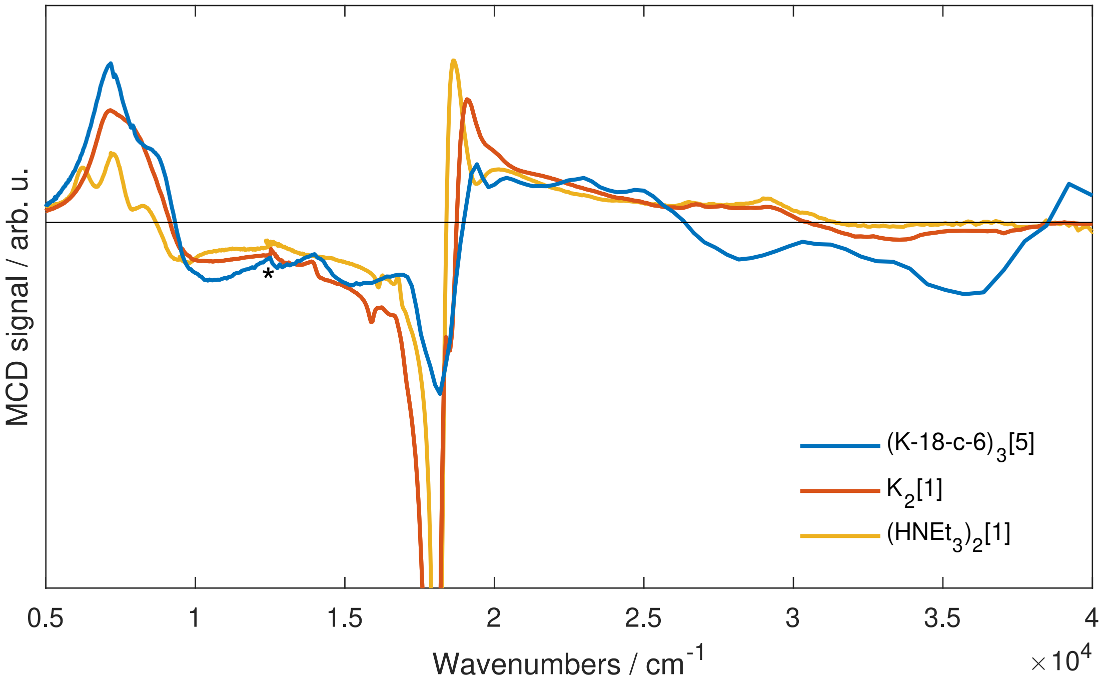

Figure 4.14: Scaled magnetic circular dichroism spectra at 1.5 K of **(K-18-c-6)$_3$[5]** at 3 T (blue), **K$_2$[1]** (red) at 4 T and $(HNEt_3)_2$[1] (yellow) at 2 T. The asterisk marks the artifact due to the detector change.

and comparable to the intensity of the near-infrared features. Additional signals with comparable intensity can be observed in the UV and visible region between 20 000 cm^{-1} and 40 000 cm^{-1} which are also present in the spectra of the mononuclear compounds but of much smaller relative intensity. Further investigation of the spectra was not performed in the scope of this work.

4.5. Summary and Conclusion

In this chapter, the magnetometric and spectroscopic investigation of the first radical-bridged dinuclear cobalt complex **$(\mathbf{K\text{-}18\text{-}c\text{-}6})_3$[5]** was presented. The magnetic properties of this compound differ significantly from those of its mononuclear building block. While the static properties simply correspond to an antiferromagnetically coupled system of the building blocks to the bridging radical, the dynamic magnetic properties are drastically changed. The magnetic relaxation times in zero field at 2 K increased to 1.7 s which corresponds to one order of magnitude compared to the mononuclear complex **$(\mathbf{K\text{-}18\text{-}c\text{-}6})_2$[1]**. Over the whole temperature range up to 20 K, the relaxation time increased by a factor of up to 320. The maximum observed relaxation time is about 9 h at an applied field of 1500 Oe.

It could be demonstrated that the reason for the prolonged relaxation times is a strong suppression of the Raman relaxation process caused by the exchange coupling. At the same time, true magnetic hysteresis could not be observed and hyperfine interactions appear to be the limiting factor of the magnetic relaxation. Investigations on single crystals at ultra-low temperatures could clarify the influence of the hyperfine interaction but could not be carried out in scope of this work.

FIR spectroscopy revealed a surprising shift of the main signal to larger energies and possible explanations are given in the corresponding section. A definite analysis could not be achieved due to experimental issues and lack of sample.

It was shown by MCD spectroscopy that the electronic structure does not change drastically by going from mono- to dinuclear but transition probabilities seem to be influenced by the changed system.

Overall it can be concluded that the aim of improving SMM properties by constructing strongly exchange coupled multispin system from known SMM building blocks has been successful. Further improved properties can likely be achieved by extending the exchange coupled systems to larger radical-bridged complexes and clusters.

5. Iron Extraction from a Podzol Extract with the Biogenic Ligand Desferrioxamine B

The project presented below was part of a collaboration with Dr. Walter Schenkeveld (Department of Environmental Geosciences, Universität Wien, now: Department of Environmental Science, Wageningen University) and his coworkers who supplied and synthesized the investigated samples. ICP-MS measurements for determination of the sample compositions were performed by Dr. Joachim Opitz (Institut für Mineralogie und Kristallchemie, Universität Stuttgart). Mössbauer spectra were measured by Dr. James Byrne in the group of Prof. Andreas Kappler (Zentrum für Angewandte Geowissenschaften, Eberhardt Karls Universität Tübingen). HFEPR and SQUID measurements of **B9**, **DFOB24h** and **FeDFOB** were performed by Monika Schneider as part of her teacher's thesis under supervision of Petr Neugebauer (Institut für Physikalische Chemie, Universität Stuttgart, now: Central European Institute of Technology, Brno). All other presented measurements were performed as part of this work.

The aims of this work are explained in the next section. Section 5.2 introduces and justifies the used methods. An overview of the investigated samples and discussion of the individual EPR and magnetometric measurements is given in Section 5.3. A comparative discussion based on these measurements and Mössbauer spectroscopy is presented in Section 5.4 followed by the summary and conclusion in Section 5.5.

5.1. Aims

Iron is an essential micronutrient for plants. Though it is heavily abundant in many soils, its bio-availability is often limited due to the poor solubility of iron-containing species. Some organisms in nature cope with this situation by releasing chelating ligands with a high affinity for iron to their environment, so-called siderophores. These ligands form highly stable complexes with naturally abundant iron from different pools such as soil solution, dissolved organic matter and even minerals. Due to the importance of iron for plant growth, this situation makes it a meaningful topic to investigate the process of iron extraction from soil, potentially leading to a better understanding of ways to increase the bio-availability of iron by fertilization with siderophores[112].

For this purpose, the iron extraction from a podzol soil extract by the biogenic, microbial ligand desferrioxamine B (DFOB) was analyzed by a variety of methods including Mössbauer and high frequency EPR spectroscopy as well as magnetometry. The aim of the investigation was to find out which insights into the extraction process (i. e. complexation of iron by DFOB) can be generated by this set of methods and if iron pools in the soil extracts can be identified which are preferentially targeted by DFOB.

5.2. Selection of Methods

Three methods were chosen for detailed investigation of the samples. These are high-frequency EPR (HFEPR) spectroscopy, SQUID magnetometry and Mössbauer spectroscopy. Mössbauer spectroscopy is an obvious choice for investigating iron species because of its absolute selectivity for this element by using ^{57}Co as radiation source. HFEPR was chosen due to its high resolution and selectivity for species with unpaired electrons (see Section 2.4.2). SQUID magnetometry is also selective for species with unpaired electrons and yields thermodynamically averaged quantities (Section 2.4.1). The selectivity for all species with unpaired electrons simultaneously is not a limitation here as all relevant species consist mainly of diamagnetic atoms plus iron (see Table 5.1). Beside these substances, only negligible amounts of additional magnetic species are present.

5.3. Investigated Systems

A set of 11 samples consisting of soil extracts, some of which were treated with the biogenic ligand desferrioxamine B (DFOB), the reference compound **FeDFOB** and reference minerals was investigated.

Sample Overview

Three of the samples (**B9**, **BUPW** and **BUPW9**) are pure soil extracts. After drying, homogenizing and sieving with a 2 mm mesh, organic and inorganic nanoparticles were extracted from them with ultra-pure water at a natural pH value of about 4 (**BUPW** and **BUPW9**) and at a set pH value of 9 (**B9**). The suspensions were then centrifuged, filtered (0.2 µm) and freeze-dried. For **BUPW9**, the resulting solid was later dissolved in water, the solution brought to pH 9, again filtered (0.2 µm) and freeze-dried.

Comparison within the set of the three pure soil extracts **B9**, **BUPW** and **BUPW9** is expected to improve the understanding of the composition of **B9** and effects of different acidity during the sample extraction from soil. This could prove useful as basis for identifying possible targeted iron pools by complexation with DFOB.

DFOB5m, **DFOB4h** and **DFOB24h** are samples where an excess of the siderophore desferrioxamine B (DFOB) was reacted with the **B9** solution for 5 minutes, 4 hours and 24 hours, respectively, as indicated in the sample names.

FeDFOB is the pure iron complex of DFOB which was synthesized from DFOB mesylate salt and $FeCl_3$.

The set of **B9** as reference sample before complexation, **DFOB5m**, **DFOB4h** and **DFOB24h** representing different extraction times and **FeDFOB** as pure complexed product allows for an analysis of the extraction process. It is intended to yield insight into extraction kinetics and effects caused by different complexation times, for example the nature of targeted iron pools, and is discussed in Section 5.4.1.

Goethite, **hematite**, **2-line ferrihydrite** and **6-line ferrihydrite** are typical minerals for the soil where the extracts originate from. They were investigated to assess their possible presence in the soil extracts **B9** and **BUPW** and if they can be identified as possible targeted iron pools.

More details about the preparation of all samples can be found in Section 6.1.2.

Composition of Samples and Normalization of Obtained Data

The compositions of both the pure and treated soil extracts were determined by inductively coupled plasma mass spectrometry (ICP-MS) and are listed in Table 5.1. The composition of **BUPW9** could not be determined because of its very limited available sample amount. **FeDFOB** was analyzed in a different context, thus,

Table 5.1: Composition of the soil extracts in weight percentages.

Ion/Material	**B9**	**BUPW**	**DFOB5m**	**DFOB4h**	**DFOB24h**	**FeDFOB**
Ca	0.1 %	0.4 %	0.1 %	0.0 %	0.0 %	
Na	11.9 %	0.4 %	9.2 %	7.5 %	7.5 %	>18.9 %
Al	1.9 %	5.9 %	1.5 %	1.2 %	1.2 %	
Fe	1.8 %	3.1 %	1.4 %	1.1 %	1.1 %	2.3 %
Si	0.1 %	1.4 %	0.1 %	0.1 %	0.1 %	
P	0.6 %		0.4 %	0.4 %	0.4 %	
S	0.2 %		0.1 %	0.1 %	0.1 %	
C						23.4 %
H						4.1 %
N						12.5 %
DOM	83.3 %	88.0 %	87.0 %	89.5 %	89.5 %	
Sum	99.9 %	99.1 %	99.9 %	99.9 %	99.9 %	

DOM: dissolved organic matter

only the contents of iron an sodium were determined by ICP-MS. Its contents of carbon, nitrogen and hydrogen were determined by elemental analysis.

According to the ICP-MS data, iron is the only potentially paramagnetic element in the samples which occurs in significant amounts. Thus, any paramagnetic signals in magnetometric or EPR measurements can be attributed to iron species or organic radicals, e. g. from humic acid. As a consequence and because of the limited knowledge about the samples' precise composition, data were referenced to the mass-wise iron content (weight-%) of the samples wherever it was available.

5.3.1. B9

B9 is the pure soil extract from a the B horizon of a podzol taken close to Schrems (Waldviertel, Lower Austria) for which a pH value of 9 was set during extraction.

Magnetometric Measurements

The magnetometric measurement of **B9** is presented in Figure 5.1. The temperature dependence of the product of the magnetic susceptibility χ with the temperature T shows its maximum value of $0.083\,\mathrm{cm^3\,K\,g_{Fe}^{-1}}$ at 300 K. Below 300 K, χT decreases gradually with decreasing temperature down to $0.066\,\mathrm{cm^3\,K\,g_{Fe}^{-1}}$ at 25 K. Below that, χT drops strongly to $0.025\,\mathrm{cm^3\,K\,g_{Fe}^{-1}}$ at 1.8 K.

The plot of the susceptibility of the zero field cooled (ZFC) and field cooled (FC) measurements versus the temperature reveals a difference between both measurements' values at low temperatures, indicating slow relaxation of magnetization in the sample. No blocking temperature T_B could be observed down to 1.8 K but an irreversibility temperature T_IRREV of 16 K. The large difference between T_B and T_IRREV means that the distribution of relaxation times is rather large. This is most probably caused by a broad range of particle sizes present in the sample.

To further investigate the time scale of slow relaxation of magnetization, dynamic susceptibility measurements in zero field and under applied field were performed. The resulting data are plotted in Figures 5.2 and A.22. At 1.8 K, where the effect should be most distinct, no out-of-phase signal and, thus, no slow relaxation of magnetization could be observed, neither at zero field nor at applied fields up to 2000 Oe. The most probable explanation for this is that the relaxation in the static measurement happens on a slower time scale than it is measured in this dynamic measurement.

HFEPR Measurements

Temperature dependent high-frequency EPR (HFEPR) spectra of **B9** were measured at 340 GHz and are shown in Figure 5.3. All measurements exhibit temperature dependent peaks at 6.05 T, 8.05 T and 12.08 T. Those two at lower fields are very weak in intensity and the peak at 12.08 T, which corresponds to a g-value of 2.01, dominates the spectrum. The signal around 8 T is very likely caused by a higher harmonic of the frequency synthesizers base frequency, which the spectrometer is known to produce for very intense signals at two-thirds of the transition field with the frequency multiplier used for this measurement. Additionally, the measurements between 10 K and 22 K show features that are located at 11.38 T and 12.36 T at 10 K. They are of low intensity compared to the main peak as can be seen in the inset in Figure 5.3 but significantly more intense than the other two mentioned peaks. With increasing temperature, they move closer to the main peak at 12.08 T. At 40 K and above, these features have merged with the main peak. Looking at the measurements at 10 K and 12 K, it can be seen that this small difference in temperature of 2 K has a considerable effect on the position of the peaks around the main peak, demonstrating that there is a very strong temperature dependence of these peaks. A similar effect has been observed in EPR spectra of magnetic nanoparticles[113–115]. It is caused by the transition of magnetic

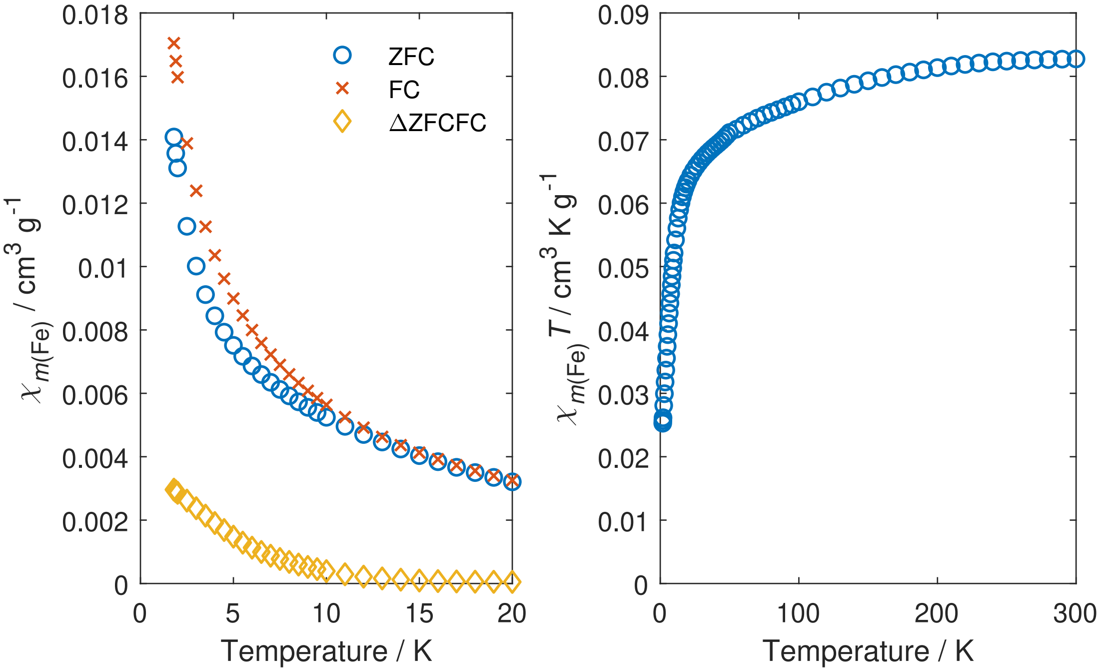

Figure 5.1: Left: ZFC and FC measurements of **B9**. Right: Temperature dependence of the susceptibility temperature product χT of **B9**. All susceptibilities are referenced to the sample's iron content.

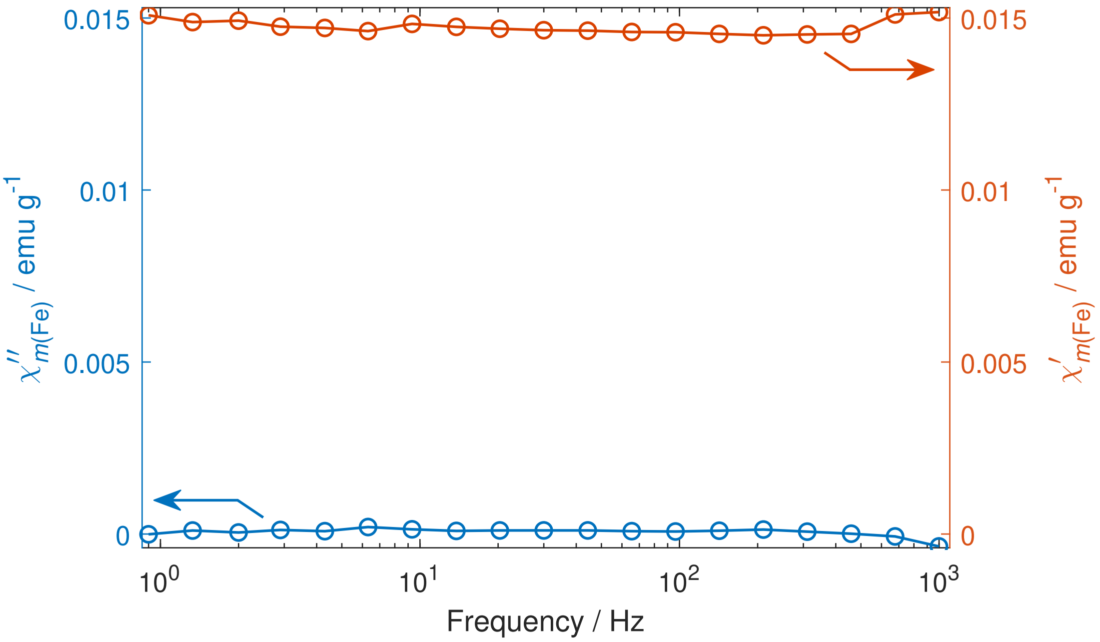

Figure 5.2: In-phase and out-of-phase susceptibility of **B9** at 1.8 K and frequencies as indicated at zero applied static field. Solid lines are guides for the eye. The data are referenced to the sample's iron content.

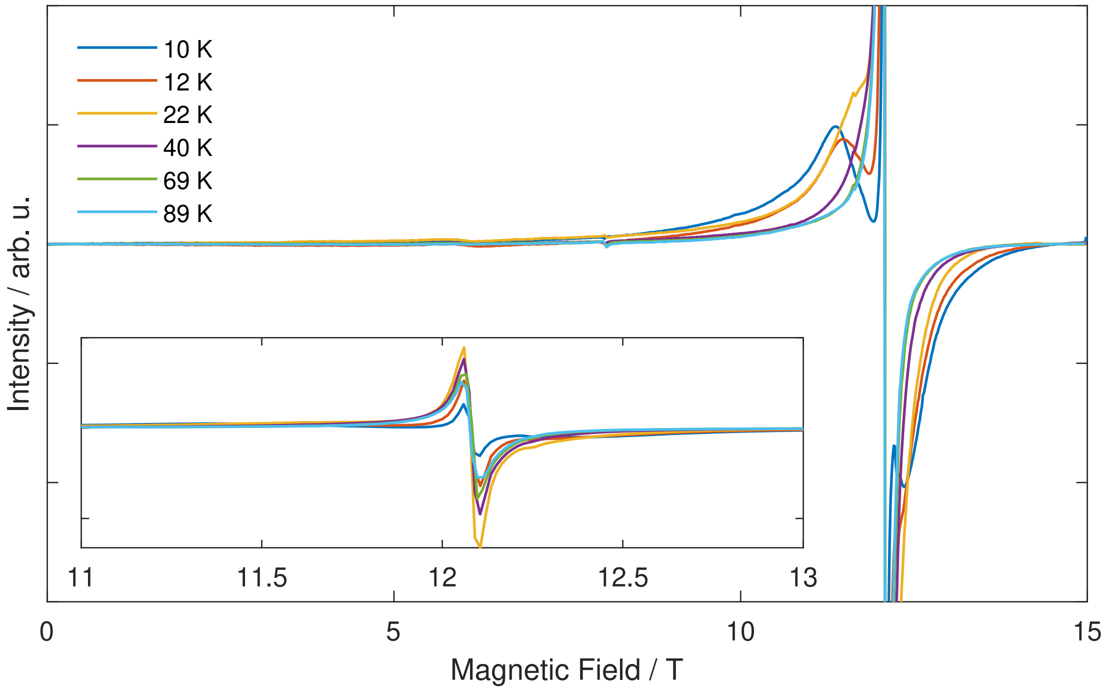

Figure 5.3: High-frequency EPR spectra of **B9** at 340 GHz and temperatures as indicated. The inset shows the complete main feature around 12.08 T.

nanoparticles from a superparamagnetic state to a magnetically ordered state with decreasing temperature. Thereby, anisotropy fields of the nanoparticles become more effective which changes the resonance position. For all soil samples in this work it is very reasonable to assume that relevant amounts of magnetic nanoparticles causing the observed behavior are present because of the used preparation procedure.

5.3.2. BUPW

BUPW is the pure soil extract from a the B horizon of a podzol with ultra-pure water resulting in a pH value of 4.

Magnetometric Measurements

Figure 5.4 shows the magnetometric measurement of **BUPW**. The plot of χT against the temperature exhibits a saturation value of 0.041 $\mathrm{cm^3\,K\,g_{Fe}^{-1}}$ at 300 K which is virtually constant down to approximately 200 K and decreases gradually

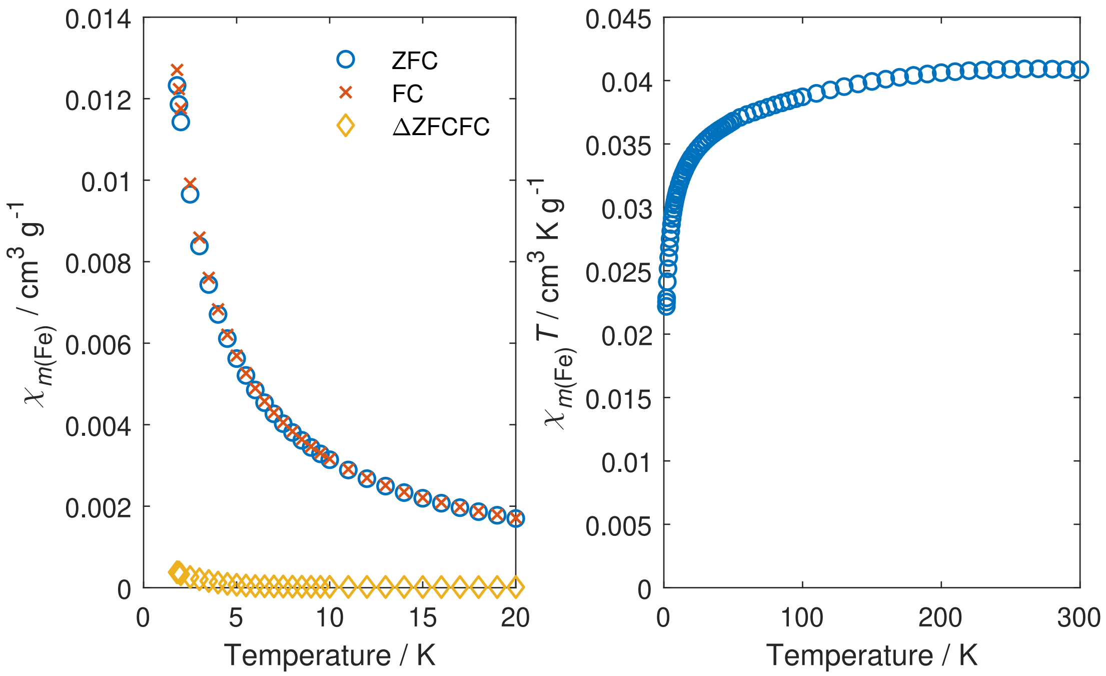

Figure 5.4: Left: ZFC and FC measurements of **BUPW**. Right: Temperature dependence of the susceptibility temperature product χT of **BUPW**. All susceptibilities are referenced to the sample's iron content.

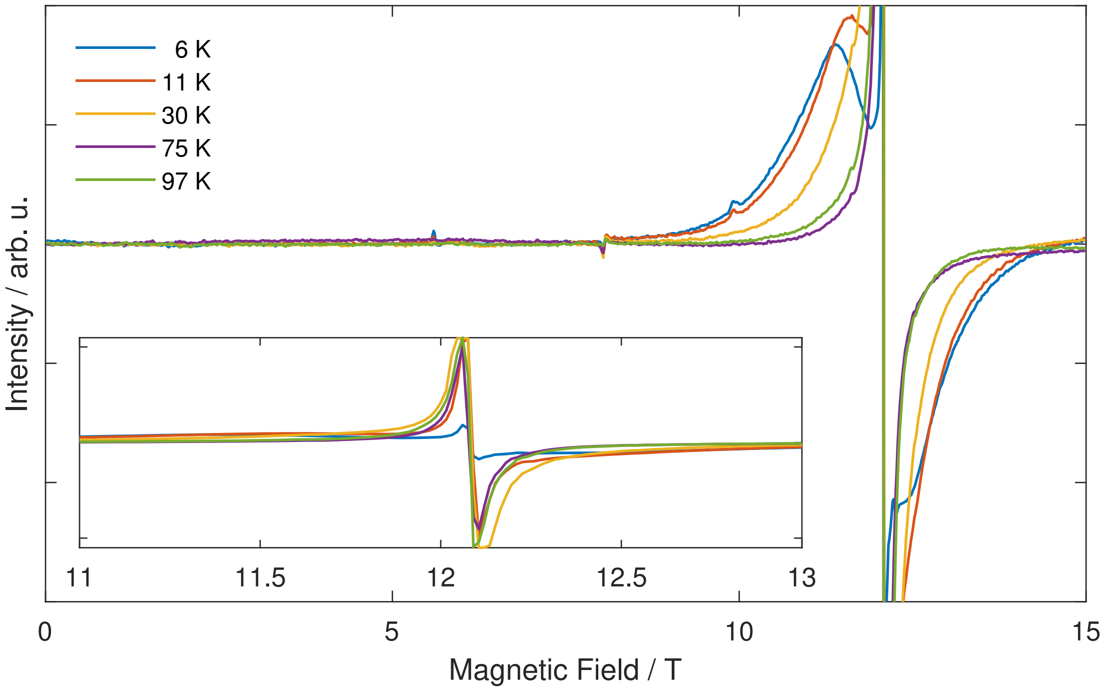

Figure 5.5: High-frequency EPR spectra of **BUPW** at 340 GHz and temperatures as indicated. The inset shows the complete main feature close to 12 T.

from there to $0.035\,\mathrm{cm^3\,K\,g_{Fe}^{-1}}$ at 30 K. At lower temperatures, χT drops strongly to $0.022\,\mathrm{cm^3\,K\,g_{Fe}^{-1}}$ at 1.8 K.

A very small difference between FC and ZFC measurements is observed at very low temperatures, indicating slow relaxation of magnetization. Compared to **B9**, this difference is much smaller and T_{IRREV} is significantly lower at 8 K. Again, no blocking temperature can be determined from the measurements down to 1.8 K and a large distribution of relaxation times can be assumed.

HFEPR Measurements

Temperature dependent high-frequency EPR spectra of **BUPW** were measured at 340 GHz and are shown in Figure 5.5. Overall, they are quite similar to the ones measured of **B9**. All measurements exhibit temperature dependent peaks at 5.60 T, 8.05 T and 12.08 T of which the one at 12.08 T ($g = 2.01$) has by far the highest intensity. Additional peaks in the measurements at 6 K and 11 K are located around the main feature at 11.39 T and 12.36 T at 6 K. For higher temperatures, these peaks move closer to the main feature and merge with it. These peaks are of lower intensity compared to the main feature, though, at 6 K the intensity ratio is only about 1:2.

5.3.3. BUPW9

BUPW9 is the pure soil extract prepared like **BUPW**. Additionally, after separation from the soil and drying, the extract was dissolved again in water and the pH value set to 9 before filtration and drying it again.

Magnetometric Measurements

Magnetometric measurements of **BUPW9** are reported in Figure 5.6. The χT curve's saturation value is $0.000\,38\,\mathrm{cm^3\,K\,g_{sample}^{-1}}$. This value is virtually constant down to 60 K from where it decreases slowly to reach $0.000\,33\,\mathrm{cm^3\,K\,g_{sample}^{-1}}$ at 12 K. The bump around 50 K can be explained by an oxygen impurity in the measurement chamber[116]. Below 12 K, χT decreases rapidly to $0.000\,29\,\mathrm{cm^3\,K\,g_{sample}^{-1}}$ at 1.8 K.

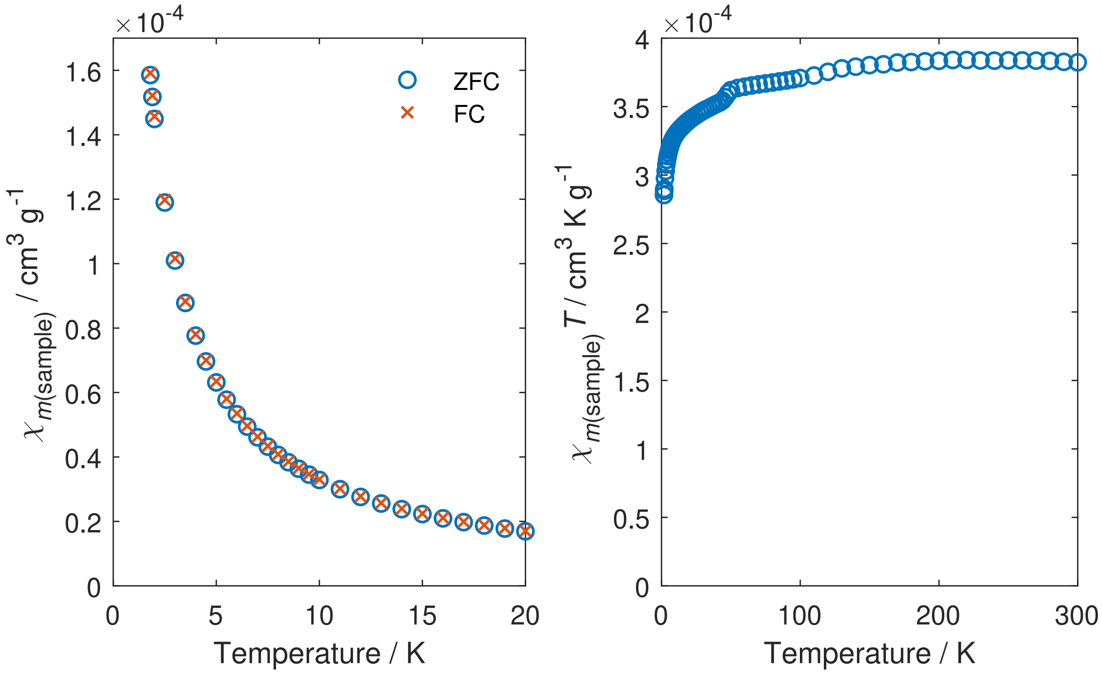

Figure 5.6: Left: ZFC and FC measurements of **BUPW9**. Right: Temperature dependence of the susceptibility temperature product χT of **BUPW9**. All susceptibilities are referenced to the sample's mass.

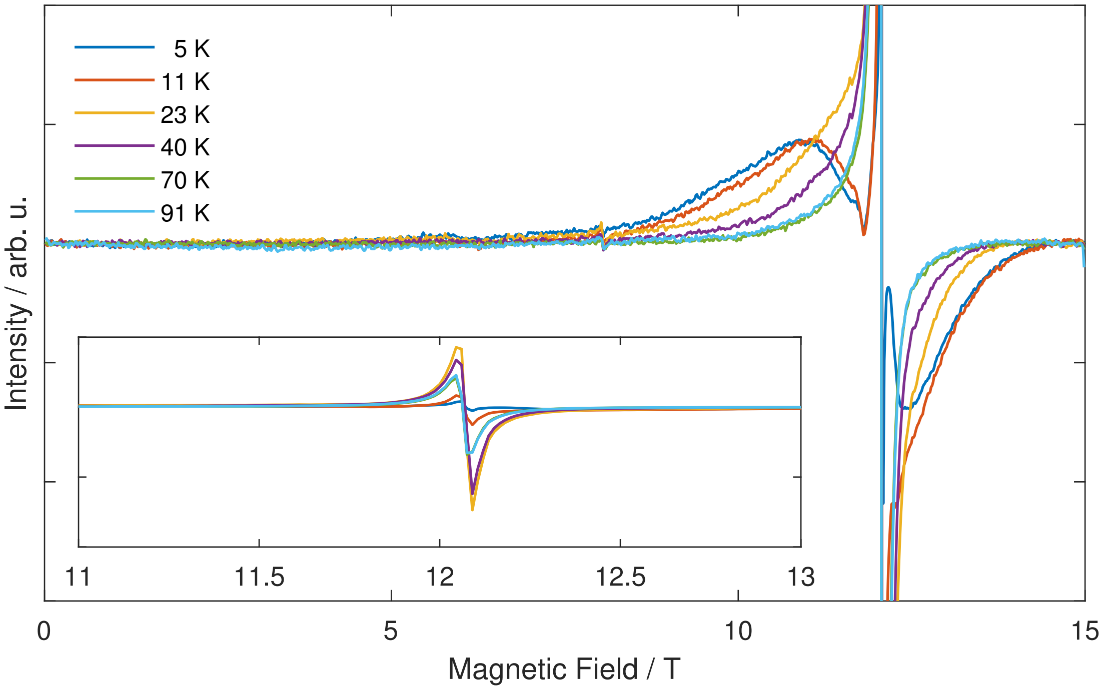

Figure 5.7: High-frequency EPR spectra of **BUPW9** at 340 GHz and temperatures as indicated. The inset shows the complete main feature close to 12 T.

Comparison of the FC and ZFC measurement shows no difference in between them, indicating the absence of slow relaxation of magnetization at these temperatures, in contrast to **B9** and **BUPW**.

HFEPR Measurements

Temperature dependent high-frequency EPR spectra of **BUPW9** were measured at 340 GHz and are shown in Figure 5.7. A very weak temperature dependent feature is observed at 8.05 T in all measurements and a very intense one at 12.06 T. Comparably weak features around the main peak at 10.95 T and 12.44 T are observed in the measurements at 5 K and 11 K which merge with the main feature at higher temperatures. Differently to the measurements of **B9** and **BUPW**, the temperature dependence of the peak at 10.95 T is much less pronounced.

5.3.4. DFOB5m

DFOB5m is a sample from **B9** which was allowed to interact with the DFOB ligand for 5 minutes in aqueous solution.

Magnetometric Measurements

Figure 5.8 shows the magnetometric measurements of **DFOB5m**. The χT value saturates at $0.078\,\mathrm{cm^3\,K\,g_{Fe}^{-1}}$ at 300 K. With decreasing temperature it decreases gradually to $0.061\,\mathrm{cm^3\,K\,g_{Fe}^{-1}}$ at 20 K. From there it drops strongly to $0.026\,\mathrm{cm^3\,K\,g_{Fe}^{-1}}$ at 1.8 K The bump around 50 K can be explained by an oxygen impurity in the measurement chamber[116].

The FC and ZFC measurements do not coincide below $T_{\mathrm{IRREV}} = 15\,\mathrm{K}$ indicating slow relaxation of magnetization below that temperature. As for **B9**, a blocking temperature could not be identified in the investigated temperature range, suggesting a large distribution of relaxation times. Overall, the measurements of **DFOB5m** are at low temperatures very similar to those of **B9** which is discussed in Section 5.4.1.

HFEPR Measurements

Temperature dependent high-frequency EPR spectra of **DFOB5m** were measured at 340 GHz and are shown in Figure 5.9. Weak features are observed at 6.14 T and

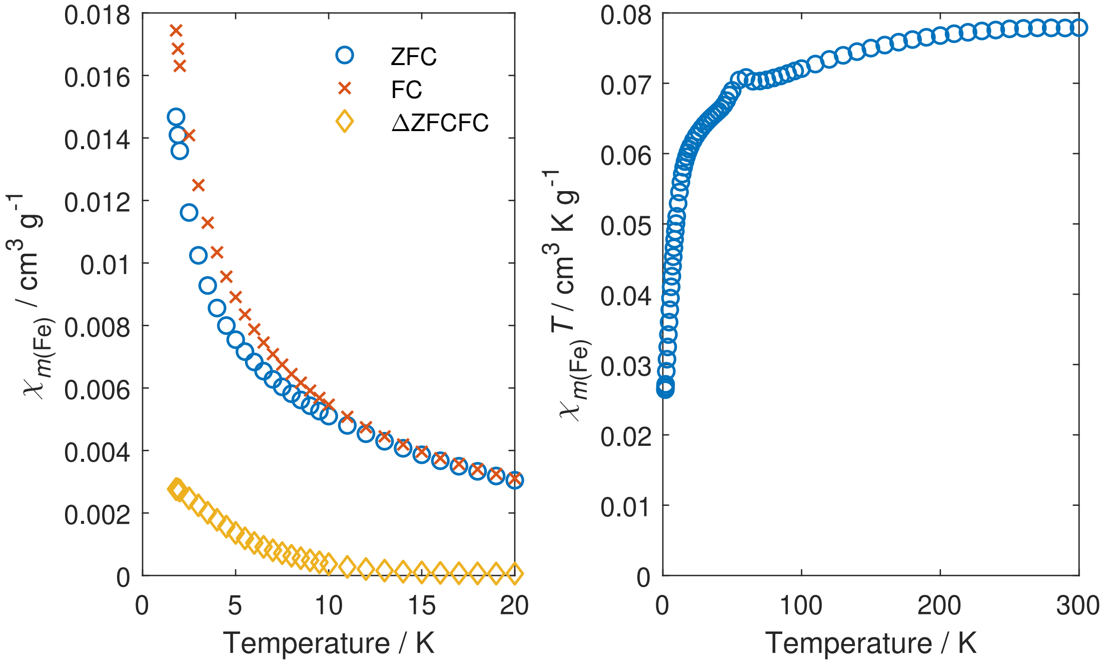

Figure 5.8: Left: ZFC and FC measurements of **DFOB5m**. Right: Temperature dependence of the susceptibility temperature product χT of **DFOB5m**. The bump at 50 K is caused by an oxygen impurity. All susceptibilities are referenced to the sample's iron content.

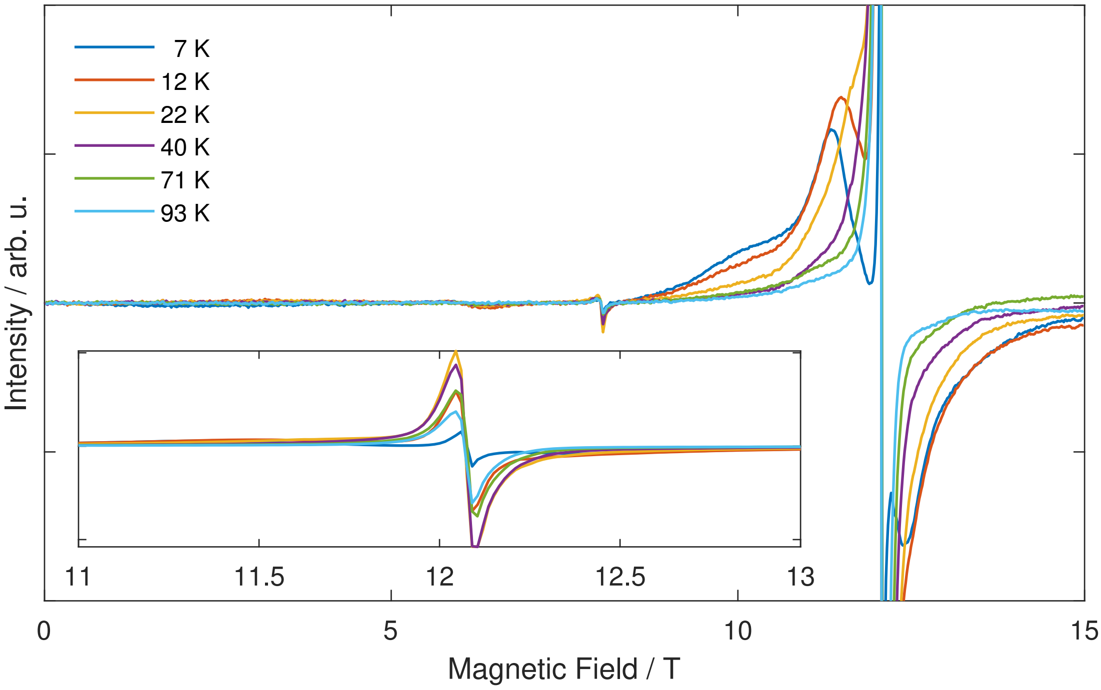

Figure 5.9: High-frequency EPR spectra of **DFOB5m** at 340 GHz and temperatures as indicated. The inset shows the complete main feature close to 12 T.

8.03 T and a very strong one at 12.08 T. Features of medium intensity are visible at 10.23 T, 11.37 T and 12.39 T. The intensity of the peak at 10.23 T decreases with increasing temperature and the peaks at 11.37 T and 12.39 T merge with the main feature at rising temperatures, similar as observed in **B9** and **BUPW**.

5.3.5. DFOB4h

DFOB4h is a sample from **B9** which interacted with the DFOB ligand for 4 hours in aqueous solution.

Magnetometric Measurements

Figure 5.10 shows the magnetometric measurements of **DFOB4h**. The saturation value of χT at 300 K is 0.107 $\mathrm{cm^3\,K\,g_{Fe}^{-1}}$. χT decreases gradually to 0.091 $\mathrm{cm^3\,K\,g_{Fe}^{-1}}$ at 22 K and then drops to 0.048 $\mathrm{cm^3\,K\,g_{Fe}^{-1}}$ at 1.8 K.

A small difference in the FC and ZFC measurements is observed below the irreversibility temperature of 13 K but, again, no blocking temperature can be identified.

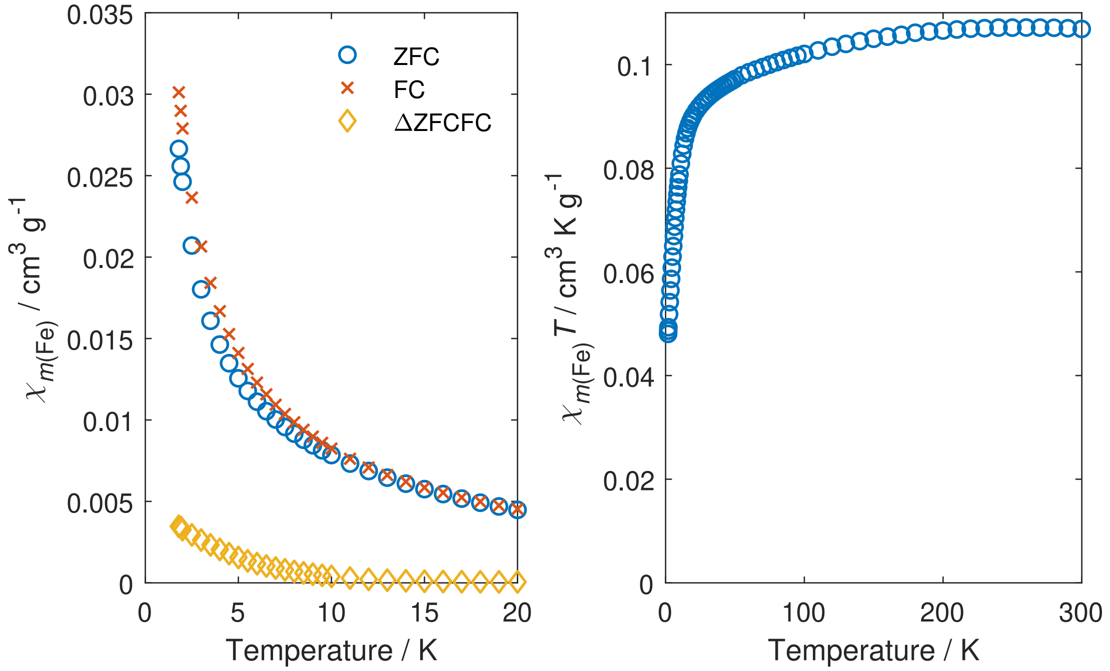

Figure 5.10: Left: ZFC and FC measurements of **DFOB4h**. Right: Temperature dependence of the susceptibility temperature product χT of **DFOB4h**. All susceptibilities are referenced to the sample's iron content.

HFEPR Measurements

Temperature dependent high-frequency EPR spectra of **DFOB4h** were measured at 340 GHz and are shown in Figure 5.11. The obtained spectra are very similar to those of **DFOB5m** and features are observed at the same or very similar position. Weak features are visible at 6.14 T and 8.03 T and the main peak at 12.07 T. Additional peaks of medium intensity are located at 10.23 T, 11.34 T and 12.48 T at 7 K. The signal at 10.23 T is clearly more pronounced than in **DFOB5m**. As for the previous samples, the peaks at 11.34 T and 12.48 T merge with the main feature at higher temperatures.

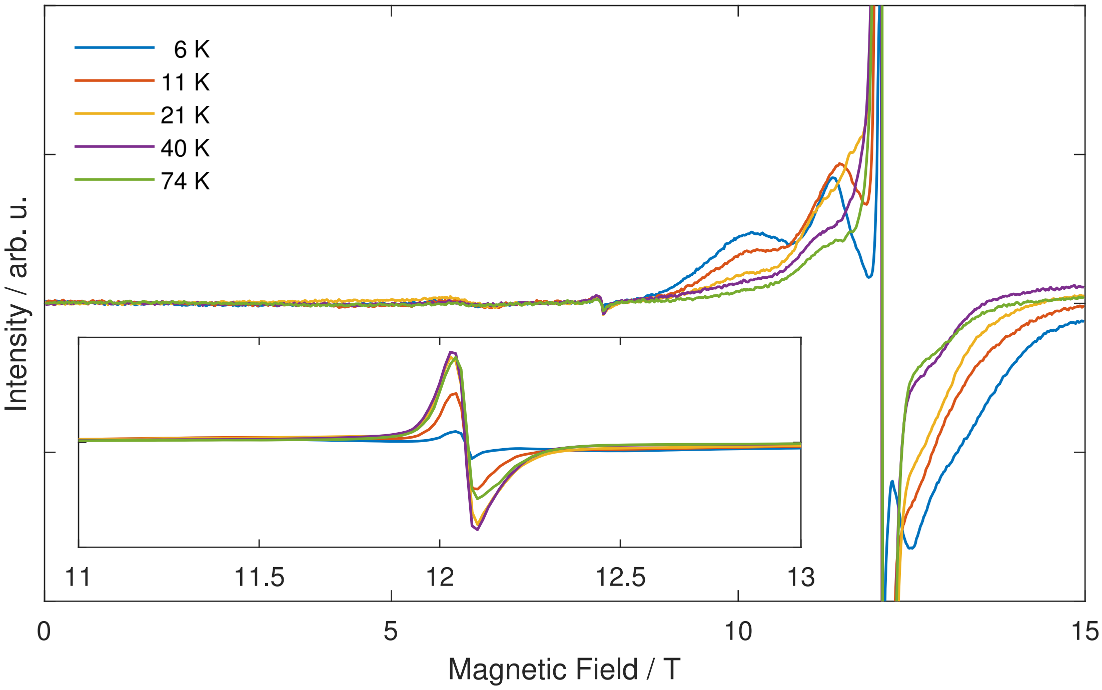

Figure 5.11: High-frequency EPR spectra of **DFOB4h** at 340 GHz and temperatures as indicated. The inset shows the complete main feature close to 12 T.

5.3.6. DFOB24h

DFOB24h is a sample from **B9** which interacted with the DFOB ligand for 24 hours in aqueous solution.

Magnetometric Measurements

The magnetometric measurements of **DFOB24h** are reported in Figure 5.12. χT saturates at 300 K with a value of $0.131\,\mathrm{cm^3\,K\,g_{Fe}^{-1}}$. To lower temperatures, χT decreases gradually to $0.114\,\mathrm{cm^3\,K\,g_{Fe}^{-1}}$ at 20 K. Below that, it drops down to $0.070\,\mathrm{cm^3\,K\,g_{Fe}^{-1}}$ at 1.8 K.

The FC and ZFC measurements do not coincide below $T_{\mathrm{IRREV}} = 13\,\mathrm{K}$ and no blocking temperature can be identified.

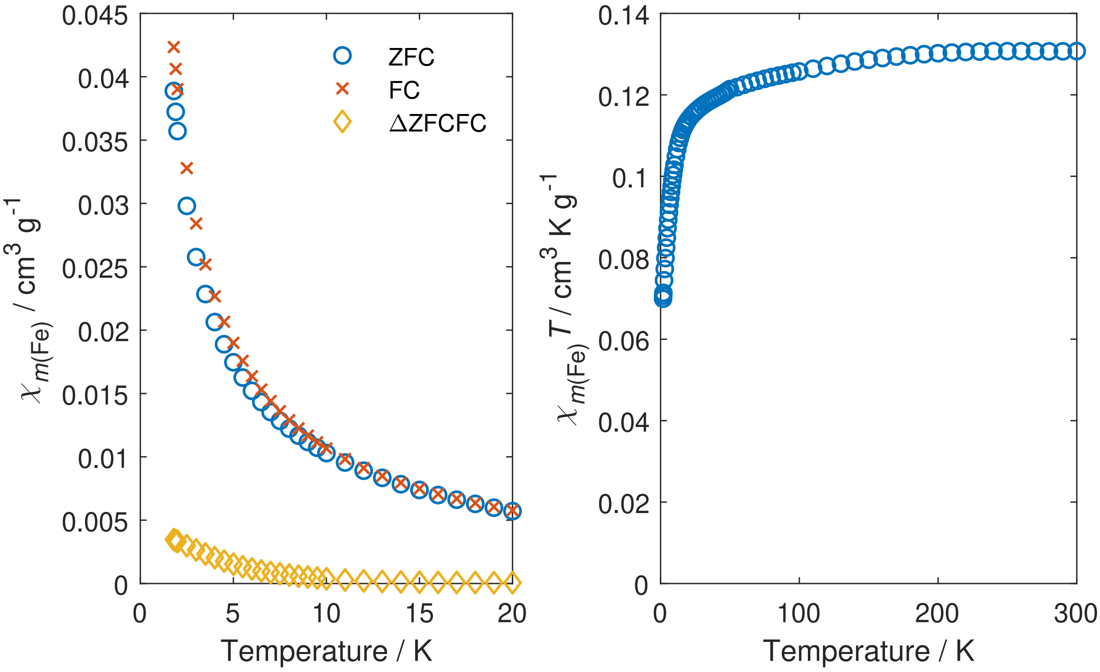

Figure 5.12: Left: ZFC and FC measurements of **DFOB24h**. Right: Temperature dependence of the susceptibility temperature product χT of **DFOB24h**. All susceptibilities are referenced to the sample's iron content.

HFEPR Measurements

Temperature dependent high-frequency EPR spectra of **DFOB24h** were measured at 340 GHz and are shown in Figure 5.13. Again, the spectra look very similar to those of **DFOB5m** and **DFOB4h**. At 6.08 T and 8.04 T the weak peaks are observed at 10 K and the main peak at 12.66 T. The latter one is slightly shifted to higher fields than in the other measurements which is also the case for the medium peak at 12.66 T. The medium peaks at 10.23 T and 11.40 T are at the same field as in the other measurements. The peaks at 11.40 T and 12.66 T merge with the main

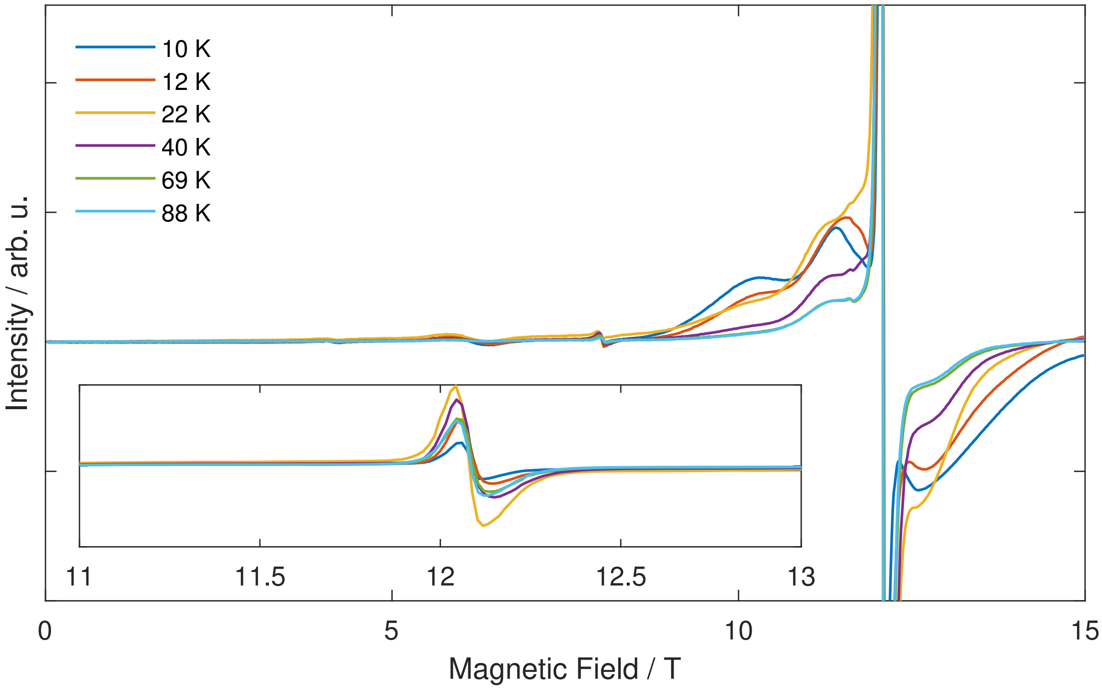

Figure 5.13: High-frequency EPR spectra of **DFOB24h** at 340 GHz and temperatures as indicated. The inset shows the complete main feature close to 12 T.

feature for rising temperatures as in the previous samples. A peak of very weak intensity, which was not observed in the spectra of any of the previous samples, is observed at 4.16 T. Its intensity decreases with increasing temperature.

5.3.7. FeDFOB

FeDFOB is the pure iron chelate of DFOB synthesized by complexation of iron with DFOB.

Magnetometric Measurements

The magnetometric measurements of **FeDFOB** (Figure 5.14) reveal a constant χT value of $0.074\,\mathrm{cm^3\,K\,g_{Fe}^{-1}}$ over nearly the complete measured range from 300 K to 7 K. Below 7 K χT decreases slightly to reach $0.070\,\mathrm{cm^3\,K\,g_{Fe}^{-1}}$ at 2.3 K. The simulation of χT based on the parameters obtained by HFEPR spectroscopy in the next section is also plotted and shows slightly higher values (between $0.076\,\mathrm{cm^3\,K\,g_{Fe}^{-1}}$ at low and $0.079\,\mathrm{cm^3\,K\,g_{Fe}^{-1}}$ at high temperatures). In this case, using a parameter set obtained by HFEPR spectroscopy for simulation is preferred over using the

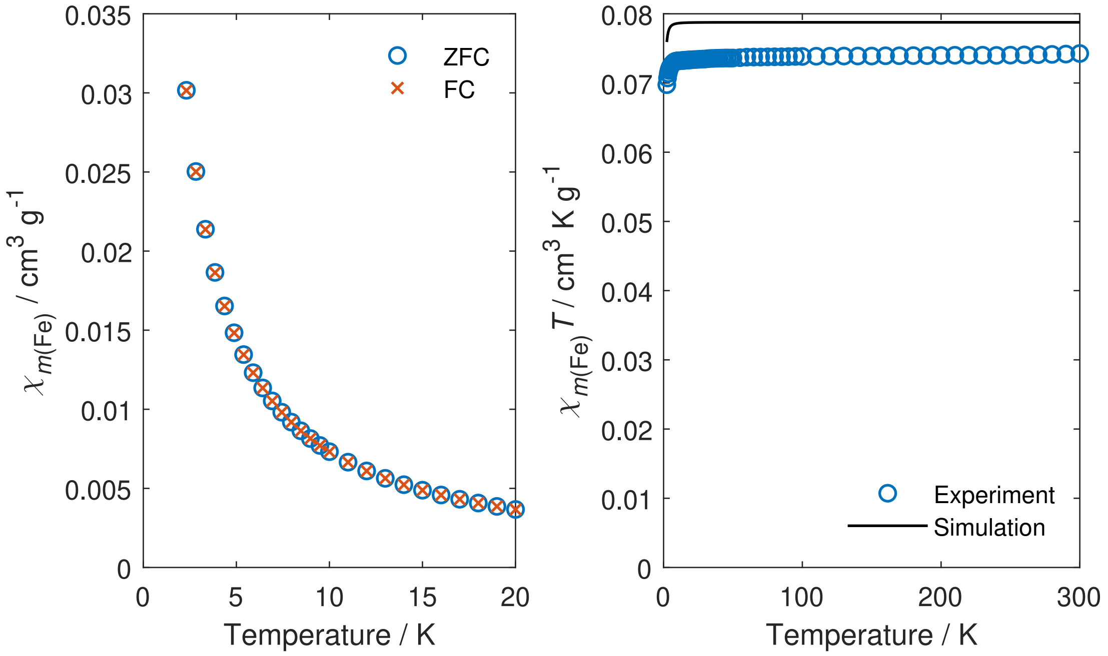

Figure 5.14: Left: ZFC and FC measurements of **FeDFOB**. Right: Experimental (blue circles) and simulated (black line) Temperature dependence of the susceptibility temperature product χT of **FeDFOB**. The simulation is based on parameters obtained from HFEPR spectroscopy. All susceptibilities are referenced to the sample's iron content.

magnetometry data to obtain an independent set because the purity of the sample is not guaranteed as is shown in Sections 5.3.12 and 5.4.1. While magnetometry measures the sum of all present species (including impurities) preventing an individual analysis, parameters of different species can be obtained independently using HFEPR spectroscopy if their features are not overlapping. While the measured and calculated values are not in absolute agreement, the overall shape of the curves matches perfectly. The difference of 6 % between them is probably caused by diamagnetic impurities like the >18.9 wt% Na (see Table 5.1). The FC and ZFC measurements coincide perfectly down to 2 K showing no presence of slow relaxation of magnetization.

HFEPR Measurements

Temperature dependent high-frequency EPR spectra of **FeDFOB** were measured at 340 GHz and are presented in Figure 5.15. The spectra show the highest number of features of the samples discussed up to here. Features of weak intensity are observed at 4.19 T, 6.27 T and 8.01 T of which the one at 4.19 T shows the by far

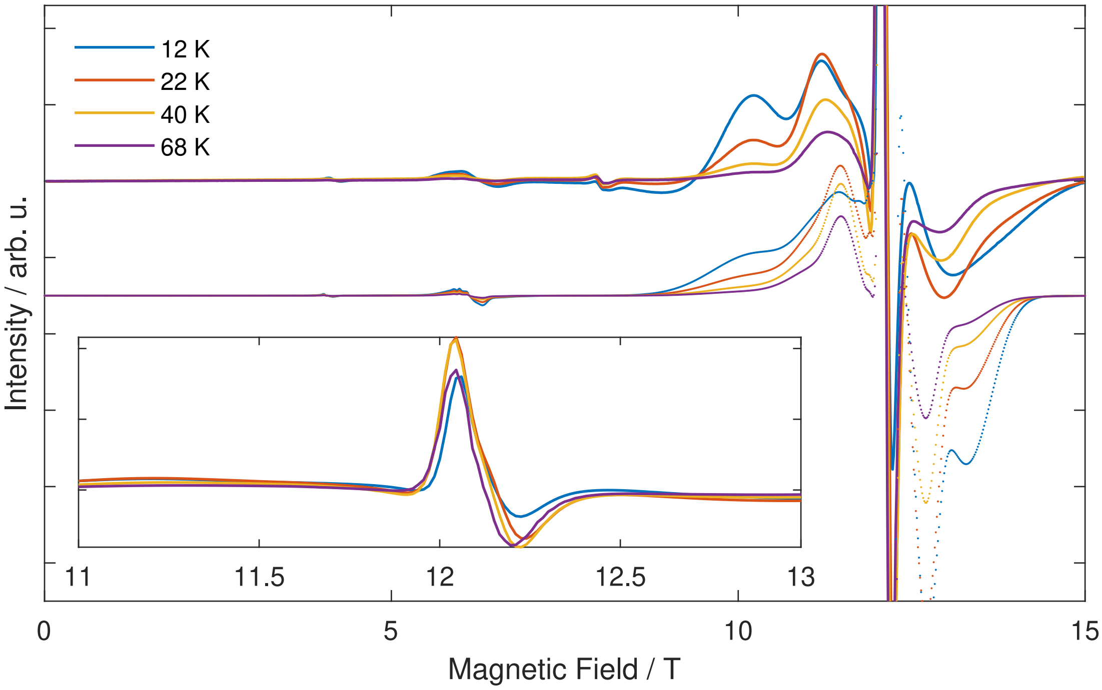

Figure 5.15: Experimental (lines, top) and simulated (dotted, bottom) high-frequency EPR spectra of **FeDFOB** at 340 GHz and temperatures as indicated. The inset shows the complete experimental main feature close to 12 T.

weakest intensity. Features of medium intensity are located at 10.26 T, 11.20 T, 11.58 T and 13.14 T at 12 K. In contrast to all previous samples, the peaks close to the main feature at 12.12 T are well separated and do not merge with it at higher temperatures.

Because **FeDFOB** is the only sample which should be a pure compound, the HFEPR spectra were fitted to determine its g-value and zero-field splitting parameters. A satisfying fit of the experimental spectra (Figure 5.15) was achieved with the parameters $S = 5/2$, $g = 2.005$, $D = -0.47\,\mathrm{cm}^{-1}$ and $E = 0.05\,\mathrm{cm}^{-1}$. Only the feature at 8.01 T, which was attributed to a harmonic caused by the spectrometer is not present in the fit. Based on the fitting parameters, the observed features can be assigned to M_S state transitions: For example, the main feature at 12.12 T corresponds to a $M_S = -{}^1\!/_2 \rightarrow M_S = {}^1\!/_2$ transition which is in agreement with the peak intensity's temperature dependence. All attributions are listed in Table 5.2.

Table 5.2: Attribution of Peaks in **FeDFOB** to M_S-transitions. The axes in parentheses describe the magnetic field direction in the molecular frame.

Peak Position / T	M_S-Transition
4.19	$-3/2 \rightarrow 3/2$ (xz)
6.27	several $\Delta M_S = 2$
10.23	$-5/2 \rightarrow -3/2$ (z)
11.20	$-3/2 \rightarrow -1/2$ (z)
11.58	$1/2 \rightarrow 3/2$ (x) $3/2 \rightarrow 5/2$ (y)
12.12	$-1/2 \rightarrow 1/2$ (z)
13.14	$1/2 \rightarrow 3/2$ (z)

5.3.8. Hematite

Magnetometric Measurements

The magnetometric measurements of **hematite** are reported in Figure 5.16. The value of χT is clearly not saturated at 300 K with $2.57 \cdot 10^{-2}\,\mathrm{cm^3\,K\,g_{sample}^{-1}}$. With decreasing temperature, χT decreases drastically to $3.62 \cdot 10^{-3}\,\mathrm{cm^3\,K\,g_{sample}^{-1}}$ at 110 K. Below that, the decrease slows down and reaches $5.2 \cdot 10^{-5}\,\mathrm{cm^3\,K\,g_{sample}^{-1}}$ at 1.8 K.

The FC static susceptibility is virtually constant between 1.8 K and 110 K at $8 \cdot 10^{-5}\,\mathrm{cm^3\,g_{sample}^{-1}}$. Above 110 K it increases slightly to reach a plateau of $8.7 \cdot 10^{-5}\,\mathrm{cm^3\,g_{sample}^{-1}}$ at 240 K at which it is constant until the end of the measured range. The ZFC susceptibility is much lower at 1.8 K with $2.88 \cdot 10^{-5}\,\mathrm{cm^3\,g_{sample}^{-1}}$ and practically constant up to 85 K from where it increases drastically to $8.4 \cdot 10^{-5}\,\mathrm{cm^3\,g_{sample}^{-1}}$ at 240 K to reach nearly the value of the FC curve.

The steep increase between 110 K and 240 K marks a Morin transition (see Section 2.3.1) with an antiferromagnetic state below the Morin temperature T_M and a ferrimagnetic state above T_M. Here, T_M was identified to be 147 K which is significantly lower than for bulk hematite ($T_\mathrm{M} \approx 260\,\mathrm{K}$[16]). This decrease of T_M is commonly explained by small particle sizes[117, 118]. For hematite crystallites with a size of 36 nm, $T_\mathrm{M} = 164\,\mathrm{K}$ has been found[118]. This implies that the hematite particles investigated here have an average size smaller 36 nm but the size distribution must be rather large as the range of the Morin transition is quite broad. On the other hand, the Morin transition is reported to vanish for particles sizes smaller than 8 nm to 20 nm[119] which gives a lower estimate for the particle size here.

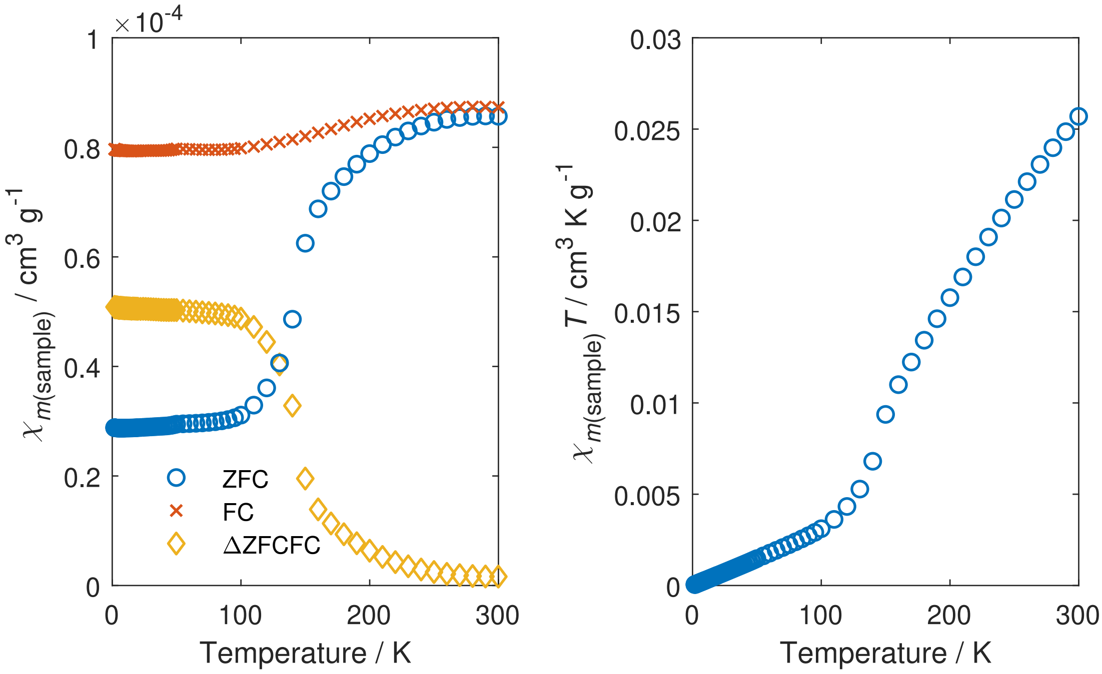

Figure 5.16: Left: ZFC and FC measurements of **hematite**. Right: Temperature dependence of the susceptibility temperature product χT of **hematite**. All susceptibilities are referenced to the sample's mass.

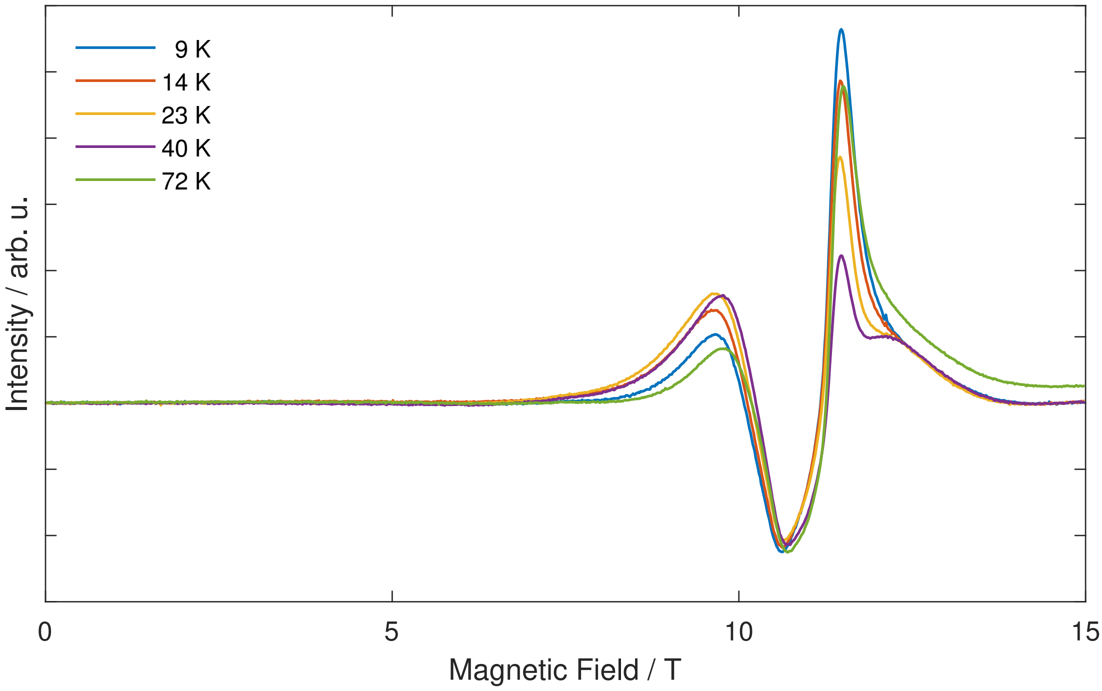

Figure 5.17: High-frequency EPR spectra of **hematite** at 340 GHz and temperatures as indicated.

HFEPR Measurements

Temperature dependent high-frequency EPR spectra of **hematite** were measured at 340 GHz and are shown in Figure 5.17. The line shape of the signal looks different to a typical first-derivative EPR line shape which is not a matter of a misaligned phase and makes it impossible to identify a proper magnetic field of the transition. Very likely, the explanation for this unusual shape is related to the fact all measurements have been performed on hematite in the antiferromagnetic state below the Morin temperature which classifies the transitions as antiferromagnetic magnetic resonance.

5.3.9. Goethite

Magnetometric Measurements

The magnetometric measurements of **goethite** are presented in Figure 5.18. The curve of χT against T shows a typical shape for an antiferromagnetic compound as it is expected for **goethite** (see Section 2.3.1). At 1.8 K, the χT value is very small with $0.000\,18\,\mathrm{cm^3\,K\,g_{sample}^{-1}}$. It increases constantly to higher temperatures to reach $0.009\,07\,\mathrm{cm^3\,K\,g_{sample}^{-1}}$ at 95 K. From there, the increase flattens but continues until the end of the measured range reaching $0.0162\,\mathrm{cm^3\,K\,g_{sample}^{-1}}$ at 300 K where χT is not saturated. The mainly temperature-independent shape results from the antiferromagnetic nature below 393 K[53].

The FC and ZFC measurements only coincide at the highest measured temperature of 300 K. Consequently, $T_{\mathrm{IRREV}} = 300\,\mathrm{K}$ and a wide distribution of relaxation times can be assumed. Since the relaxation time depends on the size of the particles and T_{IRREV} is the blocking temperature of the largest particle, a wide distribution of particle sizes is present in the sample. The ZFC curve exhibits a maximum which corresponds to a blocking temperature of $T_{\mathrm{B}} = 35\,\mathrm{K}$. Literature measurements of synthetic **goethite** samples[120] show a lower blocking temperature (20 K) and a much smaller particle size distribution but overall the results are very similar.

HFEPR Measurements

Temperature dependent high-frequency EPR spectra of **goethite** were measured at 340 GHz and are shown in Figure 5.19.

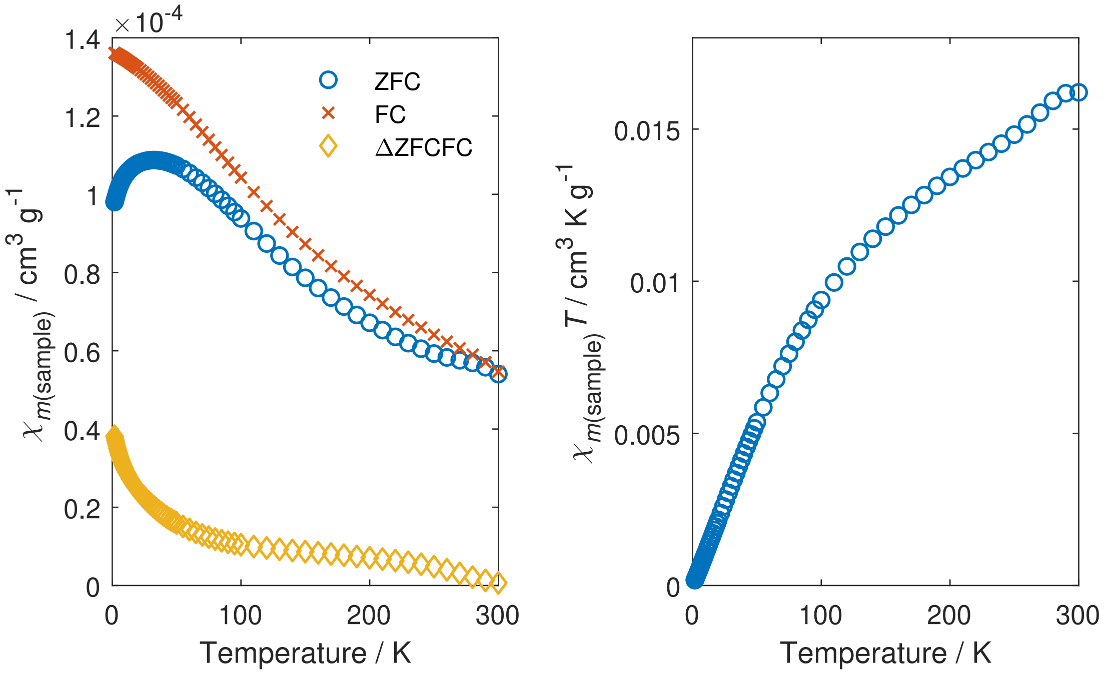

Figure 5.18: Left: ZFC and FC measurements of **goethite**. Right: Temperature dependence of the susceptibility temperature product χT of **goethite**. All susceptibilities are referenced to the sample's mass.

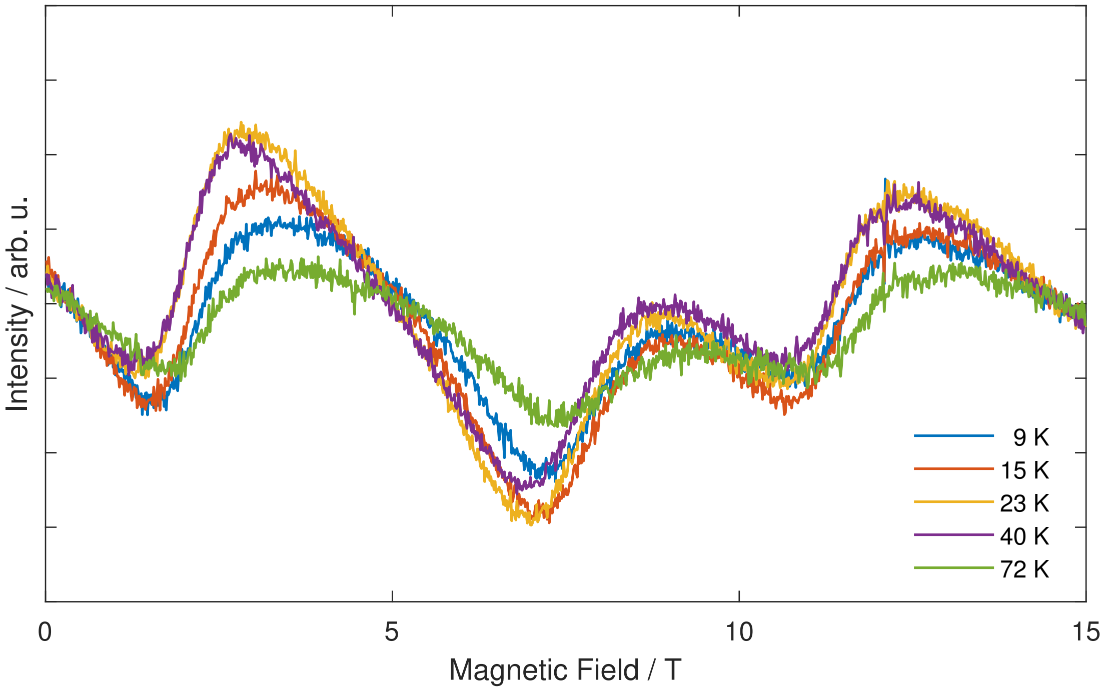

Figure 5.19: High-frequency EPR spectra of **goethite** at 340 GHz and temperatures as indicated.

The antiferromagnetic resonance spectra show several features with highest intensity at 23 K but no typical EPR signal can be identified. Measurements in literature show that already for smaller particles with lower blocking temperature no sharp EPR signals could be observed at 9.35 GHz below 40 K. The effect is attributed to an aggregation of nanoparticles with superparamagnetic behavior[120]. This finding makes it unlikely that well-resolved spectra could be obtained for measurements in high-field (where higher broadening appears) of particles with longer relaxation times.

5.3.10. 2-line Ferrihydrite

Magnetometric Measurements

Figure 5.20 shows the magnetometric measurements of **2-line ferrihydrite**. The FC and ZFC measurements coincide perfectly from 300 K to 55 K where they split up and the FC measurement forms a plateau. The ZFC measurement decreases again with its maximum corresponding to $T_\mathrm{B} = 55\,\mathrm{K}$.

The χT curve exhibits a very low value of $0.000\,40\,\mathrm{cm^3\,K\,g_{sample}^{-1}}$ at 1.8 K. χT then drastically increases to higher temperatures to reach at 70 K a value of $0.0360\,\mathrm{cm^3\,K\,g_{sample}^{-1}}$, which is then virtually constant up to 300 K showing the superparamagnetic nature of **2-line ferrihydrite**.

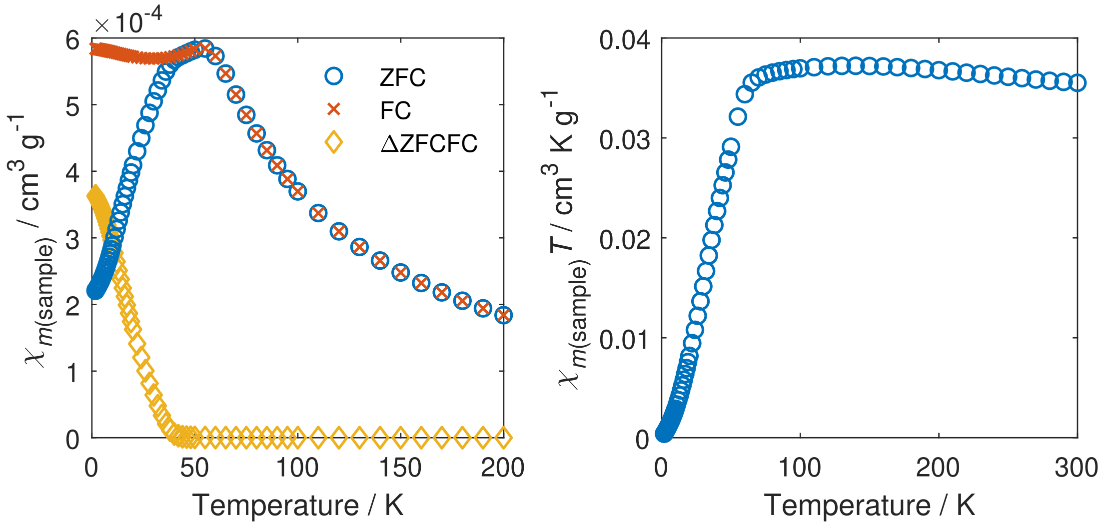

Figure 5.20: Left: ZFC and FC measurements of **2-line ferrihydrite**. Right: Temperature dependence of the susceptibility temperature product χT of **2-line ferrihydrite**. All susceptibilities are referenced to the sample's mass.

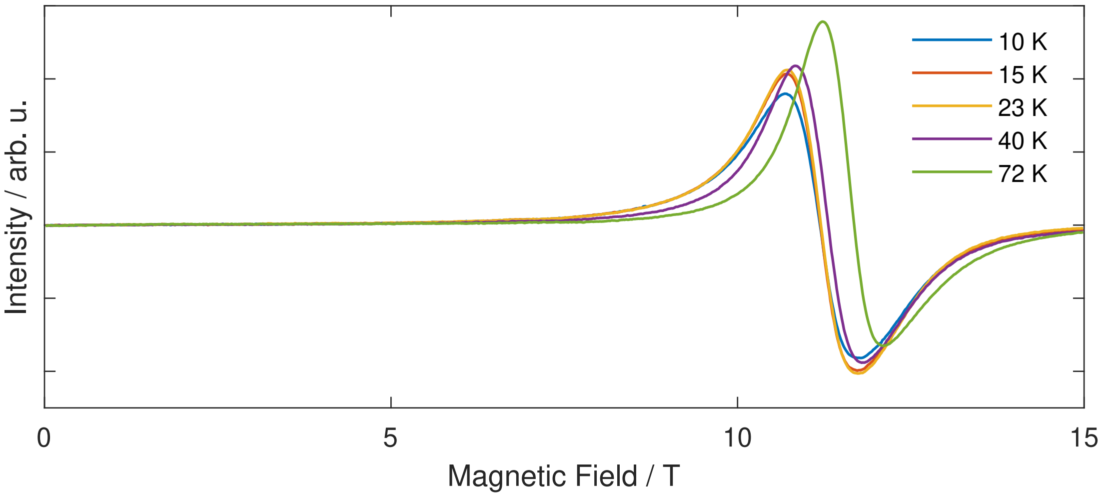

Figure 5.21: High-frequency EPR spectra of **2-line ferrihydrite** at 340 GHz and temperatures as indicated.

HFEPR Measurements

Temperature dependent high-frequency EPR spectra of **2-line ferrihydrite** were measured at 340 GHz and are shown in Figure 5.21. A signal with typical EPR line shape is observed at 11.19 T ($g = 2.17$) at temperatures significantly below the blocking temperature (10 K, 15 K and 23 K). At higher temperatures, the signal shifts to higher fields and is located at 11.68 T at 72 K. The signal intensity is virtually constant over the whole measured temperature range.

5.3.11. 6-line Ferrihydrite

Magnetometric Measurements

Magnetometric measurements of **6-line ferrihydrite** are plotted in Figure 5.22. The FC and ZFC measurements coincide down to $T_{\mathrm{IRREV}} = 100\,\mathrm{K}$ and a blocking temperature of 55 K is observed. The large difference between T_{IRREV} and T_{B} points out that a wide distribution of relaxation times and, possibly, particle sizes can be assumed. However, the extent of inhomogeneity is expected to be rather small because the absolute difference in corresponding values is very small compared to, for example, the measurements of **goethite**.

The plot of χT versus T shows the minimum value within the measured range of $0.000\,47\,\mathrm{cm^3\,K\,g_{sample}^{-1}}$ at 1.8 K. It increases continuously to $0.052\,\mathrm{cm^3\,K\,g_{sample}^{-1}}$ at

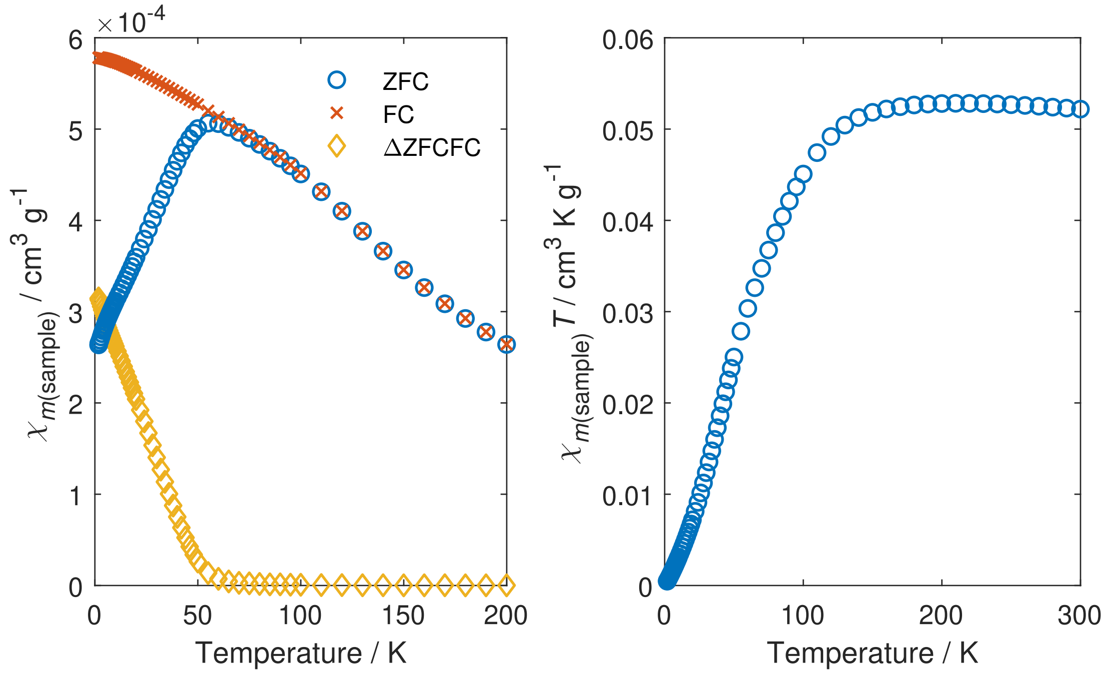

Figure 5.22: Left: ZFC and FC measurements of **6-line ferrihydrite**. Right: Temperature dependence of the susceptibility temperature product χT of **6-line ferrihydrite**. All susceptibilities are referenced to the sample's mass.

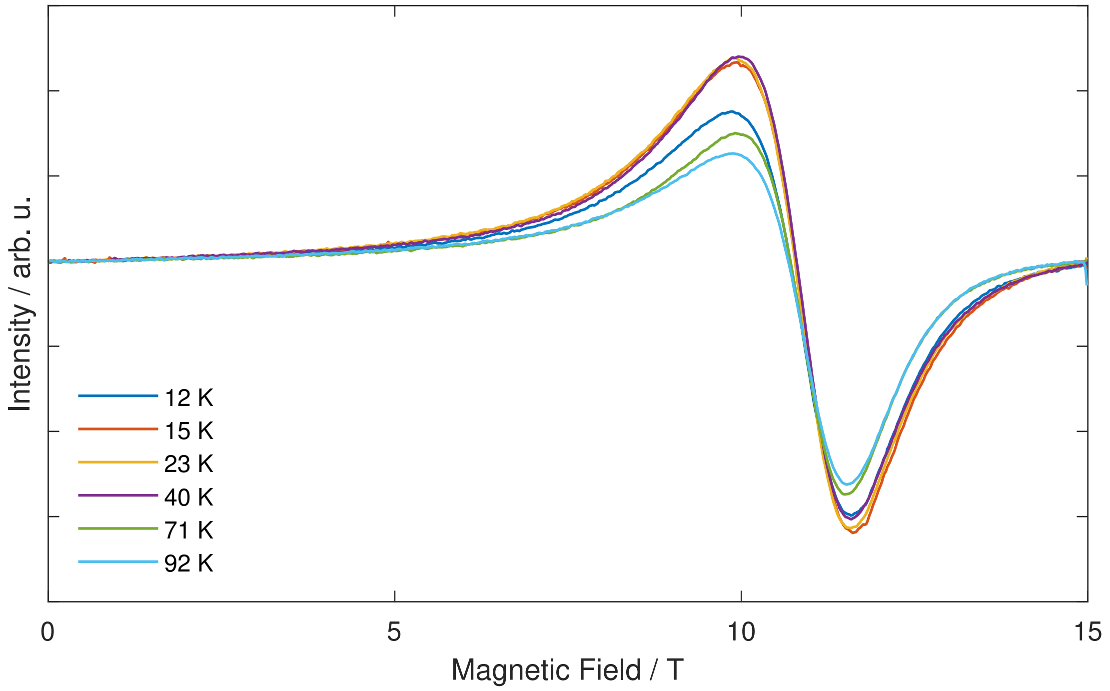

Figure 5.23: High-frequency EPR spectra of **6-line ferrihydrite** at 340 GHz and temperatures as indicated.

150 K and stays virtually constant up to 300 K indicating the superparamagnetic nature of **6-line ferrihydrite**.

HFEPR Measurements

Temperature dependent high-frequency EPR spectra of **6-line ferrihydrite** were measured at 340 GHz and are shown in Figure 5.23. One broad signal is observed at 10.68 T ($g = 2.28$). The temperature dependence shows that the measurements at 15 K, 23 K and 40 K are most intense and of equal intensity. At higher temperatures, the signal intensity decreases slightly.

5.3.12. Mössbauer Spectroscopy

Mössbauer spectra of **B9**, **BUPW**, **DFOB24h** and **FeDFOB** were measured by Dr. James Byrne in the group of Prof. Andreas Kappler (Zentrum für Angewandte Geowissenschaften, Eberhardt Karls Universität Tübingen). The spectra are presented in Figure 5.24. Each of them shows a high number of signals which cannot be attributed to a single iron species. Due to the high amount of signals, the spectra were fitted using three (**BUPW**), four (**B9**, **FeDFOB**) or five (**DFOB24h**) species. The obtained parameters are listed in Table 5.3.

The spectrum of **B9** shows eight peaks, some of which have a shoulder indicating that several features overlap. A satisfying fit was achieved using one quadrupole split site and two hyperfine field sites.

For **BUPW**, the spectrum shows three more intense peaks which most likely correspond to two partially overlapping doublets. Additionally, there are five peaks of less intensity. A set of two quadrupole split sites and two hyperfine field sites was necessary for a satisfying fit.

FeDFOB yielded a spectrum with four sharp and intense peaks and an intense multiplet around zero velocity. A decent fit was achieved using a set of one quadrupole split site and three hyperfine field sites.

For **DFOB24h**, seven intense peaks, partially with shoulders, were observed. A set of one quadrupole split site and four hyperfine field sites was used for fitting. The addition of the species marked in red was based on the observance of this species in **FeDFOB** and the assumption that it should be present here, too. The significant improvement of the fit quality justifies this procedure.

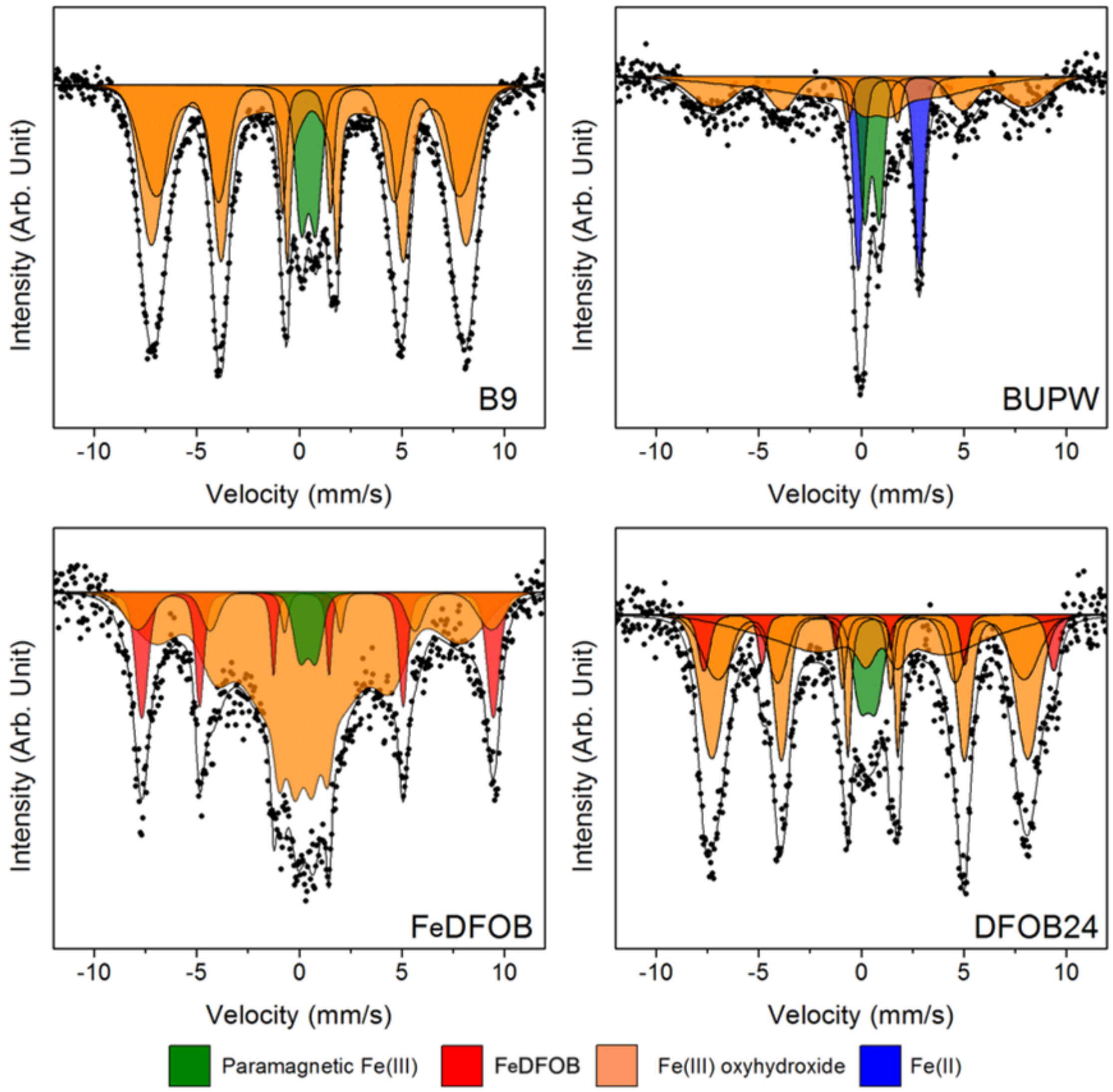

Figure 5.24: Mössbauer spectra of **B9**, **BUPW**, **FeDFOB** and **DFOB24h** at 5 K.

For all spectra, the species colored in green and labeled as paramagnetic Fe(III) corresponds to the part of the sample that is not slowly relaxing on the Mössbauer time-scale (approximately 100 ns) because the temperature is not low enough and, thus, shows only a quadrupole split doublet instead of a magnetically split sextet. This can be clearly seen by the fact that at 77 K (Figure A.23), for which a faster magnetic relaxation is expected, only this species is observed in samples **B9** and **DFOB24h**.

Beside this, the most common species in the samples are Fe(III)oxyhydroxides (marked in orange in Figure 5.24) of which more than one phase is present in all measurements. For **B9** and **DFOB24h**, their fit parameters are the same within

Table 5.3: Mössbauer fitting parameters obtained for **B9**, **BUPW**, **DFOB24h** and **FeDFOB** measured at 5 K.

Compound	Color in Figure 5.24	Isomer shift δ/ mm s^{-1}	Quadrupole splitting ΔE_Q / mm s^{-1}	Quadrupole shift ε/ mm s^{-1}	Hyperfine field B_{HF}/ T	Ratio %
B9	green	0.46(2)	0.73(41)			9.5
	orange	0.55(2)		−0.08	43(11)	53
	orange	0.39(3)		0.04	46(4)	37.5
BUPW	blue	1.35(2)	3.0(4)			24.5
	green	0.53(3)	0.7(4)			17.5
	orange	0.5(1)		−0.09	47(6)	30
	orange	0.1(8)		−0.69	26(17)	28
FeDFOB	green	0.4(1)	0.8(5)			4.9
	orange	0.3(1)		0.13	27(17)	66.5
	orange	0.7(1)		0.05	54(4)	10.7
	red	0.50(3)		0.40	53(2)	17.9
DFOB24h	green	0.3(1)	0.8(5)			7.9
	orange	0.9(4)		−0.15	29(14)	22
	orange	0.50(5)		−0.07	48(3)	39.1
	orange	0.4(1)		0.11	46(4)	22.7
	red	0.48(5)		0.38	53(1)	8.3

the corresponding error margins which is in good agreement with the fact that **DFOB24h** is based on **B9**. The presence of Fe(III)oxyhydroxides is in agreement with the synthesis procedure as they are formed in alkaline solutions[53]. Especially for **B9**, **DFOB24h** and **FeDFOB**, for which a pH value of 8.5 to 9 was set, significant amounts of Fe(III)oxyhydroxides were found.

In **BUPW**, the parameters of the Fe(III)oxyhydroxide phase with isomer shift of 0.5(1) mm s^{-1} are consistent with those of one species in **B9** and **DFOB24h**. As this phase is present in all soil extracts, its extraction must be independent of the used pH values and, thus, be a stable endmember. The second Fe(III)oxyhydroxide phase in **BUPW** differs from the second one in **B9** and **DFOB24h**, indicating that the different pH value during extraction changes the samples composition. Additionally, an Fe(II) phase is observed. This is not unexpected because **BUPW** was extracted at the natural pH of ca. 4 and Fe(II) is present in soils at lower pH values. Only above ca. pH 7.5 it is completely oxidized to Fe(III)[121].

Because **FeDFOB** is a synthesized compound, a pure composition with only one iron species would be expected. This is obviously not the case as there is clearly more than one magnetically split species present. These other species most likely formed during the synthesis of **FeDFOB** by reactions competing with the complexation with DFOB and probably have not been removed completely during purification or have formed during the storage of the sample. A significant part of the observed signals was attributed to Fe(III)oxyhydroxide species, the presence of which fits the synthesis procedure as described above. Of all species present, the one marked in red ($\delta = 0.50(3)\,\mathrm{mm\,s^{-1}}$, $\varepsilon = 0.40\,\mathrm{mm\,s^{-1}}$, $B_{\mathrm{HF}} = 53(2)\,\mathrm{T}$) was identified to be **FeDFOB**. Nonetheless, their fit parameters differ significantly from those of the species in the other samples showing that there is no relation between them.

The presence of **FeDFOB** in the **DFOB24h** sample (species with $\delta = 0.48(5)\,\mathrm{mm\,s^{-1}}$, $\varepsilon = 0.38\,\mathrm{mm\,s^{-1}}$, $B_{\mathrm{HF}} = 53(1)\,\mathrm{T}$) could be shown by the necessity to use its parameter set, which was extracted from the **FeDFOB** spectrum, to achieve a satisfying fit. This shows that the complexation of iron by DFOB can be demonstrated by Mössbauer spectroscopy.

5.4. Discussion

Summarizing the observations in Section 5.3, a variety of different magnetic species is present in the samples. The measurements of the minerals **hematite** and **goethite** show the presence of large antiferromagnetic particles. Superparamagnetic particles were observed in **B9** and **BUPW** as well as in **DFOB5m**, **DFOB4h** and **DFOB24h**. Paramagnetic species were found in **BUPW9** and **FeDFOB**.

5.4.1. Effect of Complexation Time

For a comparative analysis of the magnetometric measurements and HFEPR spectra of the soil extract **B9** with the treated extracts **DFOB5m**, **DFOB4h**, **DFOB24h** and the reference compound **FeDFOB**, the obtained data were normalized to the determined iron content as listed in Table 5.1. The aim of this comparison was to identify effects of different complexation times, for example various targeted iron pools.

Magnetometry

The temperature dependence of the susceptibility temperature product χT of **B9**, the soil extracts treated with DFOB (**DFOB5m**, **DFOB4h**, **DFOB24h**) and **FeDFOB** is presented in Figure 5.25.

The curves of **DFOB5m**, **DFOB4h** and **DFOB24h** show higher χT values with longer complexation times. At the same time, the χT products of **B9** and **DFOB5m** are very close with those of **B9** being slightly higher above 6 K. It is not surprising that these two measurements are very similar, as **DFOB5m** is a sample of **B9** which interacted with DFOB for just a very short time. In fact, the difference of 6 % is not significant compared to the measurement's uncertainties due to mass uncertainties. The values of **FeDFOB** are of intermediate size at low temperatures and the lowest ones in this set at high temperatures.

The overall trend of χT with extraction time can be analyzed best looking at high temperatures above 150 K:

1. The χT product starts at an intermediate value for the reference sample **B9** without extraction.

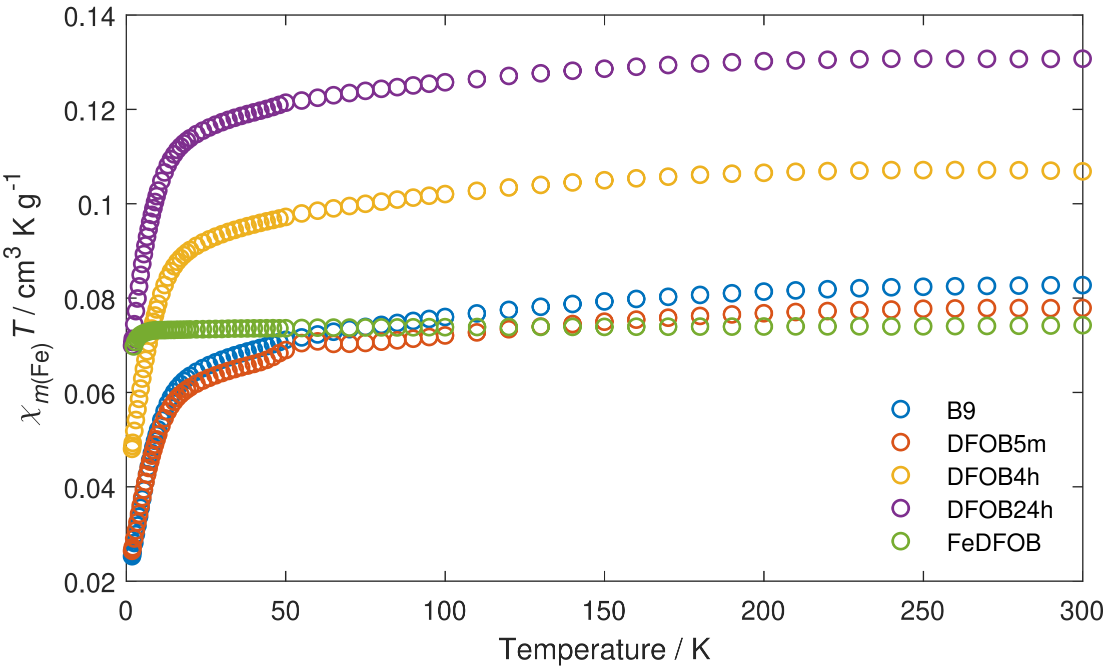

Figure 5.25: Temperature dependence of the susceptibility temperature product χT of the pure soil extract **B9**, the soil extracts treated with DFOB and **FeDFOB**. All susceptibilities are referenced to the samples' iron contents.

2. For 5 min of extraction, χT slightly decreases but stays within the error margin meaning that no significant change can be observed.
3. After 4 h of extraction, χT has drastically increased surpassing the value of **B9** by far.
4. At 24 h of extraction, χT has increased further to reach the 1.6-fold of **B9**.

The observation that χT increases for longer complexation times suggests that an antiferromagnetic species is targeted by DFOB. This process seems to take some time for significant amounts of iron to be complexed as the change in χT is only observed in the measurements after 4 h and 24 h.

HFEPR Spectroscopy

To compare the HFEPR spectra of **B9** with the treated extracts **DFOB5m**, **DFOB4h**, **DFOB24h** and the reference compound **FeDFOB**, spectra measured close to a common temperature (namely 12 K) were chosen and are presented in Figure 5.26. As mentioned in the description of the **B9** spectra (Section 5.3.1), the signals around the main feature show a pronounced temperature dependence in all soil extracts. Thus, the position of the peak around 11.50 T is a good indicator for a consistent temperature. In the chosen spectra, this peak is located at the same position in all spectra of the extracts showing a consistent temperature of the measurements.

The line shape of the **FeDFOB** signal around this position differs significantly from the one of the extracts. As **FeDFOB** is (in contrast to the other compared samples) not based on the soil extract **B9**, the signals of the extracts are not expected to be present here which explains the different line shape. However, the measured temperature of this spectrum is in good agreement with the measured temperatures of the other spectra making it a good candidate for comparison.

A comparison of all peak positions above 6 T as listed in Table 5.4 shows that features around 6.1 T, 8.0 T and 12.1 T are shared by all compounds. The peak at about 8 T was left out in the comparison as it was attributed to a harmonic of the main signal due to the spectrometer's frequency synthesizer. A peak around 11.5 T is absent only in the spectrum of **BUPW9**.

The signal around 12.3 T is present in the pure extracts, **DFOB5m** and **DFOB4h** while it is shifted to 12.7 T in **DFOB24h**. This shift results probably from a superposition of the pure extracts' features at 12.3 T and the feature of

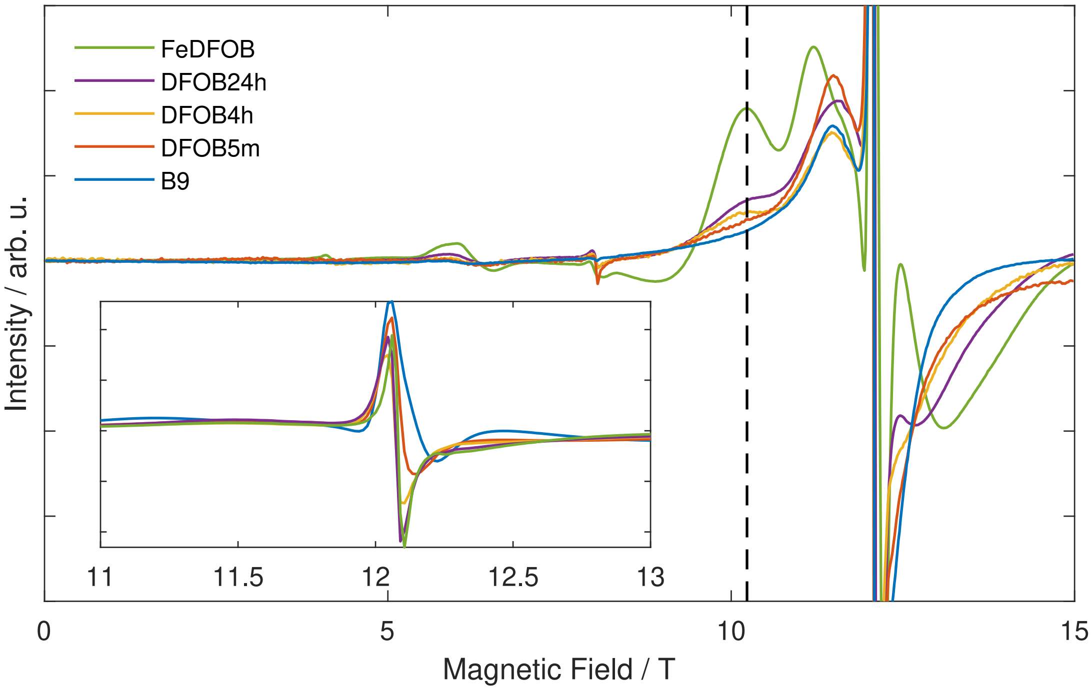

Figure 5.26: High-frequency EPR spectra of the pure soil extract **B9**, the soil extracts treated with DFOB and **FeDFOB** as reference at 340 GHz and temperatures close to 12 K. All spectra are normalized to the corresponding iron content. The dashed line marks the characteristic peak position of **FeDFOB** at 10.23 T.

Table 5.4: Peak positions of measurements closest in temperature grouped by similar positions. Peaks below 6 T in **DFOB24h**, **BUPW** and **FeDFOB** were left out for better overview.

Compound	Peak Positions / T								T / K
B9	6.03				11.48	12.08	12.26		12.1
BUPW	6.05	9.90			11.57	12.09	12.26		10.8
BUPW9	6.05			11.06		12.07	12.28		11.1
DFOB5m	6.14		10.23		11.49	12.08	12.34		12.0
DFOB4h	6.06		10.23		11.48	12.07	12.35		11.0
DFOB24h	6.14		10.23		11.51	12.10	12.70		12.5
FeDFOB	6.27		10.23	11.20	11.58	12.12		13.14	12.5

FeDFOB at 13.14 T because **DFOB24h** is the treated extract with the highest expected concentration of **FeDFOB**.

The peak around 10.23 T (marked by a dashed line in Figure 5.26) is shared by all compounds which were in contact with the biogenic ligand DFOB, indicating it as a characteristic peak for **FeDFOB**.

Only few signals are unique to a compound, such as the ones at 9.90 T (**BUPW**), 11.06 T (**BUPW9**), 11.20 T (**FeDFOB**) and 13.14 T (**FeDFOB**).

Signals shared by all compounds are striking as they are not expected because **FeDFOB** as a synthesized compound should only show signals of the specific material. An exception of this assumption is the signal at $g \approx 2$ because it is common in Fe(III) compounds[43, 96, 122, 123] and also present in the simulation of **FeDFOB** (Section 5.3.7). However, a reasonable explanation for the shared signals was already presented for the Mössbauer spectra (Section 5.3.12), where the presence of Fe(III)oxyhydroxides in **FeDFOB** from incomplete removal of excess Fe(III) was indicated.

Looking at the peaks' intensities, the comparison in Figure 5.26 shows that the most intense side peak in **FeDFOB** at 11.20 T completely disappears in the main side peak around 11.50 T for the extracts treated with DFOB. At the same time, this contribution to the intensity of the extracts side peak leads just to a barely observable broadening of the peak around 11.50 T. Consequently, this peak is unsuitable as a characteristic peak. In contrast, the second side peak in **FeDFOB** at 10.23 T is well-suited as a characteristic peak because the range around this position is free of signals in **B9**.

At this field, the differences between the spectra's intensities of the extracts (where **FeDFOB** is present) and **B9** (where no **FeDFOB** is present) were taken as a direct measure for the formed **FeDFOB** complex and, thus, extracted iron. The intensities and differences, normalized to the total iron content in the samples, are listed in Table 5.5. Figure 5.27 shows the difference in dependence of the extraction time. Additionally, the normalized intensity of **FeDFOB** is shown as an upper limit.

After 24 h of extraction, a relative spectral response of $3.56 \cdot 10^{-6}\,\mathrm{V\,mg_{Fe}^{-1}}$ is observed. In context of units, Volt refers to the spectrometer's detector signal. About a third of this extraction (36 %) takes place within the first five minutes. Another quarter (24 %) is achieved within the first four hours. The remaining 40 % are extracted over the course of the next 20 h.

Compound	Intensity at 10.23 T divided by iron / content $\mathrm{V\,mg_{Fe}^{-1}}$
B9	$3.56 \cdot 10^{-6}$
DFOB5m	$4.84 \cdot 10^{-6}$
DFOB4h	$5.70 \cdot 10^{-6}$
DFOB24h	$7.12 \cdot 10^{-6}$
FeDFOB	$1.21 \cdot 10^{-5}$

	$I - I_{\mathbf{B9}}$ / $\mathrm{V\,mg_{Fe}^{-1}}$
B9	0
DFOB5m	$1.28 \cdot 10^{-6}$
DFOB4h	$2.14 \cdot 10^{-6}$
DFOB24h	$3.56 \cdot 10^{-6}$

Table 5.5: Values of the HFEPR intensities at 10.23 T divided by the samples' iron contents for the treated extracts and **FeDFOB** as a reference.

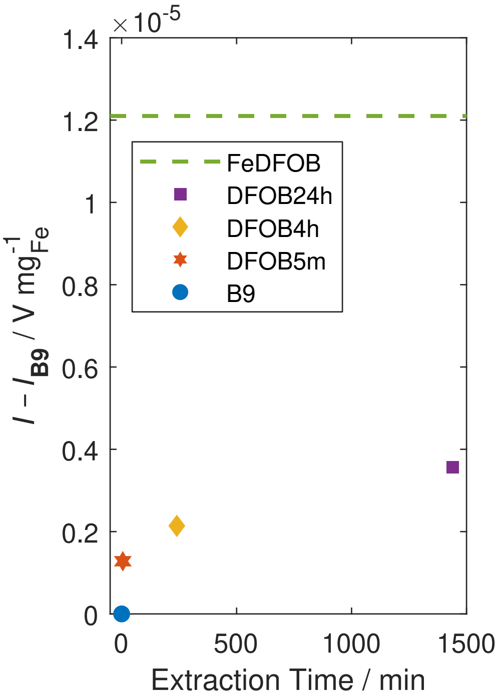

Figure 5.27: HFEPR intensities at 10.23 T divided by the samples' iron contents relative to $I_{\mathbf{B9}}$ against the extraction time (dots). The intensity of pure **FeDFOB** is plotted as the upper limit (dashed line)

An estimation of the proportionate contribution of the formed **FeDFOB** complex and **B9** to the signal in every treated extract is shown in Figure A.24. The estimate is based on the relative intensities at 10.23 T.

Conclusion

HFEPR measurements of **B9**, **DFOB5m**, **DFOB4h**, **DFOB24h** and **FeDFOB** clearly showed the formation of **FeDFOB** during complexation with significant amounts forming within the first five minutes of complexation. A probable explanation for the efficient complexation in the first five minutes is that the first targeted iron pool (i. e. the easiest accessible one) consists of organically bound iron which is coordinated by dissolved organic matter (DOM) and in solution, thus, being readily accessible for complexation. The estimated apparent stability constant of **FeDFOB** is very high with $\log K_{\mathrm{app}} \approx 22$ at pH 8[23] and exceeds that of basically all lower-coordinating organic ligands. In combination with the high availability of DFOB and the dissolved state, this leads to a rapid ligand exchange and formation of **FeDFOB**. This interpretation fits the observations from magnetometry where no significant change was observed in the first five minutes of complexation: The high-temperature χT value is determined by the spin S and the g-value. S is not expected to change at all during the described complexation while g should not differ drastically between **FeDFOB** ($g = 2.005$) and Fe^{3+} bound by lower-coordinating ligands where $g \approx 2$ is expected.

HFEPR spectroscopy is capable to measure the formation of **FeDFOB** but is not able to observe the removal of the targeted pool. At the same time, the situation is vice versa für magnetometry which makes both together an adequate set of complementary methods for this investigation. Based on the magnetometric measurements it is very likely that an antiferromagnetic species is targeted by complexation in the samples with longer extraction times. As the effect can only be seen in the measurements for complexation times larger 5 min this gives some hint that the reaction time is in the range of several minutes to hours. This leads to the assumption that the targeted iron compounds in this pool are thermodynamically more stable than Fe-DOM or the extraction is kinetically hindered by low accessibility. The most present sources of iron beside it being bound by DOM are minerals, for which both of the previous conditions are true. To learn about the nature of the targeted pool, the presence of minerals, which are possibly contained in the investigated soil, in the samples was analyzed. The results are presented in Section 5.4.3. Additionally, the effect of acidity during extraction was investigated, the results of which are presented in the next section.

An assumption about the completeness of the reaction or a precise time span after which the antiferromagnetic pool is depleted cannot be made on basis of the limited number of investigated extraction times. Likewise, which limit the extracted iron ratio tends to and if all iron can be extracted by **FeDFOB** cannot be answered based on these data.

Besides the formation of **FeDFOB** during complexation, Mössbauer spectroscopy revealed the presence of several Fe(III)oxyhydroxide species in the samples **B9**, **DFOB24h** and **FeDFOB**. For **FeDFOB**, which was supposed to be a pure substance, this is explained by its synthesis procedure. In **DFOB24h** a new species formed during complexation compared to **B9**. It remains unclear if this is directly due to the complexation process or the instability of the sample in solution.

5.4.2. Influence of Acidity During Extraction

The effect of the acidity during extraction from soil was investigated by comparing two samples with **B9**. Firstly, **BUPW** was extracted analogously to **B9** but at the soil's natural pH value of about 4. Secondly, **BUPW9** is based on **BUPW** but was again dissolved in water, its pH adjusted to 9 like in **B9**, filtered and finally freeze-dried to mimic the process for **B9**.

Magnetometry

Figure 5.28 shows the χT measurements of the pure soil extracts **B9**, **BUPW** and **BUPW9**. Because no iron content could be measured for **BUPW9**, its measurement was scaled by a factor of 216 to match $\chi T_{300\,\mathrm{K}}$ of **B9**. The reason for this scaling is that the idea behind the generation of **BUPW9** was to transform **BUPW** to **B9** by adding the treatment steps by which these samples differ. However, as can be seen in the comparative plot, this treatment did not result in the same consistence of **B9** and **BUPW9**. Thus, the extraction at pH 9 leads definitively to a different extract than finishing the extraction at pH 4 and subsequently changing the pH to 9 in a different step. By comparison of the curves of **B9** and **BUPW** in the magnetometry plot one can clearly see that substantial amounts of the antiferromagnetic particles are not extracted at low pH. Probably, the difference in accessed iron pools in the soil during extraction, depending on the used pH value, causes this different behavior. Unfortunately, magnetometry is not able to further identify the differences between **B9** and **BUPW9** on the material level.

HFEPR spectroscopy

The HFEPR spectra of extracts **B9**, **BUPW** and **BUPW9** are presented in Figure 5.29 together with the spectrum of **FeDFOB**. Their peak positions are listed in Table 5.4.

The extracts share common features at about 6.05 T, 12.08 T and 12.26 T. The prominent peak in **B9** at 11.48 T is only shared by **BUPW**. **BUPW9** instead features a signal at 11.06 T. This different position is not due to the temperature dependence of the signal positions because the temperatures are very close.

Overall, the spectra of **B9** and **BUPW** look very similar indicating a similar composition of the sample. At the same time, the spectra of **B9** and **BUPW9**

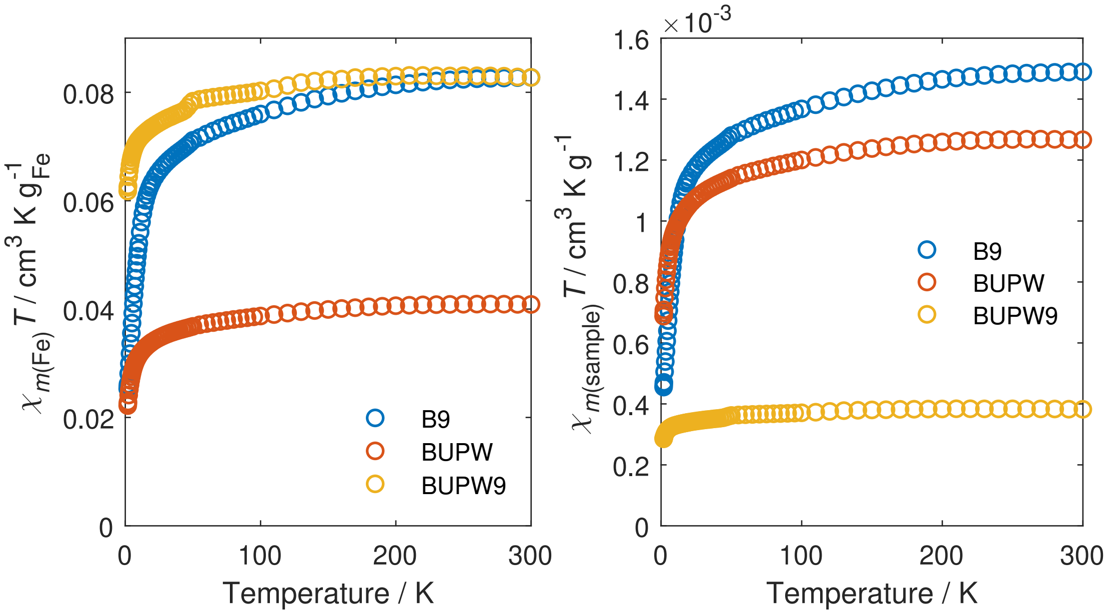

Figure 5.28: Temperature dependence of the susceptibility temperature product χT of the pure soil extracts. Left: The measurements of **B9** and **BUPW** are normalized to the corresponding iron content while the measurement of **BUPW9** is scaled by a factor of 216 to match the maximum value of **B9**. Right: The measurements are normalized to the sample masses.

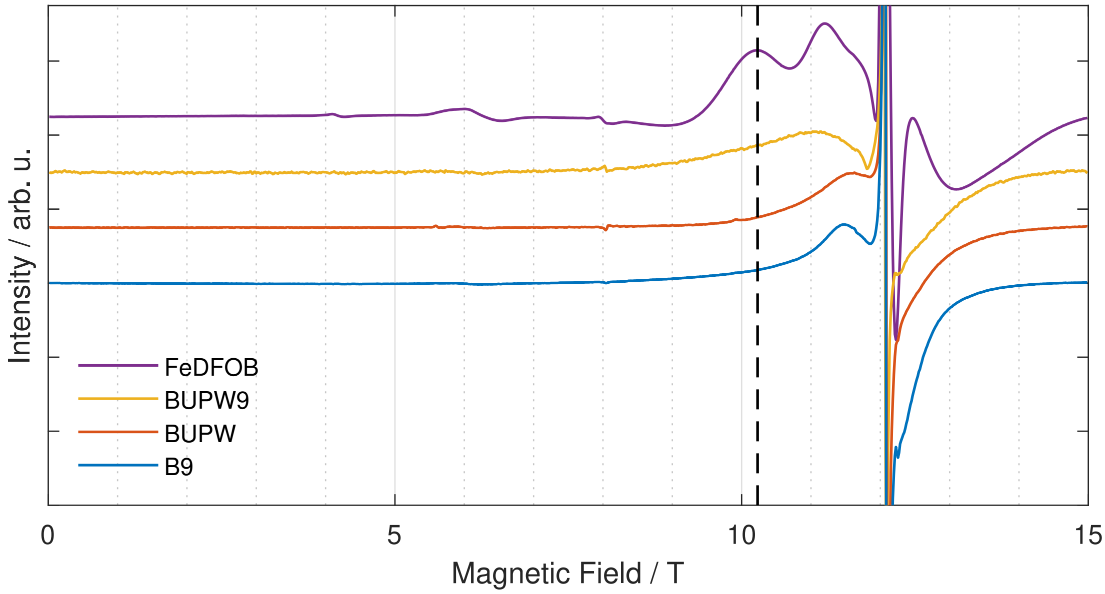

Figure 5.29: High-frequency EPR spectra of the pure soil extracts and **FeDFOB** at 340 GHz and temperatures close to 12 K. The spectra of **B9**, **BUPW** and **FeDFOB** are normalized to the corresponding iron content while the spectrum of **BUPW9** is arbitrarily scaled due to the unknown iron content. The dashed line marks the characteristic peak position of **FeDFOB** at 10.23 T.

differ significantly in one peak's position (11.48 T vs. 11.06 T) and share other features as described above.

Conclusion

The Mössbauer results of **B9** and **BUPW** support the observations from HFEPR spectroscopy that both samples are very similar (but definitively not same) as two common species between both were identified. The differing peak in the spectra of **B9** and **BUPW9**, supports the findings by magnetometry that different iron pools are accessed by different acidity during extraction. This is also assured by the fact that the extraction with ultrapure water at natural pH (approx. pH 4) yields a factor of 45 less iron in the extract than the extraction at pH 9[121].

5.4.3. Presence of Mineral Phases in Pure Soil Extracts

A set of minerals was investigated to analyze the iron pools targeted by extraction and complexation. This set consisted of **hematite**, **goethite**, **2-line ferrihydrite** and **6-line ferrihydrite**, which are typical constituents of the B horizon from which the initial soil samples were taken.

Magnetometry

The comparison of the χT measurements of the minerals and the direct soil extracts **B9** and **BUPW** is presented in Figure 5.30. A quantitative comparison between the minerals' and extracts' measurements is not possible because of the unknown iron content in the mineral samples. Without ICP-MS measurements, the iron content could be estimated via the formula weight but this is especially for the ferrihydrites very speculative due to the ill-defined water content (c. f. Section 2.3.1). Despite this, the shape of all minerals' measurements differs clearly from that of the extracts' measurements on the qualitative level. For example, the significant increase of χT of **2-line ferrihydrite** and **6-line ferrihydrite** between 20 K and 100 K is not observed in the measurements of **B9** and **BUPW**. The same holds for the continuous small increase over the whole temperature range for **goethite** and above 120 K for **hematite**.

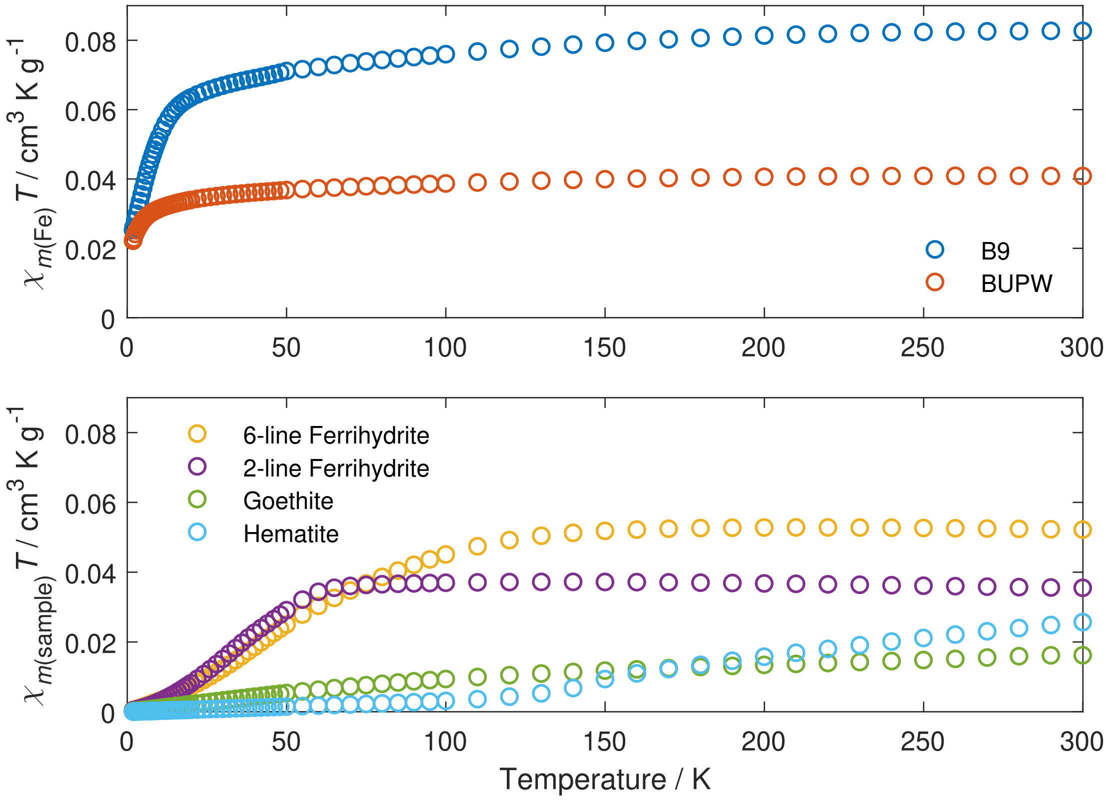

Figure 5.30: Temperature dependence of the susceptibility temperature product χT of **B9** and **BUPW** (top, referenced to iron content) and **hematite**, **goethite**, **2-line ferrihydrite** and **6-line ferrihydrite** (bottom, referenced to sample mass).

HFEPR spectroscopy

The HFEPR spectra of **B9** and **BUPW** are compared to those of **hematite** and **goethite** in Figure 5.31. Even more obvious than in the magnetometric measurements, it can be seen that there are no common features between the spectra of the soil extracts and the minerals. The same is true for the comparison of the soil extracts with **2-line ferrihydrite** and **6-line ferrihydrite** (Figure 5.32). The option that the minerals' signals are hidden beneath those of other iron species is eliminated here because HFEPR is, in contrast to magnetometry, able to resolve these different iron species independently from each other.

As only a comparative analysis based on the spectra is possible, no further definitive statements on the nature of the solubilized iron pools can be made based on the HFEPR investigations.

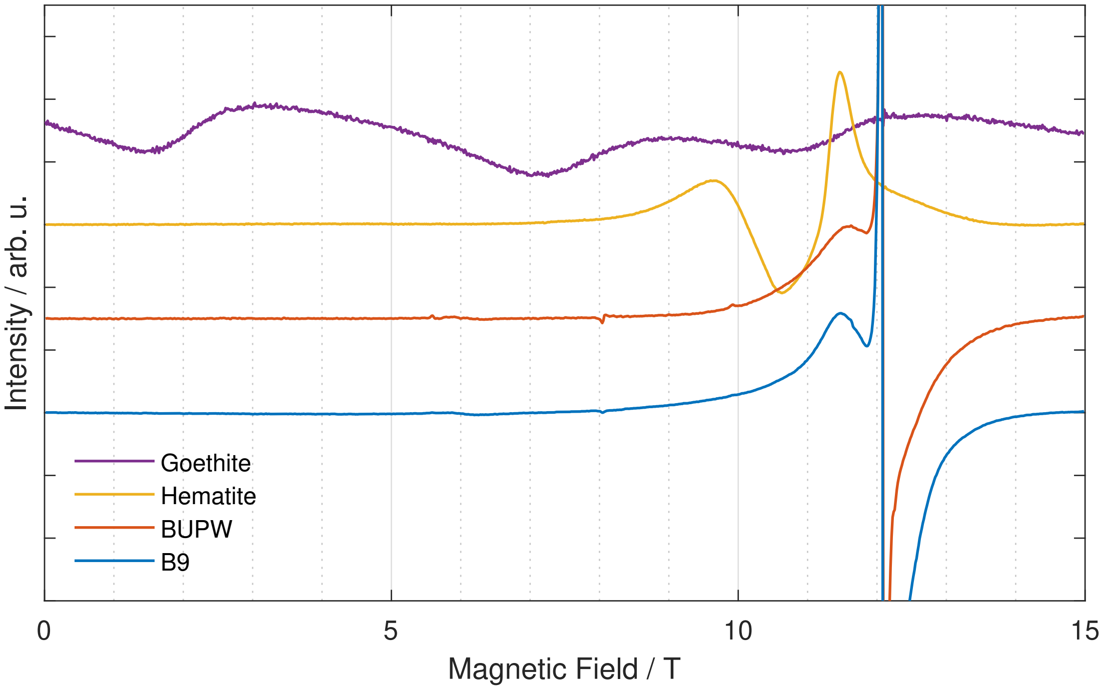

Figure 5.31: High-frequency EPR spectra of the pure soil extracts **B9** and **BUPW** in comparison with **hematite** and **goethite** at 340 GHz and temperatures close to 12 K.

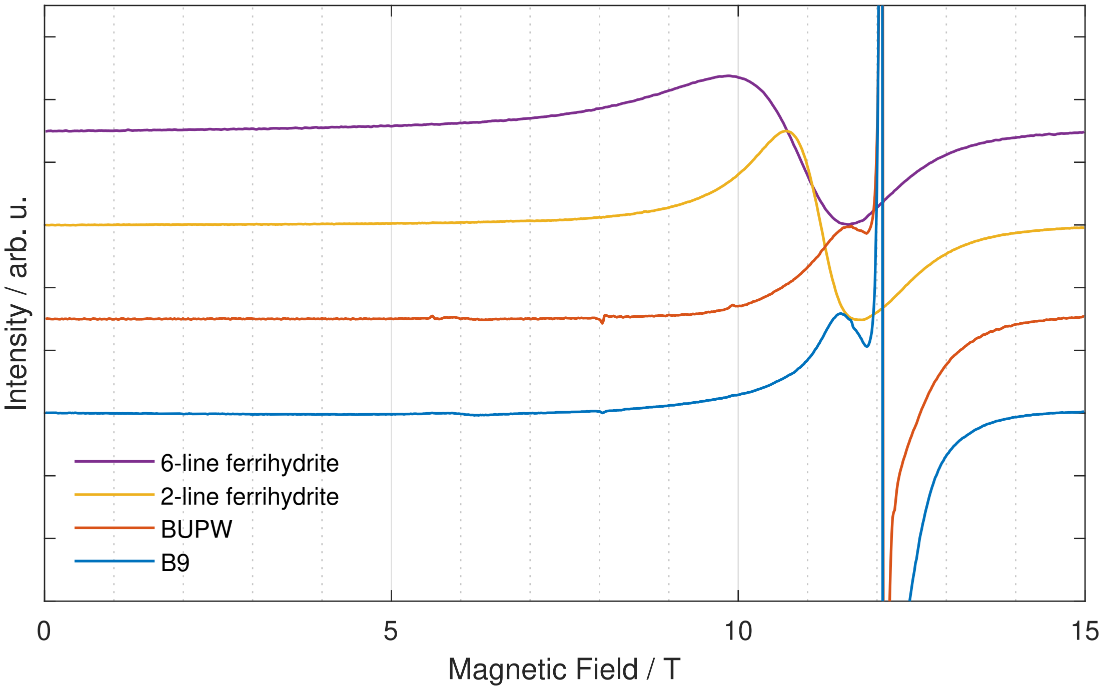

Figure 5.32: High-frequency EPR spectra of the pure soil extracts **B9** and **BUPW** in comparison with **2-line ferrihydrite** and **6-line ferrihydrite** at 340 GHz and temperatures close to 12 K.

Conclusion

Neither magnetometry nor HFEPR spectroscopy yielded indications of presence of the investigated minerals in the direct soil extracts **B9** and **BUPW**. Consequently, minerals are either not transferred from the soil into the extracts at all or their content in the extracts is too small to be detected. This insight is supported by the presence of only small amounts of mineral iron in the investigated B horizon of $100\,\mathrm{mg_{Fe}\,kg_{soil}^{-1}}$[121]. Possibly in case of **B9**, the iron is solubilized from the minerals by the treatment with sodium hydroxide solution[124] which could partially explain the difference in absolute iron content for **B9** and **BUPW**.

5.5. Summary and Conclusion

The set of selected methods, consisting of HFEPR spectroscopy, Mössbauer spectroscopy and SQUID magnetometry, has been proven able to yield new insights into the extraction of iron from a podzol by the biogenic ligand DFOB. Especially, it was possible to get direct proof of the formation of **FeDFOB** by HFEPR and Mössbauer spectroscopy.

Most pleasant, for the time-dependent complexation, the combination of all three methods revealed a conclusive picture of the occurring processes, giving a qualitative estimation of extraction kinetics. Namely, a significant amount of the iron which is available to DFOB is complexated within the first minutes (36 % within 5 min) and hours (60 % within 4 h) of extraction, as shown by HFEPR spectroscopy. Both percentages are compared to the extraction after 24 h. The iron pool targeted within the first minutes was attributed to iron bound by dissolved organic matter because the ligand exchange with DFOB is expected to happen rather fast due to the hexadentate nature of DFOB. Magnetometry revealed that the targeted iron pool for longer complexation times is an antiferromagnetic species which could not be conclusively identified. To gain a more detailed insight into the complexation kinetics, more samples with extraction times larger 24 h and between 4 h and 24 h would be needed to be investigated. At the same time, it would be useful to improve the result's statistical significance by investigating more samples with same complexation times. Additionally, the specificity of Mössbauer spectroscopy for iron could be used better by analyzing more samples with it. Regrettably, these points were not possible during this project.

Investigating samples extracted from soil at different acidity did not yield usable insights concerning the iron pools targeted by DFOB. In contrast, insight regarding the iron targeted during extraction from soil could be gained, which is mainly of antiferromagnetic nature. Additionally, an extraction at natural pH 4 and subsequent treatment at pH 9 yields a different sample composition than extracting directly at pH 9. Most probable, this is explained by different accessed iron pools at different acidity. With Mössbauer spectroscopy, an additional species was found in **BUPW** compared to **B9** but with HFEPR and magnetometry it was not possible to clarify this as the systems are overall poorly undefined.

The investigation of minerals possibly present in the podzol showed that none of the minerals **hematite**, **goethite**, **2-line ferrihydrite** and **6-line ferrihydrite** is present in the soil extracts. This means that either none of these minerals is transferred from the podzol into the samples or that the minerals are destroyed during the extraction process. For a better understanding, an analysis of the residue of extraction could have been very helpful.

6. Experimental Part

6.1. Synthesis and Structural Characterization

6.1.1. Synthesis and Structural Characterization of the Mono- and Dinuclear Fe(I), Fe(II), Co(II) and Ni(II) Complexes

The mononuclear Fe(III), Fe(II), Co(II) and Ni(II) complexes and the dinuclear Co(II) complex were synthesized and structurally characterized by Uta Albold and coworkers (Institut für Chemie und Biochemie, Freie Universität Berlin at the time). Details on the syntheses and structural data of the mononuclear complexes can be found in Reference [60]. The synthesis and crystallographic details of the dinuclear Co(II) complex are described in Reference [97].

6.1.2. Preparation and Characterization of the Soil extracts and Iron Oxides

All soil extracts, DFOB samples and **FeDFOB** were prepared by Dr. Walter Schenkeveld and coworkers (Department of Environmental Geosciences, Universität Wien, now: Department of Environmental Science, Wageningen University). The soil extracts were continuously stored at −60 °C after preparation.

Soil samples **BUPW** and **B9** were taken close to Schrems, Waldviertel, Lower Austria from the B horizon. The samples were air dried, homogenized and sieved with a 2 mm mesh. Organic and inorganic nanoparticles were extracted with ultrapure water (natural pH value approximately 4, **BUPW**) and at pH 9 (**B9**) which was adjusted by adding 1 M NaOH dropwise. The extracts were centrifuged and filtered (0.2 µm) before freeze-drying. **BUPW9** was prepared by dissolving **BUPW** in water, setting the pH to 9, filtration (0.2 µm) and freeze-drying. More details about the preparation of the extracts and their origin can be found in Literature [121].

DFOB was bought as mesylate salt from Novartis and used without further purification.

The samples **DFOB5m**, **DFOB4h** and **DFOB24h** were prepared by adding DFOB to the dissolved **B9** extract and freeze-drying the solution after 5 minutes, 4 hours and 24 hours, respectively, as indicated in the sample names. DFOB was added in 2.86-fold excess to the total iron content in the corresponding sample.

FeDFOB was synthesized by dissolving the DFOB mesylate salt in water and adding an acidified solution of $FeCl_3$ in small excess over the stochiometric ratio. Subsequently, the pH values was titrated up to 8.5. The solution was stored in the dark for several hours, filtered over 0.2 µm to remove precipitated excess iron compounds and freeze-dried.

Goethite was prepared according to literature[125].

The **hematite**, **2-line ferrihydrite** and **6-line ferrihydrite** samples were synthesized according to literature[126].

Mössbauer spectra were measured by Dr. James Byrne in the group of Prof. Andreas Kappler (Zentrum für Angewandte Geowissenschaften, Eberhardt Karls Universität Tübingen).

ICP-MS measurements for determination of the sample compositions were performed by Dr. Joachim Opitz (Institut für Mineralogie und Kristallchemie, Universität Stuttgart).

6.2. Magnetic and Spectroscopic Measurements

6.2.1. SQUID Magnetometry

Magnetic measurements were carried out on a Quantum Design MPMS 3 SQUID magnetometer. Samples were prepared by wrapping the pulverized compound in teflon tape and pressing to pellets with a diameter of 5 mm. Susceptibility measurements were performed at static fields of 1000 Oe between 1.8 K and 50 K and 10 000 Oe between 40 K and 300 K. The overlapping region was used to correct data for ferromagnetic impurities. All magnetic data, for which the sample's molecular composition was known, were corrected for diamagnetic contributions using Pascal's constants[55].

6.2.2. Far-Infrared Spectroscopy

Far-infrared spectra of $\mathbf{K_2}$[**1**] and $\mathbf{(HNEt_3)_2}$[**3**] were recorded on a Bruker VERTEX 70v FTIR spectrometer with an Hg-Arc lamp as light source and an Infrared Laboratories HDL-5 liquid helium bolometer as detector. Samples were prepared as pressed pellets of $\mathbf{K_2}$[**1**] and $\mathbf{(HNEt_3)_2}$[**3**] dispersed in icosane and placed inside an Oxford Instruments 15/17 T solenoid cryomagnet. Measurements were carried out at 5 K and magnetic fields between 0 T and 15 T. The setup was designed by Jana Midlíková (Brno University of Technology)[89].

Far-infrared spectra of $\mathbf{(K\text{-}18\text{-}c\text{-}6)_3}$[**5**] were recorded by Dr. Milan Orlita (Laboratoire National des Champs Magnétiques Intenses, Grenoble) at magnetic fields between 0 T and 11 T at 4.2 K using a Bruker IFS 66v/s FTIR spectrometer. The obtained spectra were baseline corrected using a linear model. The reference measurements were obtained under the same conditions as the sample measurements but instead of the sample an inset was placed in the beam path. Changing between sample and inset was possible in situ. The inset reduced the diameter of the beam path which was necessary to reduce the intensity of the incident light on the detector element to prevent it from being damaged by overload. The sample was prepared as a pressed pellet of $\mathbf{(K\text{-}18\text{-}c\text{-}6)_3}$[**5**] dispersed in icosane and placed inside a 11 T solenoid magnet with a composite bolometer detector element inside the magnet.

6.2.3. High-Frequency EPR Spectroscopy

High-Frequency EPR spectra in the range between 90 GHz and 700 GHz, at applied magnetic fields up to 15 T and at temperatures between 5 K and 100 K were recorded on a home-built spectrometer described in Reference [58]. Samples were prepared as pure pressed powder pellets with a diameter of 5 mm and masses between 10 mg and 25 mg.

6.2.4. Magnetic Circular Dichroism Spectroscopy

MCD spectra were recorded on a spectrometer built around an Aviv 42 CD spectrometer and an Oxford Instruments Spectromag SM4000 optical cryomagnet, allowing measurements at wavelengths between 250 nm and 2000 nm at temperatures down to 1.5 K and fields up to 10 T. Samples were prepared as mulls in fluorolube. All measurements were baseline corrected by subtraction of the measurement with antiparallel magnetic field and light beam from the measurement with parallel field and light beam.

6.3. Analysis

6.3.1. Calculation of Magnetic and Spectroscopic Data

Calculations of dc susceptibility, magnetization curves and EPR and FIR spectra based on Spin Hamiltonians were carried out using the EasySpin[127] toolbox for MATLAB.

6.3.2. Theoretical Calculations

Ab initio calculations of the mono- and dinuclear transition metal complexes were performed by Philipp Hallmen (Institut für Physikalische Chemie, Universität Stuttgart) using MOLPRO. Computational details can be found in References [81–83, 97].

Bibliography

[1] R. Sessoli, D. Gatteschi, A. Caneschi, M. A. Novak, Nature **1993**, *365*, 141–143.

[2] R. Sessoli, H. L. Tsai, A. R. Schake, S. Wang, J. B. Vincent, K. Folting, D. Gatteschi, G. Christou, D. N. Hendrickson, J. Am. Chem. Soc. **1993**, *115*, 1804–1816.

[3] E.-C. Yang, D. N. Hendrickson, W. Wernsdorfer, M. Nakano, L. N. Zakharov, R. D. Sommer, A. L. Rheingold, M. Ledezma-Gairaud, G. Christou, J. Appl. Phys. **2002**, *91*, 7382.

[4] A. M. Ako, I. J. Hewitt, V. Mereacre, R. Clérac, W. Wernsdorfer, C. E. Anson, A. K. Powell, Angew. Chem. Int. Ed. **2006**, *45*, 4926–4929.

[5] D. Wu, D. Guo, Y. Song, W. Huang, C. Duan, Q. Meng, O. Sato, Inorg. Chem. **2009**, *48*, 854–860.

[6] M. S. Fataftah, J. M. Zadrozny, D. M. Rogers, D. E. Freedman, Inorg. Chem. **2014**, *53*, 10716–10721.

[7] S. Demir, I.-R. Jeon, J. R. Long, T. D. Harris, Coord. Chem. Rev. **2015**, *289-290*, 149–176.

[8] C. A. P. Goodwin, F. Ortu, D. Reta, N. F. Chilton, D. P. Mills, Nature **2017**, *548*, 439–442.

[9] F.-S. Guo, B. M. Day, Y.-C. Chen, M.-L. Tong, A. Mansikkamäki, R. A. Layfield, Science **2018**, *362*, 1400–1403.

[10] M. Murugesu, M. Habrych, W. Wernsdorfer, K. A. Abboud, G. Christou, J. Am. Chem. Soc. **2004**, *126*, 4766–4767.

[11] F. Neese, D. A. Pantazis, Faraday Discuss. **2011**, *148*, 299–314.

[12] Y. Rechkemmer, F. D. Breitgoff, M. van der Meer, M. Atanasov, M. Hakl, M. Orlita, P. Neugebauer, F. Neese, B. Sarkar, J. van Slageren, Nat. Commun. **2016**, *7*, 10467.

[13] J. W. Kadereit, C. Körner, P. Nick, U. Sonnewald, *Strasburger - Lehrbuch der Pflanzenwissenschaften*, 38. Auflage, Springer Spektrum, Berlin and Heidelberg, **2021**.

[14] W. D. C. Schenkeveld, R. Dijcker, A. M. Reichwein, E. J. M. Temminghoff, W. H. van Riemsdijk, Plant Soil **2008**, *303*, 161–176.

[15] W. D. C. Schenkeveld, E. J. M. Temminghoff, A. M. Reichwein, W. H. van Riemsdijk, Plant Soil **2010**, *332*, 69–85.

[16] J. W. Stucki, B. A. Goodman, U. Schwertmann, *Iron in Soils and Clay Minerals*, Springer Netherlands, Dordrecht, **1987**.

[17] J. Bartolomé, F. Luis, J. F. Fernández (eds.), *Molecular Magnets: Physics and Applications*, Springer, Heidelberg, **2014**.

[18] G. Aromí, E. K. Brechin in *Single-molecule magnets and related phenomena*, (Eds.: R. Winpenny, G. Aromí), Structure and Bonding 122, Springer, Berlin, **2006**, pp. 1–67.

[19] J. B. Neilands, J. Biol. Chem. **1995**, *270*, 26723–26726.

[20] G. Winkelmann, Biometals **2007**, *20*, 379–392.

[21] J. A. Garibaldi, J. B. Neilands, Nature **1956**, *177*, 526–527.

[22] S. M. Kraemer, D. E. Crowley, R. Kretzschmar in, Advances in Agronomy 91, Academic Press, **2006**, pp. 1–46.

[23] Z. Yehuda, Y. Hadar, Y. Chen, J. Agric. Food. Chem. **2003**, *51*, 5996–6005.

[24] D. Gatteschi, R. Sessoli, J. Villain, *Molecular Nanomagnets*, Oxford University Press, **2006**.

[25] C. Benelli, D. Gatteschi, *Introduction to Molecular Magnetism: From Transition Metals to Lanthanides*, Wiley-VCH, Weinheim, Germany, **2015**.

[26] D. Jiles, *Introduction to Magnetism and Magnetic Materials*, 2. ed., Chapman & Hall, London, **1998**.

[27] S. Chikazumi, *Physics of magnetism*, John Wiley & Sons, New York, London, and Sydney, **1964**.

[28] A. Hubert, R. Schäfer, *Magnetic domains: The Analysis of Magnetic Microstructures*, Springer, Berlin, **1998**.

[29] S. T. Liddle, J. van Slageren, Chem. Soc. Rev. **2015**, *44*, 6655–6669.

[30] R. Fontana, G. Decad, A Ten Year (2008-2017) Storage Landscape: LTO Tape Media, HDD, NAND, 34th International Conference on Massive Storage Systems and Technology, **2018**.

[31] A. Baniodeh, N. Magnani, Y. Lan, G. Buth, C. E. Anson, J. Richter, M. Affronte, J. Schnack, A. K. Powell, npj Quantum Mater. **2018**, *3*, 10.

[32] A. L. Barra, D. Gatteschi, R. Sessoli, Phys. Rev. B **1997**, *56*, 8192–8198.

[33] F. Neese, E. I. Solomon, Inorg. Chem. **1998**, *37*, 6568–6582.

[34] P. C. Bunting, M. Atanasov, E. Damgaard-Møller, M. Perfetti, I. Crassee, M. Orlita, J. Overgaard, J. van Slageren, F. Neese, J. R. Long, Science **2018**, *362*, eaat7319.

[35] C. R. Ganivet, B. Ballesteros, G. de La Torre, J. M. Clemente-Juan, E. Coronado, T. Torres, Chem. Eur. J. **2013**, *19*, 1457–1465.

[36] J. D. Rinehart, M. Fang, W. J. Evans, J. R. Long, J. Am. Chem. Soc. **2011**, *133*, 14236–14239.

[37] J. D. Rinehart, M. Fang, W. J. Evans, J. R. Long, Nat. Chem. **2011**, *3*, 538.

[38] S. Demir, M. I. Gonzalez, L. E. Darago, W. J. Evans, J. R. Long, Nat. Commun. **2017**, *8*, 2144.

[39] S. Demir, J. M. Zadrozny, M. Nippe, J. R. Long, J. Am. Chem. Soc. **2012**, *134*, 18546–18549.

[40] P. Zhang, M. Perfetti, M. Kern, P. P. Hallmen, L. Ungur, S. Lenz, M. R. Ringenberg, W. Frey, H. Stoll, G. Rauhut, J. van Slageren, Chem. Sci. **2018**, *9*, 1221–1230.

[41] I.-R. Jeon, J. G. Park, D. J. Xiao, T. D. Harris, J. Am. Chem. Soc. **2013**, *135*, 16845–16848.

[42] M. Atanasov, D. Aravena, E. Suturina, E. Bill, D. Maganas, F. Neese, Coord. Chem. Rev. **2015**, *289-290*, 177–214.

[43] R. Boča, Coord. Chem. Rev. **2004**, *248*, 757–815.

[44] C. J. Ballhausen, *Introduction to Ligand Field Theory*, McGraw-Hill Book Comp., New York, **1962**.

[45] A. B. P. Lever, *Inorganic Electronic Spectroscopy*, *Vol. 1*, Elsevier, Amsterdam, London, and New York, **1968**.

[46] F. Hund, Z. Physik **1925**, *33*, 345–371.

[47] W. Pauli, Z. Physik **1925**, *31*, 765–783.

[48] Y. Tanabe, S. Sugano, J. Phys. Soc. Jpn. **1954**, *9*, 766–779.

[49] A. D. Liehr, C. Ballhausen, Ann. Phys. **1959**, *6*, 134–155.

[50] D. M. L. Goodgame, M. Goodgame, F. A. Cotton, J. Am. Chem. Soc. **1961**, *83*, 4161–4167.

[51] R. J. Lancashire, Tanabe-Sugano diagrams via spreadsheets, `http://wwwchem.uwimona.edu.jm/courses/Tanabe-Sugano/TSspread.html` (last accessed on 2019-10-29).

[52] V. Alekseenko, A. Alekseenko, J. Geochem. Explor. **2014**, *147*, 245–249.

[53] R. M. Cornell, U. Schwertmann, *The Iron Oxides: Structure, Properties, Reactions, Occurences and Uses*, VCH, Weinheim, **1996**.

[54] O. Kahn, *Molecular Magnetism*, VCH, New York, **1993**.

[55] G. A. Bain, J. F. Berry, J. Chem. Educ. **2008**, *85*, 532.

[56] A. Abragam, B. Bleaney, *Electron Paramagnetic Resonance of Transition Ions*, Oxford University Press, Oxford, **2013**.

[57] J. A. Weil, J. R. Bolton, *Electron Paramagnetic Resonance: Elementary Theory and Practical Applications*, 2nd ed., Wiley-Interscience, Hoboken, NJ, **2007**.

[58] P. Neugebauer, D. Bloos, R. Marx, P. Lutz, M. Kern, D. Aguilà, J. Vaverka, O. Laguta, C. Dietrich, R. Clérac, J. van Slageren, Phys. Chem. Chem. Phys. **2018**, *20*, 15528–15534.

[59] W. R. Mason, *A practical guide to magnetic circular dichroism spectroscopy*, Wiley-Interscience, Hoboken, NJ, **2007**.

[60] H. Bamberger, U. Albold, J. Dubnická Midlíková, C.-Y. Su, N. Deibel, D. Hunger, P. P. Hallmen, P. Neugebauer, J. Beerhues, S. Demeshko, F. Meyer, B. Sarkar, J. van Slageren, Inorg. Chem. **2021**, *60*, 2953–2963.

[61] F.-S. Guo, B. M. Day, Y.-C. Chen, M.-L. Tong, A. Mansikkamäki, R. A. Layfield, Angew. Chem. Int. Ed. **2017**, *56*, 11445–11449.

[62] J. M. Zadrozny, D. J. Xiao, M. Atanasov, G. J. Long, F. Grandjean, F. Neese, J. R. Long, Nat. Chem. **2013**, *5*, 577–581.

[63] X.-N. Yao, J.-Z. Du, Y.-Q. Zhang, X.-B. Leng, M.-W. Yang, S.-D. Jiang, Z.-X. Wang, Z.-W. Ouyang, L. Deng, B.-W. Wang, S. Gao, J. Am. Chem. Soc. **2017**, *139*, 373–380.

[64] S. Vaidya, S. Tewary, S. K. Singh, S. K. Langley, K. S. Murray, Y. Lan, W. Wernsdorfer, G. Rajaraman, M. Shanmugam, Inorg. Chem. **2016**, *55*, 9564–9578.

[65] T. J. Woods, M. F. Ballesteros-Rivas, S. Gómez-Coca, E. Ruiz, K. R. Dunbar, J. Am. Chem. Soc. **2016**, *138*, 16407–16416.

[66] R. Boča, C. Rajnák, J. Titiš, D. Valigura, Inorg. Chem. **2017**, *56*, 1478–1482.

[67] M. Atzori, L. Tesi, E. Morra, M. Chiesa, L. Sorace, R. Sessoli, J. Am. Chem. Soc. **2016**, *138*, 2154–2157.

[68] M. Ding, G. E. Cutsail, D. Aravena, M. Amoza, M. Rouzières, P. Dechambenoit, Y. Losovyj, M. Pink, E. Ruiz, R. Clérac, J. M. Smith, Chem. Sci. **2016**, *7*, 6132–6140.

[69] D. E. Freedman, W. H. Harman, T. D. Harris, G. J. Long, C. J. Chang, J. R. Long, J. Am. Chem. Soc. **2010**, *132*, 1224–1225.

[70] D. Weismann, Y. Sun, Y. Lan, G. Wolmershäuser, A. K. Powell, H. Sitzmann, Chemistry **2011**, *17*, 4700–4704.

[71] G.-L. Li, S.-Q. Wu, L.-F. Zhang, Z. Wang, Z.-W. Ouyang, Z.-H. Ni, S.-Q. Su, Z.-S. Yao, J.-Q. Li, O. Sato, Inorg. Chem. **2017**, *56*, 8018–8025.

[72] N. Ge, Y.-Q. Zhai, Y.-F. Deng, Y.-S. Ding, T. Wu, Z.-X. Wang, Z. Ouyang, H. Nojiri, Y.-Z. Zheng, Inorg. Chem. Front. **2018**, *5*, 2486–2492.

[73] R. C. Poulten, M. J. Page, A. G. Algarra, J. J. Le Roy, I. López, E. Carter, A. Llobet, S. A. Macgregor, M. F. Mahon, D. M. Murphy, M. Murugesu, M. K. Whittlesey, J. Am. Chem. Soc. **2013**, *135*, 13640–13643.

[74] J. Miklovič, D. Valigura, R. Boča, J. Titiš, Dalton Trans. **2015**, *44*, 12484–12487.

[75] K. E. R. Marriott, L. Bhaskaran, C. Wilson, M. Medarde, S. T. Ochsenbein, S. Hill, M. Murrie, Chem. Sci. **2015**, *6*, 6823–6828.

[76] W. Lin, T. Bodenstein, V. Mereacre, K. Fink, A. Eichhöfer, Inorg. Chem. **2016**, *55*, 2091–2100.

[77] D. Lomjanský, J. Moncol', C. Rajnák, J. Titiš, R. Boča, Chem. Commun. **2017**, *53*, 6930–6932.

[78] J. Titiš, V. Chrenková, C. Rajnák, J. Moncol, D. Valigura, R. Boča, Dalton Trans. **2019**, *48*, 11647–11650.

[79] F. H. Allen, O. Kennard, D. G. Watson, L. Brammer, A. G. Orpen, R. Taylor, J. Chem. Soc. Perkin Trans. 2 **1987**, S1.

[80] J. M. Zadrozny, J. Telser, J. R. Long, Polyhedron **2013**, *64*, 209–217.

[81] P. P. Hallmen, C. Köppl, G. Rauhut, H. Stoll, J. van Slageren, J. Chem. Phys. **2017**, *147*, 164101.

[82] S. Lenz, H. Bamberger, P. P. Hallmen, Y. Thiebes, S. Otto, K. Heinze, J. van Slageren, Phys. Chem. Chem. Phys. **2019**, *21*, 6976–6983.

[83] P. P. Hallmen, H.-J. Werner, D. Kats, S. Lenz, G. Rauhut, H. Stoll, J. van Slageren, Phys. Chem. Chem. Phys. **2019**, *21*, 9769–9778.

[84] H.-H. Cui, F. Lu, X.-T. Chen, Y.-Q. Zhang, W. Tong, Z.-L. Xue, Inorg. Chem. **2019**, *58*, 12555–12564.

[85] M. R. Saber, K. R. Dunbar, Chem. Commun. **2014**, *50*, 12266–12269.

[86] E. Carl, S. Demeshko, F. Meyer, D. Stalke, Chemistry **2015**, *21*, 10109–10115.

[87] R. Herchel, L. Váhovská, I. Potočňák, Z. Trávníček, Inorg. Chem. **2014**, *53*, 5896–5898.

[88] L. Chen, S.-Y. Chen, Y.-C. Sun, Y.-M. Guo, L. Yu, X.-T. Chen, Z. Wang, Z. W. Ouyang, Y. Song, Z.-L. Xue, Dalton Trans. **2015**, *44*, 11482–11490.

[89] J. Midlíková, Master's Thesis, Brno University of Technology, Brno, **2018**.

[90] L. Banci, A. Bencini, C. Benelli, R. Bohra, J.-M. Dance, D. Gatteschi, V. K. Jain, R. C. Mehrotra, A. Tressaud, R. G. Woolley, C. Zanchini, *Structures versus Special Properties*, Springer, Berlin and Heidelberg, **1982**.

[91] A. T. Kowal, I. C. Zambrano, I. Moura, J. J. G. Moura, J. LeGall, M. K. Johnson, Inorg. Chem. **1988**, *27*, 1162–1166.

[92] S.-D. Jiang, D. Maganas, N. Levesanos, E. Ferentinos, S. Haas, K. Thirunavukkuarasu, J. Krzystek, M. Dressel, L. Bogani, F. Neese, P. Kyritsis, J. Am. Chem. Soc. **2015**, *137*, 12923–12928.

[93] J. Krzystek, J.-H. Park, M. W. Meisel, M. A. Hitchman, H. Stratemeier, L.-C. Brunel, J. Telser, Inorg. Chem. **2002**, *41*, 4478–4487.

[94] R. Ruamps, R. Maurice, L. Batchelor, M. Boggio-Pasqua, R. Guillot, A. L. Barra, J. Liu, E.-E. Bendeif, S. Pillet, S. Hill, T. Mallah, N. Guihéry, J. Am. Chem. Soc. **2013**, *135*, 3017–3026.

[95] S. Gómez-Coca, E. Cremades, N. Aliaga-Alcalde, E. Ruiz, Inorg. Chem. **2014**, *53*, 676–678.

[96] M. Azarkh, P. Gast, A. B. Mason, E. J. J. Groenen, G. Mathies, Phys. Chem. Chem. Phys. **2019**, *21*, 16937–16948.

[97] U. Albold, H. Bamberger, P. P. Hallmen, J. van Slageren, B. Sarkar, Angew. Chem. Int. Ed. **2019**, *58*, 9802–9806.

[98] M. Pinsky, D. Avnir, Inorg. Chem. **1998**, *37*, 5575–5582.

[99] A. Ferguson, A. Parkin, J. Sanchez-Benitez, K. Kamenev, W. Wernsdorfer, M. Murrie, Chem. Commun. **2007**, 3473–3475.

[100] Y.-S. Ding, K.-X. Yu, D. Reta, F. Ortu, R. E. P. Winpenny, Y.-Z. Zheng, N. F. Chilton, Nat. Commun. **2018**, *9*, 3134.

[101] I. Krivokapic, C. Noble, S. Klitgaard, P. Tregenna-Piggott, H. Weihe, A.-L. Barra, Angew. Chem. Int. Ed. **2005**, *44*, 3613–3616.

[102] J. A. DeGayner, K. Wang, T. D. Harris, J. Am. Chem. Soc. **2018**, *140*, 6550–6553.

[103] D. Yoshihara, S. Karasawa, N. Koga, J. Am. Chem. Soc. **2008**, *130*, 10460–10461.

[104] D. Yoshihara, S. Karasawa, N. Koga, Polyhedron **2011**, *30*, 3211–3217.

[105] T. J. Woods, M. F. Ballesteros-Rivas, S. M. Ostrovsky, A. V. Palii, O. S. Reu, S. I. Klokishner, K. R. Dunbar, Chemistry **2015**, *21*, 10302–10305.

[106] S. Fortier, J. J. Le Roy, C.-H. Chen, V. Vieru, M. Murugesu, L. F. Chibotaru, D. J. Mindiola, K. G. Caulton, J. Am. Chem. Soc. **2013**, *135*, 14670–14678.

[107] X. Ma, E. A. Suturina, S. De, P. Négrier, M. Rouzières, R. Clérac, P. Dechambenoit, Angew. Chem. Int. Ed. **2018**, *57*, 7841–7845.

[108] E. M. Fatila, M. Rouzières, M. C. Jennings, A. J. Lough, R. Clérac, K. E. Preuss, J. Am. Chem. Soc. **2013**, *135*, 9596–9599.

[109] B. S. Dolinar, D. I. Alexandropoulos, K. R. Vignesh, T. James, K. R. Dunbar, J. Am. Chem. Soc. **2018**, *140*, 908–911.

[110] B. S. Dolinar, S. Gómez-Coca, D. I. Alexandropoulos, K. R. Dunbar, Chem. Commun. **2017**, *53*, 2283–2286.

[111] G. Brunet, M. Hamwi, M. A. Lemes, B. Gabidullin, M. Murugesu, Commun. Chem. **2018**, *1*, 141.

[112] Zehava Yehuda, Yitzhak Hadar, Yona Chen, Plant Soil **2012**, *350*, 379–391.

[113] M. Fittipaldi, L. Sorace, A.-L. Barra, C. Sangregorio, R. Sessoli, D. Gatteschi, PCCP **2009**, *11*, 6555–6568.

[114] M. Fittipaldi, C. Innocenti, P. Ceci, C. Sangregorio, L. Castelli, L. Sorace, D. Gatteschi, Phys. Rev. B **2011**, *83*, 104409.

[115] M. Fittipaldi, R. Mercatelli, S. Sottini, P. Ceci, E. Falvo, D. Gatteschi, PCCP **2016**, *18*, 3591–3597.

[116] Quantum Design, Oxygen Contamination: MPMS Application Note 1014-210B, **1997-04-03**, `https://www.qdusa.com/siteDocs/appNotes/1014-210.pdf` (last accessed on 2021-02-28).

[117] Amin, Arajs, Phys. Rev. B **1987**, *35*, 4810–4811.

[118] R. D. Zysler, D. Fiorani, A. M. Testa, L. Suber, E. Agostinelli, M. Godinho, Phys. Rev. B **2003**, *68*, 212408.

[119] H. M. Lu, X. K. Meng, J. Phys. Chem. C **2010**, *114*, 21291–21295.

[120] C. Carbone, F. Di Benedetto, P. Marescotti, C. Sangregorio, L. Sorace, N. Lima, M. Romanelli, G. Lucchetti, C. Cipriani, Mineral. Petrol. **2005**, *85*, 19–32.

[121] E. Neubauer, W. D. C. Schenkeveld, K. L. Plathe, C. Rentenberger, F. von der Kammer, S. M. Kraemer, T. Hofmann, Sci. Total Environ. **2013**, *461-462*, 108–116.

[122] A. M. Ferretti, A.-L. Barra, L. Forni, C. Oliva, A. Schweiger, A. Ponti, J. Phys. Chem. B **2004**, *108*, 1999–2005.

[123] T. Okamoto, E. Ohmichi, S. Okubo, H. Ohta, J. Phys. Soc. Jpn. **2018**, *87*, 013702.

[124] K. Ishikawa, T. Yoshioka, T. Sato, A. Okuwaki, Hydrometallurgy **1997**, *45*, 129–135.

[125] H. Zhang, M. Bayne, S. Fernando, B. Legg, M. Zhu, R. L. Penn, J. F. Banfield, J. Phys. Chem. C **2011**, *115*, 17704–17710.

[126] R. M. Cornell, U. Schwertmann, *The Iron Oxides: Structure, Properties, Reactions, Occurences and Uses*, 2nd edition, Wiley-VCH, Weinheim, **2003**.

[127] S. Stoll, A. Schweiger, J. Magn. Reson. **2006**, *178*, 42–55.

A. Appendix

A.1. Mononuclear Complexes

A.1.1. Cobalt

Zero-Field-Cooled Field-Cooled Measurements

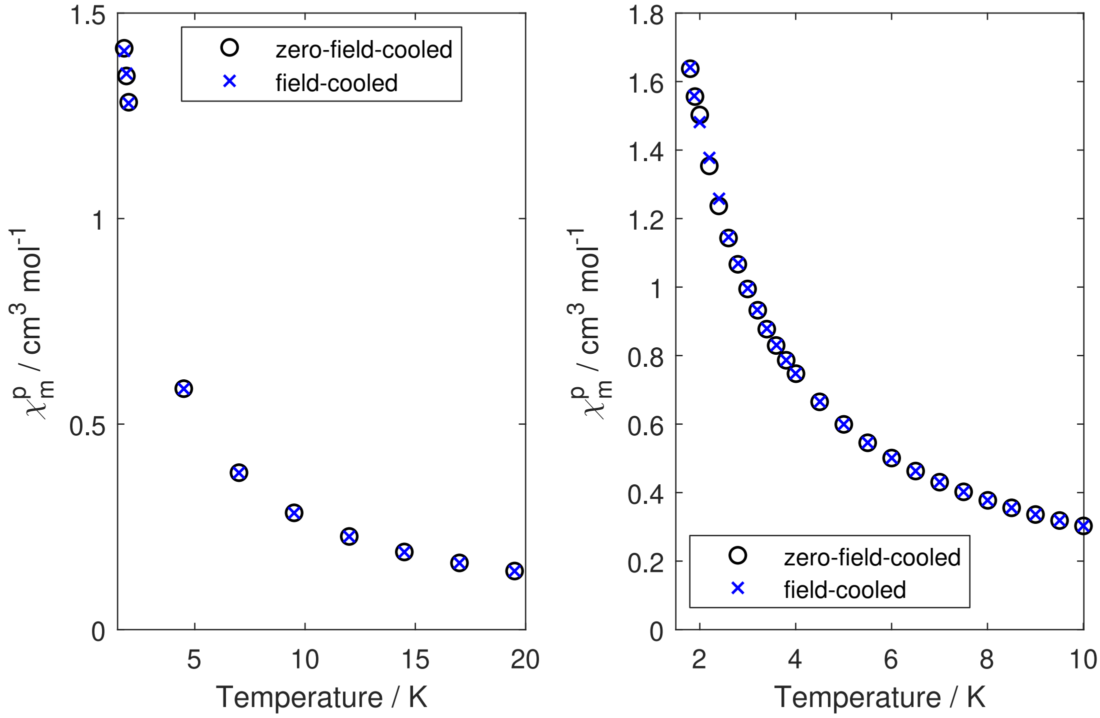

Figure A.1: Zero-field-cooled field-cooled measurement of $\mathbf{K_2[1]}$ (left) and $\mathbf{(HNEt_3)_2[2]}$ (right).

Dynamic Susceptibility Measurements of $K_2[1]$ in External Field

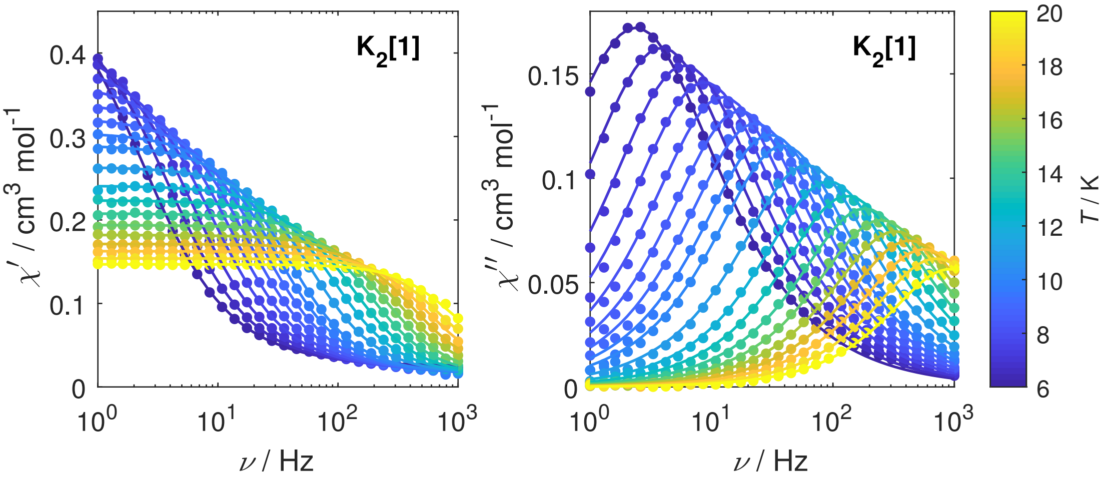

Figure A.2: In-phase (left) and out-of-phase (right) susceptibility of $\mathbf{K_2[1]}$ at frequencies and temperatures as indicated and 1000 Oe static field. Solid lines are simultaneous fits of in-phase and out-of-phase signals.

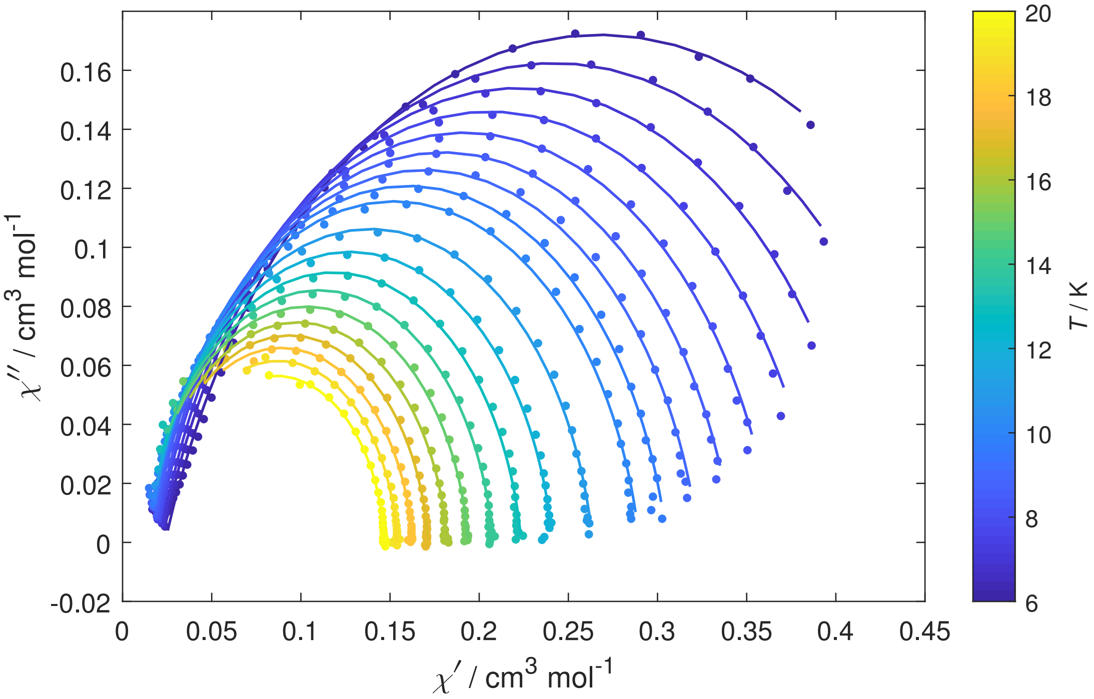

Figure A.3: Argand plot of $\mathbf{K_2[1]}$ at different temperatures and 1000 Oe static field. Solid lines correspond to best fits.

Fit Parameters of ac Susceptibility Measurements

Table A.1: Parameters obtained for simultaneous fitting of in-phase and out-of-phase susceptibility of $\mathbf{K_2[1]}$ at various temperatures and zero external dc field.

T / K	χ_T / $\mathrm{cm^3\,K\,mol^{-1}}$	χ_S / $\mathrm{cm^3\,K\,mol^{-1}}$	$\tau/10^{-4}$ s	α
6.5	0.472	0.061	36.7	0.441
7.0	0.431	0.064	31.7	0.396
7.5	0.398	0.065	27.3	0.353
8.0	0.371	0.062	22.9	0.323
8.5	0.347	0.061	19.6	0.293
9.0	0.326	0.057	16.5	0.268
9.5	0.308	0.055	14.2	0.245
10.0	0.292	0.051	12.0	0.227
11.0	0.265	0.048	8.9	0.196
12.0	0.242	0.044	6.7	0.165
13.0	0.224	0.040	5.2	0.146
14.0	0.208	0.038	4.1	0.131
15.0	0.194	0.036	3.2	0.109
16.0	0.182	0.035	2.6	0.094
17.0	0.172	0.034	2.1	0.085
18.0	0.163	0.033	1.7	0.078

Table A.2: Parameters obtained for simultaneous fitting of in-phase and out-of-phase susceptibility of **K_2[1]** at various temperatures and 1000 Oe external dc field.

T / K	χ_T / cm^3 K mol^{-1}	χ_S / cm^3 K mol^{-1}	$\tau/10^{-4}$ s	α
6	0.511	0.024	670.9	0.217
6.5	0.462	0.022	410.0	0.190
7	0.422	0.021	265.6	0.166
7.5	0.392	0.019	181.9	0.155
8	0.365	0.018	128.4	0.141
8.5	0.343	0.017	92.9	0.132
9	0.323	0.016	69.2	0.125
9.5	0.305	0.015	52.5	0.116
10	0.290	0.015	40.8	0.110
11	0.264	0.015	26.1	0.101
12	0.241	0.014	17.4	0.090
13	0.224	0.013	12.1	0.089
14	0.208	0.013	8.7	0.084
15	0.194	0.013	6.4	0.079
16	0.182	0.014	4.9	0.074
17	0.171	0.016	3.7	0.063
18	0.163	0.015	2.8	0.070
19	0.154	0.021	2.3	0.051
20	0.147	0.025	1.7	0.048

Table A.3: Parameters obtained for simultaneous fitting of in-phase and out-of-phase susceptibility of **(K-18-c-6)$_2$[1]** at various temperatures and zero external dc field.

T / K	χ_T / cm^3 K mol^{-1}	χ_S / cm^3 K mol^{-1}	τ / 10^{-4} s	α
3	1.526	0.0001	4201.6	0.659
4	1.096	0.0002	1426.7	0.612
5	0.848	0.009	650.6	0.551
6	0.645	0.025	286.1	0.444
7	0.517	0.034	151.7	0.333
8	0.431	0.037	86.6	0.236
9	0.379	0.034	54.2	0.186
10	0.337	0.033	34.5	0.140
11	0.305	0.029	22.8	0.122
12	0.279	0.029	15.9	0.093
13	0.257	0.026	11.3	0.082
14	0.238	0.027	8.5	0.063
15	0.223	0.027	6.5	0.056
16	0.209	0.025	5.0	0.048
17	0.197	0.024	3.8	0.046
18	0.187	0.027	3.1	0.032
19	0.179	0.028	2.4	0.034
20	0.169	0.030	1.9	0.025
21	0.161	0.033	1.5	0.023

Table A.4: Parameters obtained for simultaneous fitting of in-phase and out-of-phase susceptibility of **$(HNEt_3)_2$[2]** at various temperatures and zero external dc field.

T / K	χ_T / $cm^3\,K\,mol^{-1}$	χ_S / $cm^3\,K\,mol^{-1}$	τ / 10^{-4} s	α
5	0.694	0.037	260.9	0.402
6	0.564	0.038	143.5	0.312
7	0.476	0.035	82.3	0.245
8	0.414	0.032	50.6	0.196
9	0.366	0.027	31.8	0.163
10	0.329	0.026	21.3	0.130
11	0.299	0.023	14.6	0.112
12	0.274	0.024	10.5	0.093
13	0.254	0.022	7.7	0.081
14	0.236	0.020	5.8	0.077
15	0.220	0.020	4.5	0.067
16	0.206	0.022	3.6	0.054
17	0.195	0.023	2.9	0.046
18	0.184	0.026	2.5	0.032

Zero-Field FIR Spectra of K_2[1] an d$(HNEt_3)_2$[3]

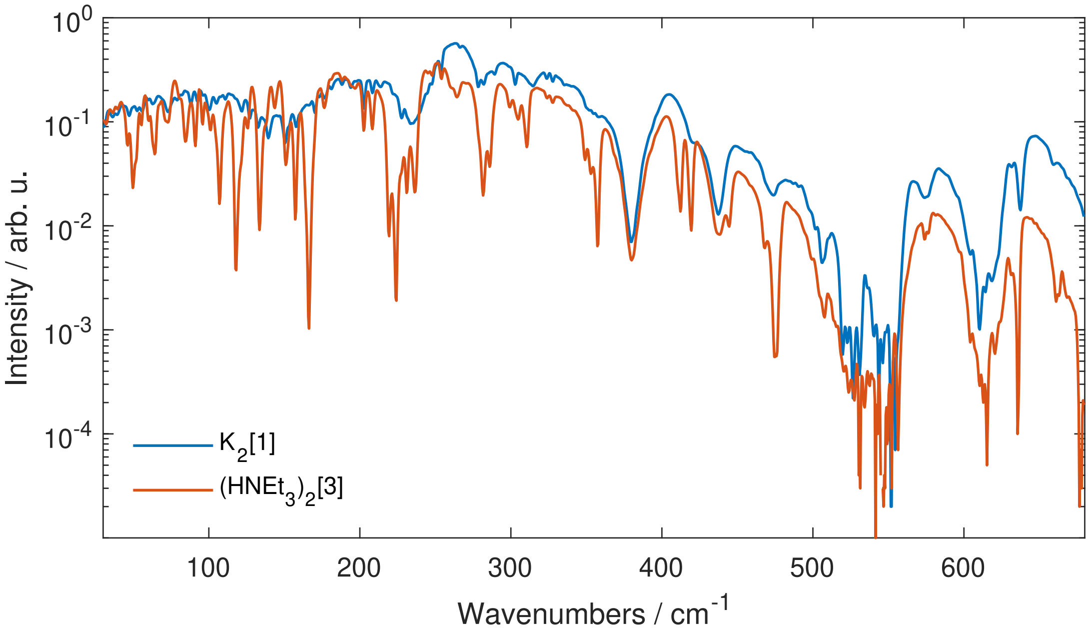

Figure A.4: Far-infrared spectra of **K_2[1]** and **$(HNEt_3)_2$[3]** at 5 K and 0 T.

A.1.2. Nickel

Magnetization Measurements

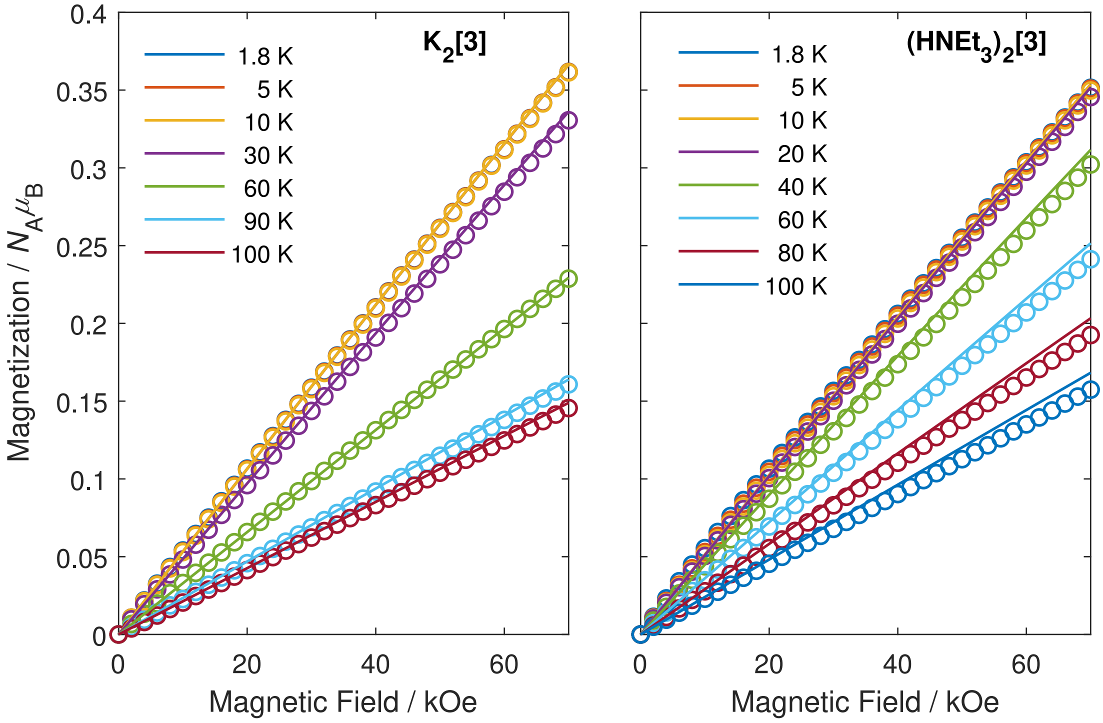

Figure A.5: Molecular magnetization of the nickel complexes versus magnetic field at temperatures as indicated. Solid lines are fits achieved by simultaneous fitting with $\chi T - T$ measurements ($\mathbf{K_2[3]}$) and FIR spectra ($\mathbf{(HNEt_3)_2[3]}$).

Dynamic Susceptibility Measurements of $K_2[3]$

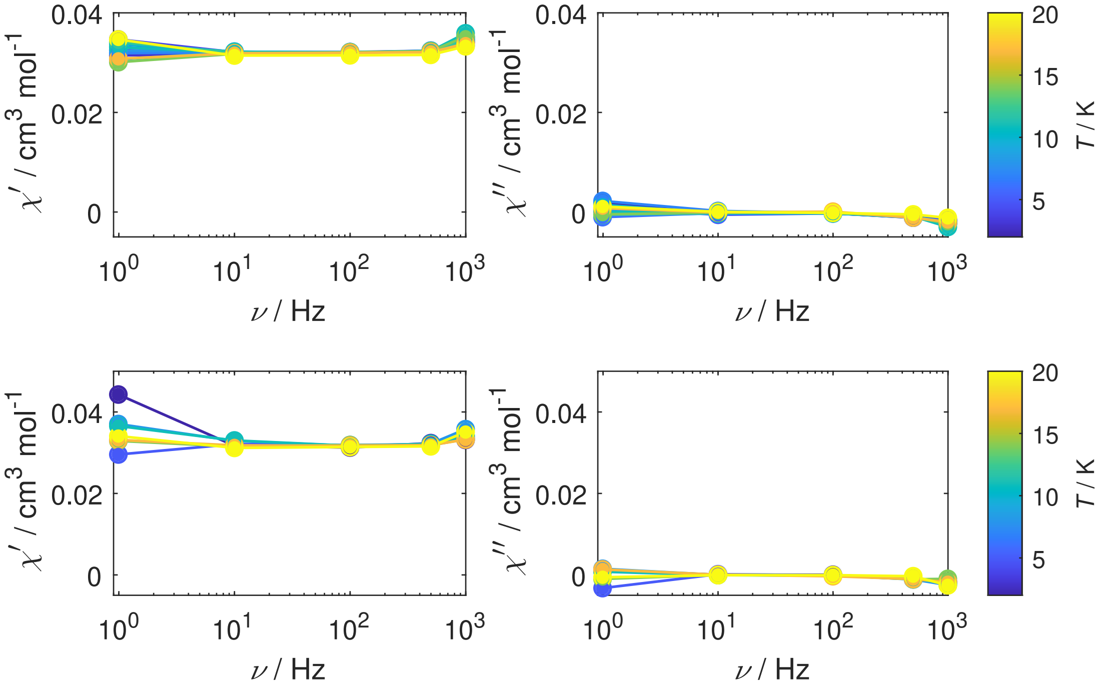

Figure A.6: In-phase (left) and out-of-phase (right) susceptibility of $\mathbf{K_2[3]}$ in zero (top) and 1000 Oe (bottom) applied static field at frequencies and temperatures as indicated. Solid lines are guides to the eye.

MCD spectra of $K_2[3]$

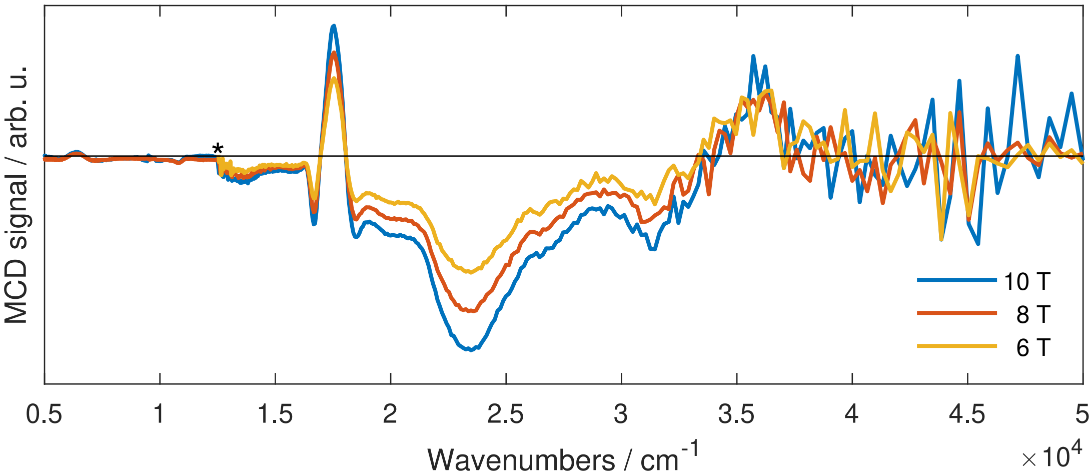

Figure A.7: MCD spectra of $\mathbf{K_2[3]}$ at 1.5 K and magnetic fields as indicated. The asterisk marks the artifact due to detector change.

A.1.3. Iron

Dynamic Susceptibility Measurements of $(HNEt_3)_2[4]$

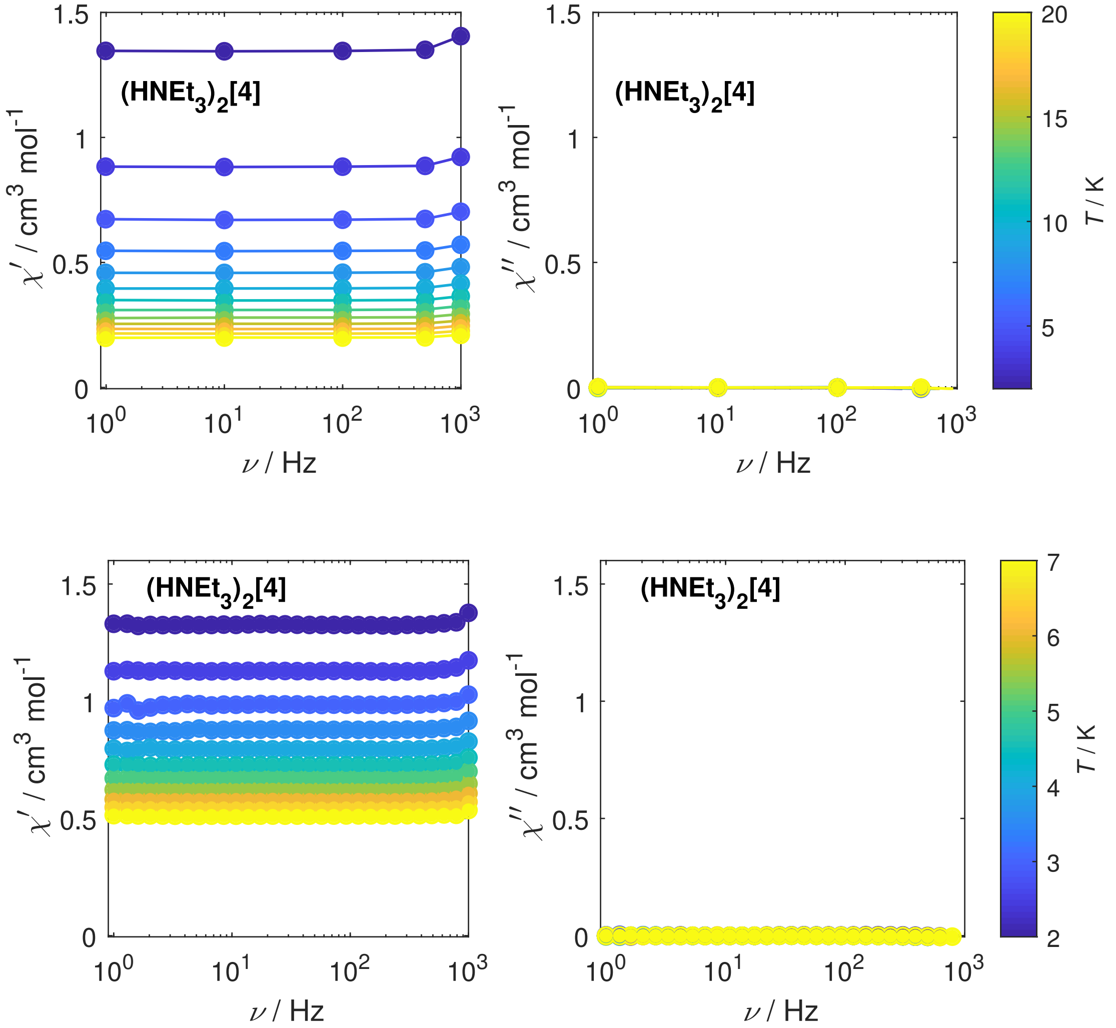

Figure A.8: In-phase (left) and out-of-phase (right) susceptibility of $\mathbf{(HNEt_3)_2[4]}$ in zero (top) and 1000 Oe (bottom) applied static field at frequencies and temperatures as indicated. Solid lines are guides to the eye.

HFEPR spectra of $(HNEt_3)_2[4]$

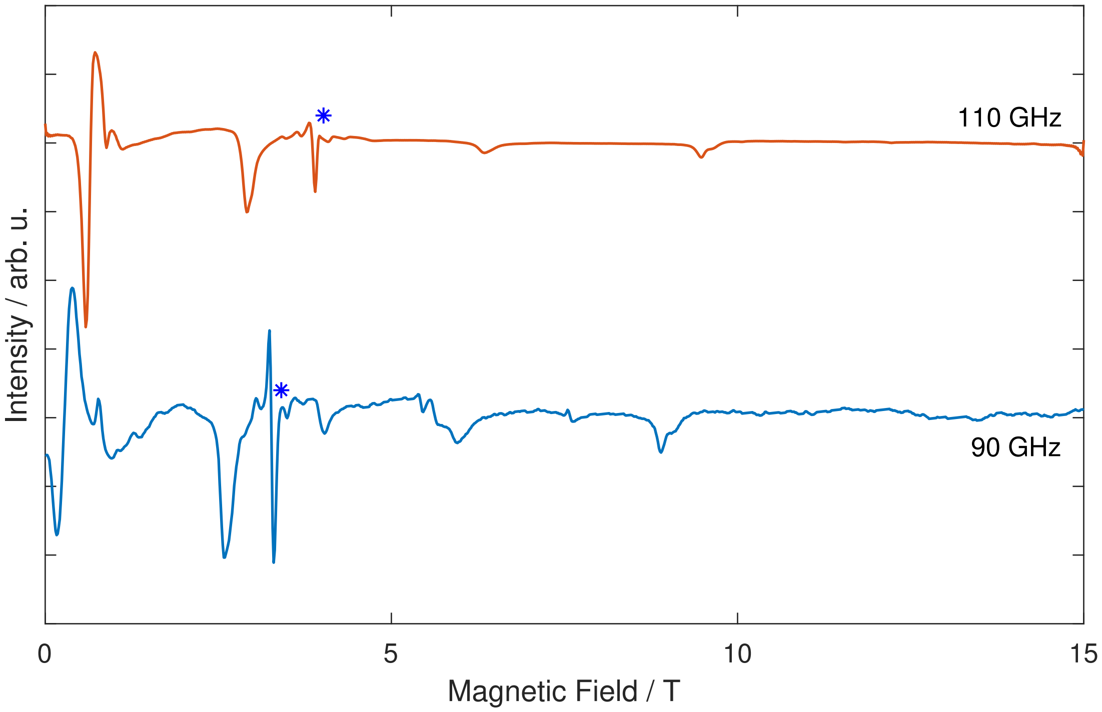

Figure A.9: High-frequency EPR measurements of $\mathbf{(HNEt_3)_2[4]}$ at 10 K and frequencies as indicated. $g = 2$-signals are marked with an asterisk.

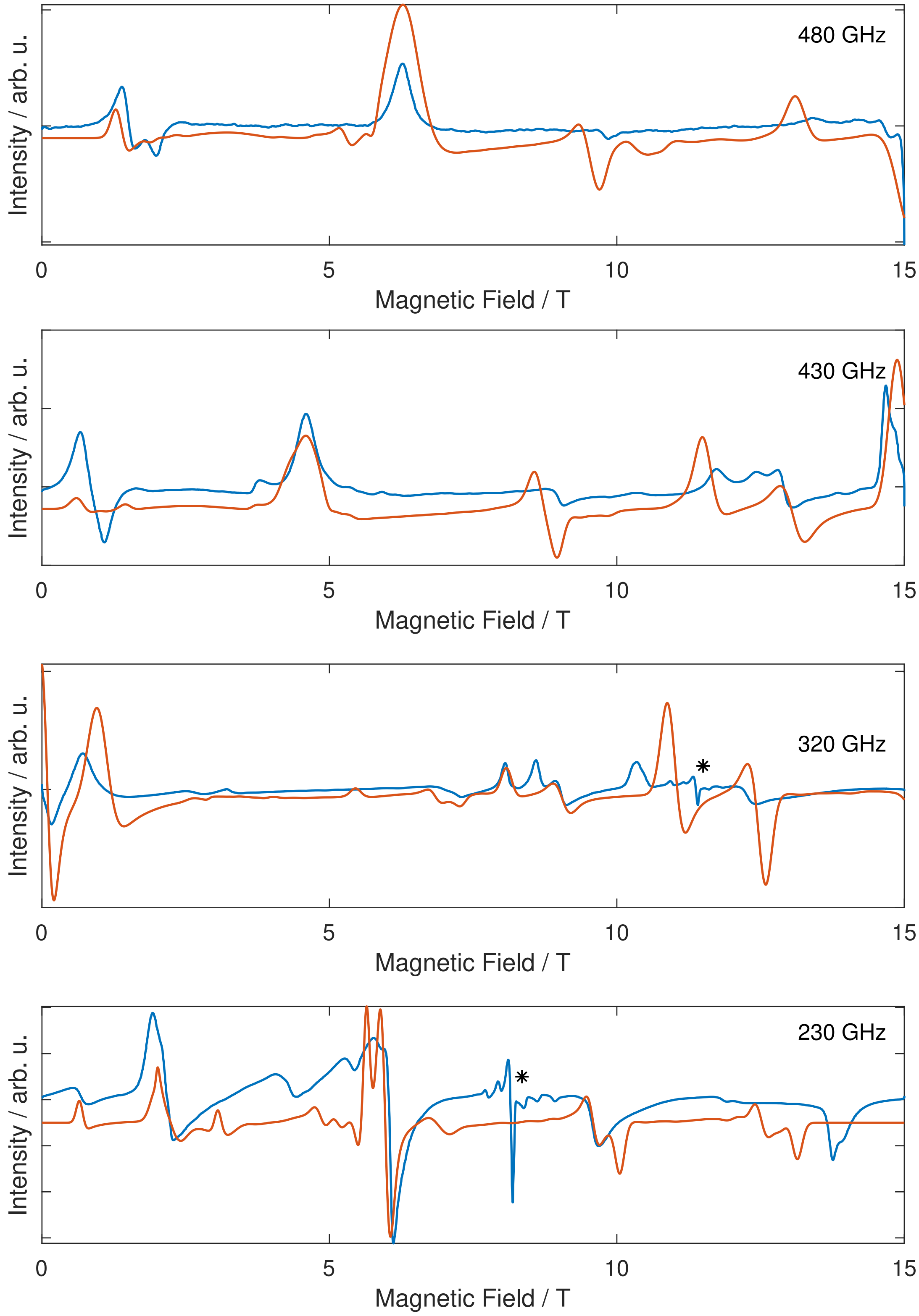

Figure A.10: Zoom of the high-frequency EPR measurements and simulations of **$(HNEt_3)_2$[4]** at 12 K and frequencies as indicated. $g = 2$-signals are marked with an asterisk.

Dynamic Susceptibility Measurements of (HNEt$_3$)[4]

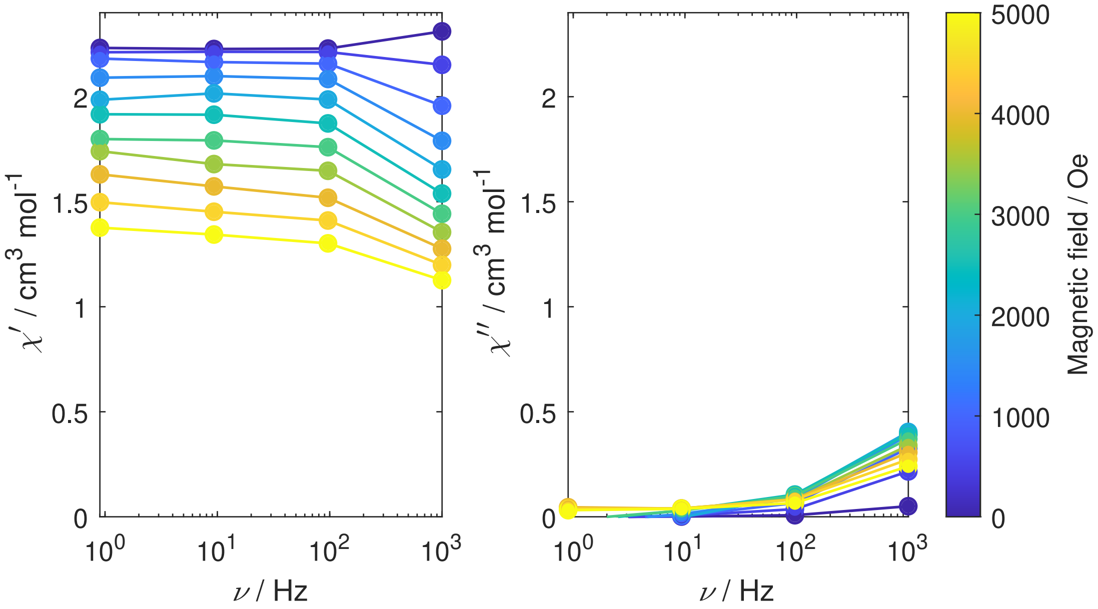

Figure A.11: In-phase (left) and out-of-phase (right) susceptibility of **(HNEt$_3$)[4]** at applied fields, frequencies and temperatures as indicated. Solid lines are guides to the eye.

HFEPR spectra of (HNEt$_3$)[4]

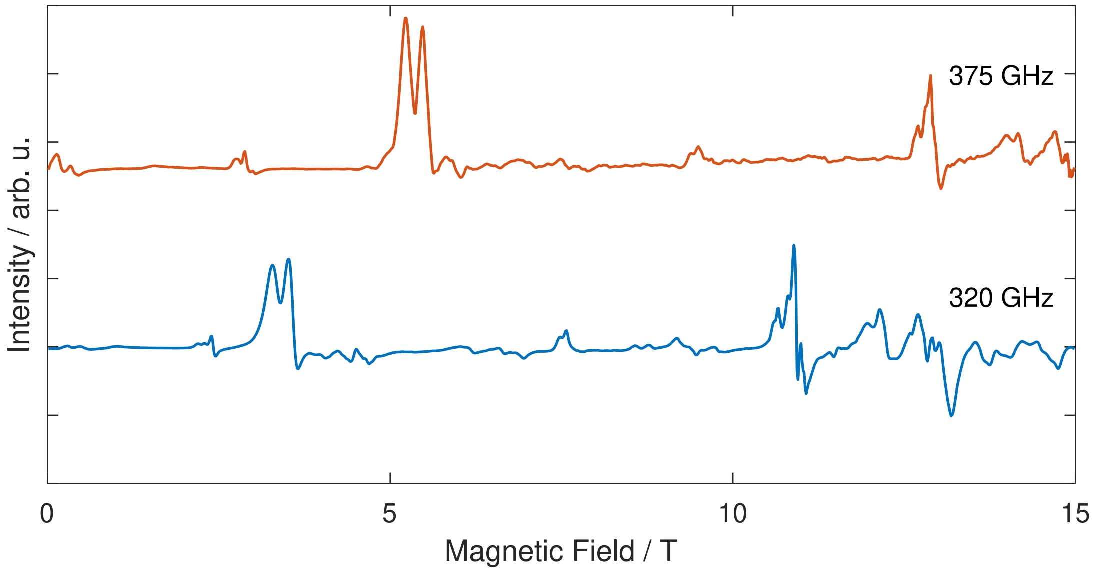

Figure A.12: High-frequency EPR measurements of **(HNEt$_3$)[4]** at 5 K and frequencies as indicated.

A.2. Radical-Bridged Dinuclear Cobalt Complex

A.2.1. Fit Parameters of ac Susceptibility Measurements

Table A.5: Parameters obtained for simultaneous fitting of in-phase and out-of-phase susceptibility of **(K-18-c-6)$_3$[5]** at various temperatures and zero external dc field.

Temperature / K	χ_T / $\mathrm{cm^3\,mol^{-1}}$	χ_S / $\mathrm{cm^3\,mol^{-1}}$	τ / s	α
2	3.51	0.067	1.7	0.397
3	2.50	0.050	0.99	0.346
4	1.90	0.040	0.66	0.311
5	1.54	0.033	0.48	0.298
6	1.28	0.029	0.38	0.299
7	1.11	0.028	0.31	0.308
8	0.99	0.026	0.27	0.324
9	0.88	0.026	0.23	0.328
10	0.79	0.026	0.21	0.338
11	0.72	0.026	0.19	0.342
12	0.65	0.028	0.17	0.338
13	0.60	0.031	0.16	0.343
14	0.56	0.033	0.15	0.345
15	0.52	0.036	0.14	0.351
16	0.50	0.037	0.14	0.366
17	0.48	0.037	0.12	0.385
18	0.45	0.038	0.090	0.393
19	0.44	0.039	0.067	0.422
20	0.41	0.041	0.036	0.416
21	0.39	0.042	0.018	0.413
22	0.36	0.047	0.0082	0.388
23	0.35	0.052	0.0039	0.366
24	0.33	0.065	0.0021	0.318
25	0.31	0.071	0.0011	0.287
26	0.30	0.080	0.000 62	0.248
27	0.29	0.098	0.000 39	0.183
28	0.28	0.097	0.000 23	0.192
29	0.27	0.104	0.000 15	0.150

A.2.2. Comparison Between AC and DC Susceptibility Values

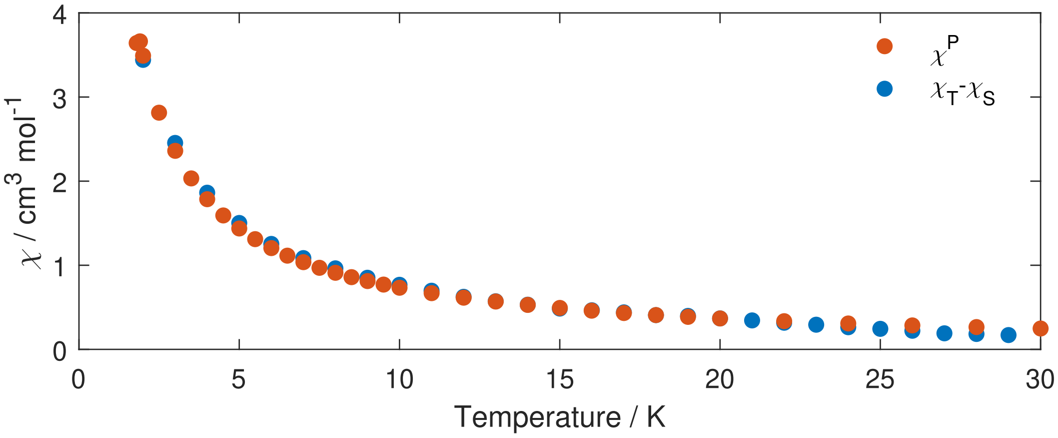

Figure A.13: Comparison between $\chi_T - \chi_S$ (ac measurement) and χ^P (dc measurement at 100 Oe) of **(K-18-c-6)$_3$[5]**, demonstrating that the entire sample is involved in the slow relaxation.

A.2.3. DC Magnetization Decay Measurements

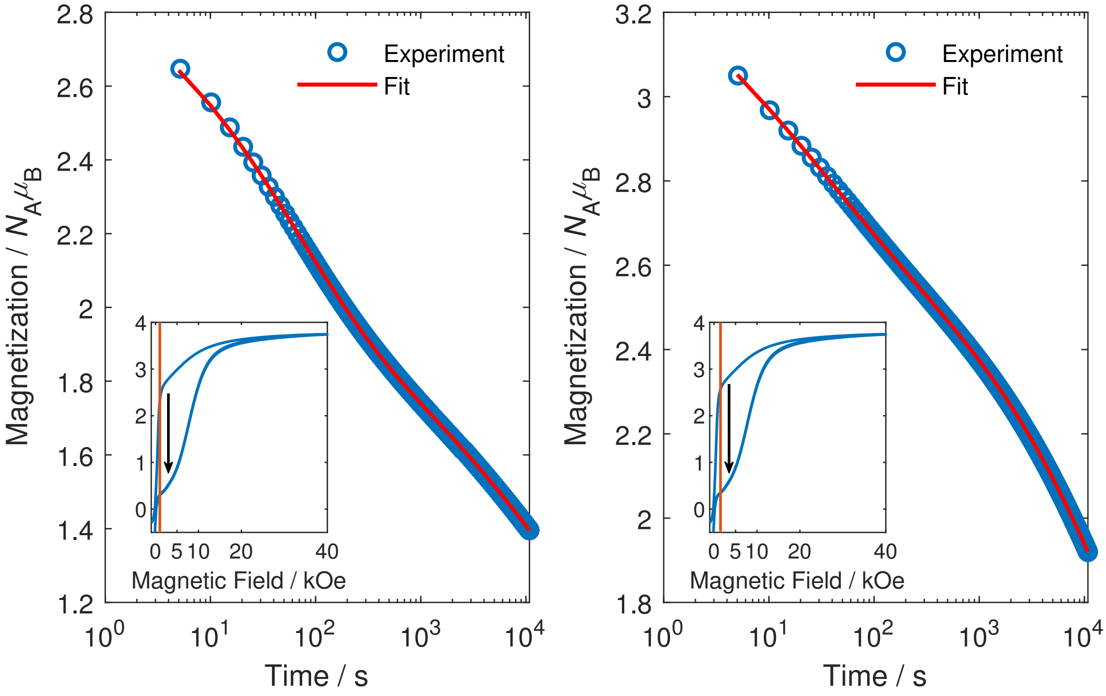

Figure A.14: DC magnetization decay curves as a function of time (circles) and corresponding fits (line) of **(K-18-c-6)$_3$[5]** at 1.8 K and 1000 Oe (left) and 1500 Oe (right). The insets show the positions in the hysteresis loop.

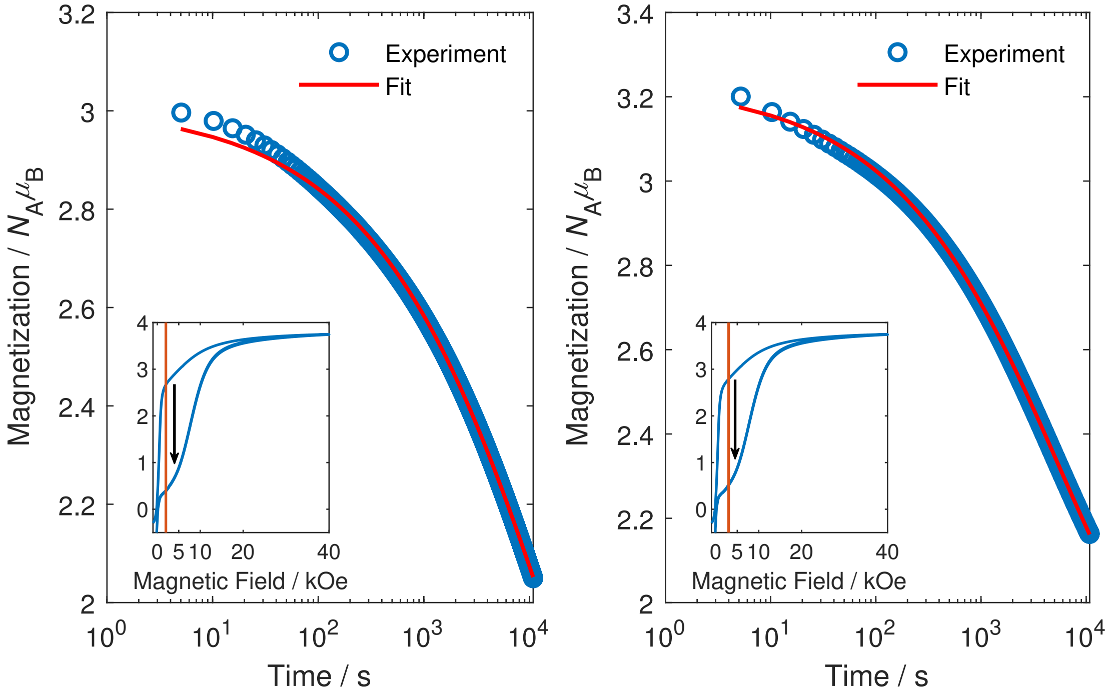

Figure A.15: DC magnetization decay curves as a function of time (circles) and corresponding fits (line) of **(K-18-c-6)$_3$[5]** at 1.8 K and 2000 Oe (left) and 3000 Oe (right). The insets show the positions in the hysteresis loop.

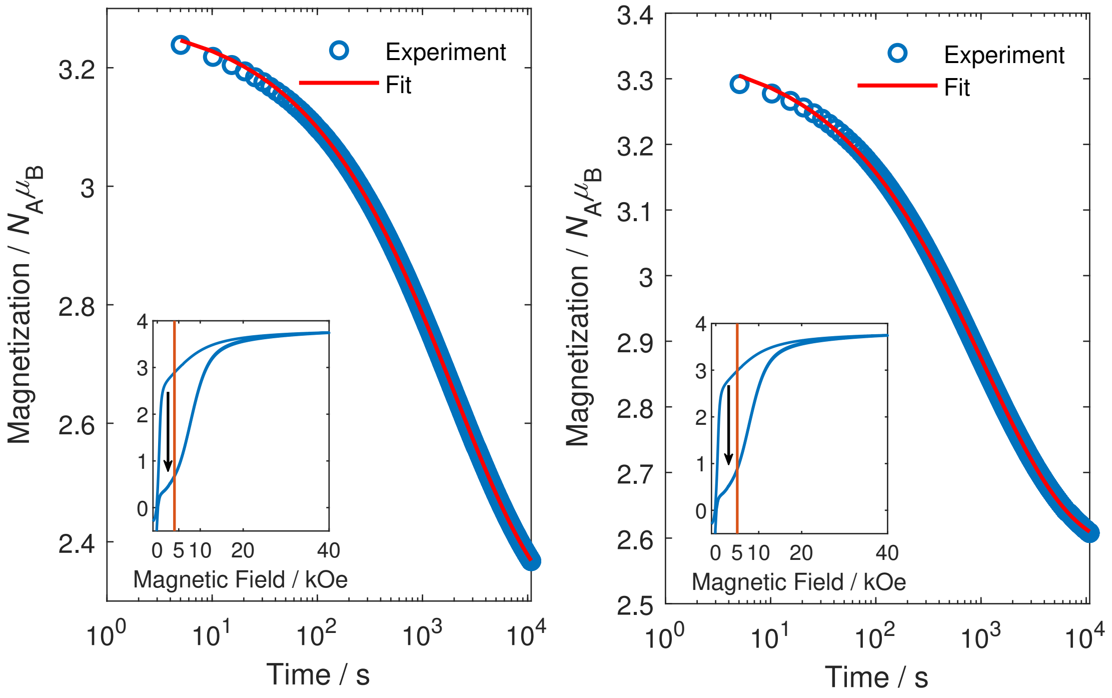

Figure A.16: DC magnetization decay curves as a function of time (circles) and corresponding fits (line) of **(K-18-c-6)$_3$[5]** at 1.8 K and 4000 Oe (left) and 5000 Oe (right). The insets show the positions in the hysteresis loop.

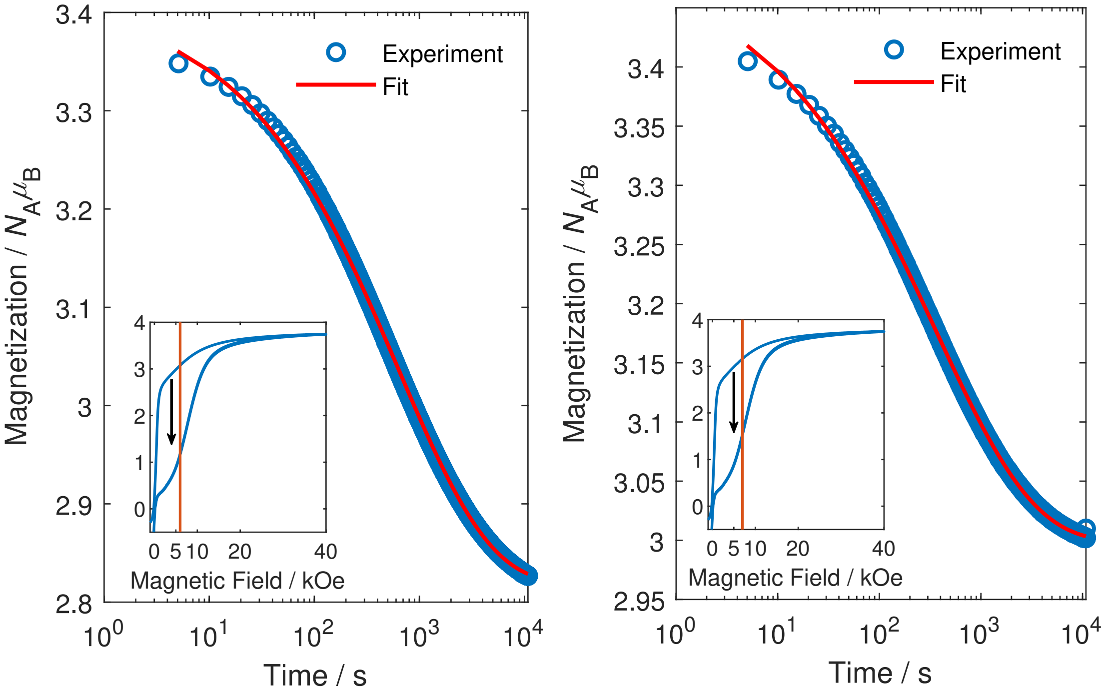

Figure A.17: DC magnetization decay curves as a function of time (circles) and corresponding fits (line) of **(K-18-c-6)$_3$[5]** at 1.8 K and 6000 Oe (left) and 7000 Oe (right). The insets show the positions in the hysteresis loop.

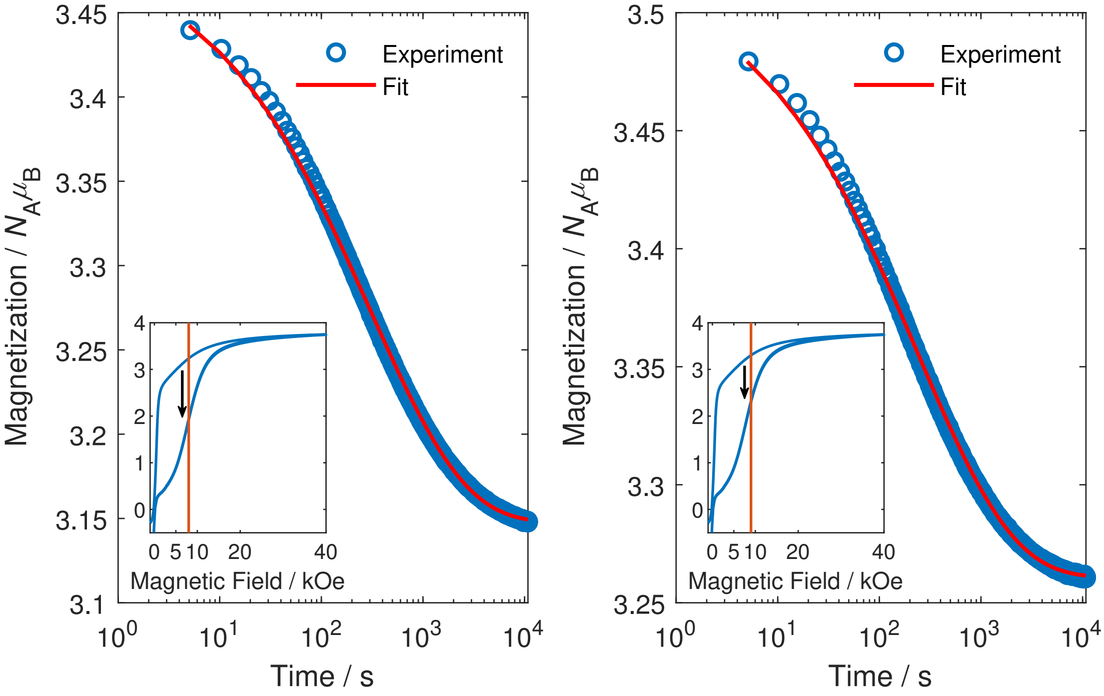

Figure A.18: DC magnetization decay curves as a function of time (circles) and corresponding fits (line) of **(K-18-c-6)$_3$[5]** at 1.8 K and 8000 Oe (left) and 9000 Oe (right). The insets show the positions in the hysteresis loop.

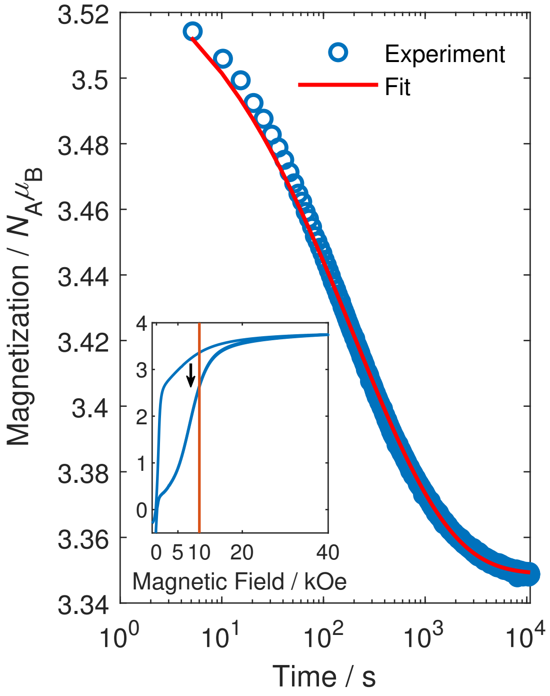

Figure A.19: DC magnetization decay curve as a function of time (circles) and corresponding fit (line) of **(K-18-c-6)$_3$[5]** at 1.8 K and 10 000 Oe. The inset shows the position in the hysteresis loop.

Table A.6: Fit parameters of dc magnetization decay curves of **(K-18-c-6)$_3$[5]** based on Equations 4.2 and 4.3 with numerical errors.

T / K	H / Oe	$M_1(0)$ / $N_A\mu_B$	b_1	τ_1 / s	$M_2(0)$ / $N_A\mu_B$	b_2	τ_2 / s	M_∞ / $N_A\mu_B$
1.8	500	2.285(3)	0.3955(6)	17.5(8)				0.332 64(4)
1.8	1000	1.517(1)	0.2998(4)	27 350(60)	0.774(1)	0.4883(5)	46.09(4)	0.684$^{(a)}$
1.8	1500	1.6974(2)	0.4304(1)	32 736(6)	0.7752(3)	0.3535(1)	13.87(1)	1.007$^{(a)}$
1.8	2000	1.6995(7)	0.4426(5)	16 550(10)				1.31$^{(a)}$
1.8	3000	1.435(4)	0.466(1)	5560(40)				1.794(3)
1.8	4000	1.0182(6)	0.5183(4)	2061(1)				2.2721(3)
1.8	5000	0.7662(7)	0.5243(6)	1058(1)				2.5837(2)
1.8	6000	0.594(1)	0.495(1)	633(2)				2.8185(1)
1.8	7000	0.4859(7)	0.449(7)	360(1)				2.998 53(7)
1.8	8000	0.3418(9)	0.466(1)	304(2)				3.147 61(7)
1.8	9000	0.2591(8)	0.459(1)	238(2)				3.2607(5)
1.8	10 000	0.1966(6)	0.457(1)	201(1)				3.348 93(3)

(a) Values fixed to those expected on the basis of the Hamiltonian to avoid overparametrization and reach proper fit convergence.

A.2.4. Far-Infrared Measurements

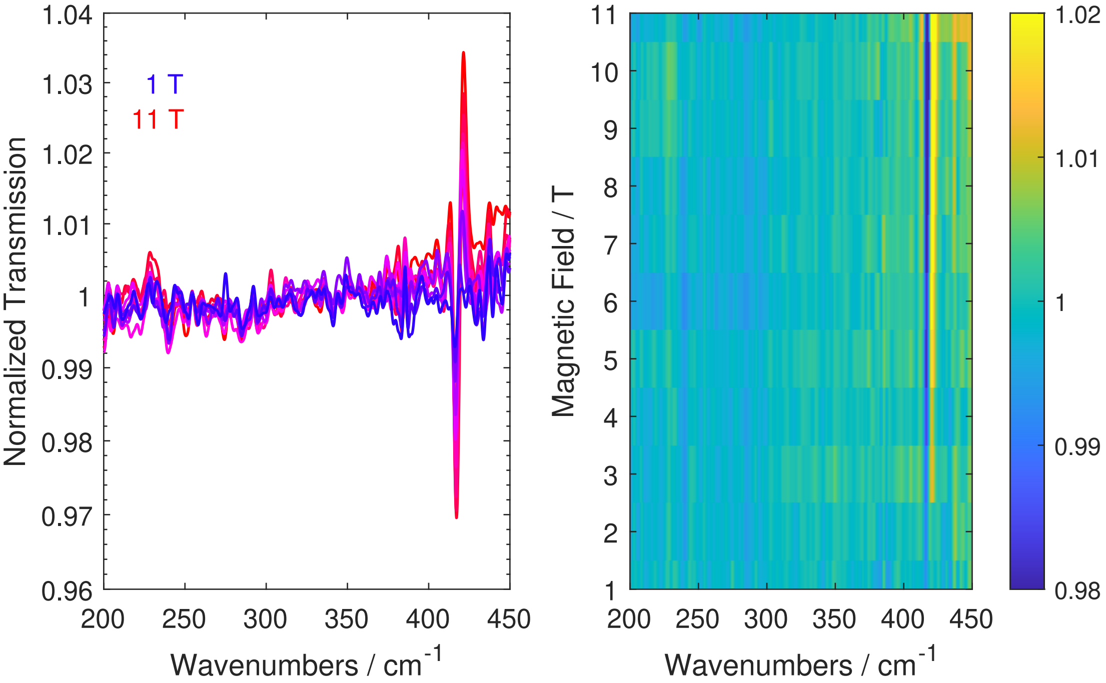

Figure A.20: Field dependence of the FIR measurements of **(K-18-c-6)$_3$**[**5**] between 200 cm^{-1} and 450 cm^{-1} at 4.2 K.

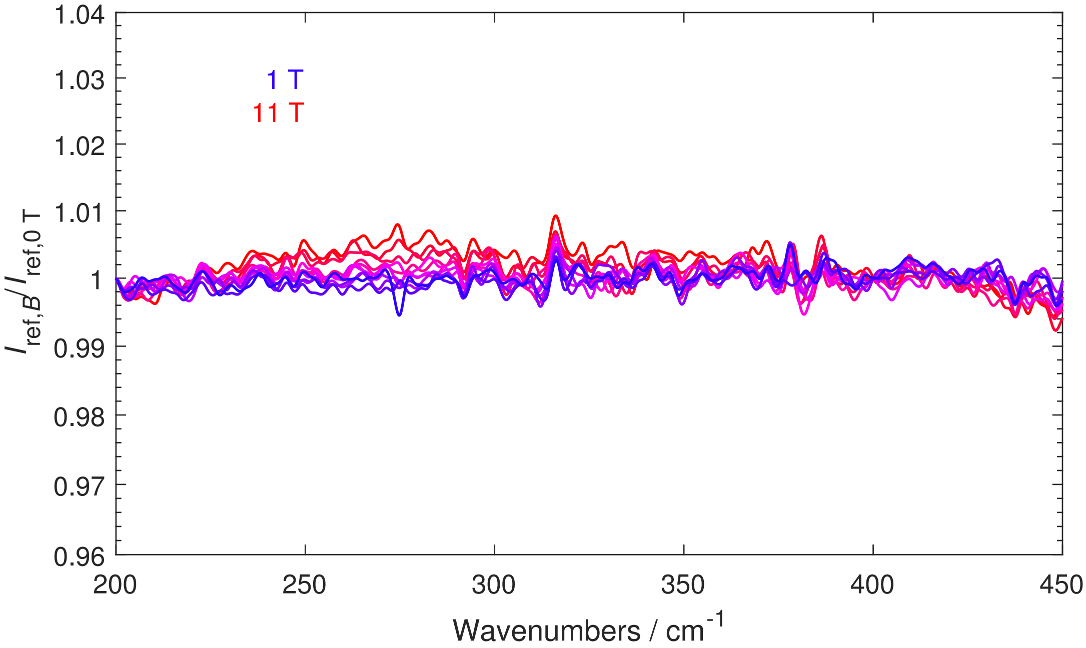

Figure A.21: Field dependence of the FIR reference transmission spectra between 200 cm^{-1} and 450 cm^{-1} at 4.2 K. The transmission spectra were obtained by dividing the reference spectra at each field by the reference spectrum at zero field.

A.3. Iron Extraction from a Podzol Extract with the Biogenic Ligand Desferrioxamine B

A.3.1. Dynamic Susceptibility Measurements of B9 at Applied Field

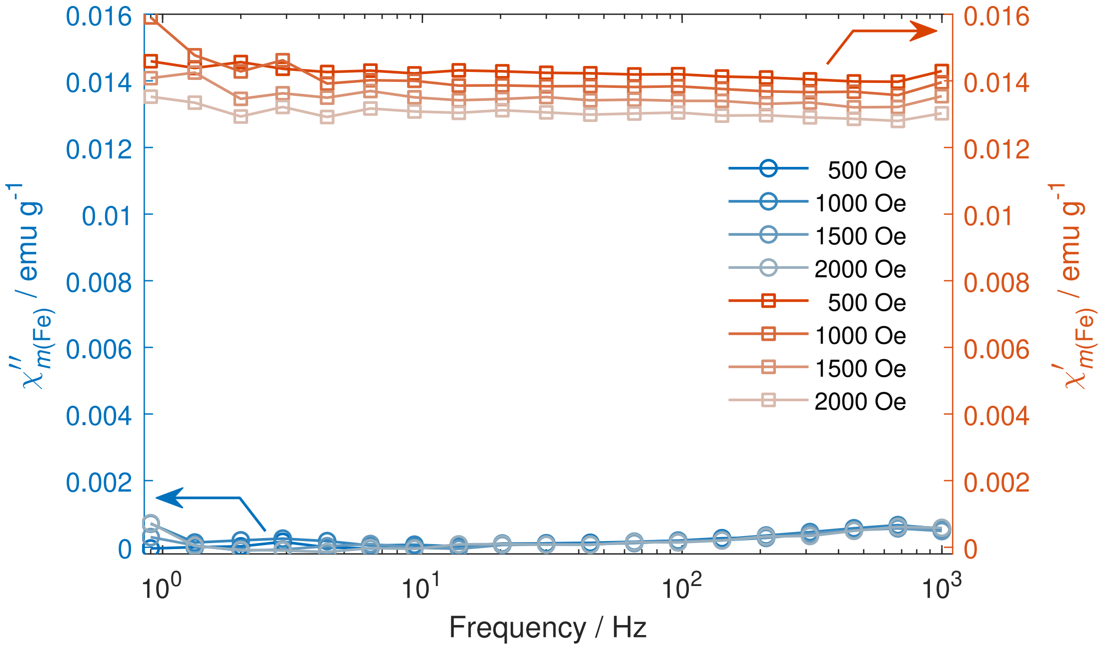

Figure A.22: In-phase and out-of-phase susceptibility of **B9** at 1.8 K and frequencies as indicated under applied static field. Solid lines are guides for the eye. The data are referenced to the sample's iron content.

A.3.2. Mössbauer Spectra at 77 K

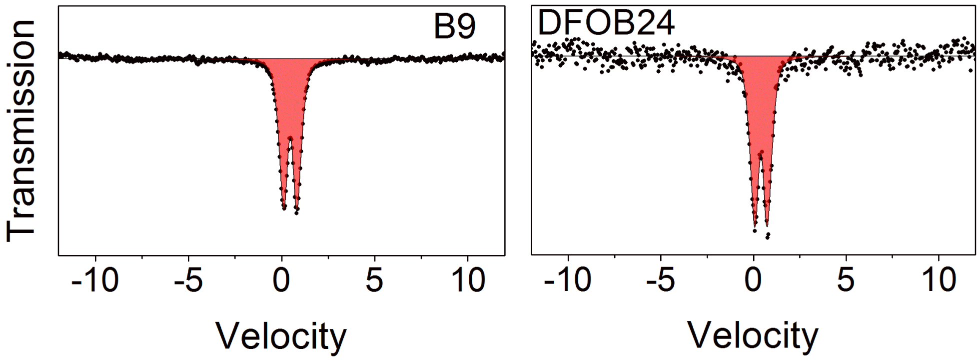

Figure A.23: Mössbauer spectra of **B9** and **DFOB24h** at 77 K.

A.3.3. Contribution of FeDFOB and B9 to the Spectra of Treated Soil Extracts

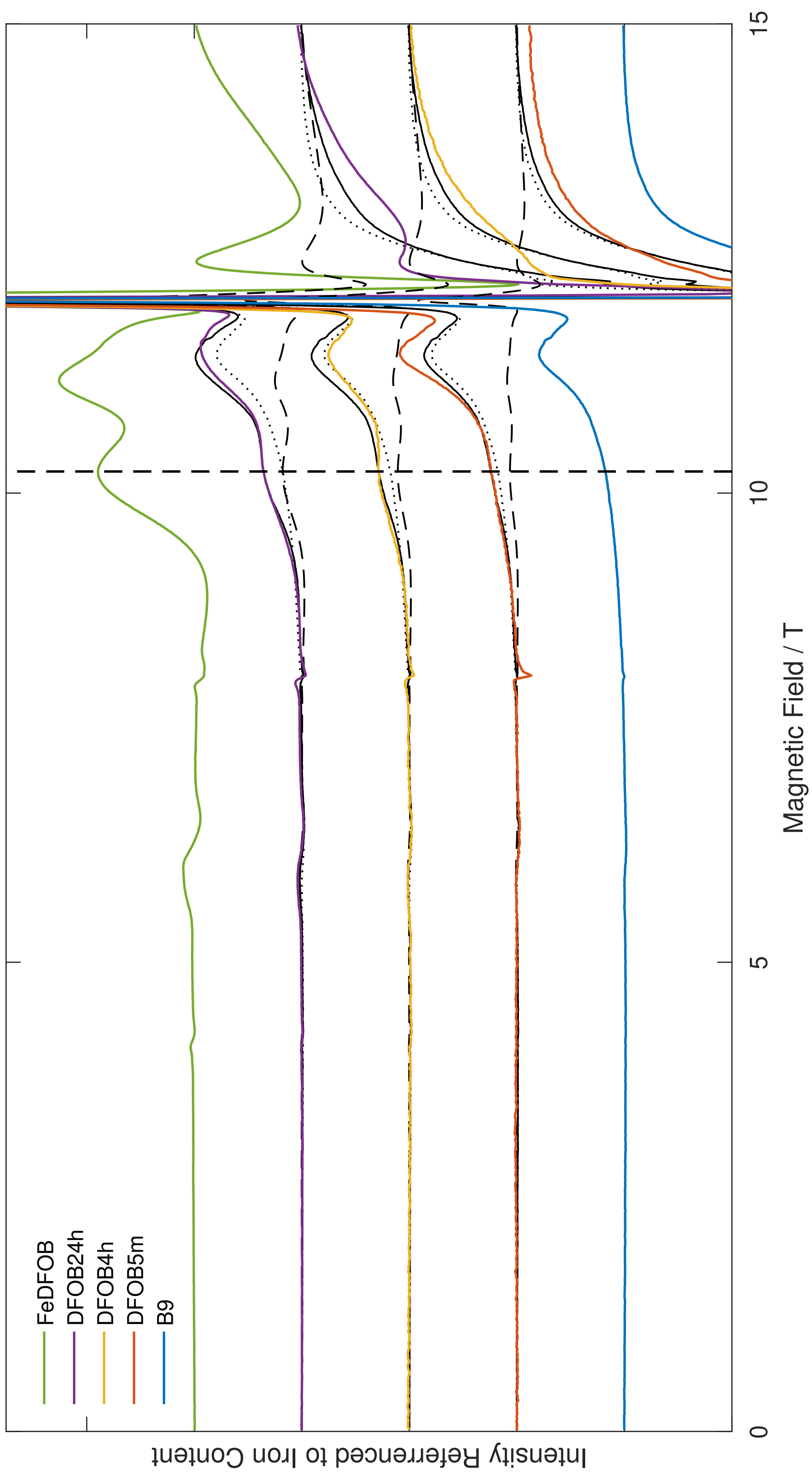

Figure A.24: High-frequency EPR spectra of the pure and treated soil extracts and **FeDFOB** as reference at 340 GHz and temperatures close to 12 K (colored lines). All spectra are normalized to the corresponding iron content. The vertical line marks the characteristic peak position of **FeDFOB** at 10.23 T. The black spectra indicate the proportionate contributions of **FeDFOB** (dashed), **B9** (dotted) and their sum (solid) to the spectra based on the relative intensities at 10.23 T.